General Disclaimer

One or more of the Following Statements may affect this Document

- This document has been reproduced from the best copy furnished by the organizational source. It is being released in the interest of making available as much information as possible.

- This document may contain data, which exceeds the sheet parameters. It was furnished in this condition by the organizational source and is the best copy available.

- This document may contain tone-on-tone or color graphs, charts and/or pictures, which have been reproduced in black and white.

- This document is paginated as submitted by the original source.

- Portions of this document are not fully legible due to the historical nature of some of the material. However, it is the best reproduction available from the original submission.

NASA TECHNICAL MEMORANDUM

NASA TM-73,175

NASA TM-73,175

AN AERODYNAMIC INVESTIGATION OF TWO 1.83-METER-DIAMETER FAN SYSTEMS DESIGNED TO DRIVE A SUBSONIC WIND TUNNEL

V. Robert Page, William T. Eckert, and Kenneth W. Mort

Ames Research Center, NASA

and

Ames Directorate, USAAMRDL, AVRADCOM
Ames Research Center
Moffett Field, Calif. 94035

September 1977

AN AERODYNAMIC INVESTIGATION OF TWO 1.83-METER-DIAMETER FAN SYSTEMS DESIGNED TO DRIVE A SUBSONIC WIND TUNNEL

V. Robert Page, William T. Eckert*, and Kenneth W. Mort

Ames Research Center, NASA
and
Ames Directorate, USAAMRDL, AVRADCOM
Ames Research Center
Moffett Field, CA 94035

SUMMARY

An experimental, aerodynamic investigation was made of two 1.83 m (6 ft) diameter (.15 scale) fan systems which are being considered for the repowered drive section of the 40- by 80-Foot Wind Tunnel at NASA Ames Research Center. One system was low-speed, the other was high-speed.

The low-speed fan was tested at various stagger angles from 32.9° to 62.9°. At a fan blade stagger angle of 40.8° and operating at a tip speed of 115 m/sec (377 ft/sec), the low-speed fan developed 207.3 m (680 ft) of head.

The high-speed fan had a design blade stagger angle of 56.2° and was tested at this stagger angle only. The high-speed fan operating at 191.5 m/sec (628.3 ft/sec) developed 207.3 m (680 ft) of head.

This report presents the radial distributions of static pressure coefficients, total pressure coefficients, and angles of swirl. The radial surveys were conducted at four azimuth locations in front of the fan, and repeated downstream of the fan. Data were taken for various flow control devices and for two inlet contraction lengths. The parameters of mass flow and fan rotational speed setting are tabulated for each configuration, along with the resulting fan system efficiencies.

---

*USAAMRDL, AVRADCOM, Ames Research Center

NOTATION

c	airfoil chord, cm (in)
DELTA PS/Q	Static pressure coefficient, referenced to atmospheric pressure at survey station, non-dimensionalized by the mass-weighted average dynamic pressure at the survey station
DELTA PT/Q	Total pressure coefficient difference referenced to atmospheric pressure at survey station, non-dimensionalized by the mass-weighted average dynamic pressure at the survey station
D-1	Flow distortion configuration; see figure 1(g)
D-2	Flow distortion configuration; see figure 1(g)
H	Normalized total pressure rise, % of design value
h_p	Fan power input, % of design value
MF	Mass flow, % of design value
N	Fan rotational speed, % of design value
R	Radial distance from fan centerline, m(ft)
R_c	Airfoil camber radius (see figure 2(a)), cm (in)
RT	Tip radius, m (ft)
Swirl	Rotational angle of flow with respect to fan shaft centerline, positive in direction of rotation, deg
t_{max}/c	Maximum airfoil thickness-to-chord ratio
δ	Possible variation from indicated value of parameter
η	Fan efficiency, based on average weight flow, isentropic developed head, and shaft power input: $\frac{\text{(weight flow)} \cdot \text{(head)}}{\text{(power)}}$
ξ	Fan stagger angle measured at 0.75 RT (see figure 2(a)), deg

ϕ Airfoil camber angle (see figure 2(a)), deg

$\not\in$ Centerline

Subscripts

max maximum

r fan rotor

s stator

All dimensional units are SI (English)

INTRODUCTION

The main drive power system of the 40- by 80-Foot (12.2- by 24.4-meter) Wind Tunnel is being redesigned to increase the maximum testing speed. The design concept for the drive unit is a variable-speed motor/variable-pitch fan combination with two modes of operation. Lower wind tunnel speeds are to be attained by varying motor speed at fixed blade pitch, and higher air speeds will be achieved by varying the fan blade pitch at constant fan speed.

Two fans have been under study for the drive system. A high-speed fan with a tip speed of 191.5 m/s (628.3 ft/s), and a low-speed fan having a tip speed of 114.9 m/s (377 ft/s). The high-speed fan was predicted to have higher efficiency but substantially more noise than the low speed fan. To verify these studies, two fan systems (i.e., two fans and two stators) were designed, fabricated, assembled, and tested. The performance data are presented in this report and the acoustic data are described in reference 1.

The test stand used for this investigation was a .15-scale model of the entire drive system including the nacelle, fan diffuser, and enclosure. Two inlet contractions and various flow-straightening and distortion devices were tested. Data describing the diffuser performance are presented in reference 2.

MODEL AND APPARATUS

Test Stand Assembly

Photographs and sketches of the basic geometry of the model test stand are presented in figure 1. A three-quarter front view showing the bellmouth inlet is shown in figure 1(a). A three-quarter rear view (figure 1(b)) shows the outside of the diffuser area and the exit doors. Figure 1(c) is a close-up view of the low speed fan showing the 1.22 m (4 ft) throat transition. This contraction length was later increased to 2.13 m (7 ft). The transition transformed the approximately 2.11 m (6.92 ft) square duct into a circular duct with a diameter of about 1.84 m (6.03 ft). A side-view sketch with pertinent dimensions and details is presented in figure 1(d). The two transition lengths are shown in figure 1(e).

From the 10.4 m (34 ft) station ("station" denotes distance from inlet face of test stand - see figure 1(d)) to the 13.3 m (43.6 ft) station, the inside diameter was approximately 1.84 m (6.03 ft) and contained the centerbody. The centerbody was .91 m (3 ft) in diameter, mounted on faired struts, and contained a 1.12 MW (1500 hp) variable-frequency electric drive motor; the fan was cantilevered off the forward end of the motor and the tail fairing cantilevered off the aft end into the diffuser.

The diffuser was 4.06 m (13.32 ft) long and, with the tail cone fairing used, gave an equivalent diffuser cone angle of about 11.4°.

The constant-area section aft of the diffuser was about 2.21 m (7.25 ft) high by 2.08 m (6.83 ft) wide and almost 6.4 m (21 ft) long. The two doors at the outlet had a common hinge and were opened equally to produce the desired mass flow.

Coordinates for the nose cone spinner and support struts are presented in Table I.

Fan Rotor and Stator

The rotor blade and stator vane design consisted of wrapping a modified C-4 airfoil blade thickness distribution (Table II) around a circular-arc mean line. Blade geometric characteristics are presented in figure 2 for the high-speed and low-speed fan systems. Figure 2(a) is a sketch of a blade section with geometric definitions. High-speed fan geometric characteristics are shown in figures 2(b) and 2(c) and the low-speed fan characteristics are presented in figures 2(d) and 2(e). The solidity at the 3/4 radius is given in Table III. The low-speed fan had a design blade stagger angle of 40.8°, and operating at a tip speed of 114.9 m/sec (377 ft/sec) developed 207 m (680 ft) of head. The high-speed fan had a design blade stagger angle of 56.2°, and operating at a tip speed of 191.5 m/sec (628 ft/sec) developed 207 (680 ft) of head. The weight flow and power were the same for both fans, 1632.5 N/sec (367 lb/sec) and 376.7×10^{3} W (505 hp) respectively (see Table III).

Flow Control Devices

Figures 1(f) and 1(g) show the various devices used to control the flow or alter the boundary layer. The flow control devices consisted of a honeycomb, the honeycomb with a uniform screen, a non-uniform, layered distortion screen, and a moderate vertical wall or air dam.

The honeycomb (figure 1(f)) used was 25.4 cm (10 in) deep with 19 mm (.75 in) cells; this was initially installed about 3.67 m (12 ft) downstream of the diffuser to prevent upstream distortion from the exit doors. The honeycomb was removed early in the study and attached to the coarse wire screen (figure 1(c)) at the 5.5 m (18 ft) station. The honeycomb at this new location was used to straighten the flow going into the fan.

With the honeycomb installed at the 5.5 m station, an inlet screen (figure 1(f)) was added at the 7.93 m (26 ft) station to help control the inflow. The screen was window screen with a mesh of 14 by 18 per square 25 mm (1 in) and each strand of wire had a diameter of .279 mm (.011 in).

A distortion screen (of the same 14 by 18 mesh screen) was attached (fig. 1(g)) in front of the coarse wire screen as shown in figure 1(f) in an attempt to duplicate the expected distorted flow (from boundary-layer-build-up) going into the full-scale fans. The screen (designated D-1) was installed horizontally across the lower one-half of the duct;

with one layer completely covering the lower one-half of the duct, plus a second layer over the lower one-quarter of the duct, and a third layer over the lower one-eighth of the duct.

In a further attempt to simulate the low-energy boundary layer entering the full-scale fan, a partial blockage (designated D-2, figure 1(g)) was employed. The blockage consisted of a vertical wall across the width of the duct at the 7.93 (26 ft) station, produced approximately the same boundary layer flow conditions that exist in the 40- by 80-Foot Wind Tunnel.

Instrumentation

Three types of data were taken, leading to the results presented in this report. First, the fan rotational speed was measured with a magnetic pick-up device and a frequency counter. Second, the flow temperatures were measured at the test-stand inlet and at the fan discharge by thermocouples and were read out on digital voltmeters. Finally, all pressure data were measured using multiple-tube, water manometers and were recorded photographically. The pressure measuring stations are shown in figure 1(d); a static-pressure ring just downstream of the bellmouth entrance, total pressure rakes just upstream of the fan contraction, and a traversing survey probe near the fan station.

The survey probe measured total and static pressures and flow angularity in the circumferential direction (swirl). Measurements were made at three longitudinal stations: just upstream of the fan

rotor, between the rotor and stators, and just downstream of the stators (see figure 1(d)). The distributions were measured at four, equally-spaced locations around the annulus, designated as port, starboard, top, and bottom.

TEST PROCEDURE

A flow calibration was run on a 0.305 m (1.0 ft) square model of the inlet bellmouth. The calibration was conducted using a pre-calibrated, standard ASME long-radius flow nozzle. The calibrated mass flow of the inlet was based on the static pressure drop at the throat and the temperature at the entrance.

The testing procedure used was to make probe surveys at constant fan-speed and constant mass-flow settings for a given blade angle setting. When a series of runs had been made at various mass-flow settings and fan speeds, the probe was moved to a new location and the same procedure repeated.

REDUCTION OF DATA

Calibration and Accuracies

The traversing survey probe was calibrated in the Ames 7- by 10-Foot (2.13- by 3.05-m) Wind Tunnel using a separately calibrated reference probe as a standard.

The pressure readings which were used to determine the various flow parameters were accurate to about $\pm$ 0.64 mm ($\pm$ 0.025 in) of vertical water column height. The survey probe installation errors were about $\pm$ 0.25 deg for the port and starboard locations and about $\pm$ 0.5 deg for the top and bottom azimuth positions. The temperature measurements were accurate to about $\pm$ 1.1° C ($\pm$ 2°F). The fan speed settings were accurate to about 2 rev/min or less than 0.2% of the values used in the data reduction. The shaft torque measurements were accurate to within 40 N-m (30 ft-lb).

The effects of the calibration errors and uncertainties for the survey probe results are presented in figure 3 as functions of swirl angle. The uncertainties for four other pertinent parameters (input power, mass flow, total pressure rise (head), and efficiency) are summarized in Table IV.

Data Sources and Handling

The performance parameters presented were determined from different sources in various ways. The total and static pressure coefficients and swirl angle distributions presented in the figures were determined from the survey probe data taken at several discrete points across the fan annulus. The dynamic pressure used for non-dimensionalizing the pressure coefficients was a mass-weighted average over the entire traverse survey. The mass flow values were based on the static pressure and temperatures measured at the inlet bellmouth. The total pressure rise across the fan (head) was calculated from the average mass-weighted total pressure at the survey station and the average total pressure at the rakes upstream of the contraction (see figure 1(d)). The input power values were based on the fan rotational speed and on measured shaft torque. The fan system efficiency was determined from the weight flow, total pressure rise and input power.

INTERPRETATION OF RESULTS

Caution must be used in the interpretation of the pressure coefficient and efficiency data. The total and static pressure coefficient data are referenced to atmospheric pressure. The fan efficiencies (and head rises) are based on data measured about 2.7 m (9 ft) upstream of the fan disc. Therefore, these data are low due to the losses of the contraction and some of the upstream ducting. "Fan only" or "fan and stator" results may be determined by subtracting upstream measurement parameters (0.3 m upstream of the fan) from those measured just downstream of the component(s) of interest.

PRESENTATION OF DATA

The low-speed fan was studied over a wide range of blade stagger angles. The data are presented in figures 4 through 33 in ascending order beginning with the lowest stagger angle, $\xi = 32.9^{\circ}$, and ending with the highest stagger angle tested (62.9°). Figures 34 and 35 show the results for the high-speed fan. An index to the figures is presented in Table V.

The data presented are the static pressure and total pressure coefficients and swirl angle as functions of radial location for various configurations and stagger angles. The data are subdivided within their stagger-angle groups by the parameters varied: the stations, azimuths, speeds, and flow settings.

For the low-speed fan the widest coverage of variables occurred at the design blade stagger angle; these data are presented in figures 17 through 26. Figures 17, 18, and 19 present data taken upstream of the fan. Figures 17 and 19 show data taken with the original contraction installed. Figure 18 shows the data for the longer modified contraction. Figure 19 presents data taken between the fan and stator for both contractions; i.e., original and then modified, with and without the D-1 inflow distortion configuration. Figures 23 through 26 present data taken downstream of the stator. (The inlet honeycomb was not installed for the data of figure 23.) Figures 23 through 25 present data with the original contraction installed. The data with the D-1 inflow

distortion configuration (taken downstream of the stator) are presented in figure 25. The modified-contraction data are presented for this station in figure 26. The exit doors of the model test stand were off for one series of runs only; these data are presented in figure 24. At "off-design" conditions (i.e., $\xi \neq 40.8^{\circ}$ for the low-speed fan) the configurations tested were held to a bare minimum and reflect conditions pertinent to the full-scale drive fans. The data in figures 27 through 33 are for the longer stagger angles and the two contraction lengths.

The high-speed fan data presented in figure 34 were taken downstream of the stator for all four azimuths. Figure 35 shows the data taken upstream of the fan at the port azimuth. All high-speed fan data were taken without the inlet honeycomb or screen and with the original contraction installed.

DISCUSSION

The data are presented, for the most part, without analysis or comparison. However, figures 36 and 37 present a summary of the experimental aerodynamic performance (head rise and efficiency) as compared to the predicted design points of reference 3. Reasonably good agreement was achieved between analytical and experimental results.

REFERENCES

1. Soderman, Paul T. and Page, V. Robert: Acoustic Performance of Two 1.83-Meter Diameter Fans Designed for a Wind Tunnel Drive System. NASA TP-1008, 1977.

2. Eckert, William T.; Johnston, James P.; Mort, Kenneth W.; and Page, V. Robert: An Experimental Investigation of the Effects of Swirling and Distorted Inflow on the Aerodynamic Performance of a 1.84-Meter Diameter, 11.4-Degree, Annular Diffuser. Prospective NASA TM.

3. Anon: Design of Fans and Model Test Stand for Simulating the Proposed New Fan Power Section of the 40- by 80-Foot NASA-Ames Wind Tunnel. By the Applied Mechanics Branch, Mechanical Engineering Laboratory, Corporate Research and Development, General Electric Company, Schenectady, New York 12301, under Contract No. NAS2-7477, December 1973.

TABLE I.- Contour coordinates for rotor nose cone spinner and nacelle support struts

Spinner		Strut	
Distance from leading edge ÷ maximum diameter	Local radius ÷ maximum diameter	Distance from leading edge ÷ chord	Half thickness ÷ chord
0	0	.007	.009
.028	.137	.014	.013
.056	.192	.025	.017
.083	.233	.0625	.025
.111	.266	.101	.031
.167	.319	.175	.039
.250	.378	.25	.044
.333	.421	.351	.046
.500	.476	.5	.044
.722	.5	.701	.034
.889	.5	.800	.026
		.95	.009
		1.0	0

Maximum nacelle diam. = .914 m (3 ft)

Leading edge radius ÷ chord = .0087

TABLE II.- Basic thickness distribution for a 10% thick airfoil, % chord

Distance from leading edge	Half-thickness, % chord	
	C-4	1/7-Scale model
1.25	1.65	1.65
2.5	2.27	2.27
5.0	3.08	3.08
7.7	3.62	3.62
10	4.02	4.02
15	4.55	4.55
20	4.83	4.83
30	5.0	5.0
40	4.89	4.875
50	4.57	4.512
60	4.05	3.921
70	3.37	3.148
80	2.54	2.205
90	1.6	1.137
95	1.09	.523
100	.56	0

TABLE III - FAN SYSTEM DESIGN PARAMETERS

COMPLETE SYSTEM

Parameter	Design Value
Hub-to-tip diameter ratio	0.5
Drive power, W (HP)	376.7×10^3 (505)
Total pressure rise (head), m (ft) of air	207.3 (680)
Weight flow, N/sec (lb/sec)	1632.5 (367)

ROTOR ONLY

Parameter	Low-Speed Fan	High-Speed Fan
Number of blades	15	9
Solidity at 3/4 radius (chord • No. of blades ÷ circumference)	0.5540	0.2318
Stagger angle at 3/4 radius, deg.	40.8	56.2
Rotational speed, rev/min	1200	2000
Tip speed, m/sec (ft/sec)	115 (377)	191.5 (628.3)

STATOR ONLY

Parameter	Low-Speed System	High-Speed System
Number of blades	23	13
Chord, cm (in)	11.13 (4.38)	15.70 (6.18)
Solidity at 3/4 radius	0.5941	0.4734
Stagger angle at 3/4 radius, deg.	4.28	1.89

TABLE IV - DATA PARAMETER UNCERTAINTIES

Parameter	Uncertainties	
	Low-Speed Fan	High-Speed Fan
Fraction of design input power	± 0.014	± 0.023
Fraction of design mass flow	± 0.008	± 0.008
Fraction of design total pressure rise (head)	± 0.005	± 0.005
Fan system efficiency, percent	± 1.6	± 2.4

TABLE V. FIGURE INDEX

Figure Number	Stagger Angle	Probe Location							Nominal Mass Flow	Rotational Speeds	Inflow Control						Contraction		Remarks
		Station			Azimuth						Inlet Honeycomb		Inlet Screen		Distortion Configuration				
	Deg	Upstream of Fan	Between Fan & Stator	Downstream of Stator	Port	Top	Starboard	Bottom	% of Design	% of Design	In	Out	In	Out	D-1	D-2	Original	Modified	
4	32.9			x	x	x	x	x	Variable	70,100		x		x			x		
5	35.4	x			x	x	x	x	Variable	100	x			x			x		
6	35.4	x			x		x	x	Variable	90,100		x		x			x		Exit honeycomb installed
7	35.4		x		x	x	x	x	Variable	100	x			x			x		
8	35.4			x	x	x	x	x	Variable	90,100		x		x			x		Exit honeycomb installed
9	35.4			x	x	x	x	x	Variable	Variable	x			x			x		
10	38	x				x			Variable	100	x			x				x	
11	38	x				x		x	95	100	x			x		x		x	35% solid blockage distortion @ 7.92 m (26 ft)
12	38		x			x			Variable	100	x			x				x	
13	38		x			x		x	95	100	x			x		x		x	35% solid blockage distortion @ 7.92 m (26 ft)
14	38			x	x	x	x	x	Variable	100	x			x				x	
15	38			x	x	x	x	x	95	100	x		x					x	
16	38			x		x		x	95	100	x			x		x		x	35% solid blockage distortion @ 7.92 m (26 ft)
17	40.8	x			x				Variable	100	x			x			x		
18	40.8	x			x	x	x		Variable	Variable	x			x				x	
19	40.8	x			x	x	x	x	Variable	100	x			x	x		x		
20	40.8		x		x				Variable	100	x			x			x		
21	40.8		x		x	x	x		Variable	100	x			x				x	
22	40.8		x		x	x	x	x	Variable	100	x			x	x		x		

TABLE V. FIGURE INDEX, CONCLUDED

Figure Number	Stagger Angle	Probe Location							Nominal Mass Flow	Rotational Speeds	Inflow Control						Contraction		Remarks
		Station			Azimuth						Inlet Honeycomb		Inlet Screen		Distortion Configuration				
	Deg	Upstream of Fan	Between Fan & Stator	Downstream of Stator	Port	Top	Starboard	Bottom	% of Design	% of Design	In	Out	In	Out	D-1	D-2	Original	Modified	
23	40.8			x	x	x	x	x	Variable	100		x		x			x		
24	40.8			x	x	x	x	x	Variable	100	x			x			x		Exit doors on & off
25	40.8			x	x	x	x	x	Variable	100	x			x	x		x		
26	40.8			x	x	x			Variable	100	x			x				x	
27	45.2			x	x	x	x	x	Variable	70,100		x		x			x		
28	52.8	x					x		Variable	100	x			x			x		
29	52.8		x				x		Variable	100	x			x			x		
30	52.8			x			x		Variable	100	x			x			x		
31	62.9	x			x				Variable	100	x			x				x	
32	62.9			x	x				Variable	100	x			x			x		
33	62.9			x	x				Variable	100	x			x				x	
34	56.2			x	x	x	x	x	Variable	100		x		x			x		High-Speed Fan Data
35	56.2	x			x				Variable	100		x		x			x		High-Speed Fan Data
36	-								Variable	100									η vs MF
37	-								Variable	100									H vs MF

(a) Three-quarter front view of complete test stand

Figure 1.- Geometry of test stand and component hardware.

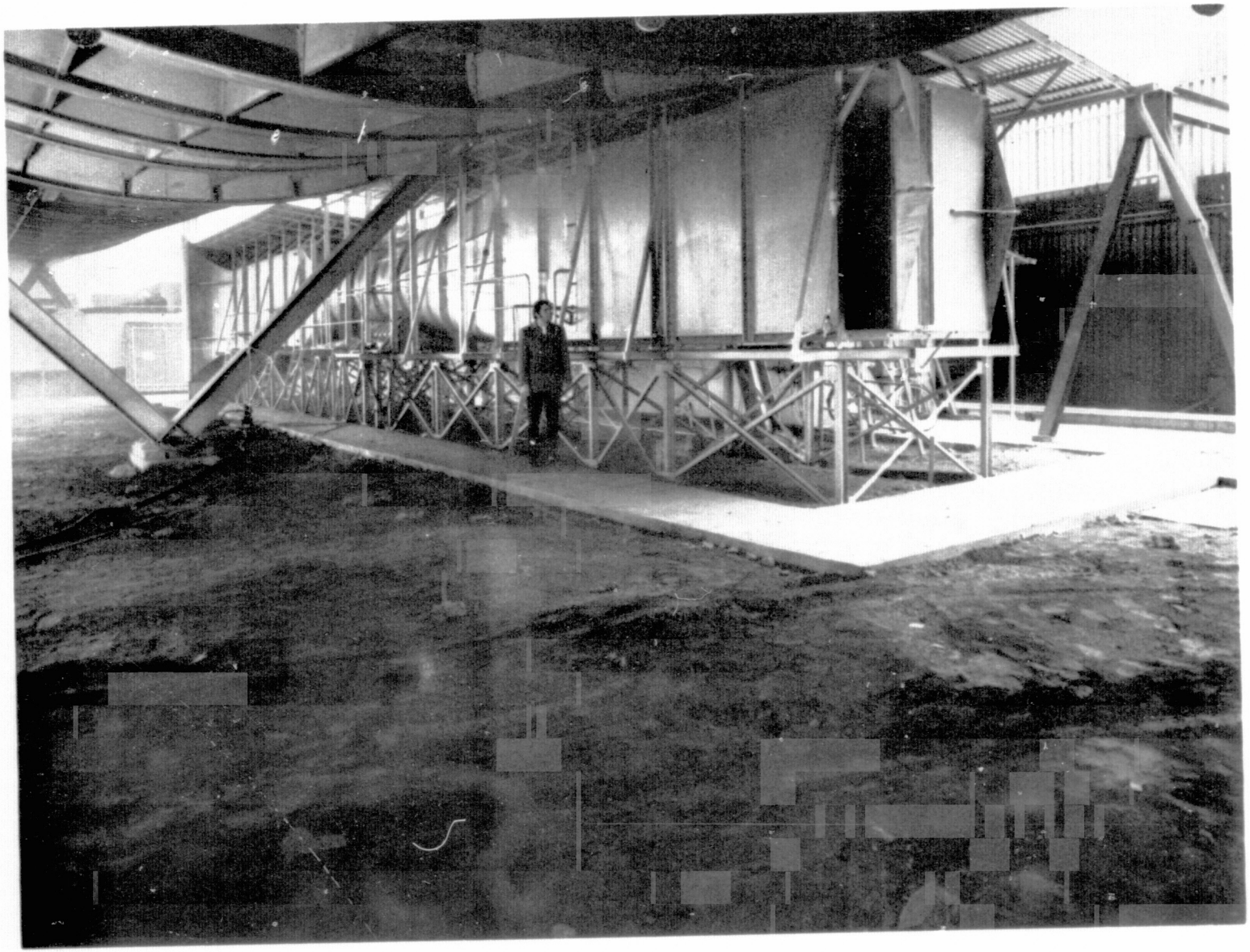

b. - Three-quarter rear view

Figure 1. - Continued.

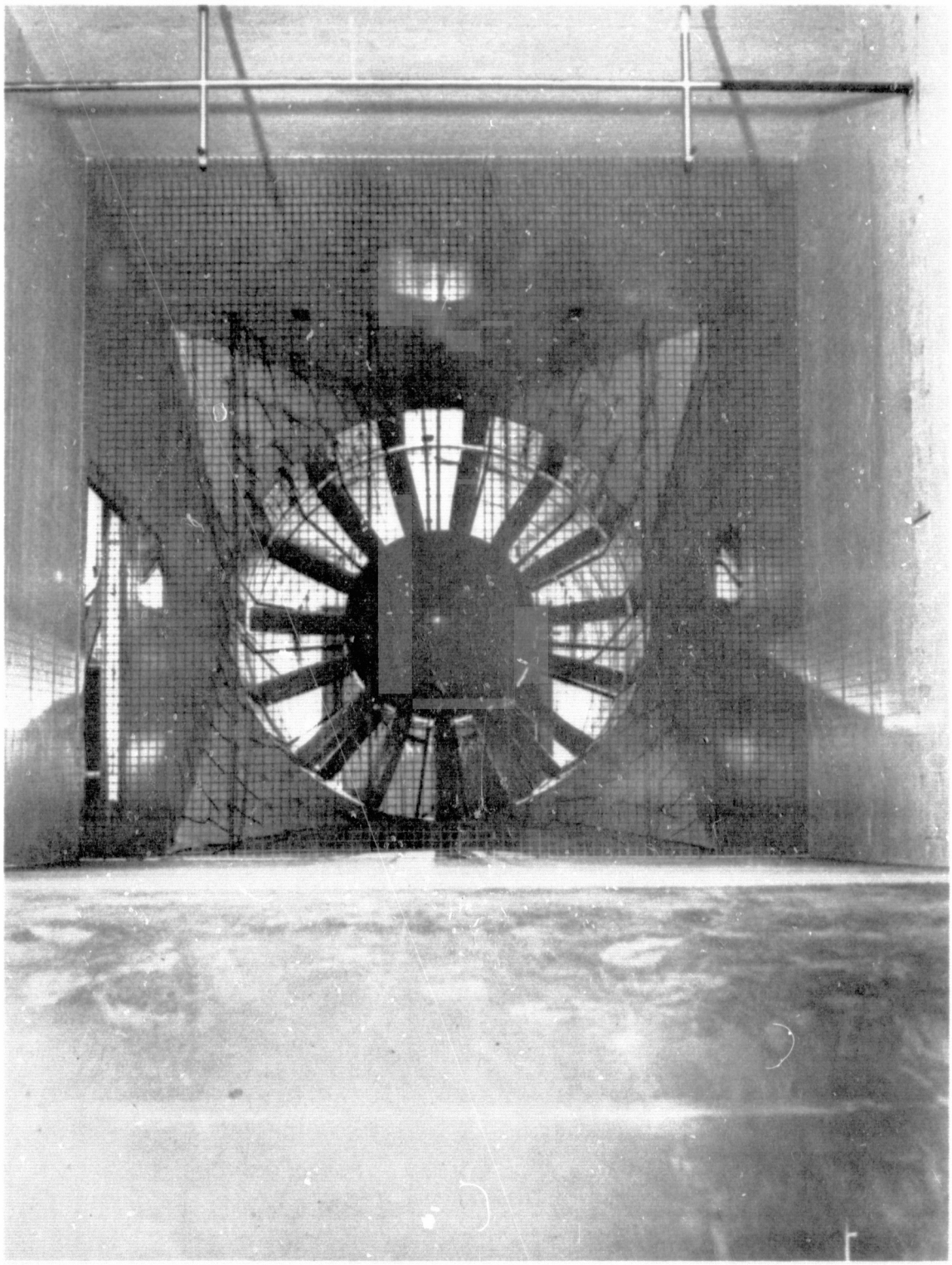

c. - Front-view close-up; inside of duct and fan

Figure 1. - Concluded.

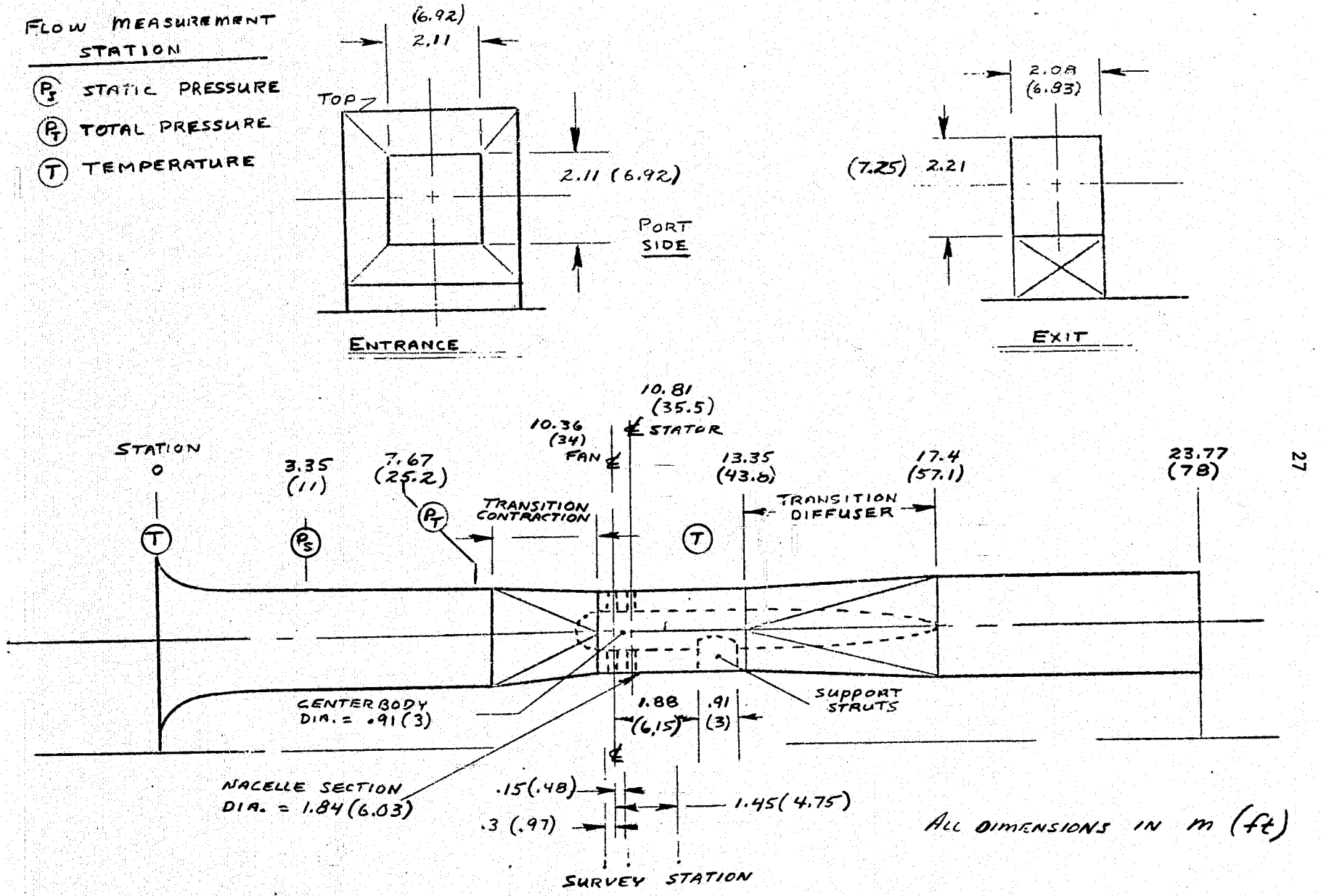

(d) Test stand sideview

Figure 1.- Continued.

1d

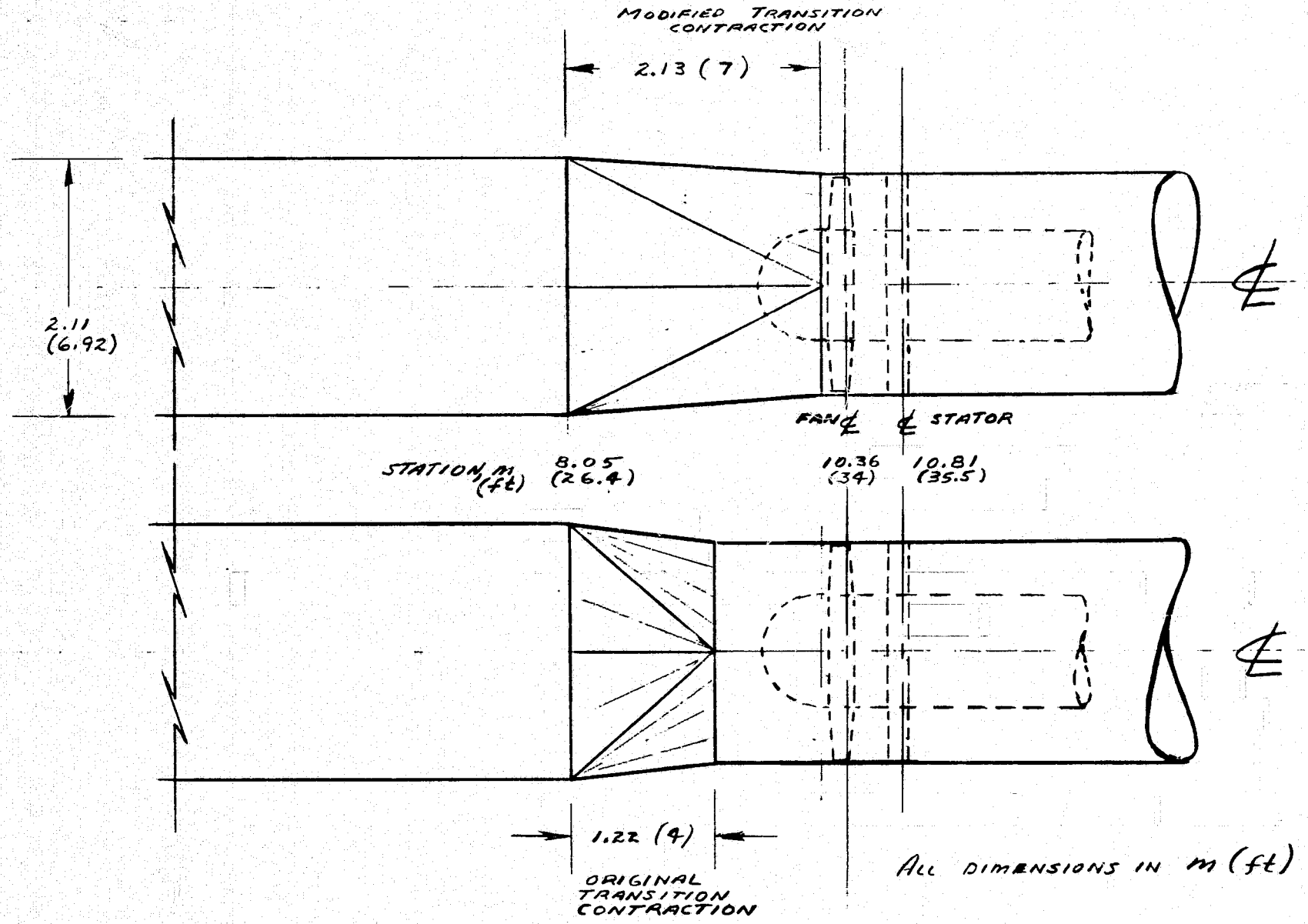

(e) Transition contractions

Figure 1.- Continued.

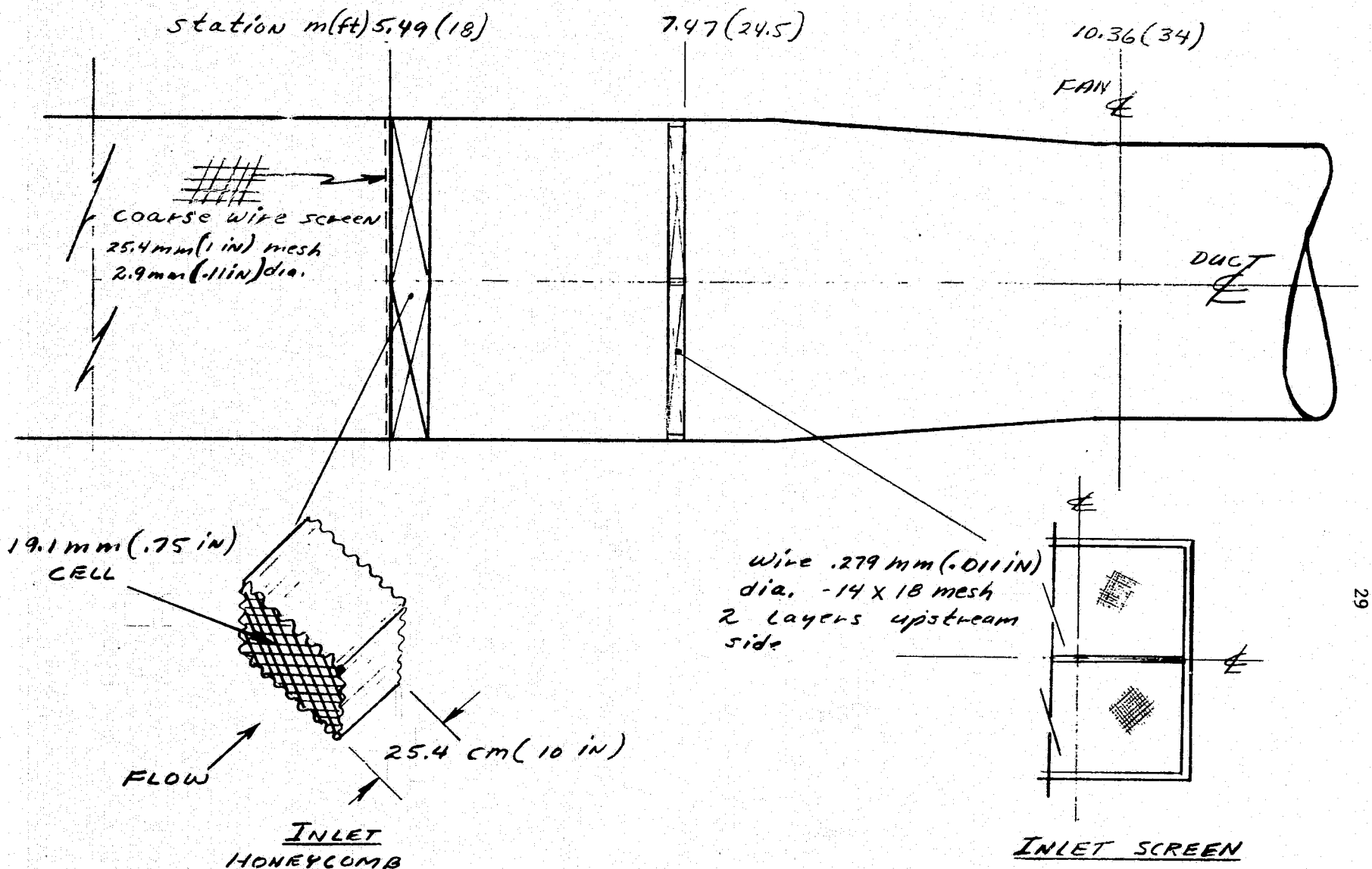

(f) Inlet honeycomb and screen

Figure 1.- Continued.

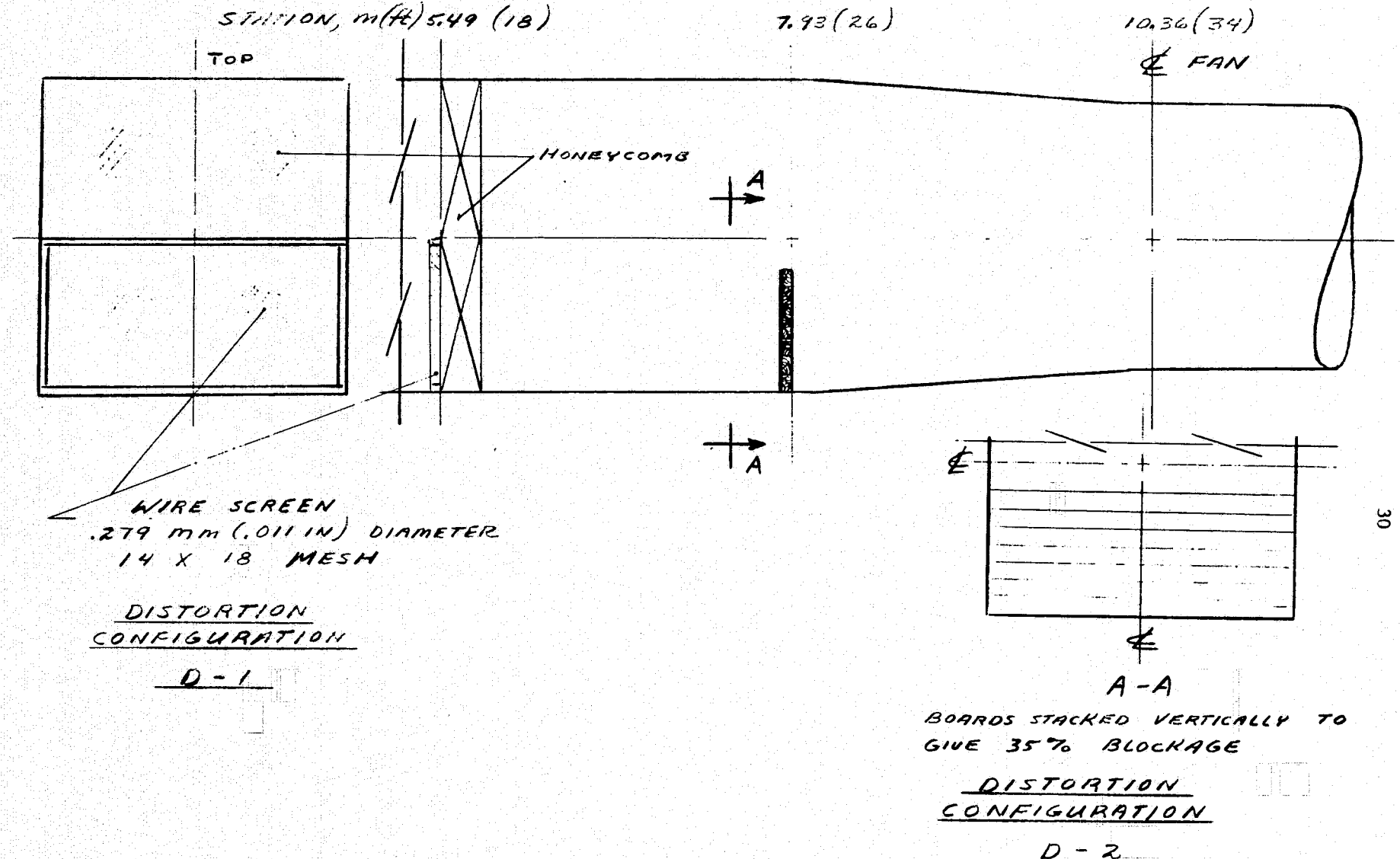

(g) Distortion configurations

Figure 1.- Concluded.

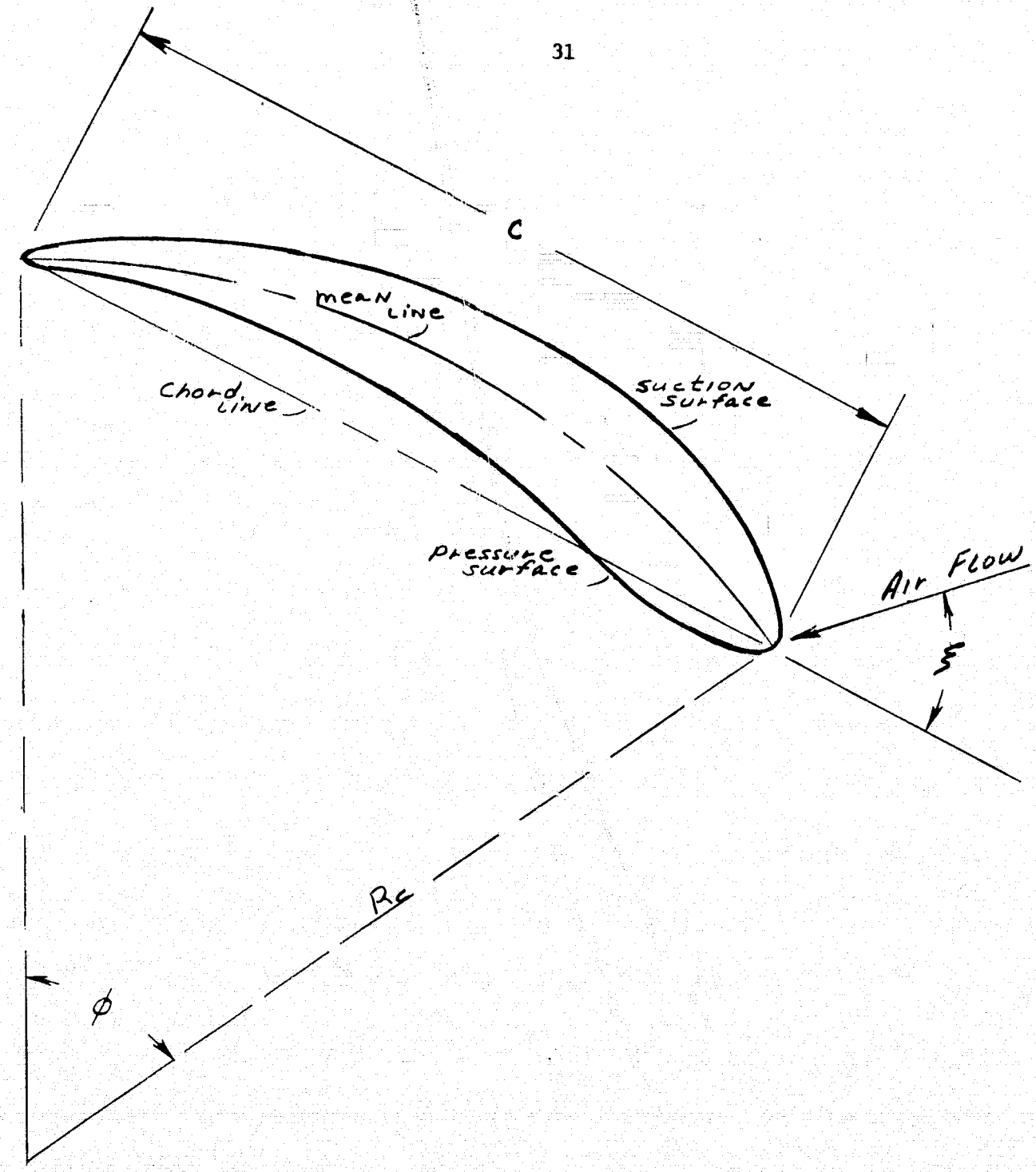

(a) Fan blade geometric definitions

Figure 2.- Fan system geometry for the high-speed and low-speed fans.

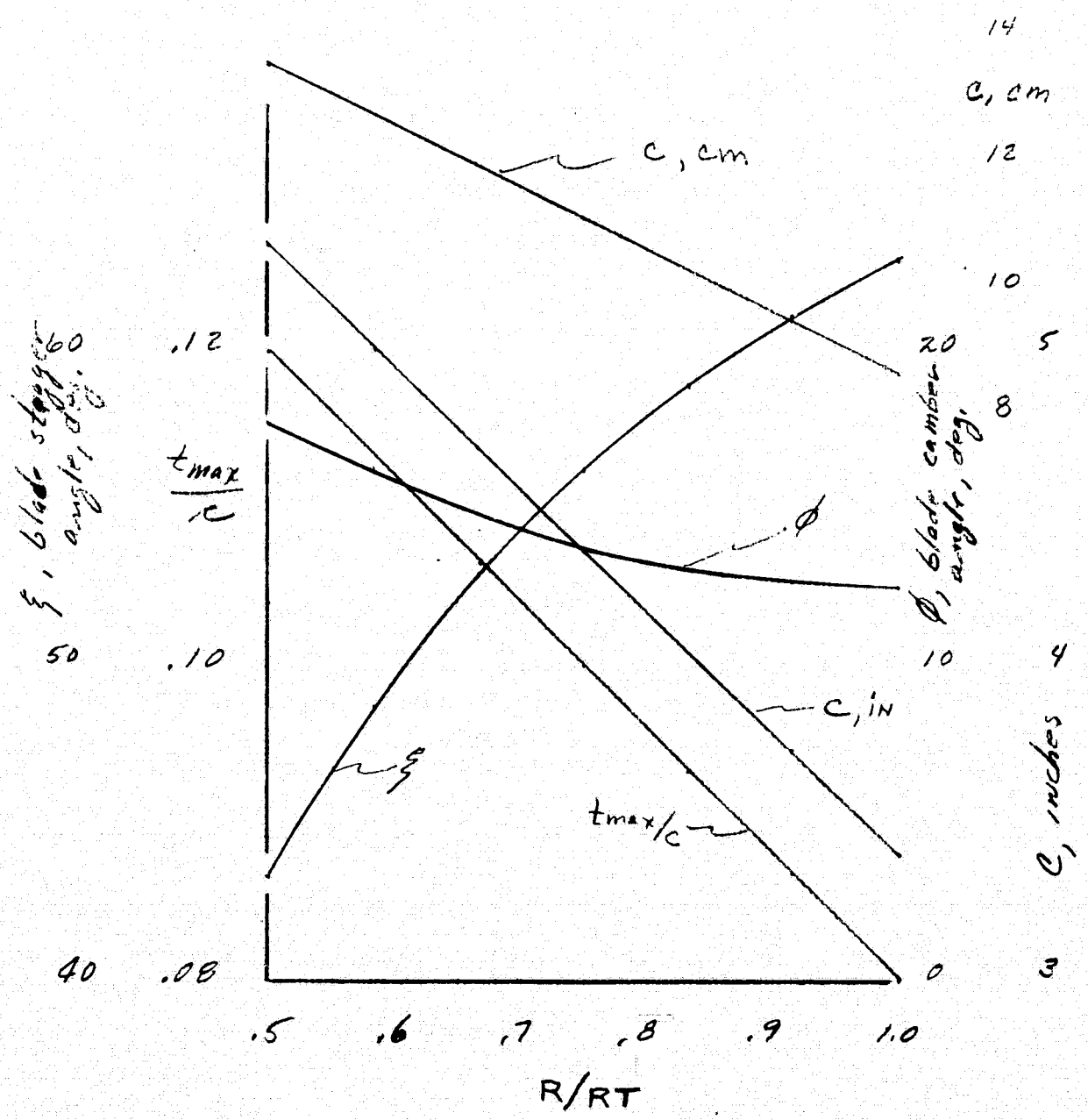

(b) High-speed fan rotor blade geometry: stagger angle, chord, camber angle, and thickness ratio variation with radial location.

Figure 2.- Continued.

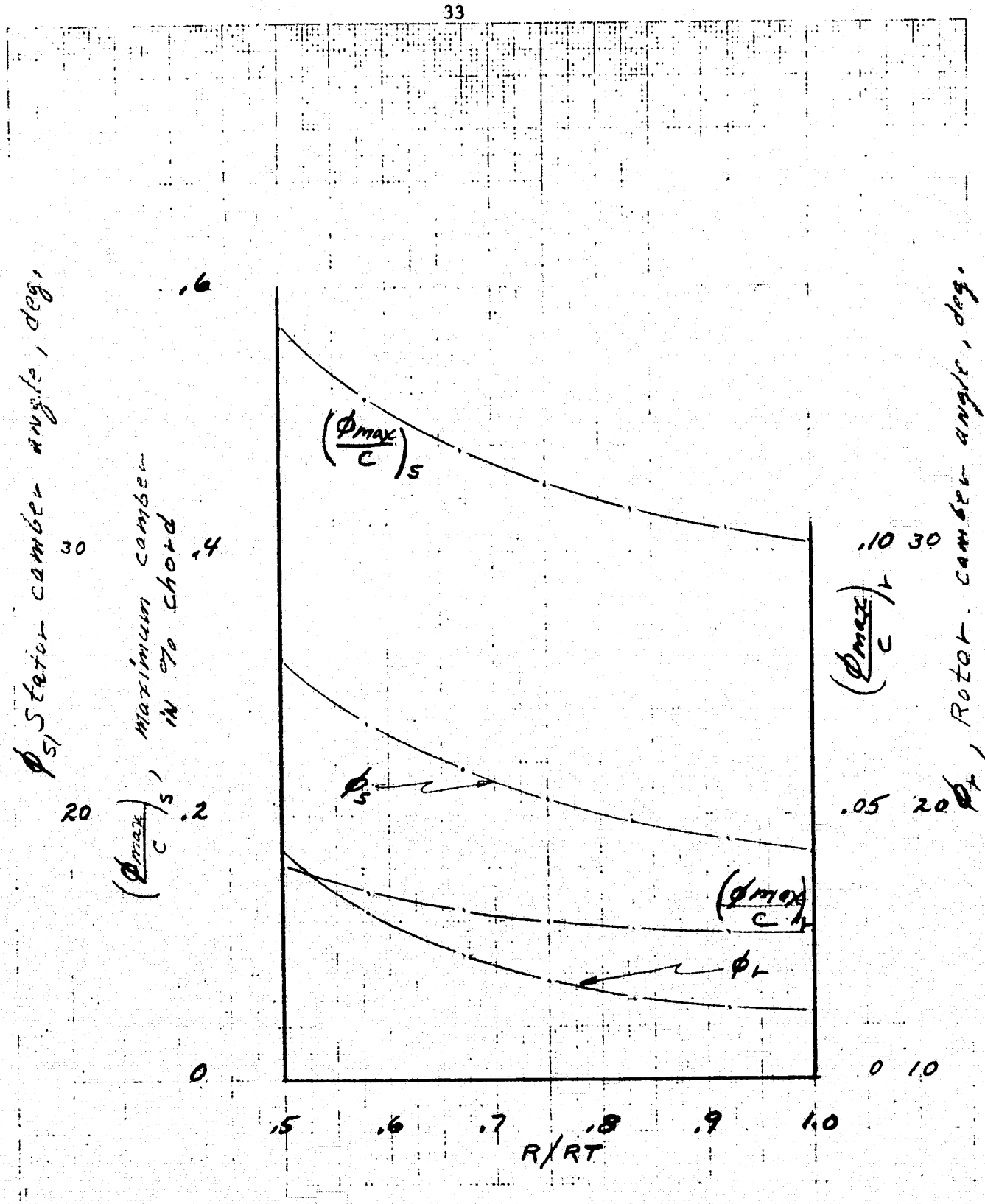

(c) High-speed fan camber and maximum camber variation with radial location.

Figure 2.- Continued.

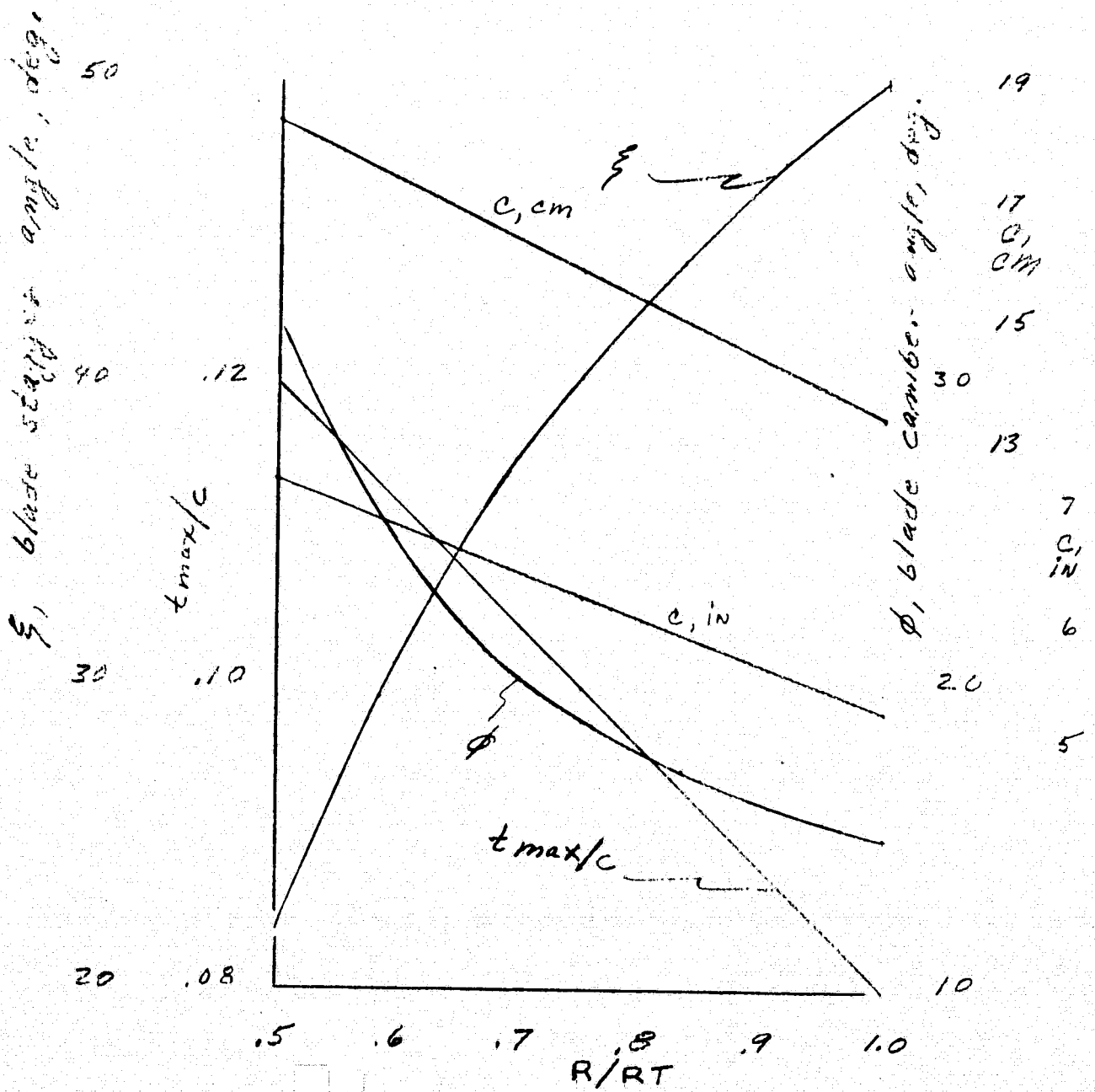

(d) Low-speed fan rotor blade geometry: stagger angle, chord, camber angle, and maximum thickness ratio variation with radial location.

Figure 2.- Continued.

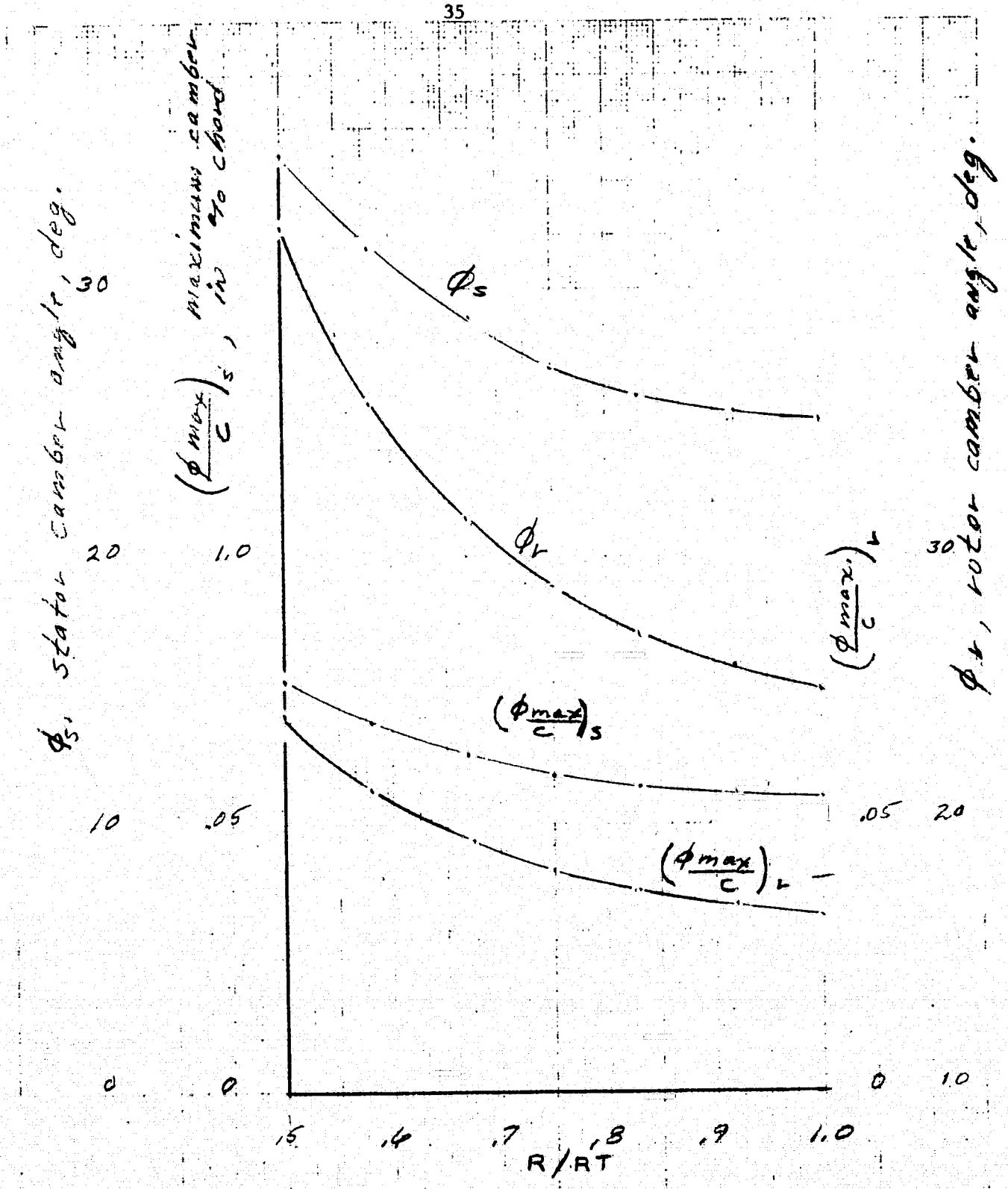

(e) Low-speed fan camber and maximum camber variation with radial location.

Figure 2.- Concluded.

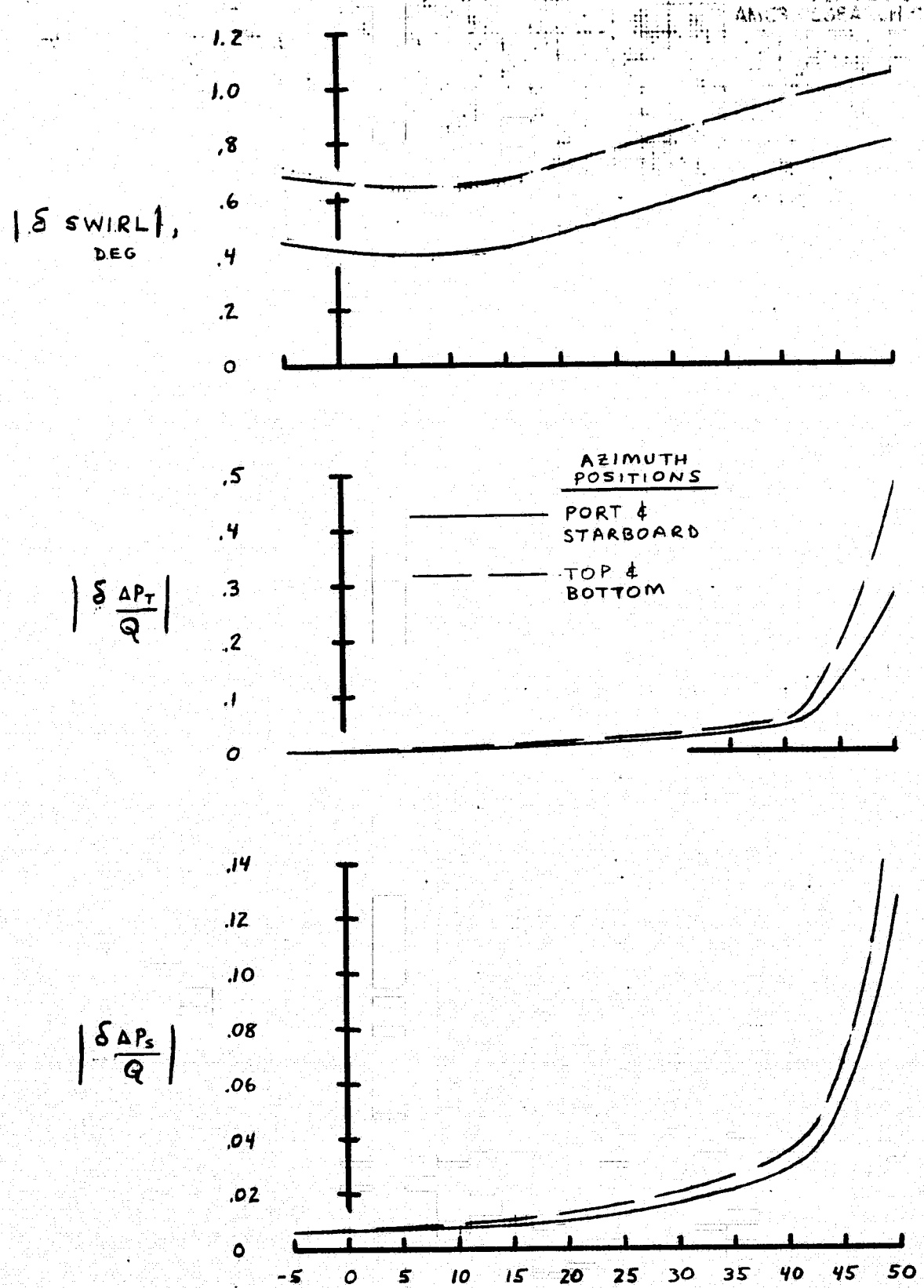

Figure 3.- Variation in magnitude of uncertainties in swirl and in pressure coefficients with angle of swirl.

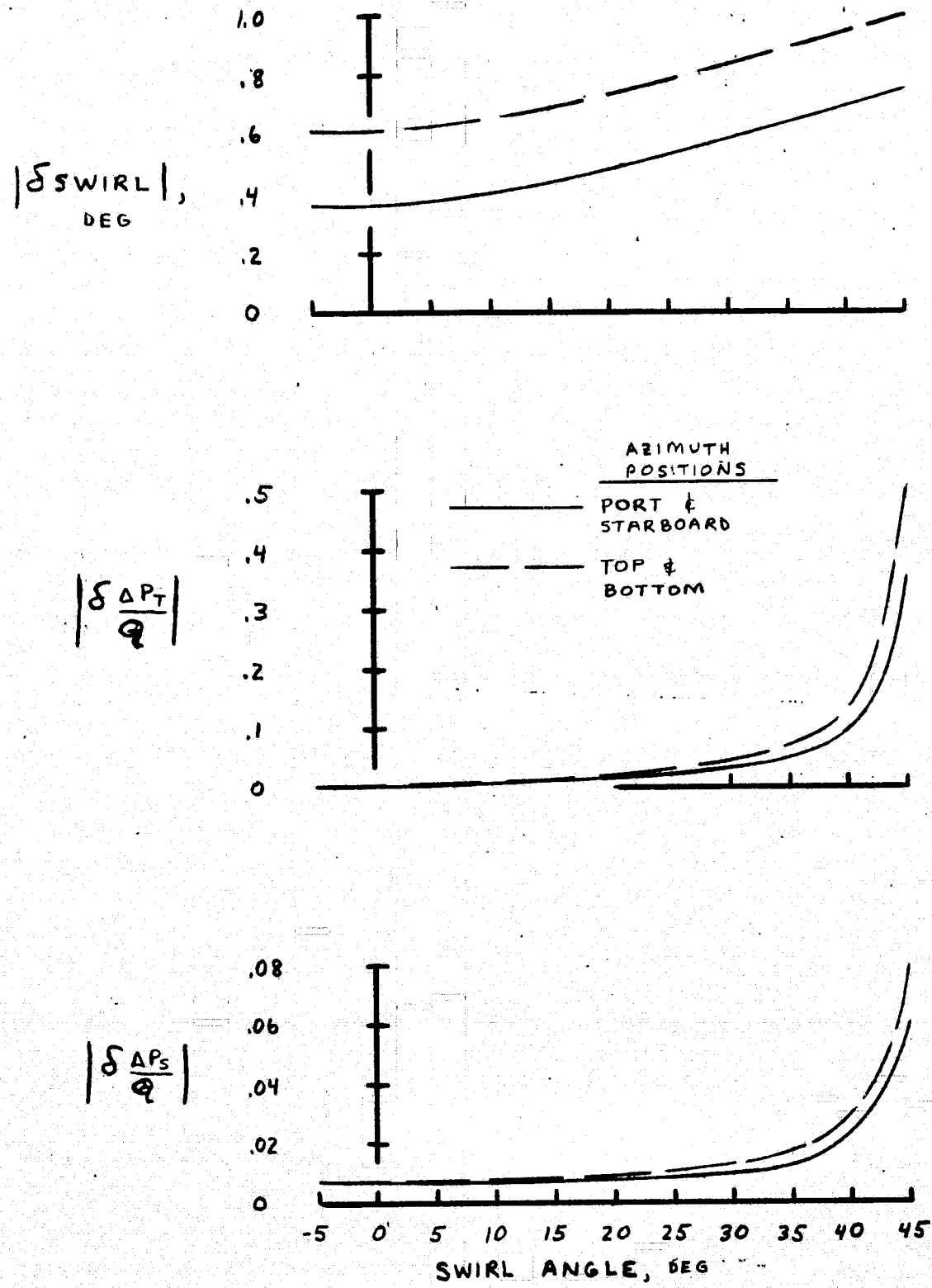

(b) High-speed fan

Figure 3.- Concluded.

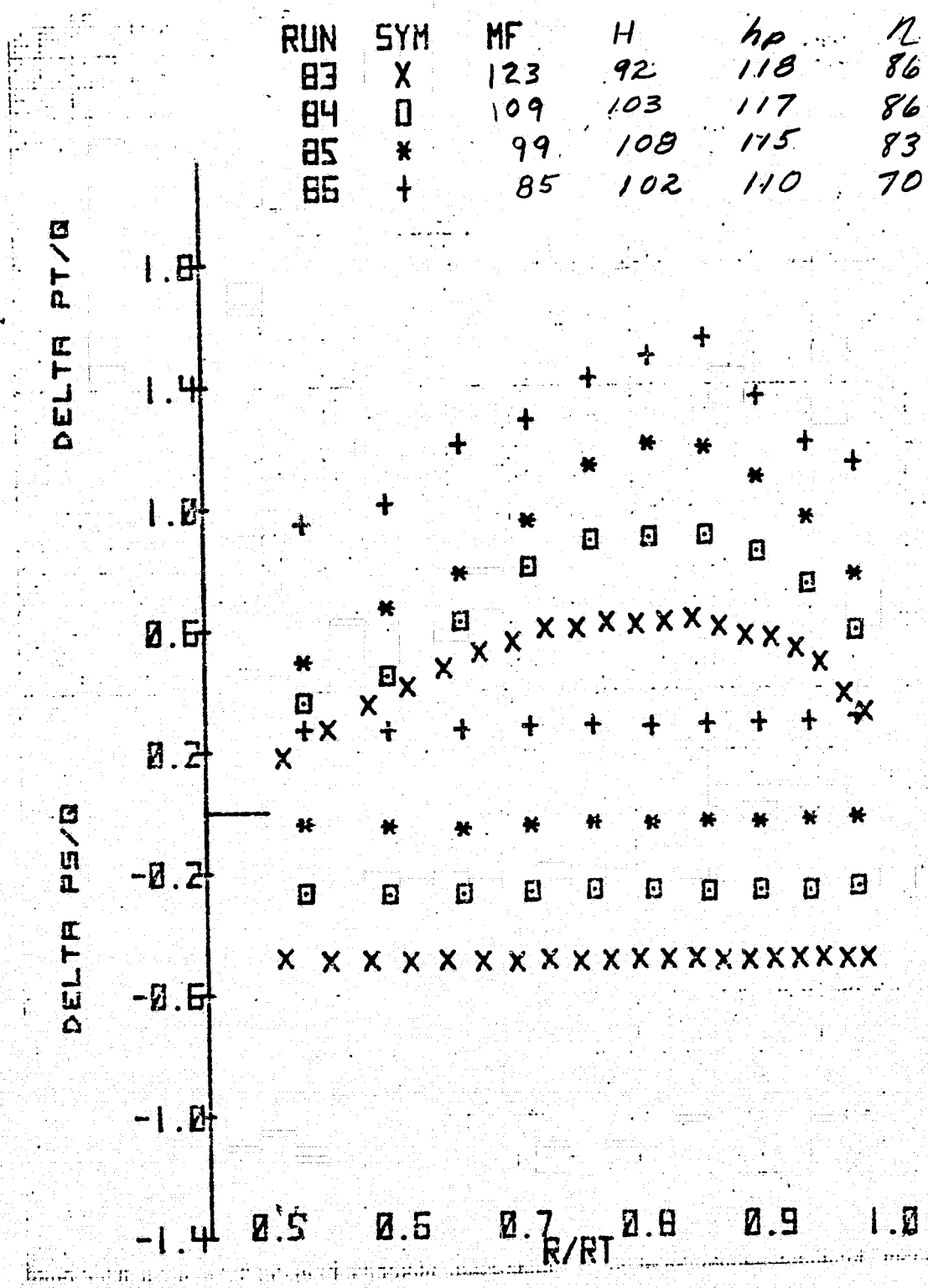

N = 100%

(a) Port azimuth.

Figure 4.- Radial variation of total pressure coefficient, static pressure coefficient, and swirl angle downstream of the stators for several azimuths and mass flows: original contraction, $\xi = 32.9°$.

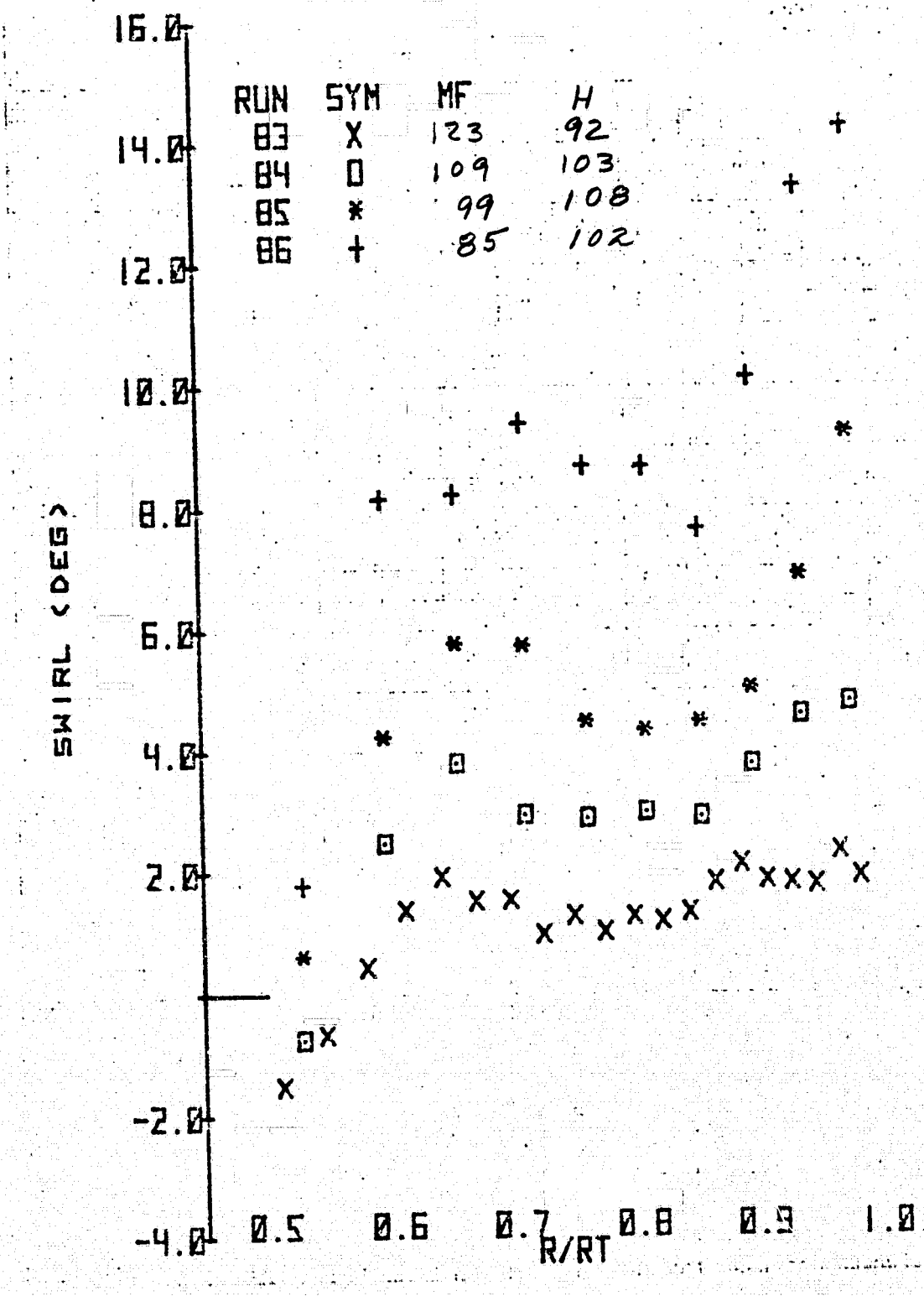

N = 100%
(a) Port azimuth - continued.

Figure 4.- Continued.

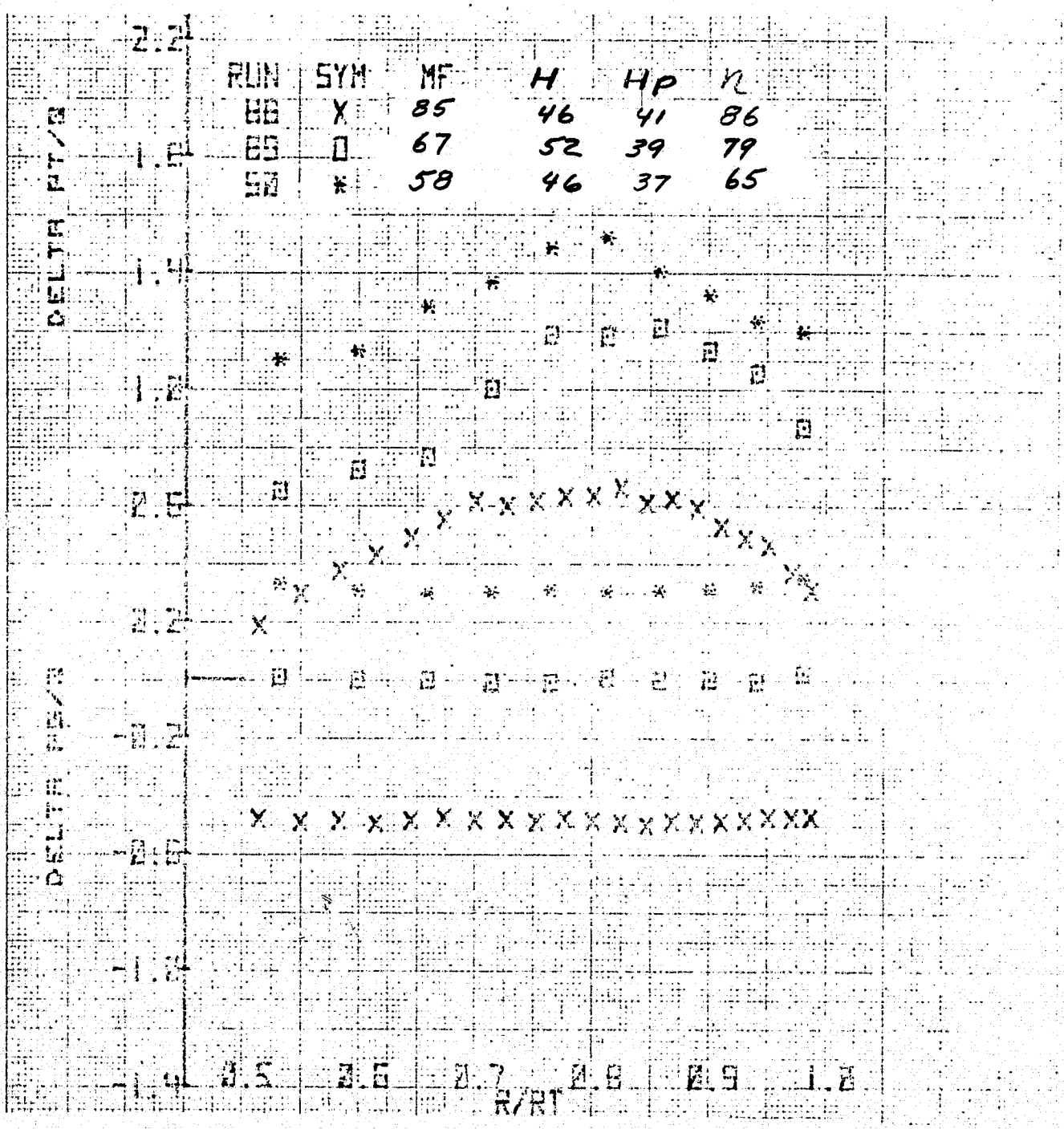

N = 70%

(a) Port azimuth - continued.

Figure 4.- Continued.

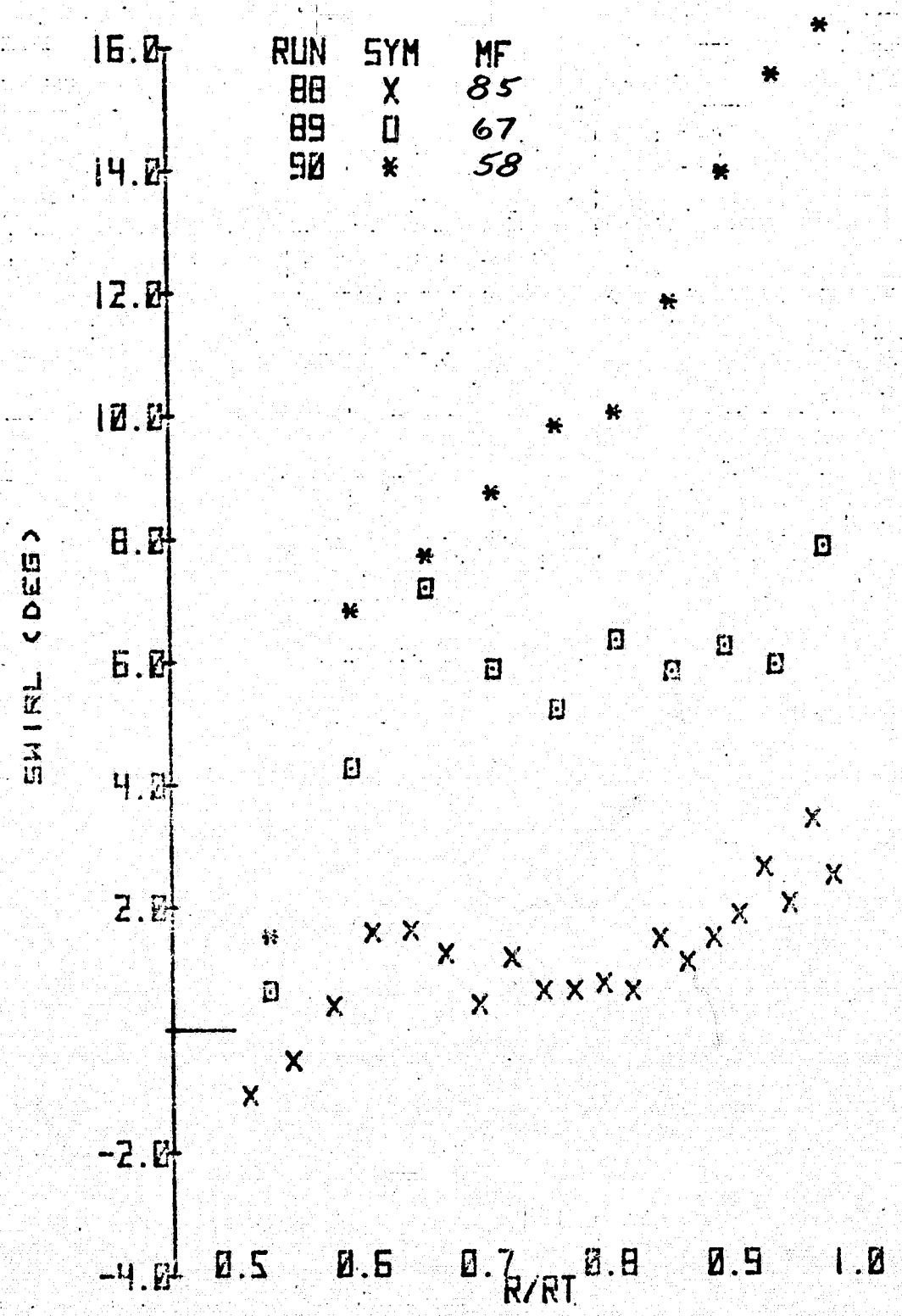

N = 70%

(a) Port azimuth - concluded.

Figure 4.- Continued.

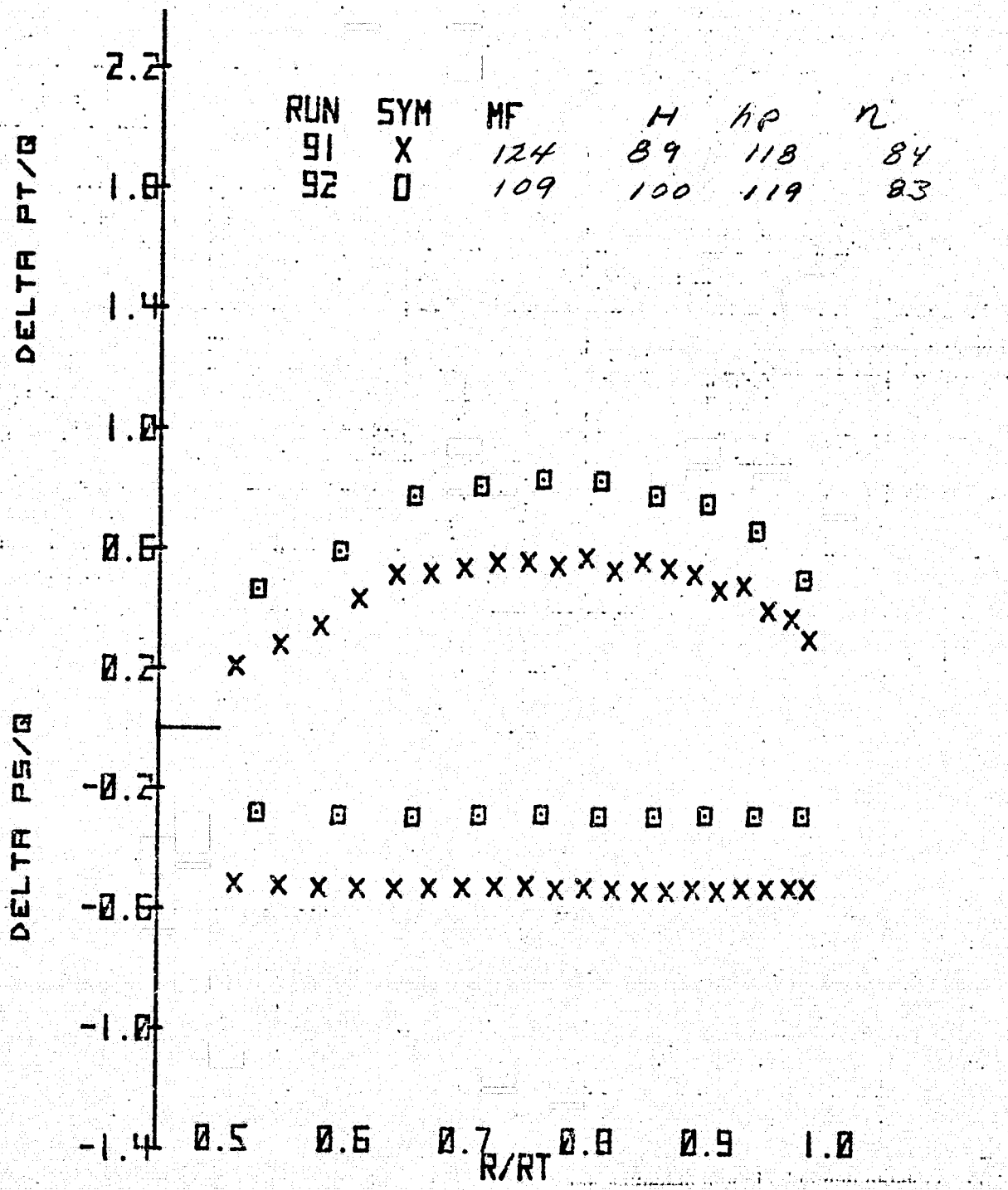

N = 100%
(b) Top azimuth.

Figure 4.- Continued.

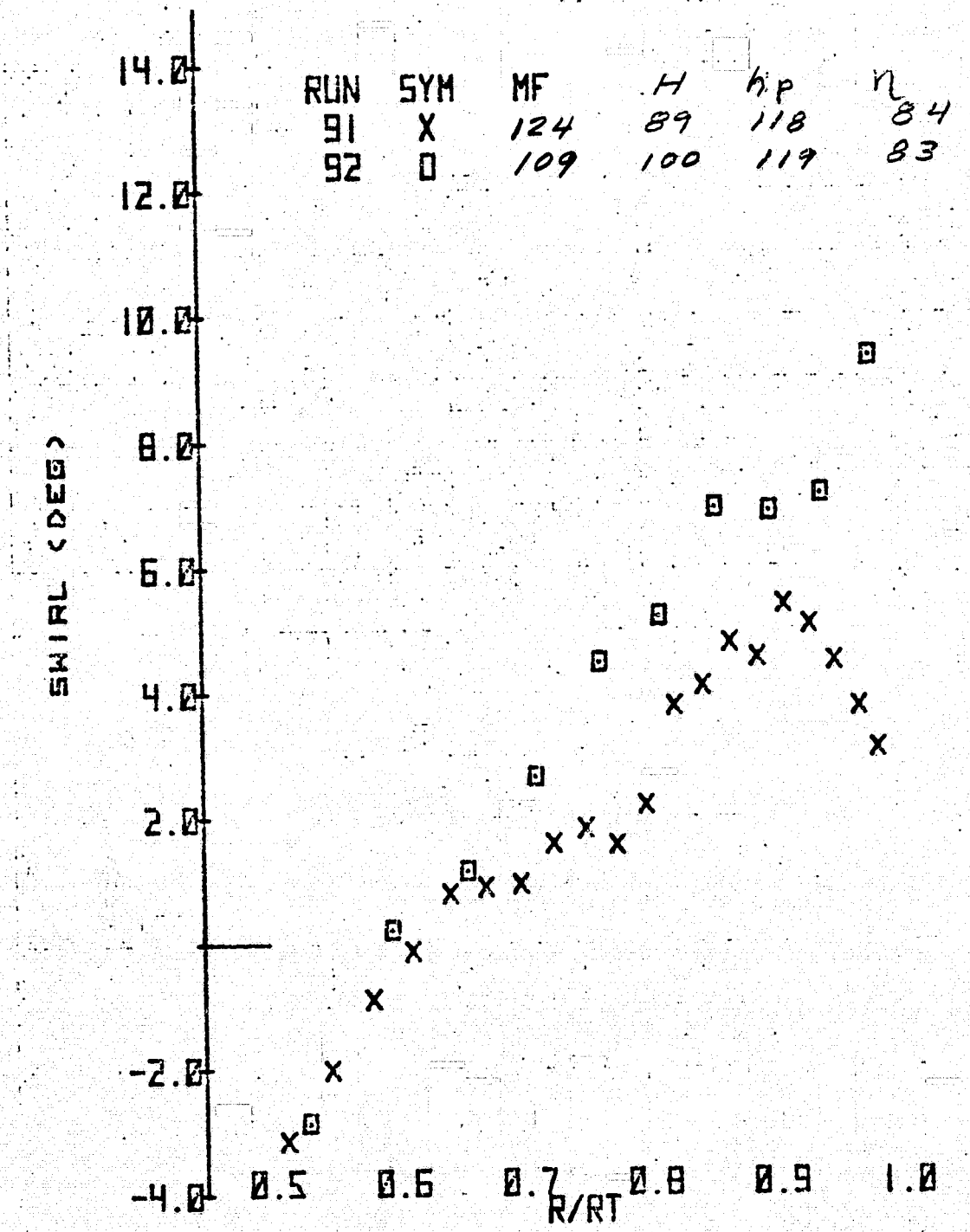

N = 100%

(b) Top azimuth - concluded.

Figure 4.- Continued.

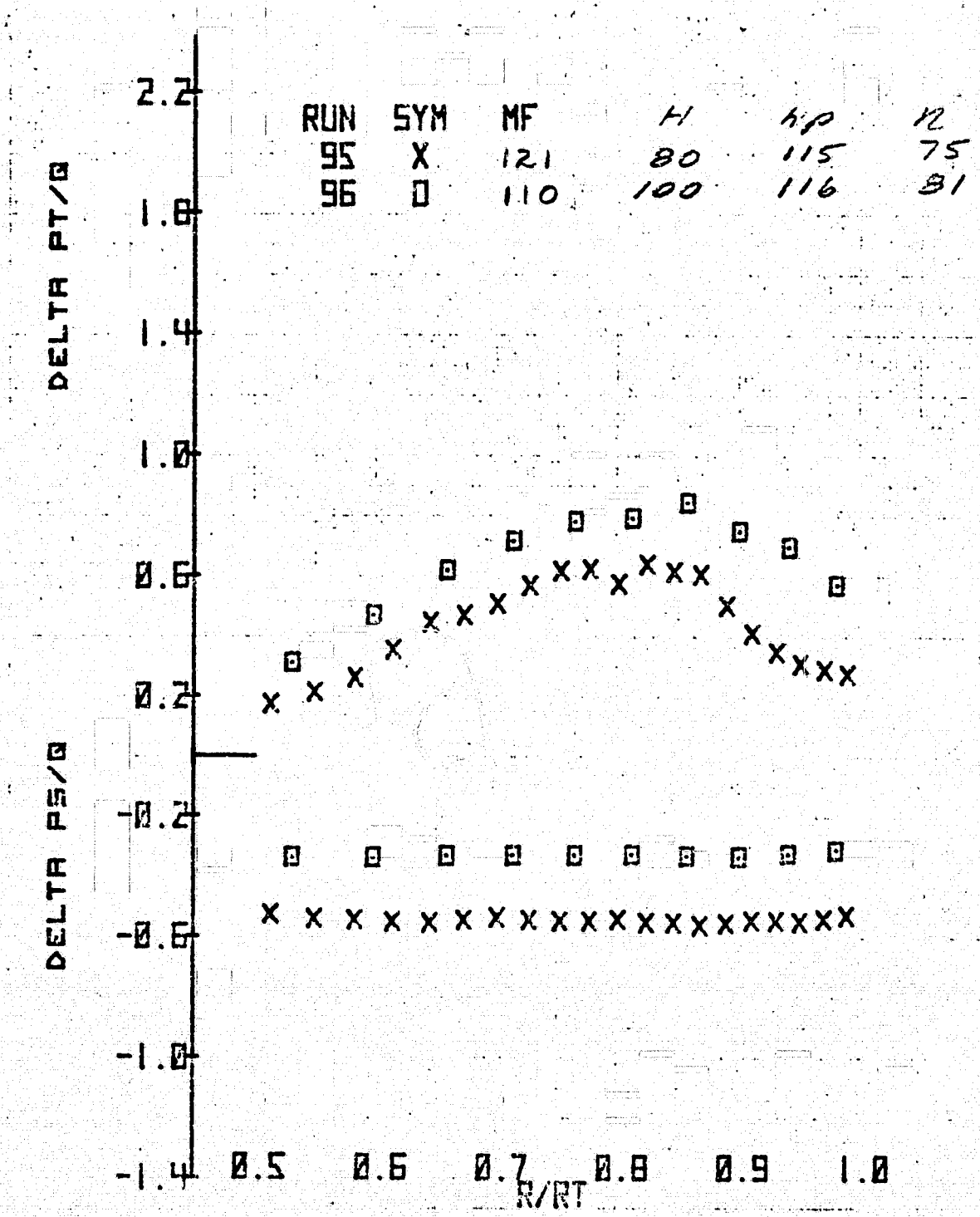

N = 100%
(c) Starboard azimuth.

Figure 4.- Continued.

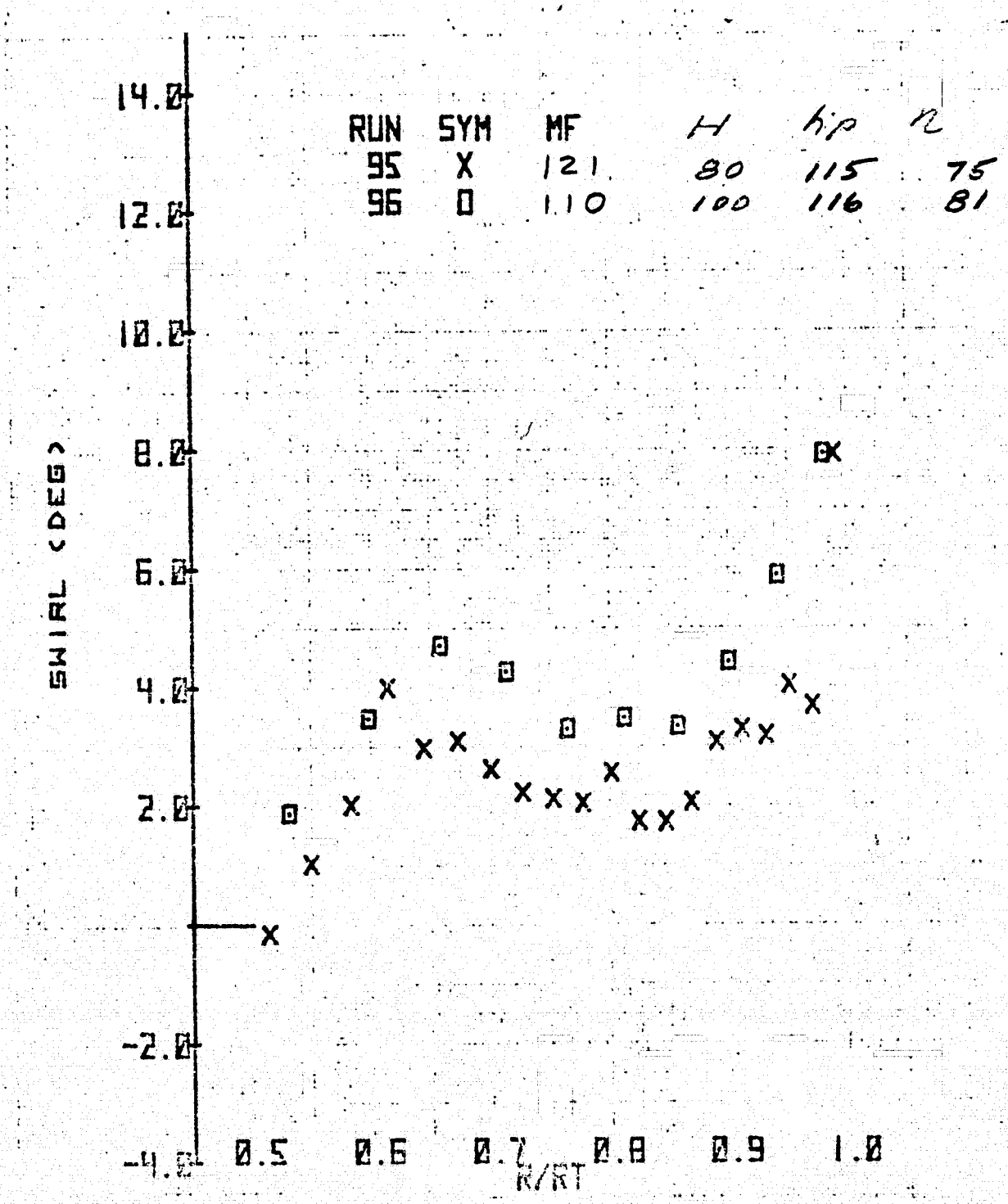

N = 100%

(c) Starboard azimuth - concluded.

Figure 4.- Continued.

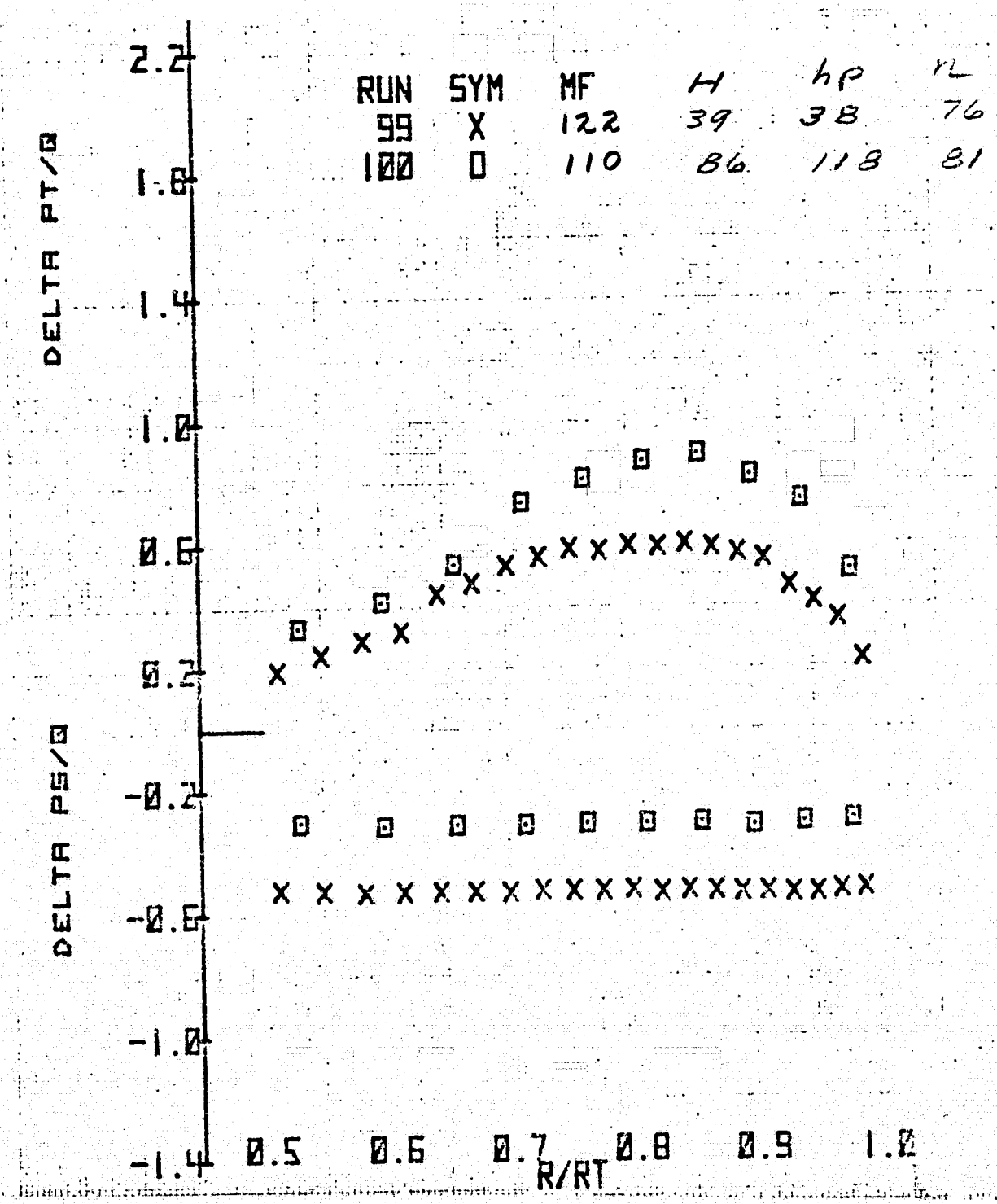

N = 100%
(d) Bottom azimuth.

Figure 4.- Continued.

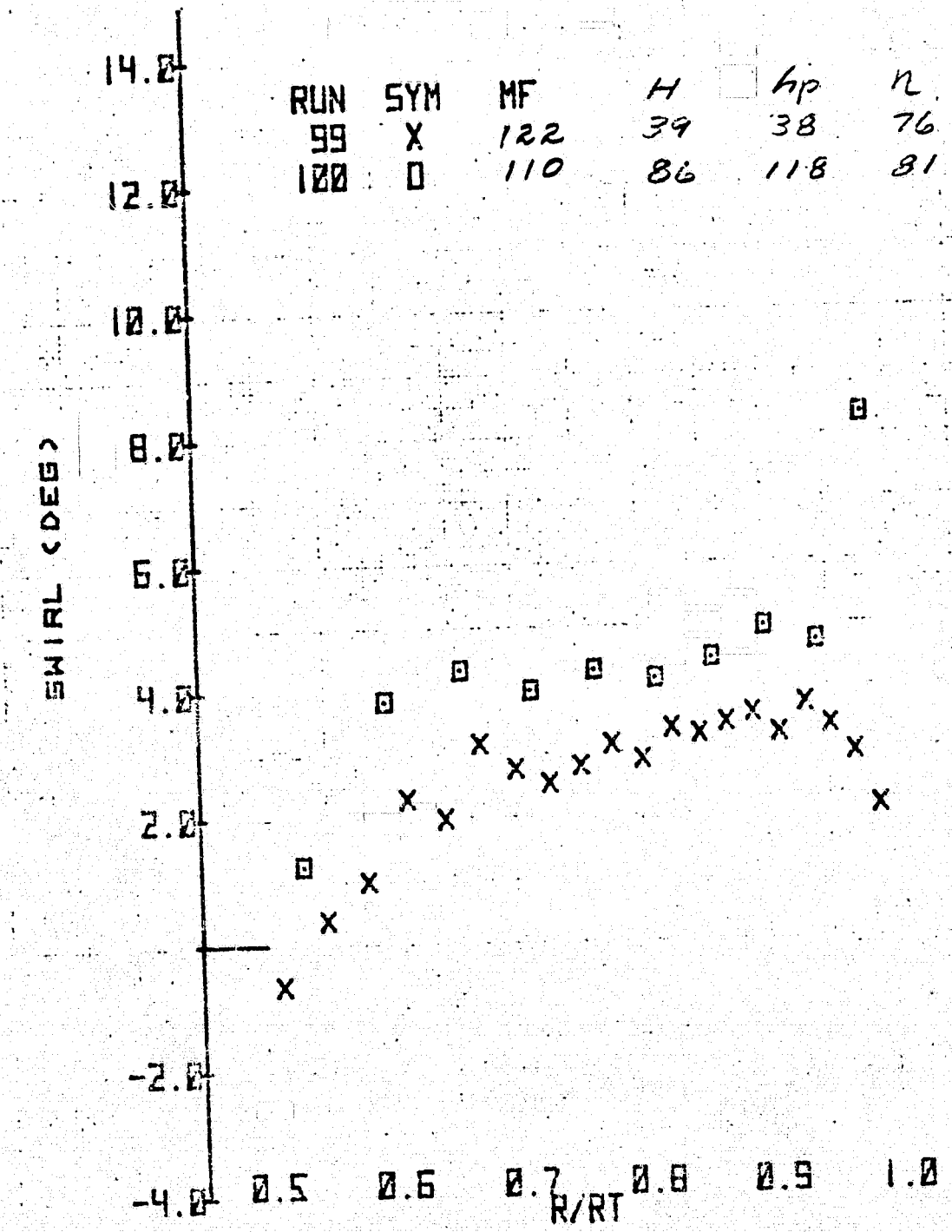

N = 100%

(d) Bottom azimuth - concluded.

Figure 4.- Concluded.

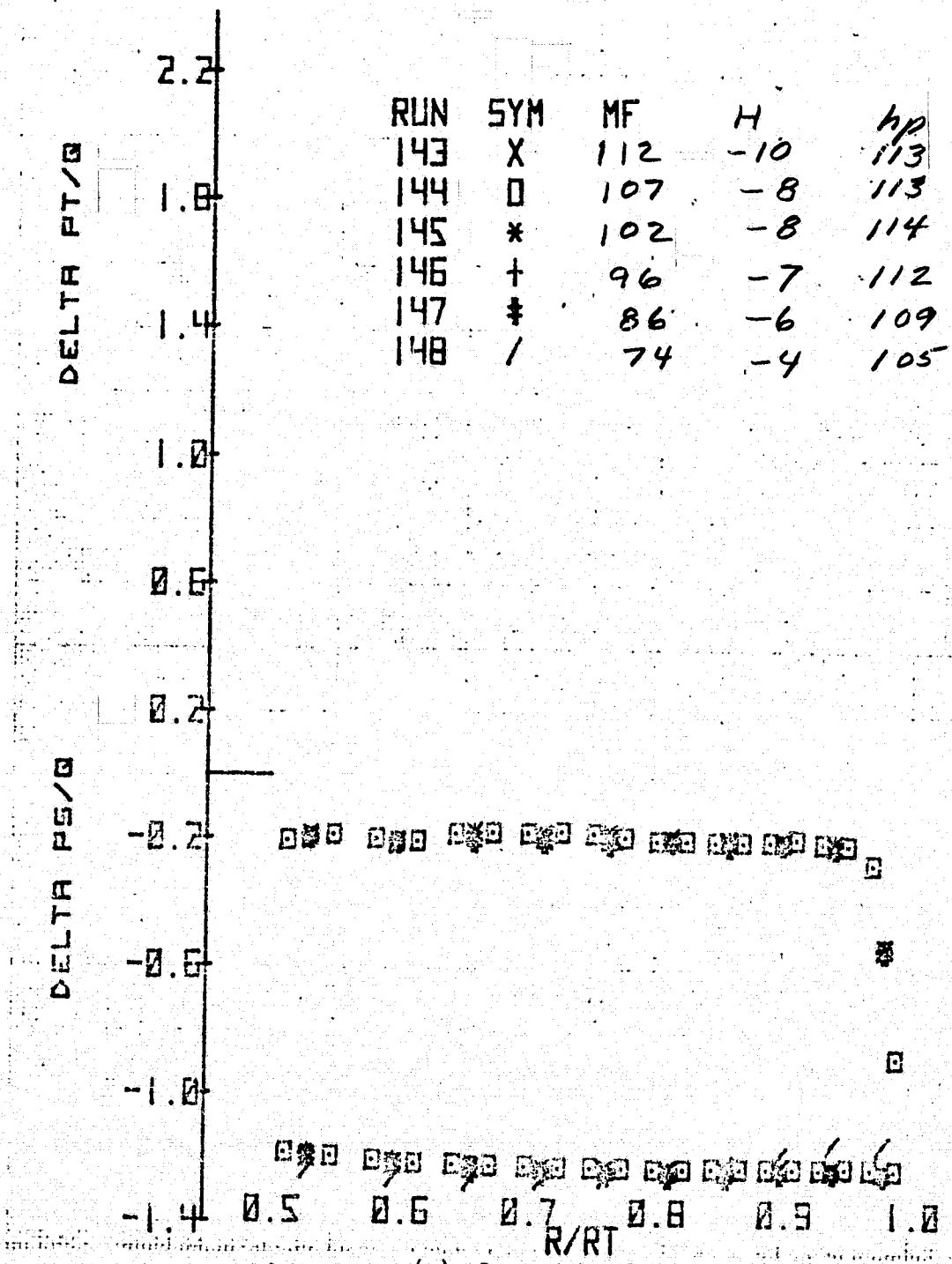

(a) Port azimuth.

Figure 5.- Radial variation of total pressure coefficient, static pressure coefficient, and swirl angle upstream of the rotor for several azimuths, and mass flows; N = 100%, ξ = 35.4°, inlet honeycomb in, original contraction.

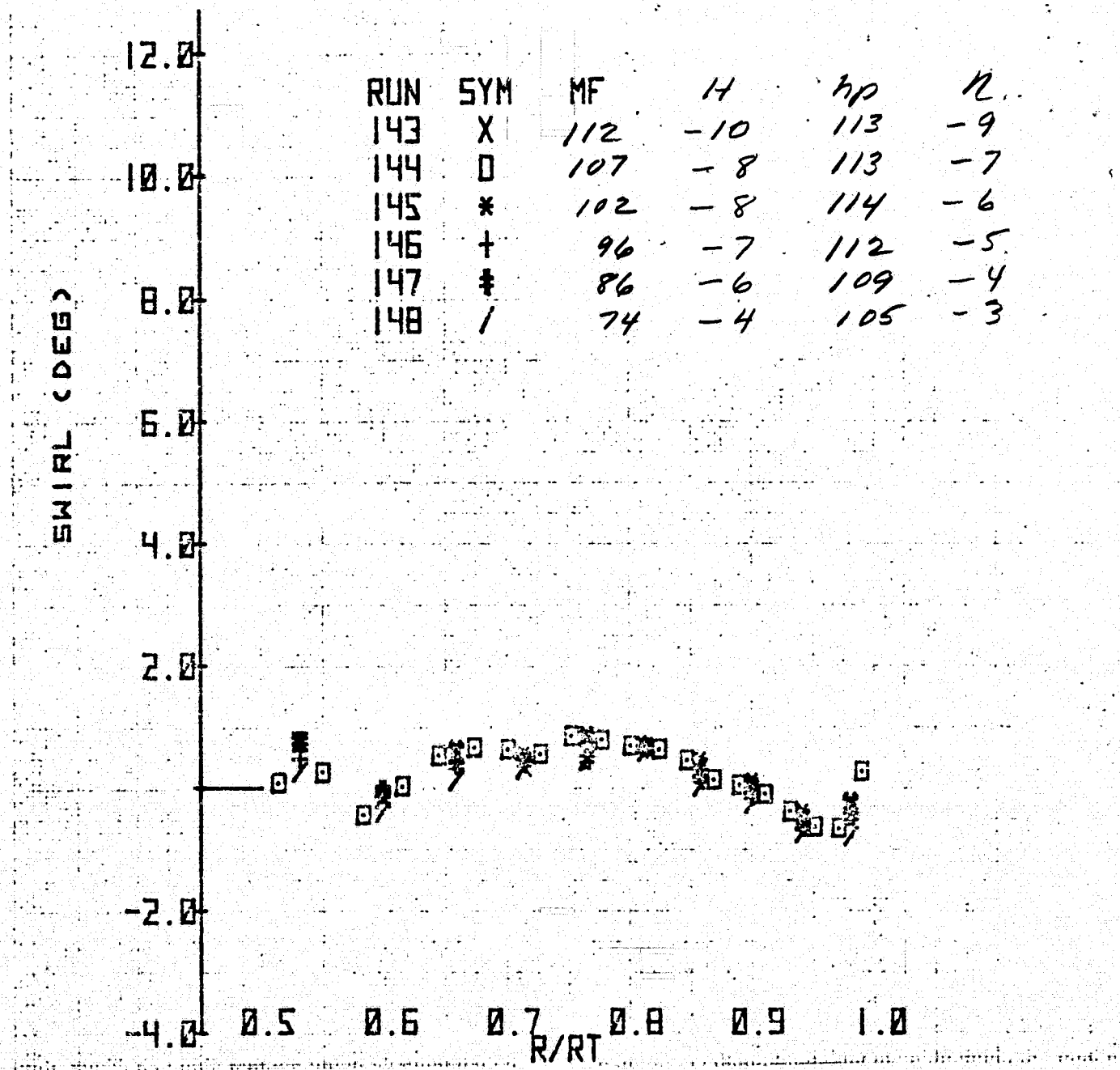

(a) Port azimuth - concluded.

Figure 5.- Continued.

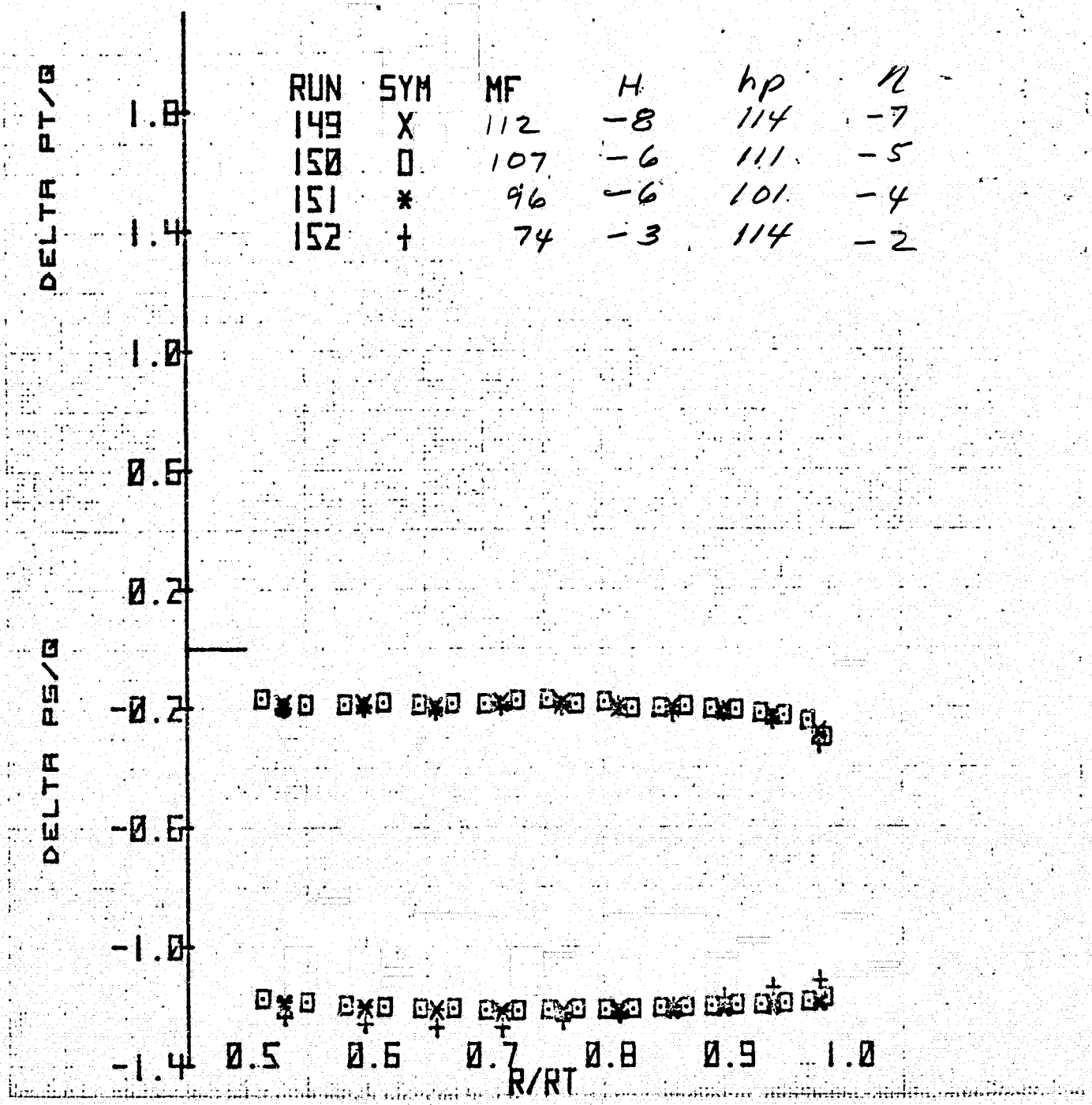

(b) Top azimuth.

Figure 5.- Continued.

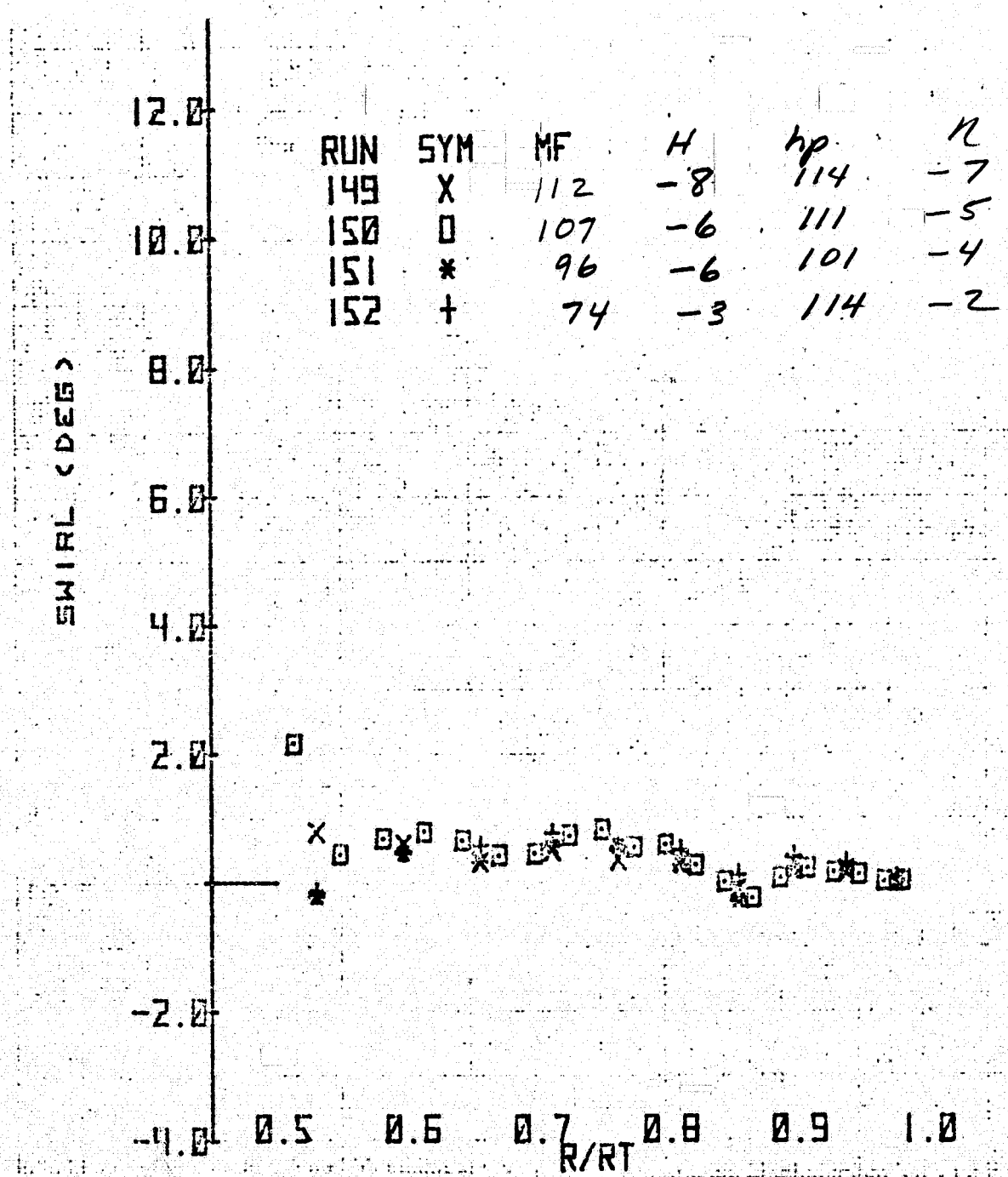

(b) Top azimuth - concluded.

Figure 5.- Continued.

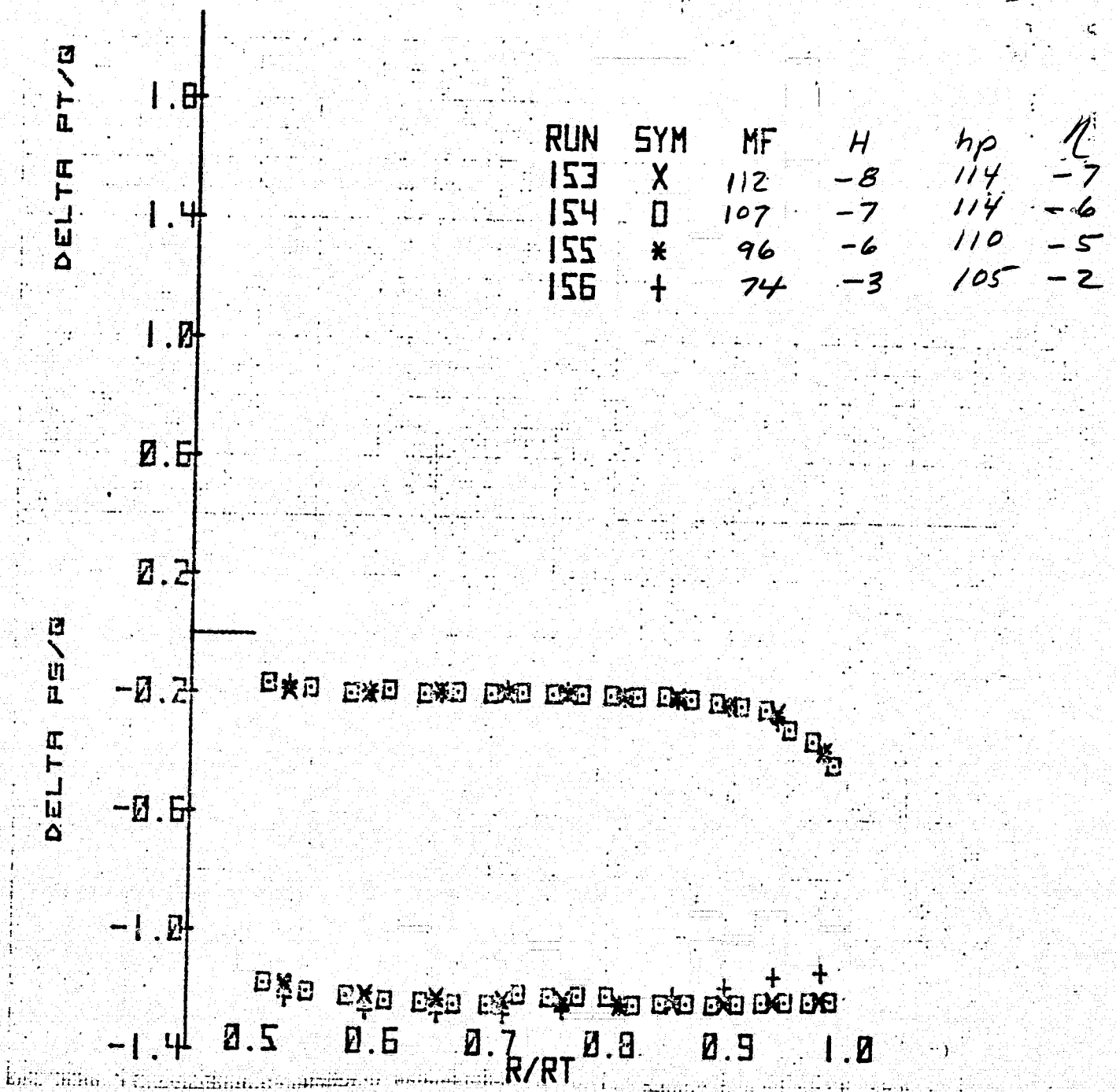

(c) Starboard azimuth.

Figure 5.- Continued.

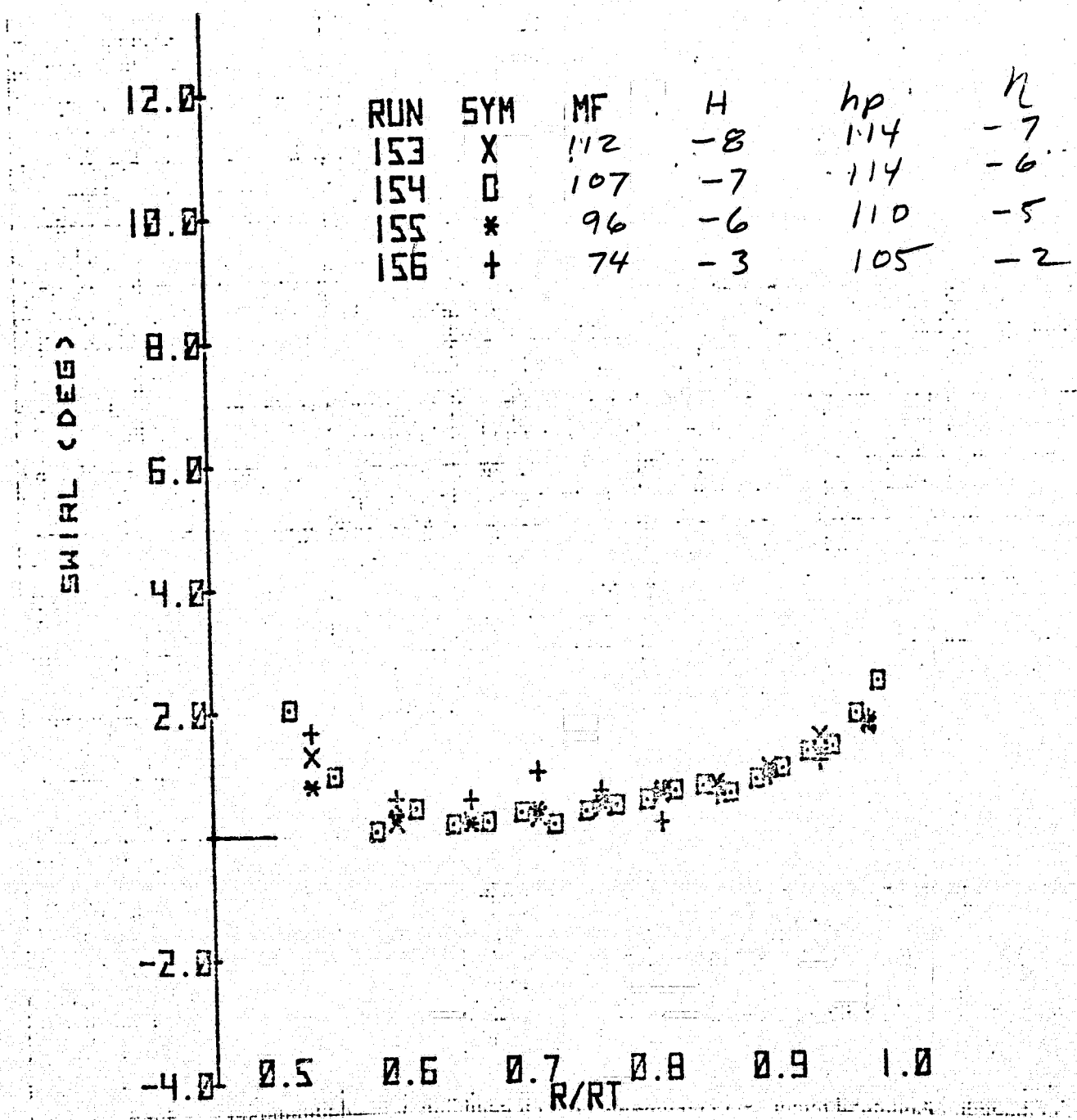

(c) Starboard azimuth - concluded.

Figure 5.- Continued.

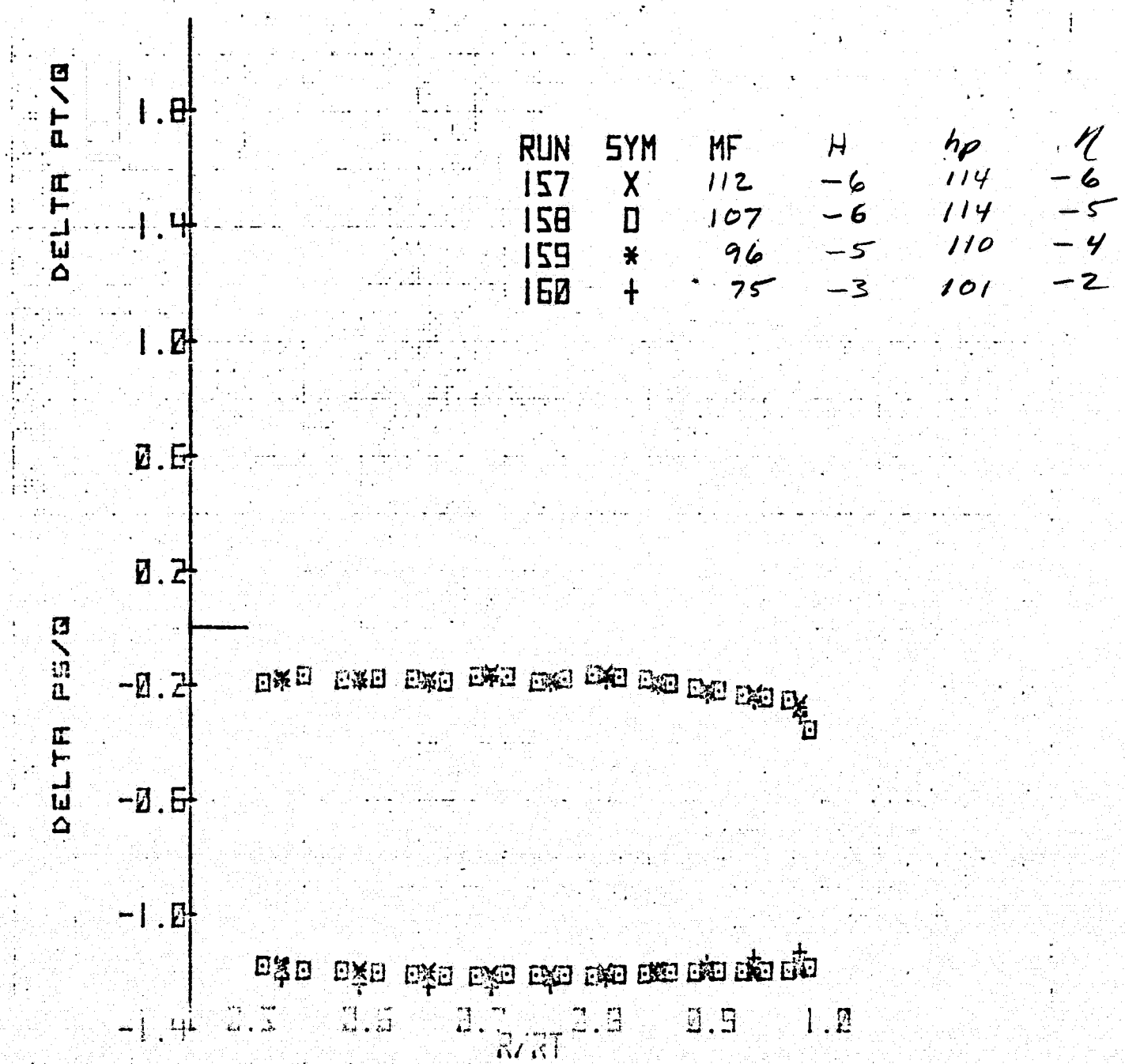

(d) Bottom azimuth.

Figure 5.- Continued.

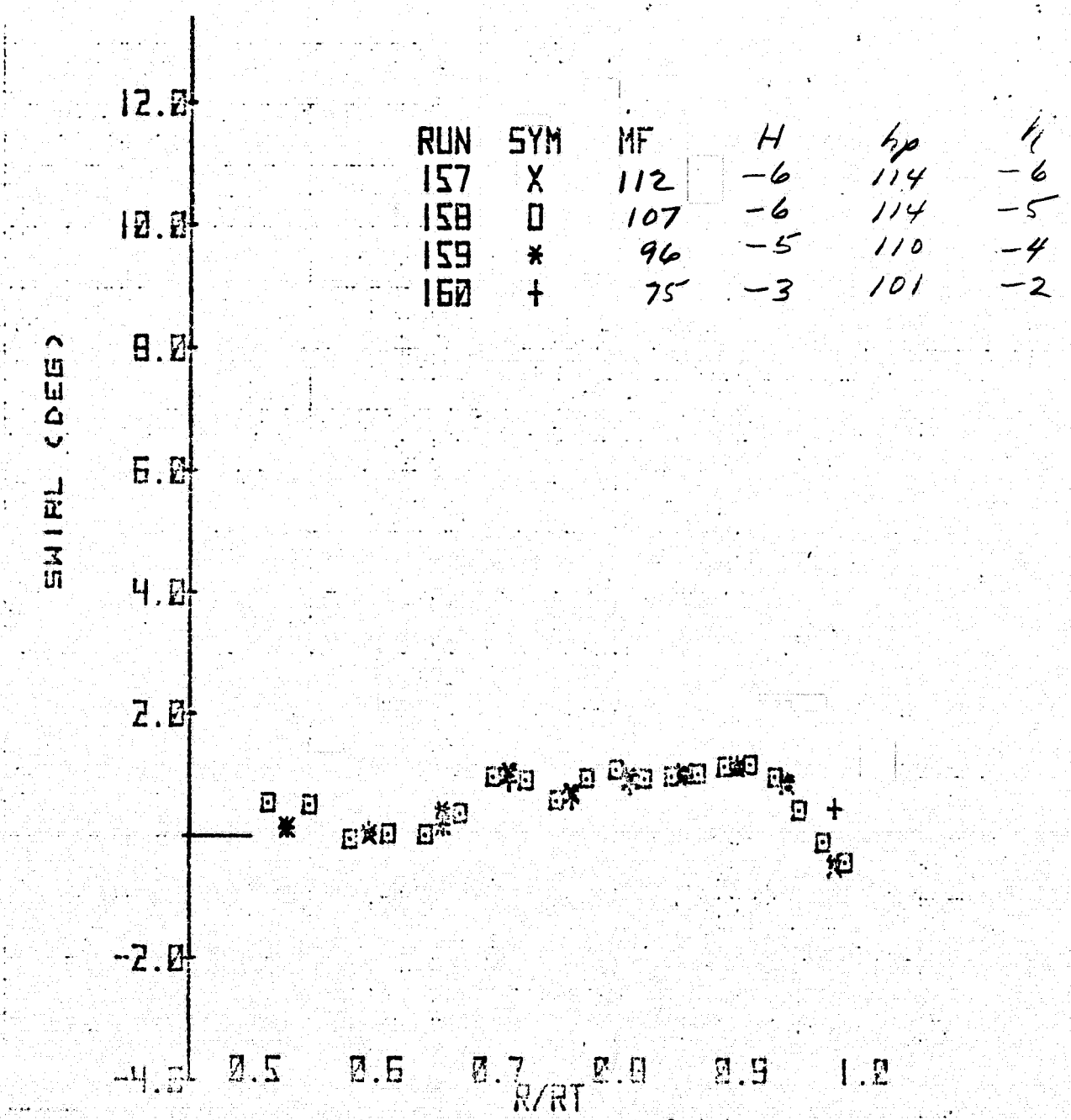

(d) Bottom azimuth - concluded.

Figure 5.- Concluded.

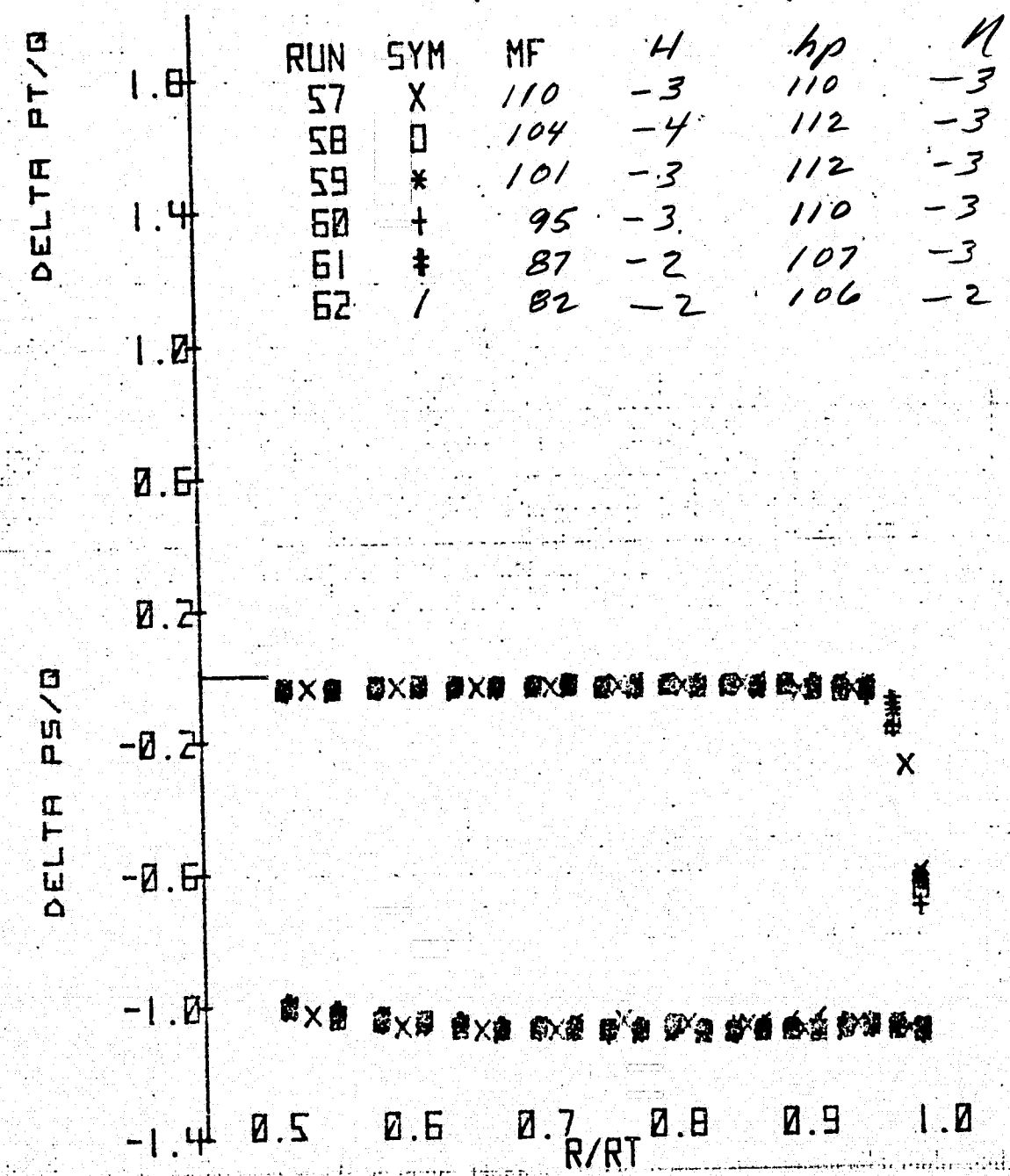

N = 100%

(a) Port azimuth.

Figure 6.- Radial variation of total pressure coefficient, static pressure coefficient and swirl angle upstream of the rotor for several azimuths and mass flows; ξ = 35.4°, exit honeycomb in, original contraction.

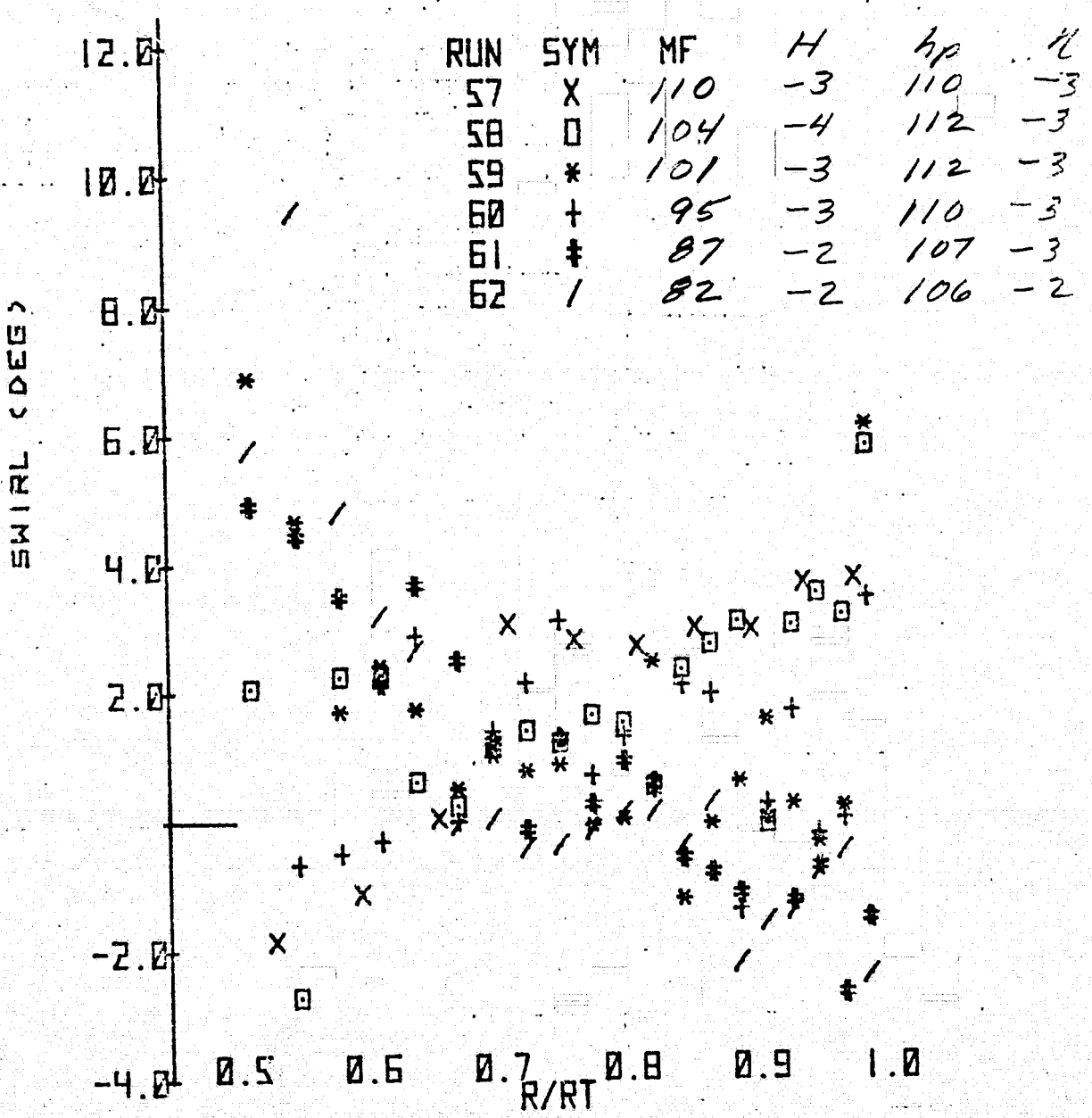

N = 100%

(a) Port azimuth - continued.

Figure 6.- Continued.

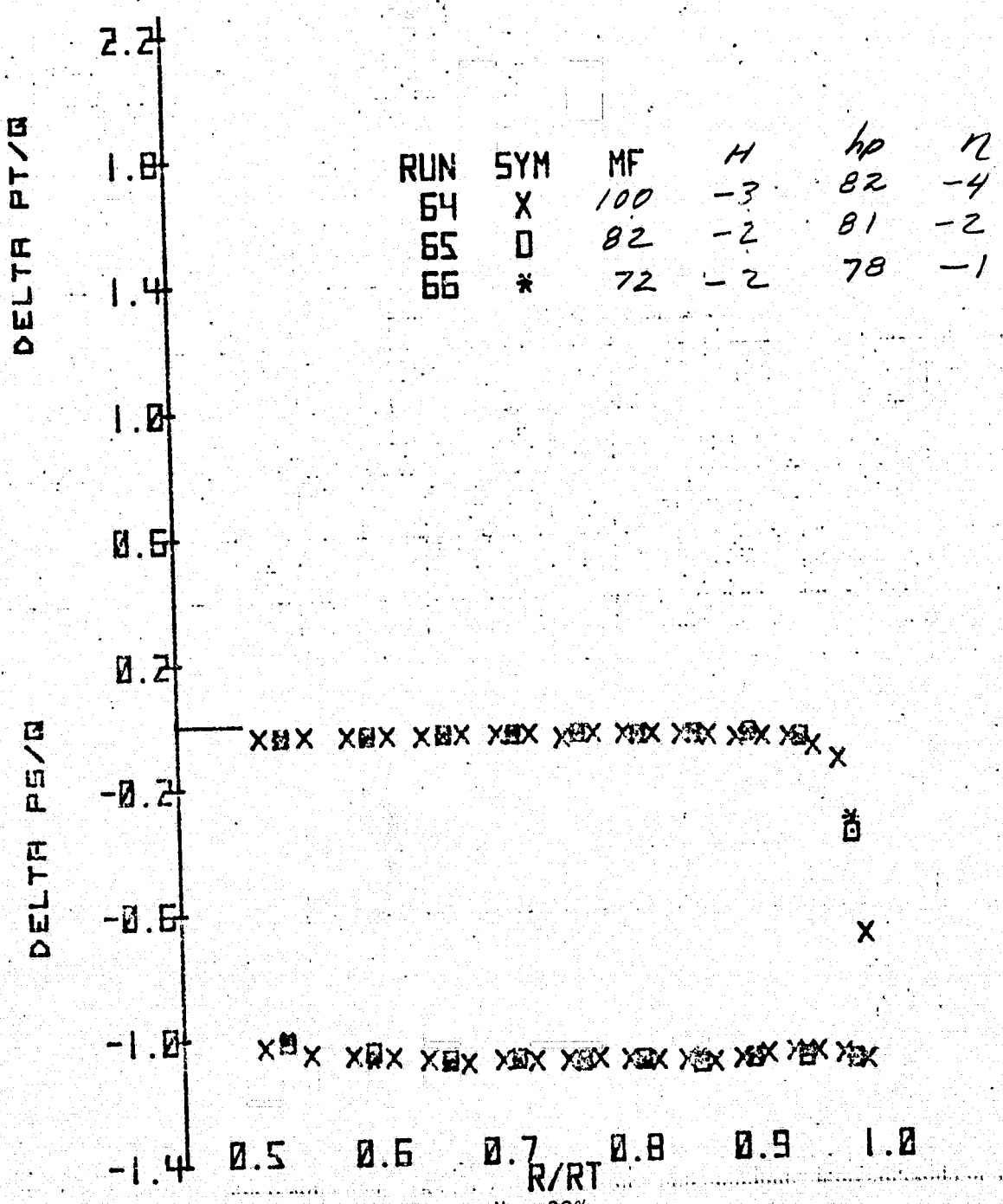

N = 90%

(a) Port azimuth - continued.

Figure 6.- Continued.

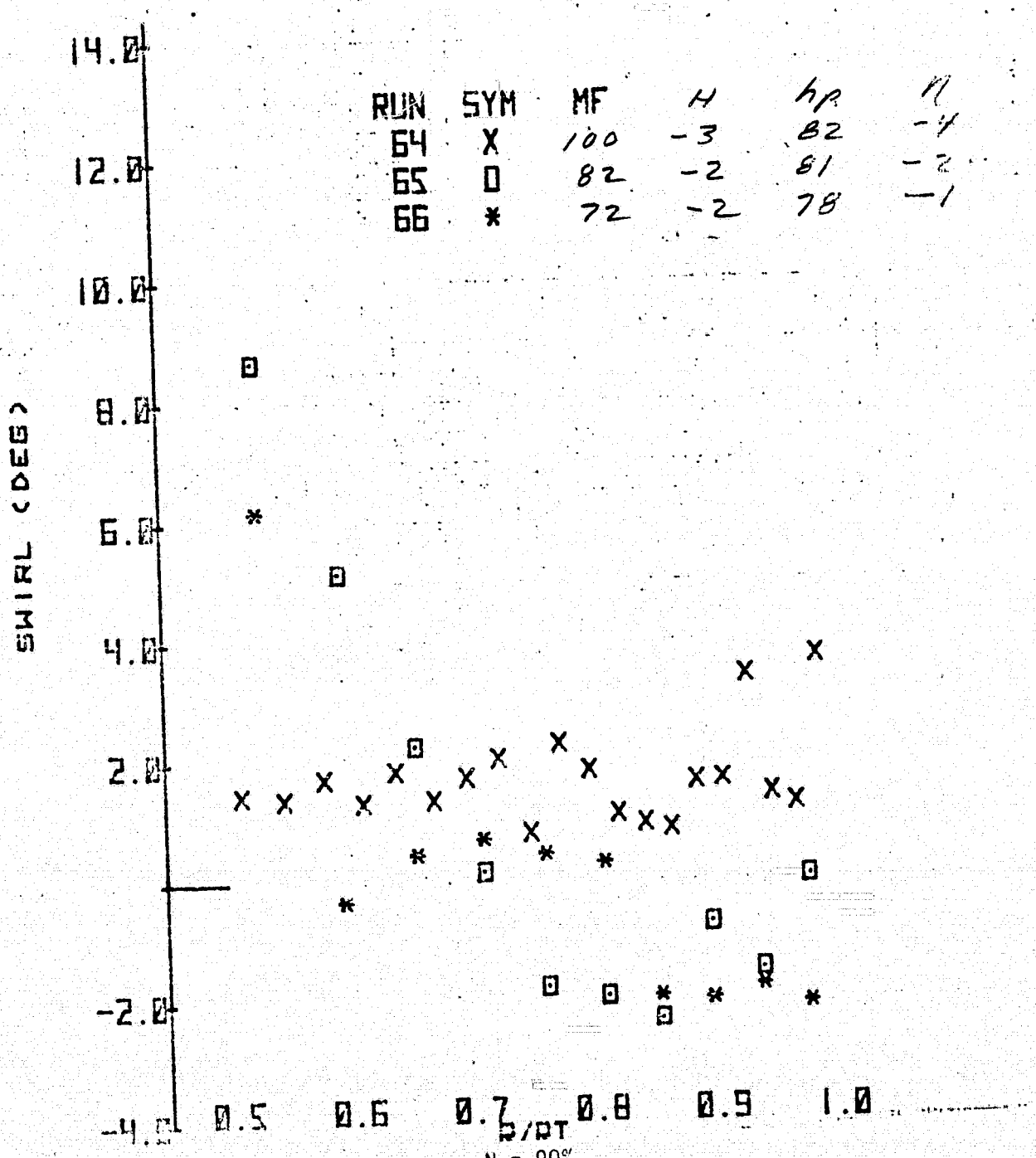

(a) Port azimuth - concluded.

Figure 6.- Continued.

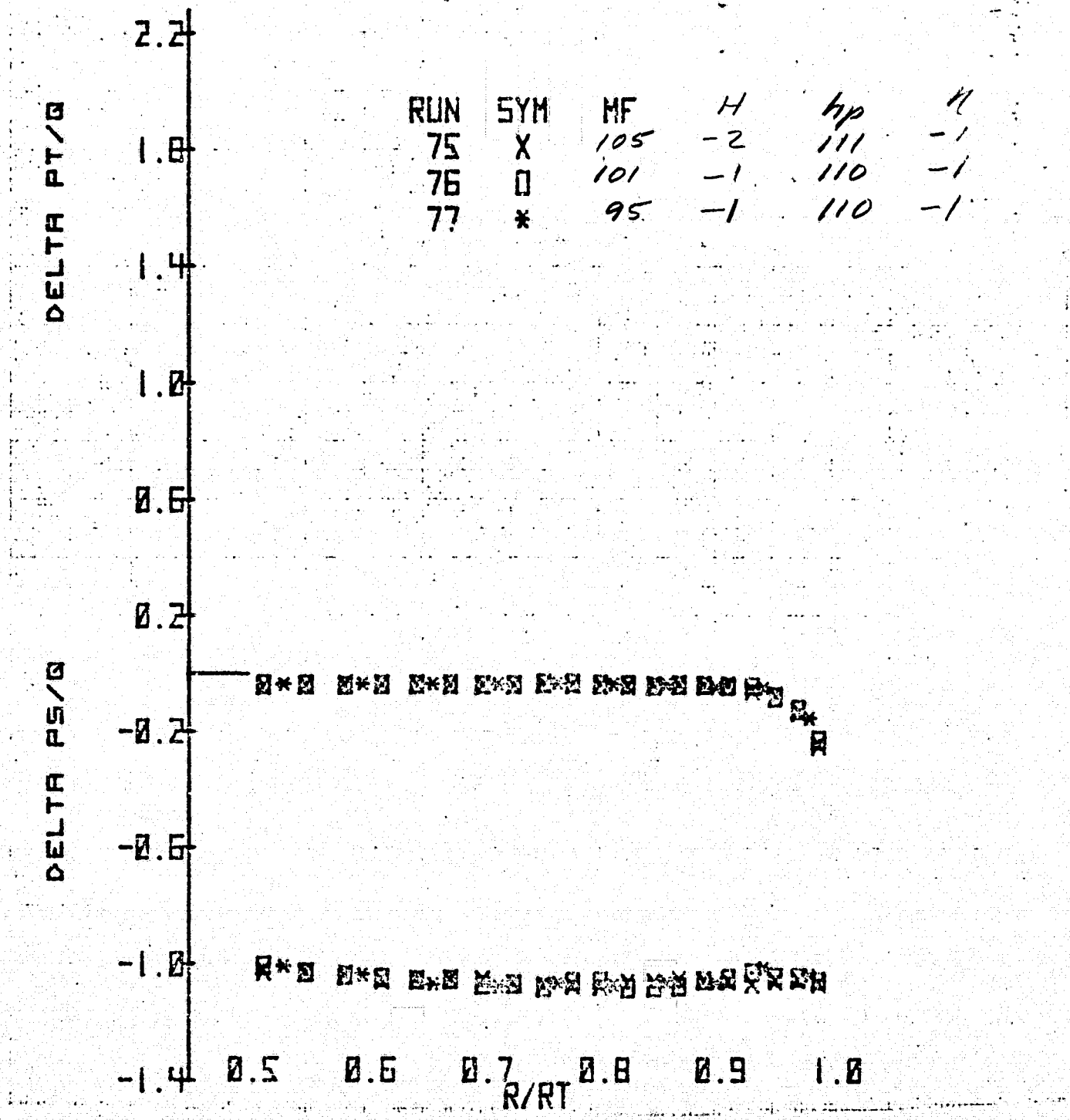

N = 100%

(b) Starboard azimuth.

Figure 6.- Continued.

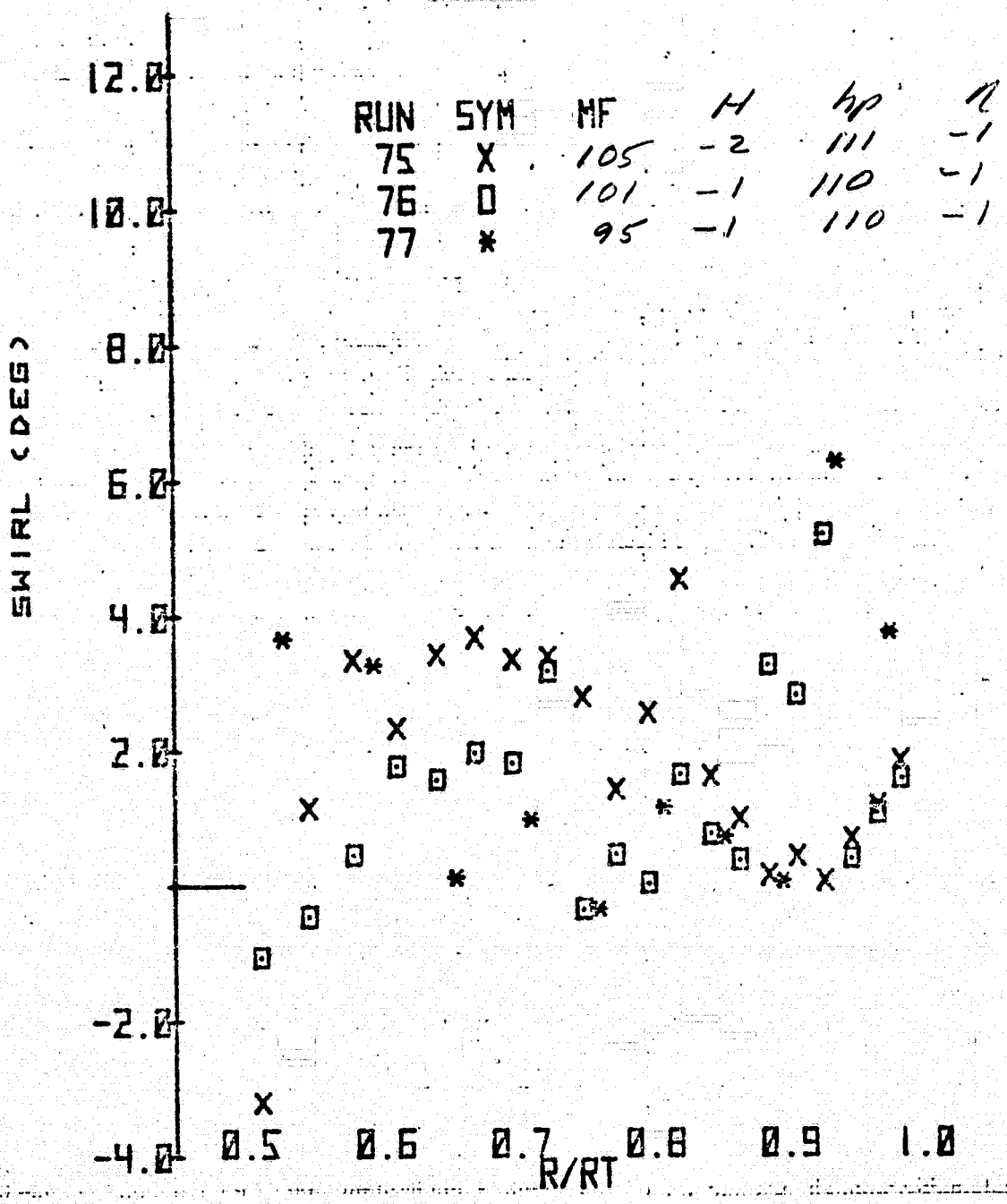

N = 100%

(b) Starboard azimuth - concluded.

Figure 6.- Continued

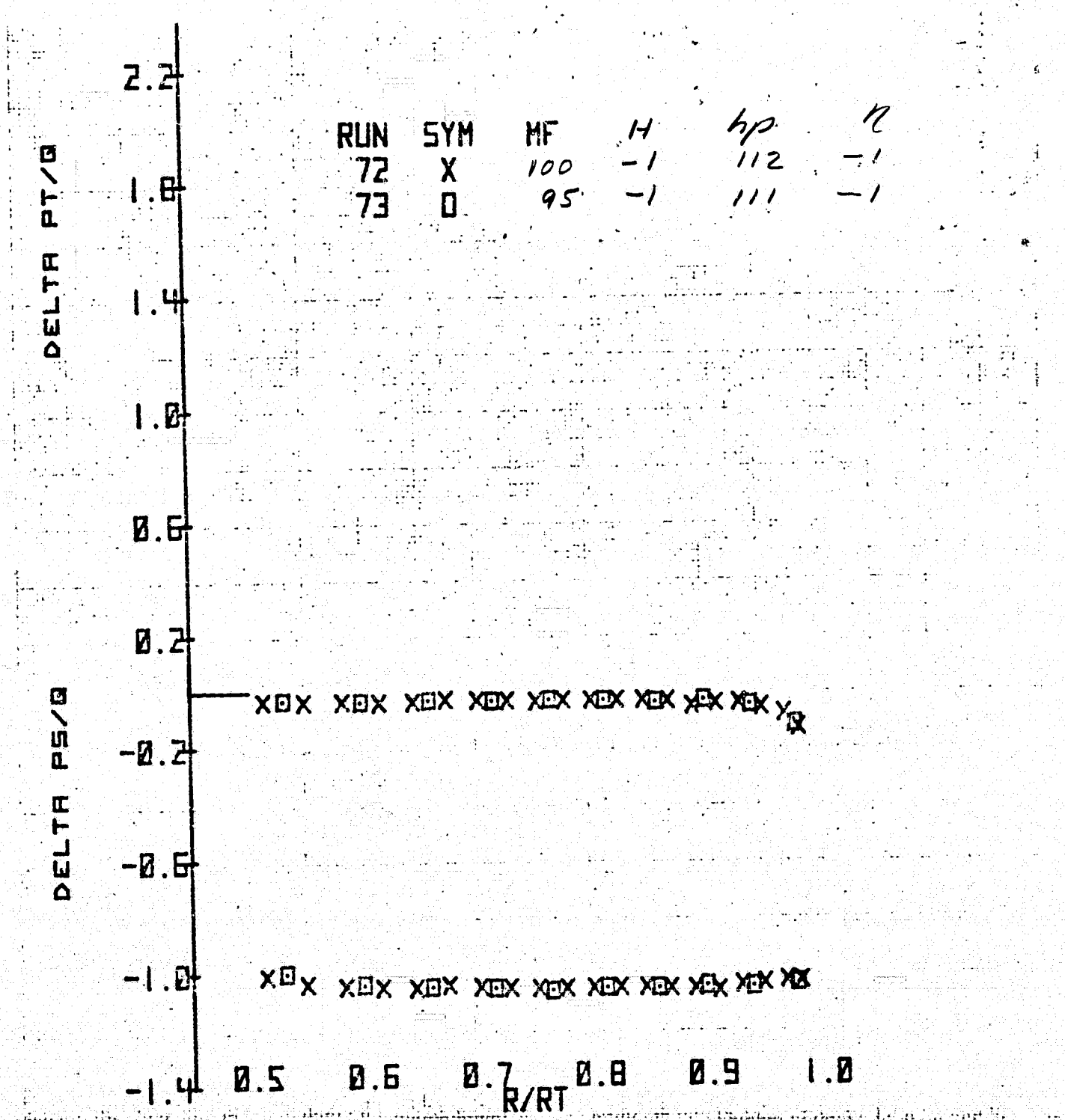

N = 100%

(c) Bottom azimuth.

Figure 6.- Continued

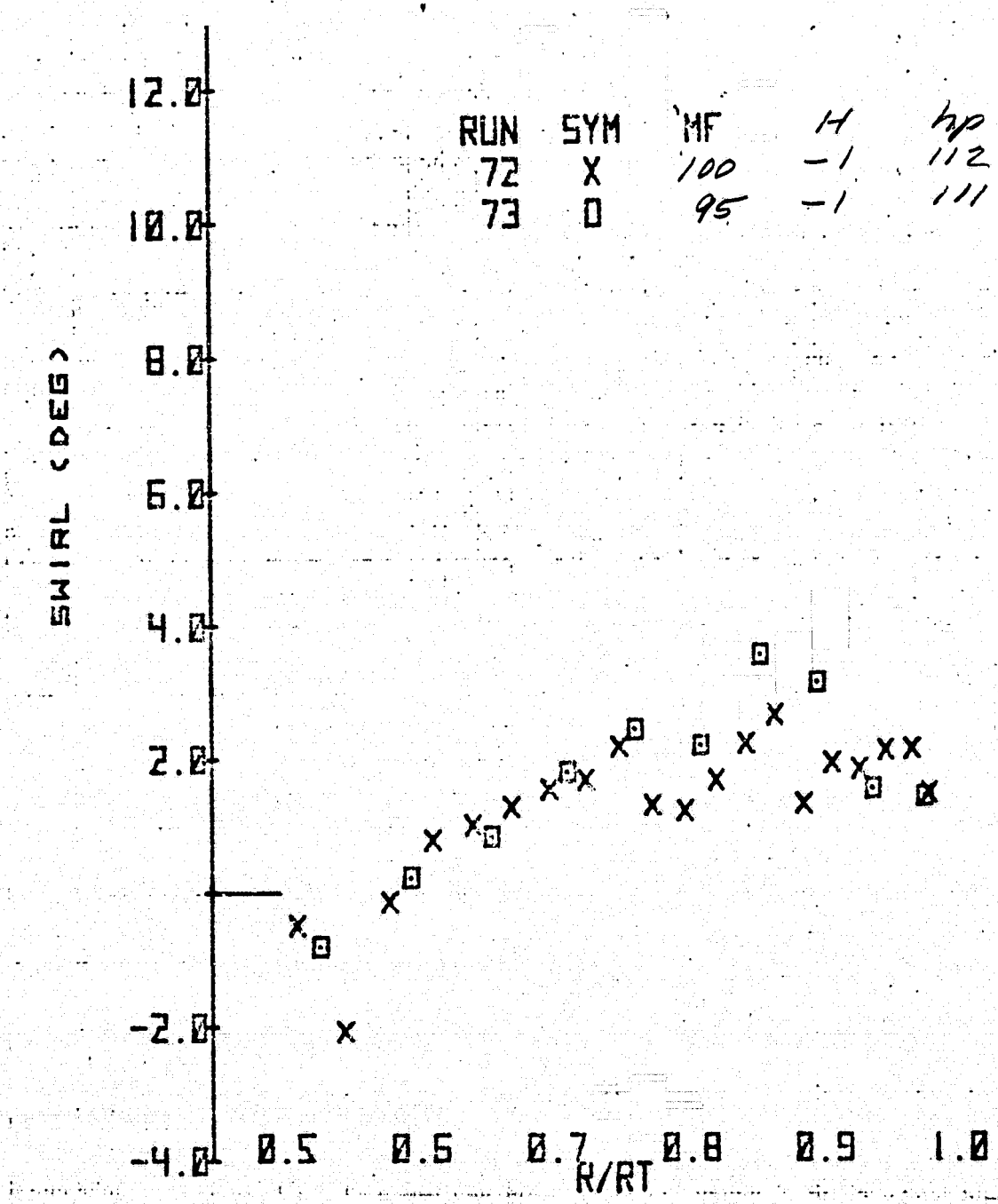

N = 100%

(c) Bottom azimuth - concluded.

Figure 6.- Concluded.

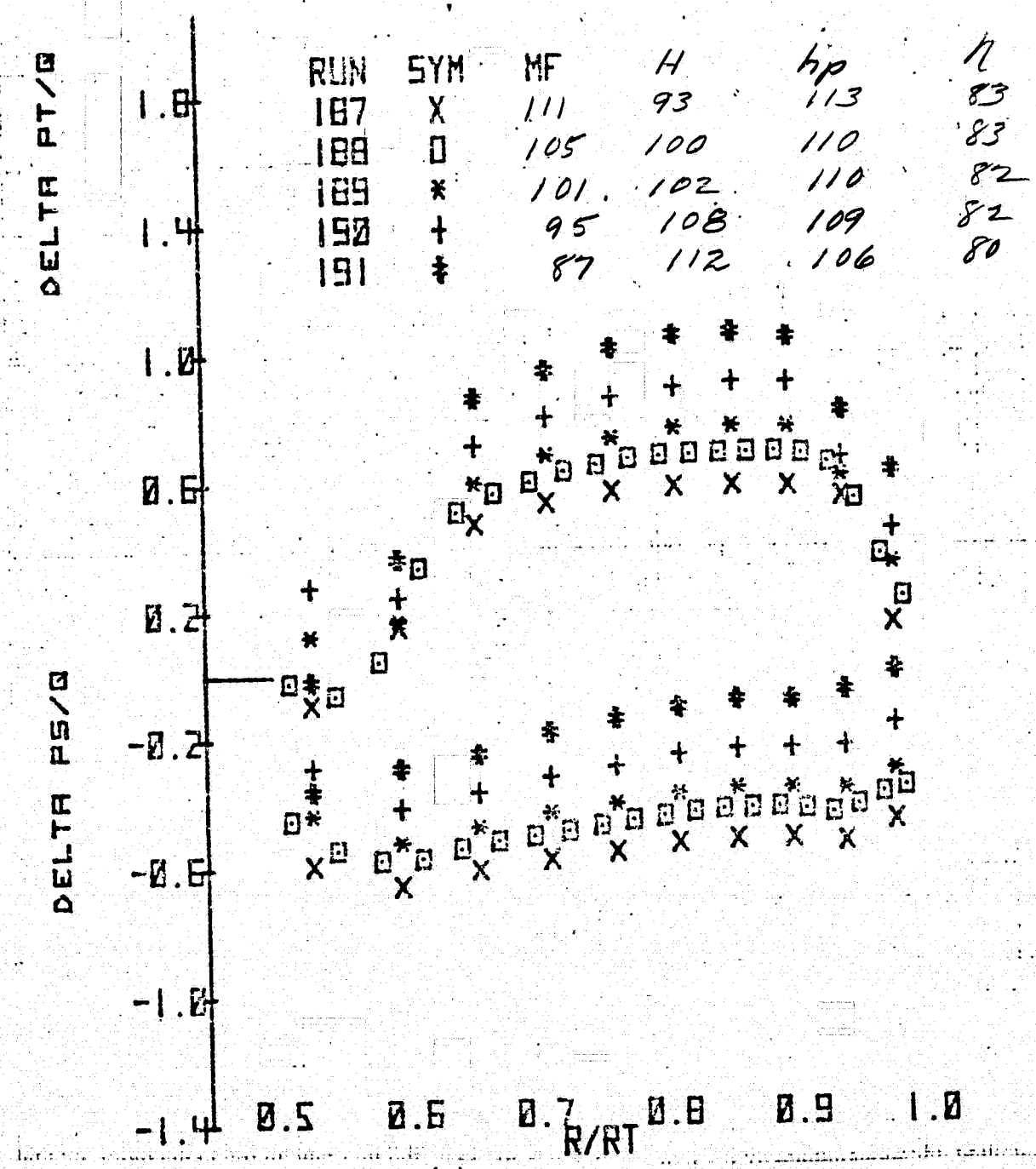

(a) Port azimuth.

Figure 7.- Radial variation of total pressure coefficient, static pressure coefficient, and swirl angle between fan and stator for several azimuths and mass flows; ξ = 35.4°, inlet honeycomb in, original contraction.

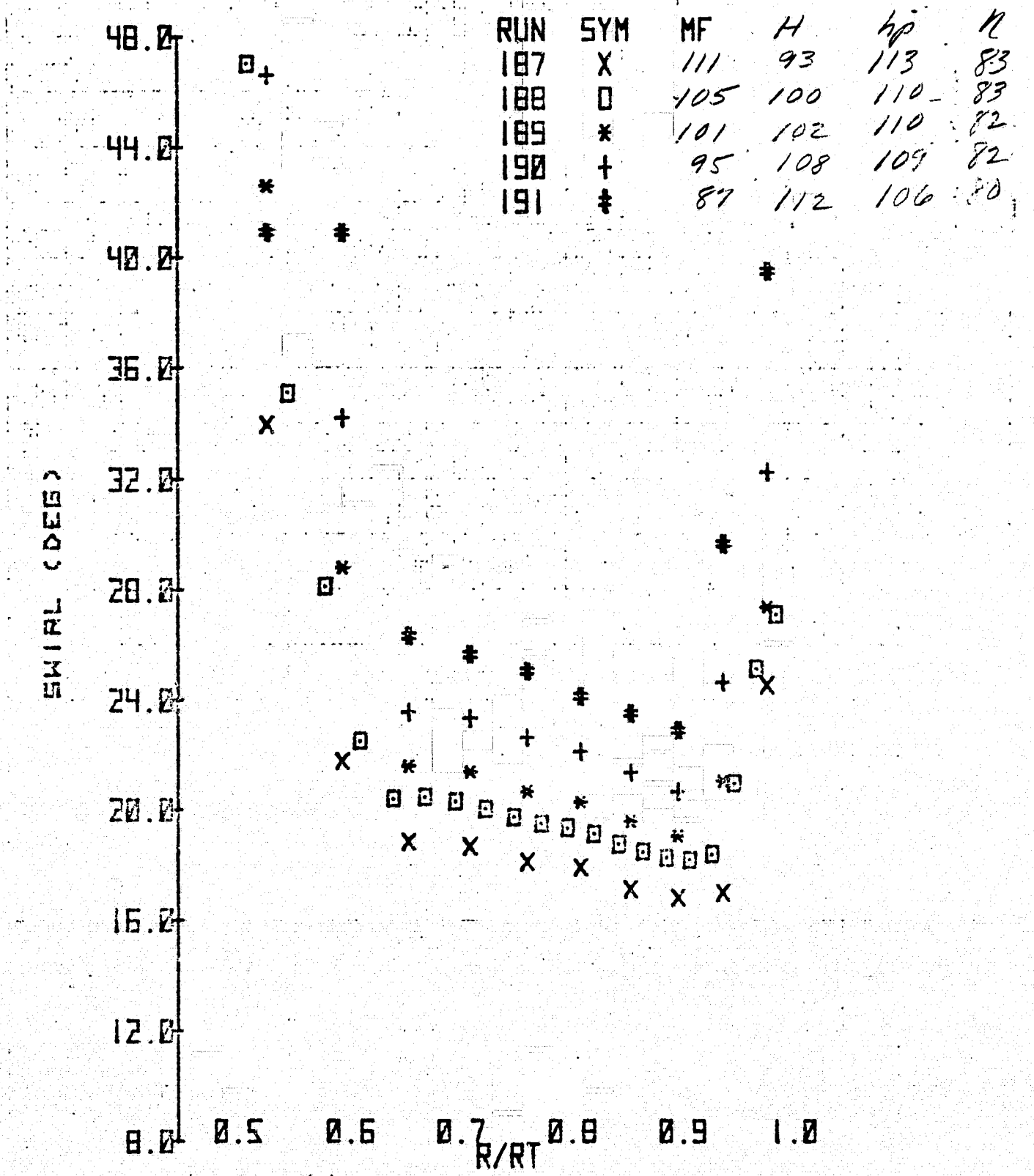

(a) Port azimuth - concluded.

Figure 7.- Continued.

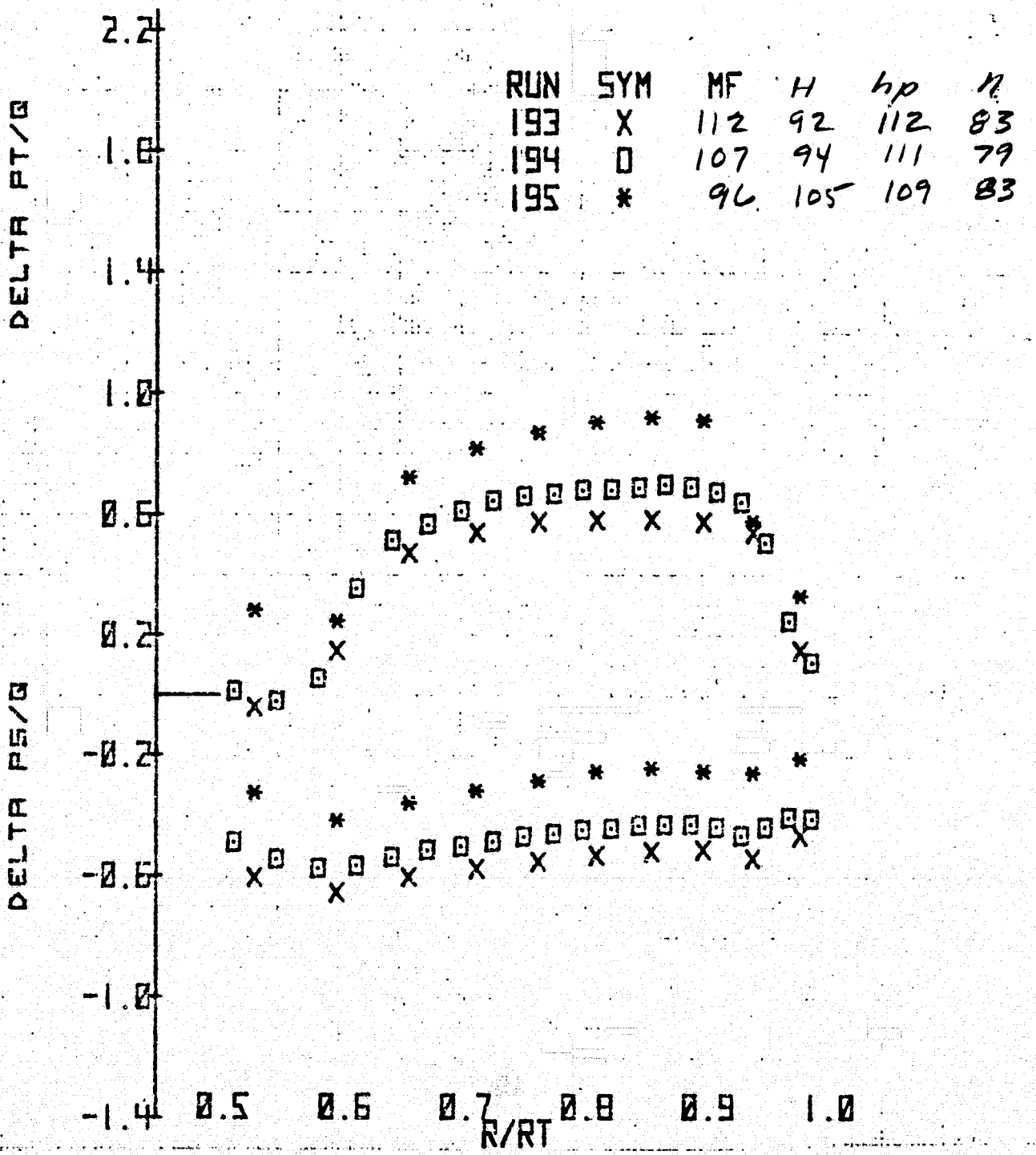

(b) Top azimuth.

Figure 7.- Continued.

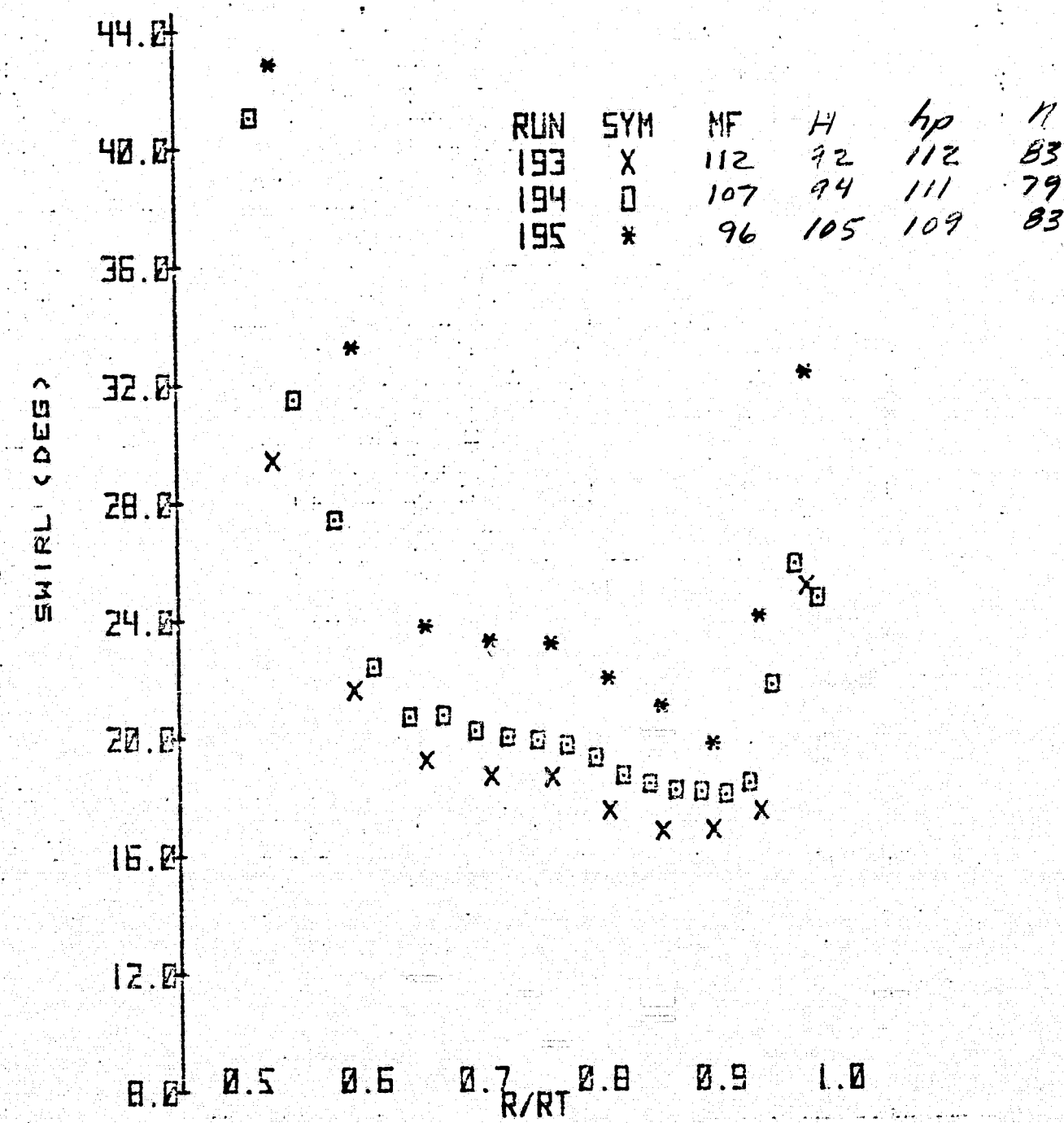

(b) Top azimuth - concluded.

Figure 7.- Continued.

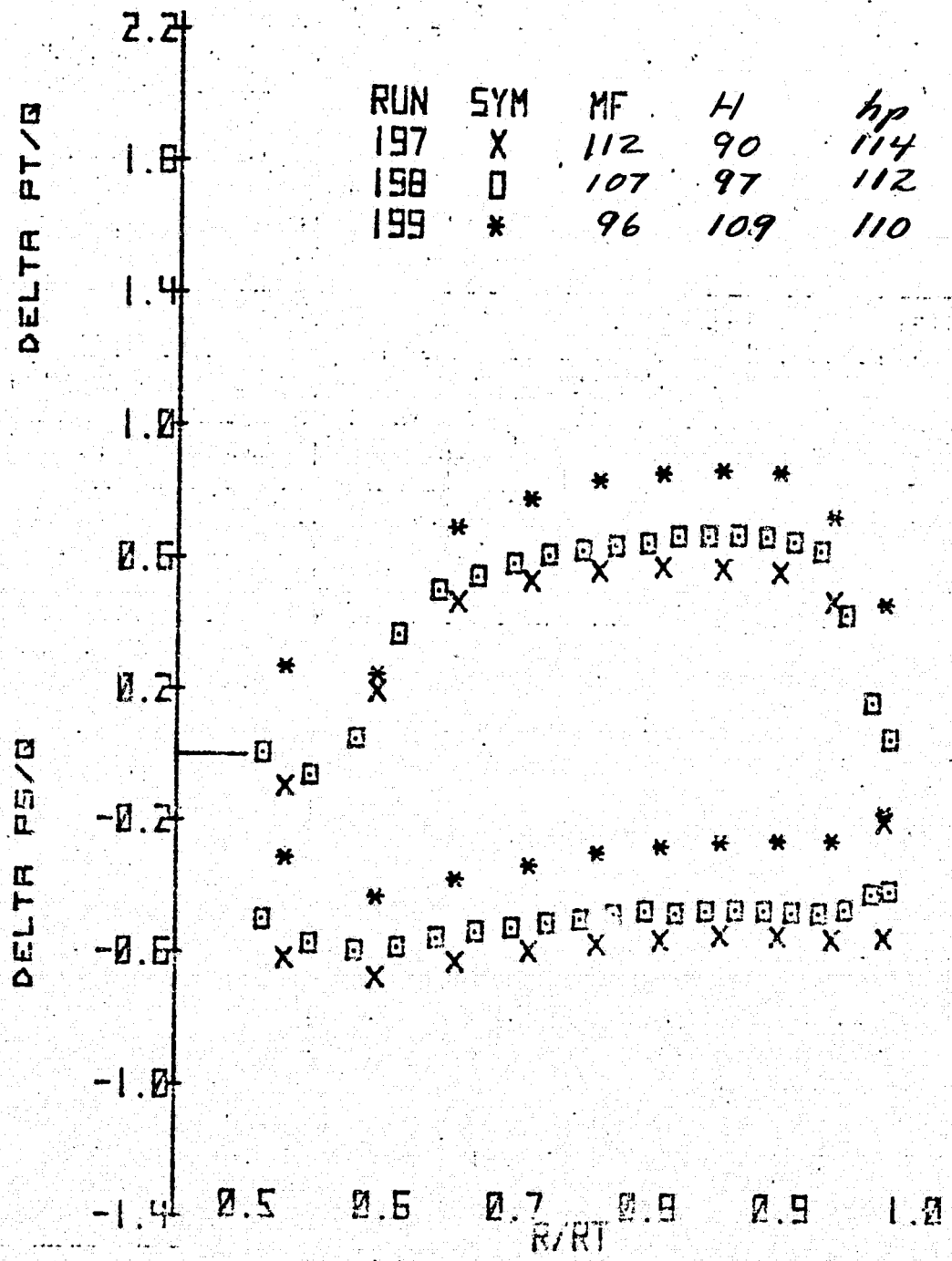

(c) Starboard azimuth.

Figure 7.- Continued.

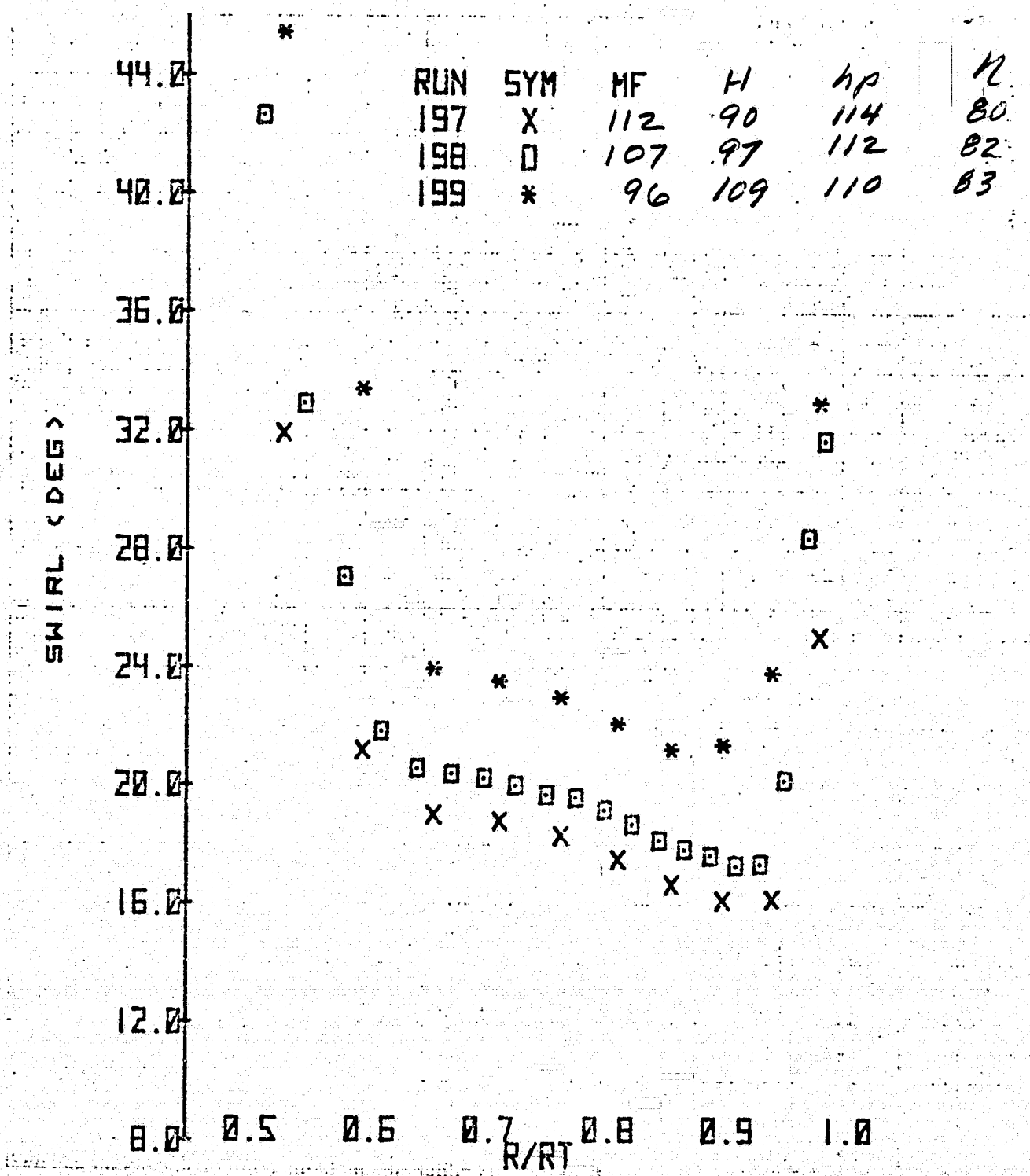

(c) Starboard azimuth - concluded.

Figure 7.- Continued.

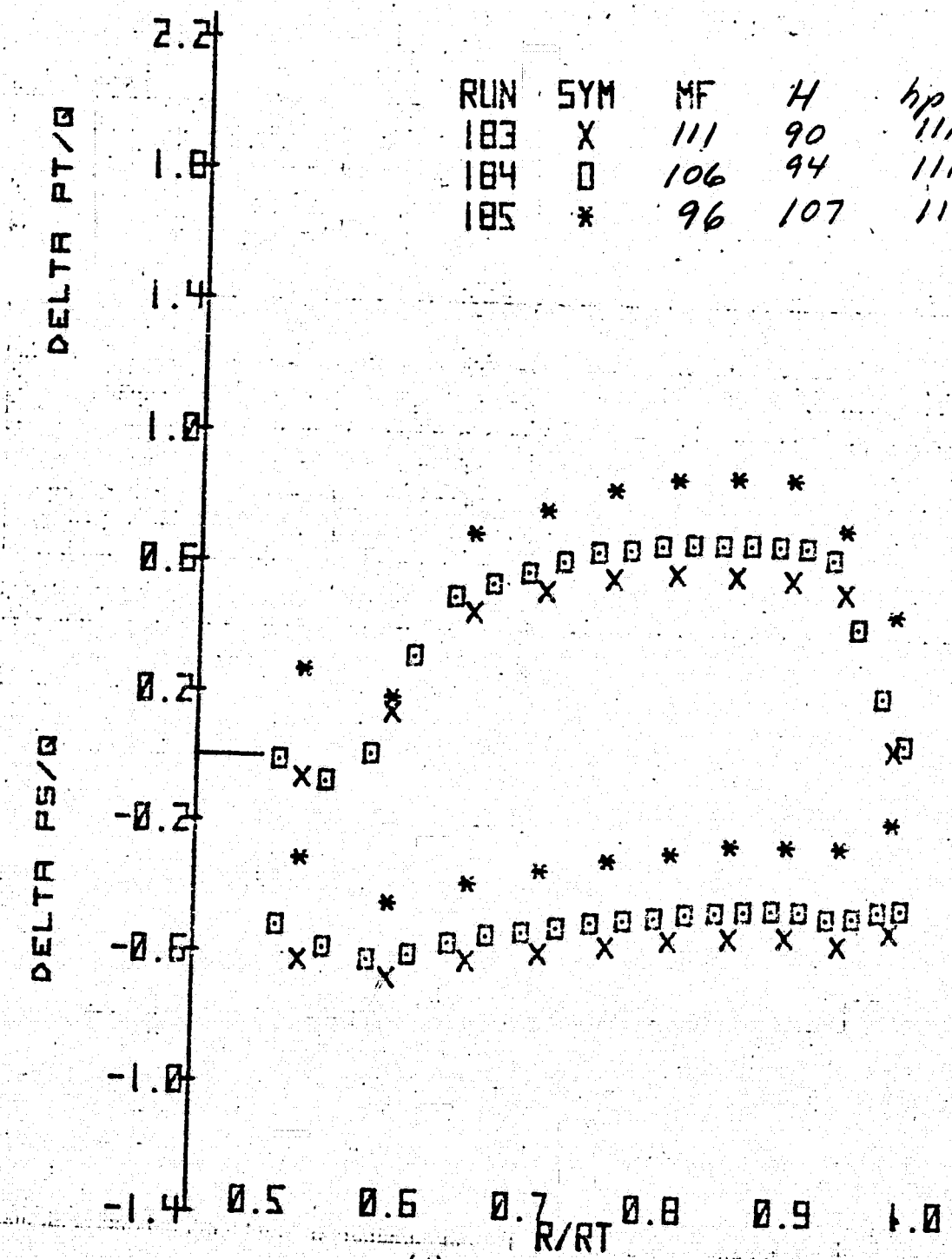

(d) Bottom azimuth.

Figure 7.- Continued.

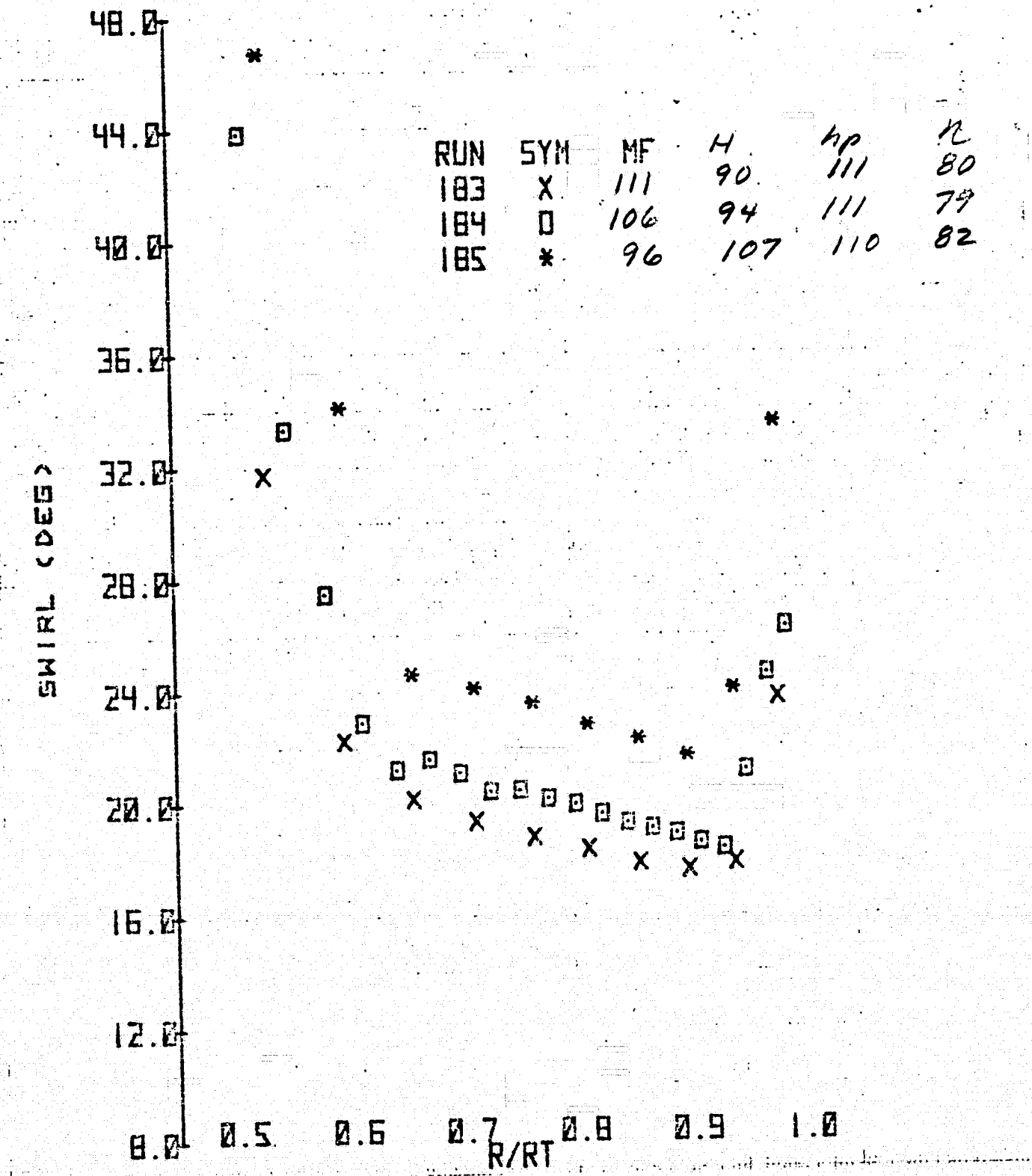

(d) Bottom azimuth - concluded.

Figure 7.- Concluded.

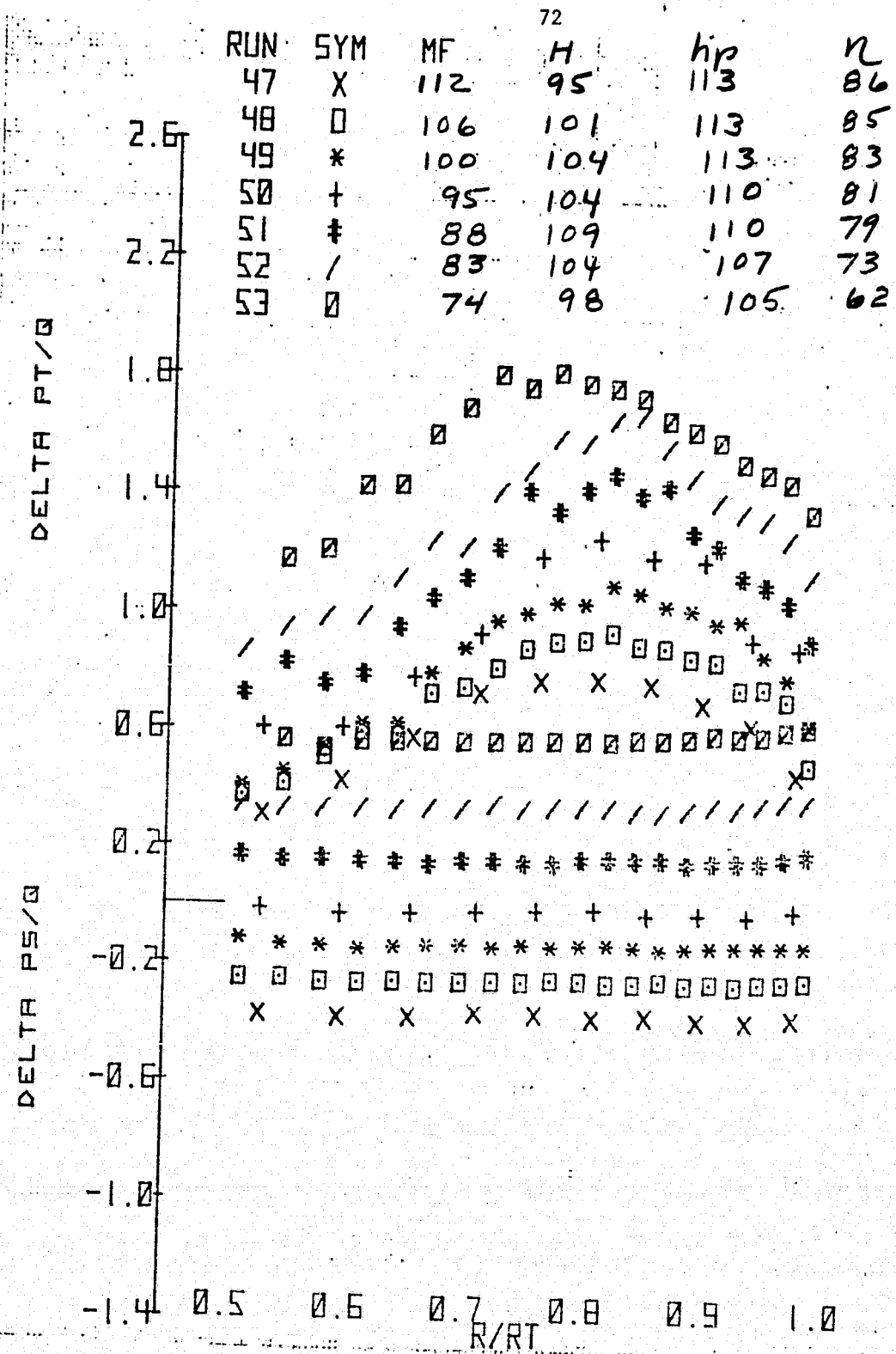

N = 100%

(a) Port azimuth.

Figure 8.- Radial variation of total pressure coefficient, static pressure coefficient, and swirl angle downstream of stators for several azimuths and mass flows; ξ = 35.4°, exit honeycomb in, original contraction.

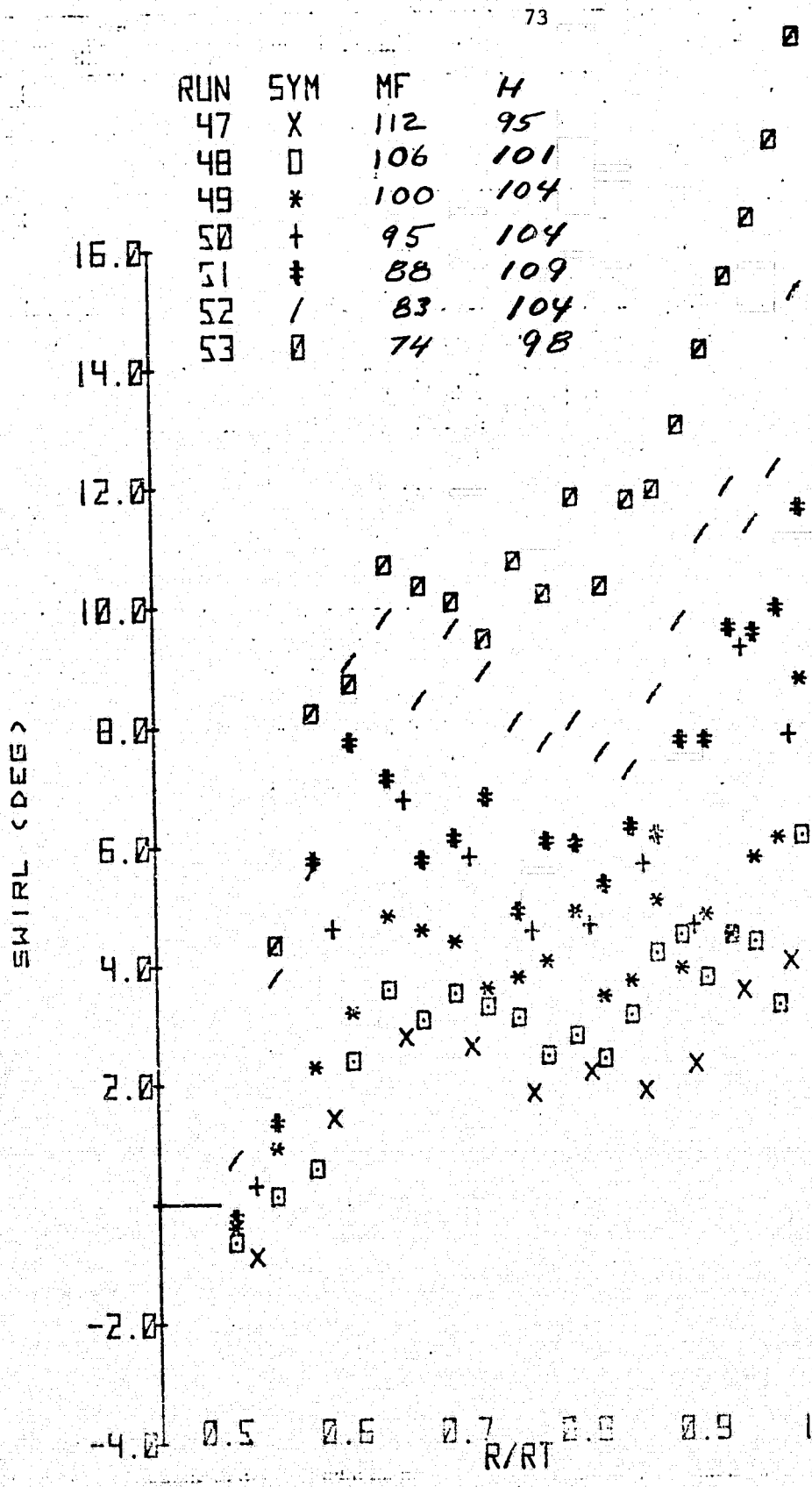

N = 100%

(a) Port azimuth - continued.

Figure 8.- Continued.

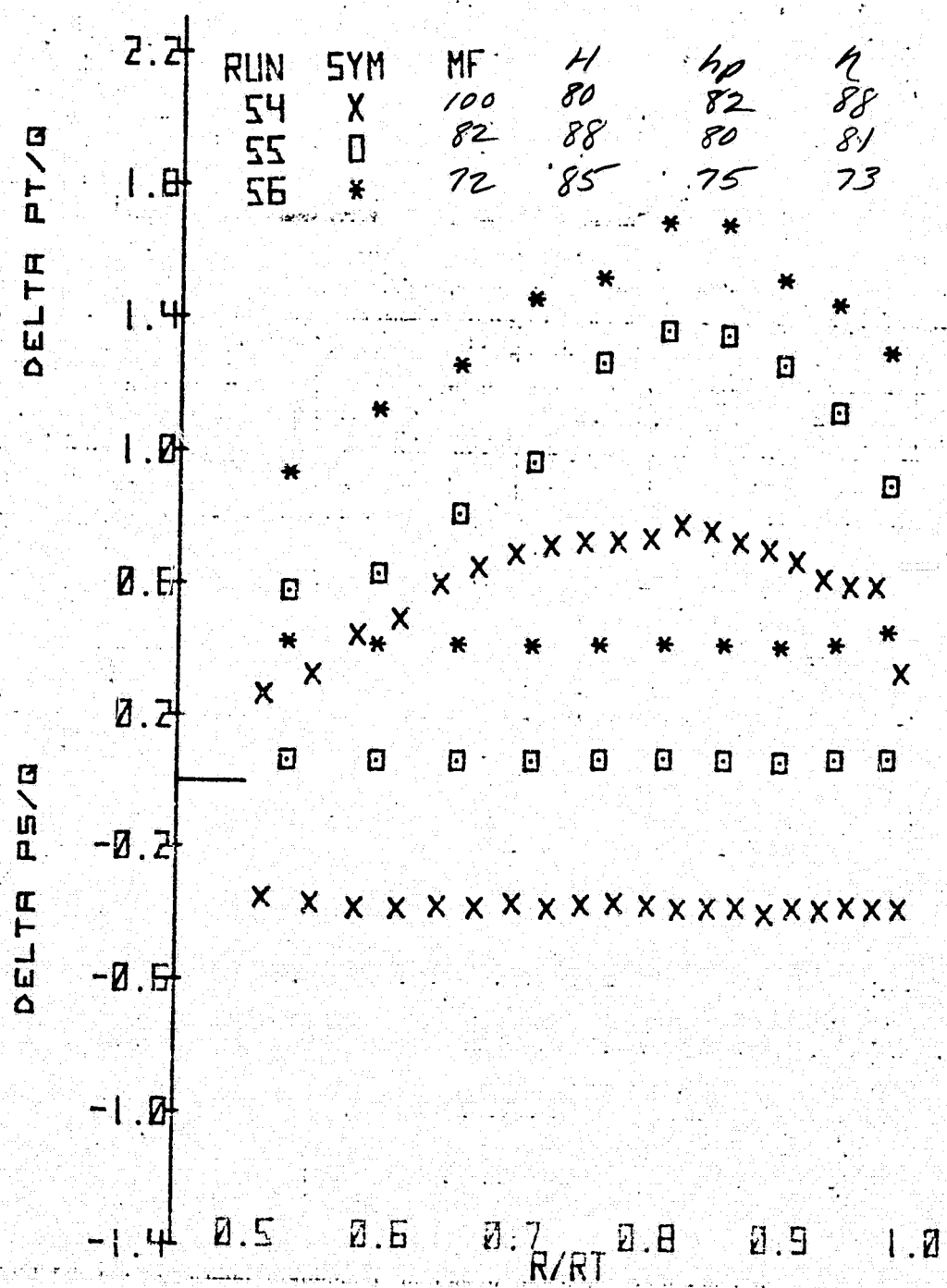

N = 90%

(a) Port azimuth - continued.

Figure 8.- Continued.

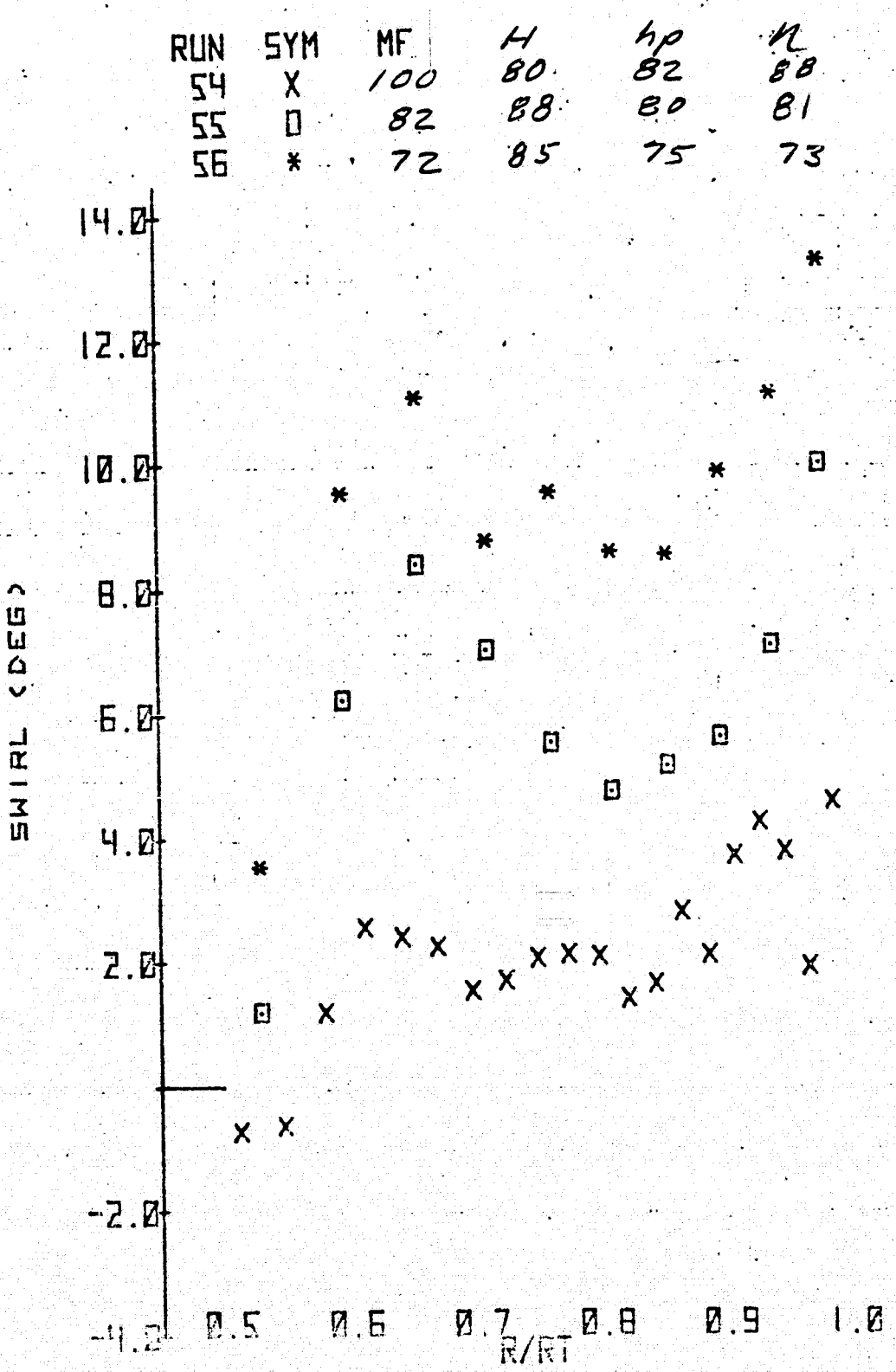

N = 90%

(a) Port azimuth - concluded.

Figure 8.- Continued.

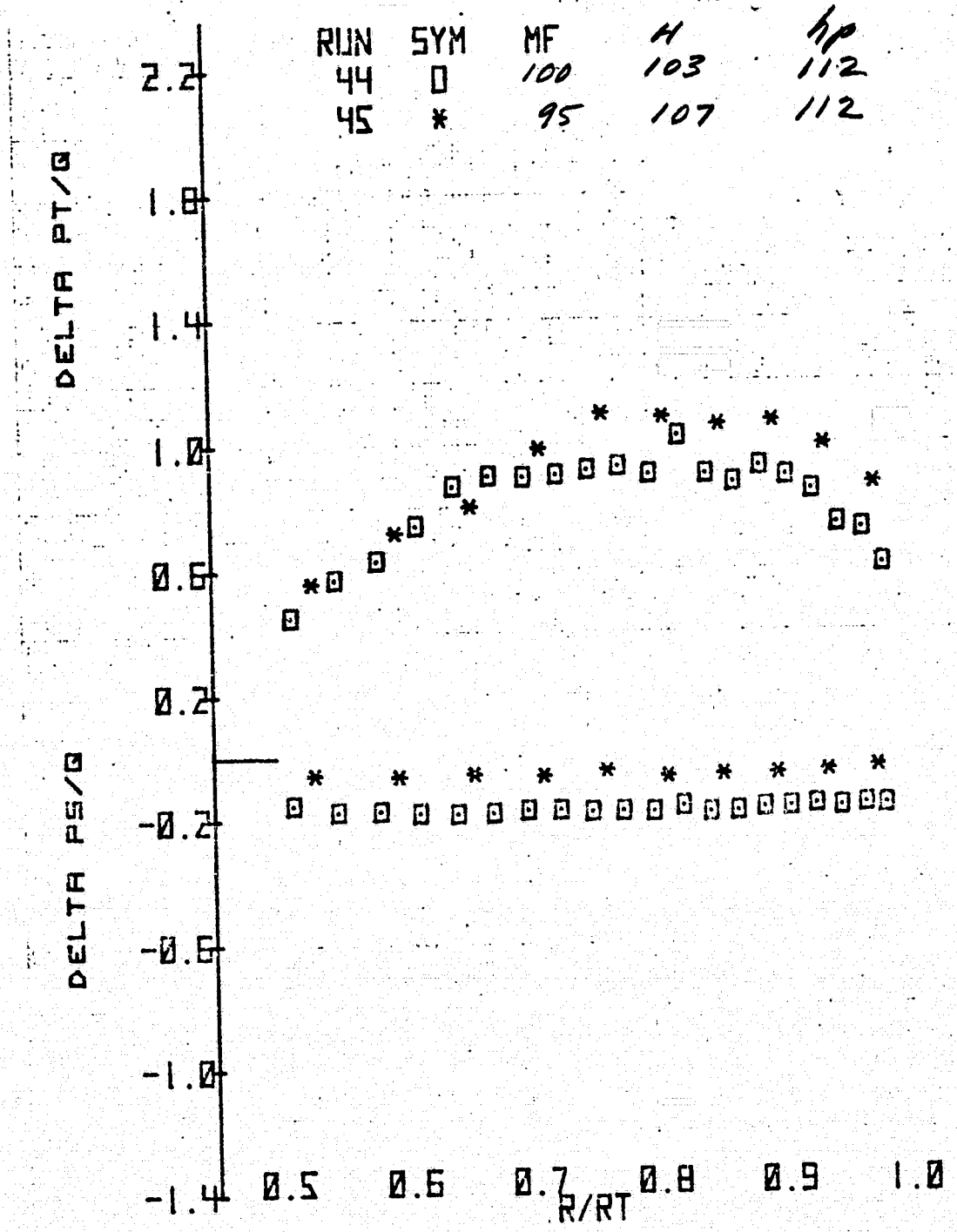

N = 100%

(b) Top azimuth.

Figure 8.- Continued.

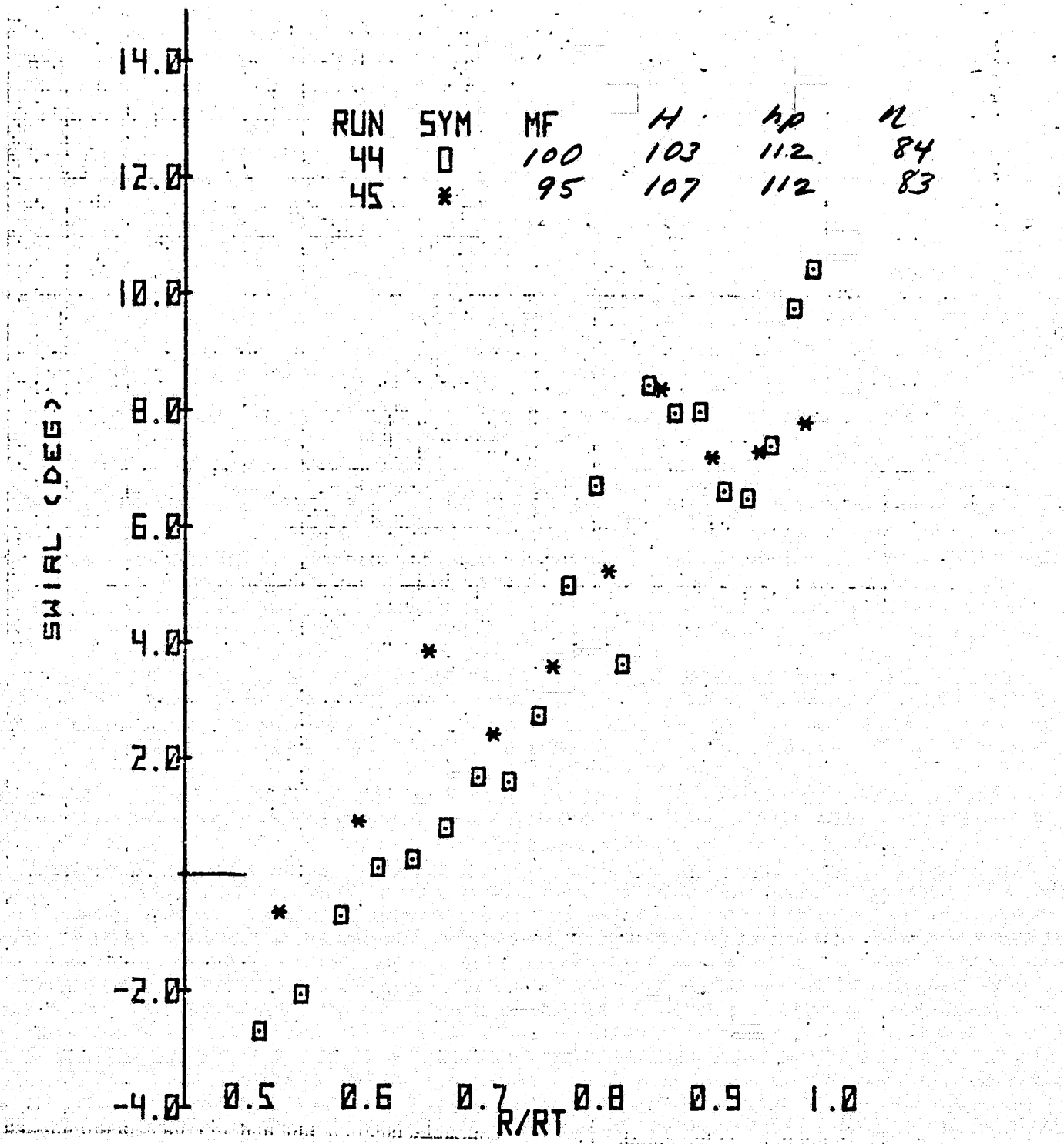

N = 100%

(b) Top azimuth - concluded.

Figure 8.- Continued.

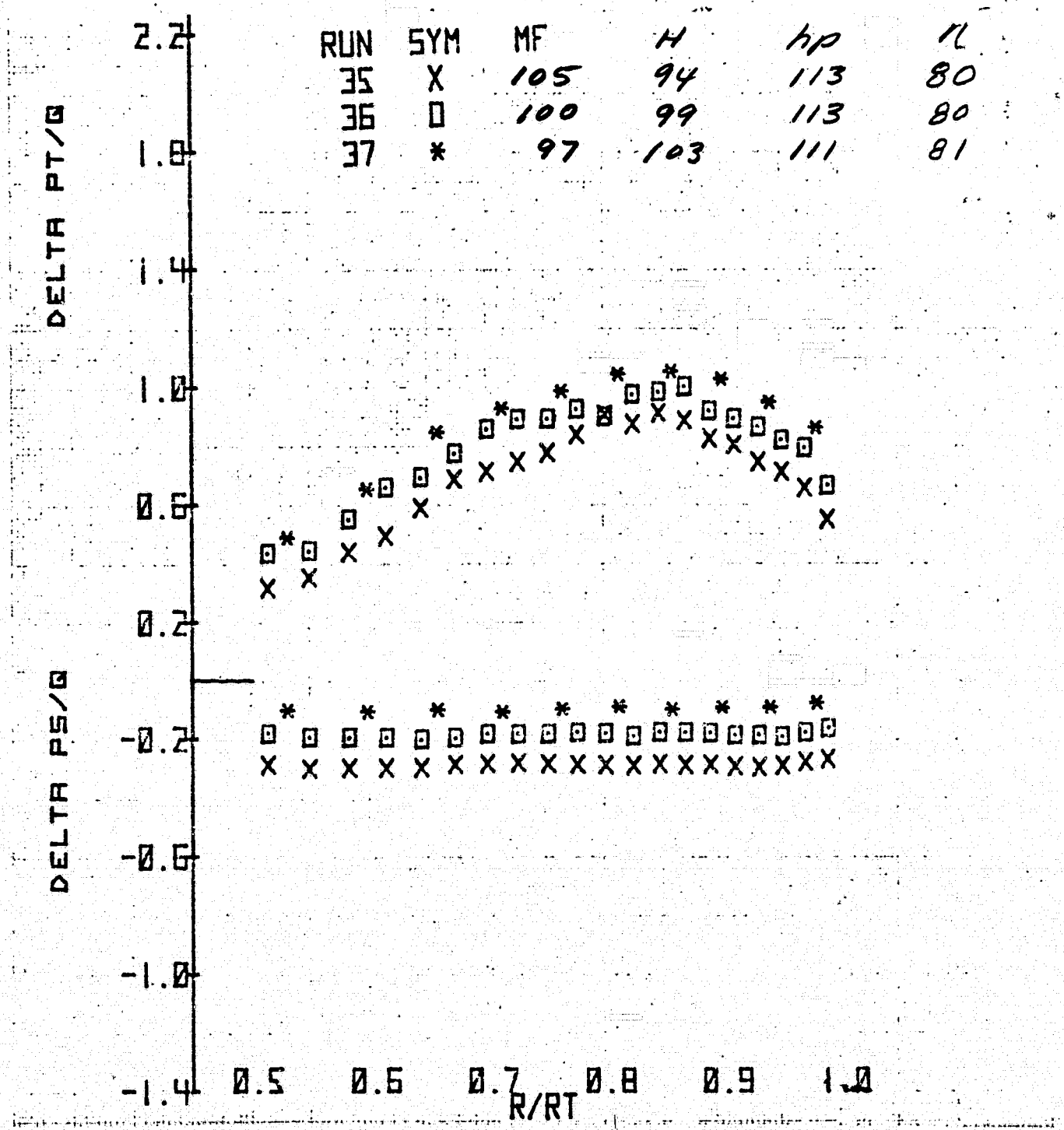

N = 100%

(c) Starboard azimuth.

Figure 8.- Continued.

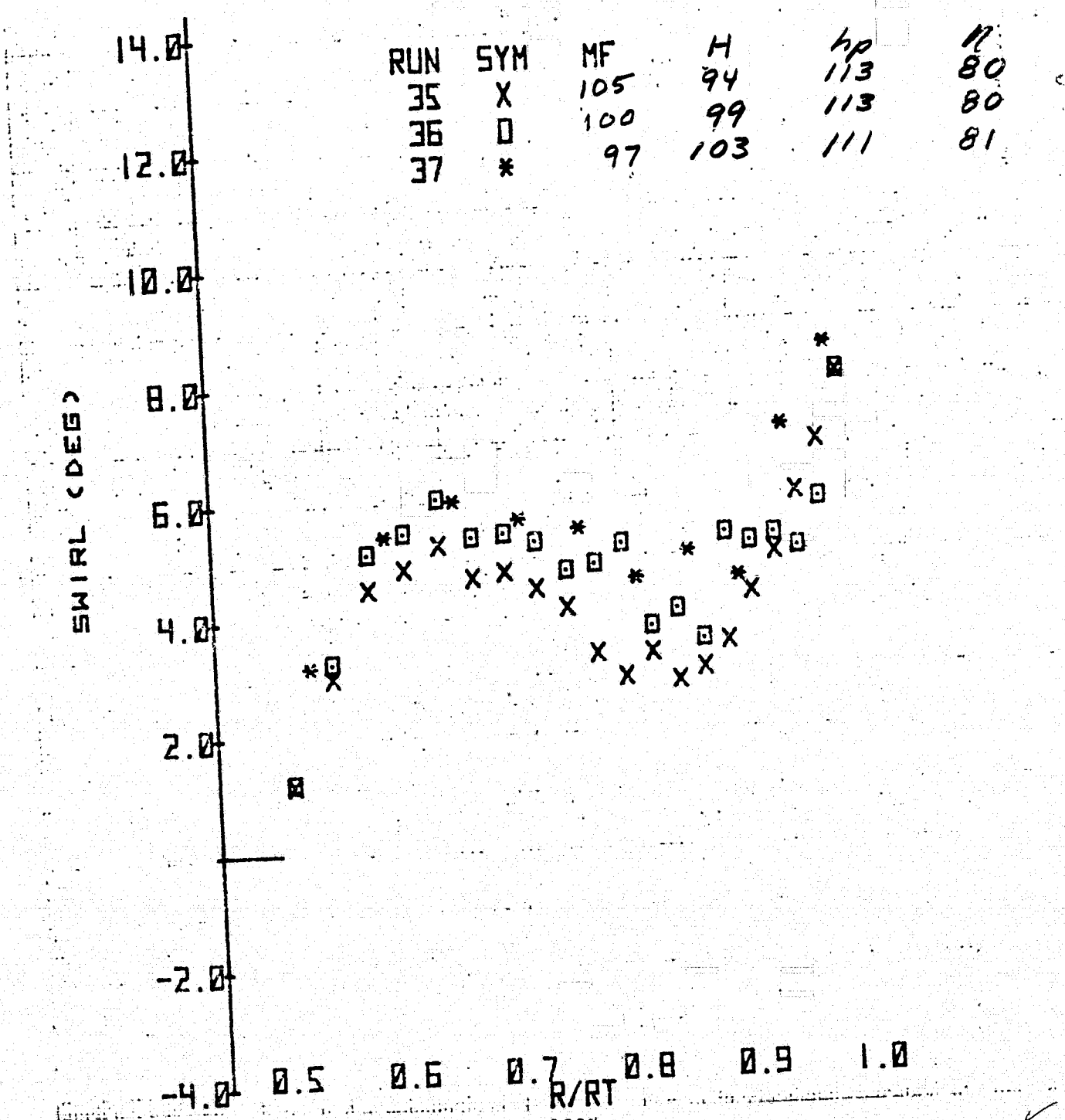

N = 100%

(c) Starboard azimuth - concluded.

Figure 8.- Continued.

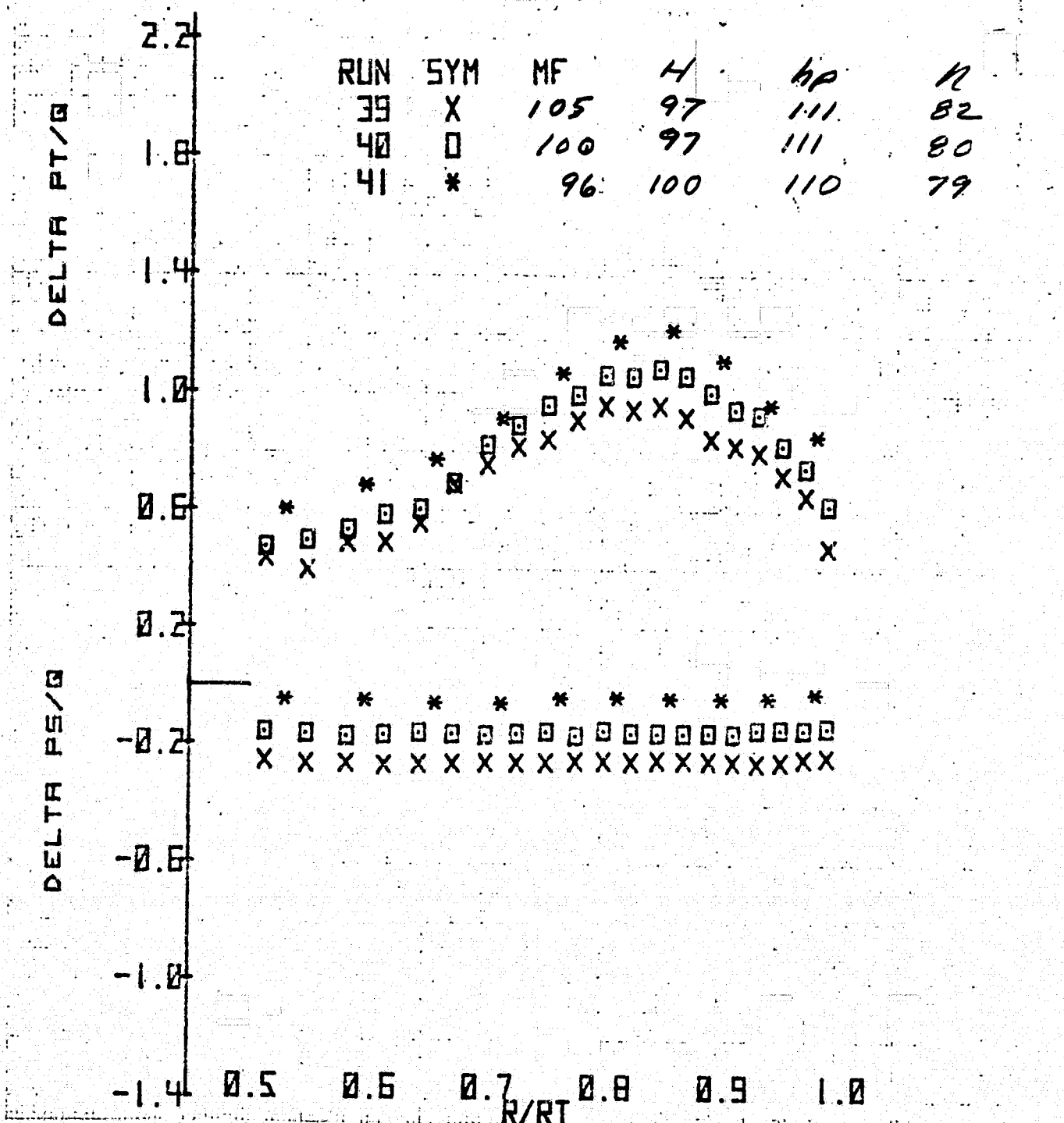

N = 100%

(d) Bottom azimuth.

Figure 8.- Continued.

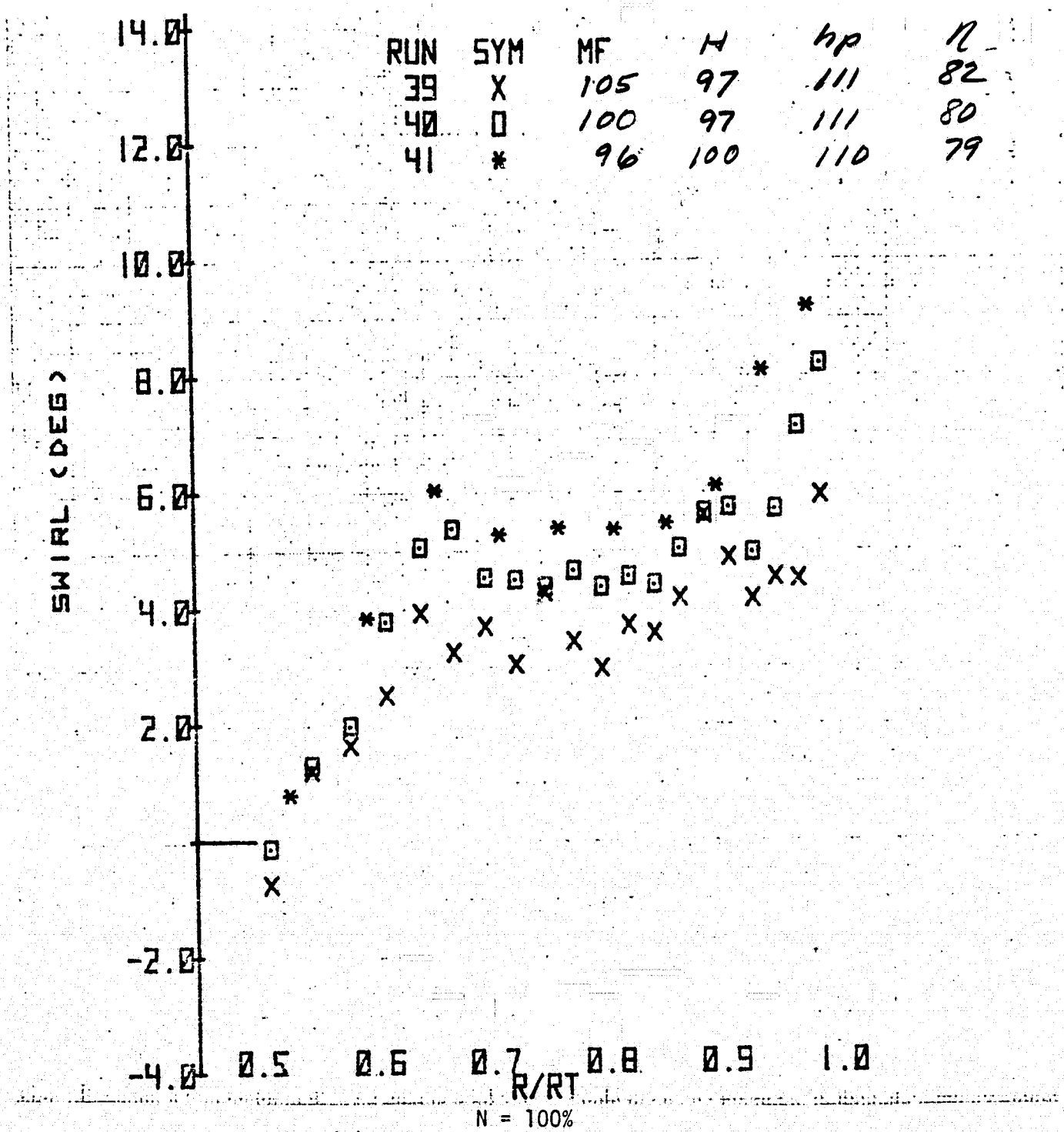

(d) Bottom azimuth - concluded.

Figure 8.- Concluded.

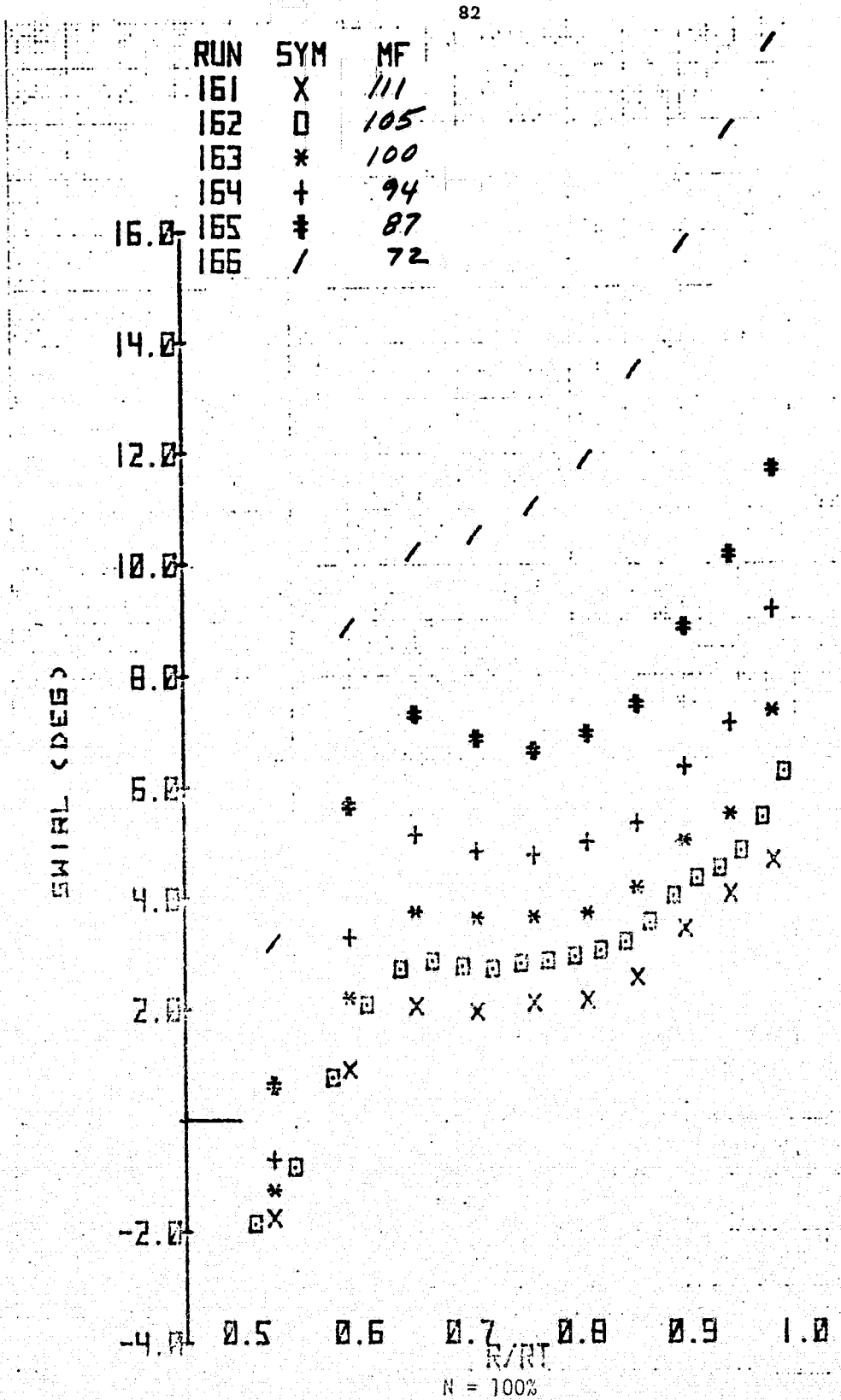

(a) Port azimuth.

Figure 9.- Radial variation of total pressure coefficient, static pressure coefficient, and swirl angle downstream of stators for several azimuths and mass flows; original contraction, inlet honeycomb in, and ξ = 35.4°.

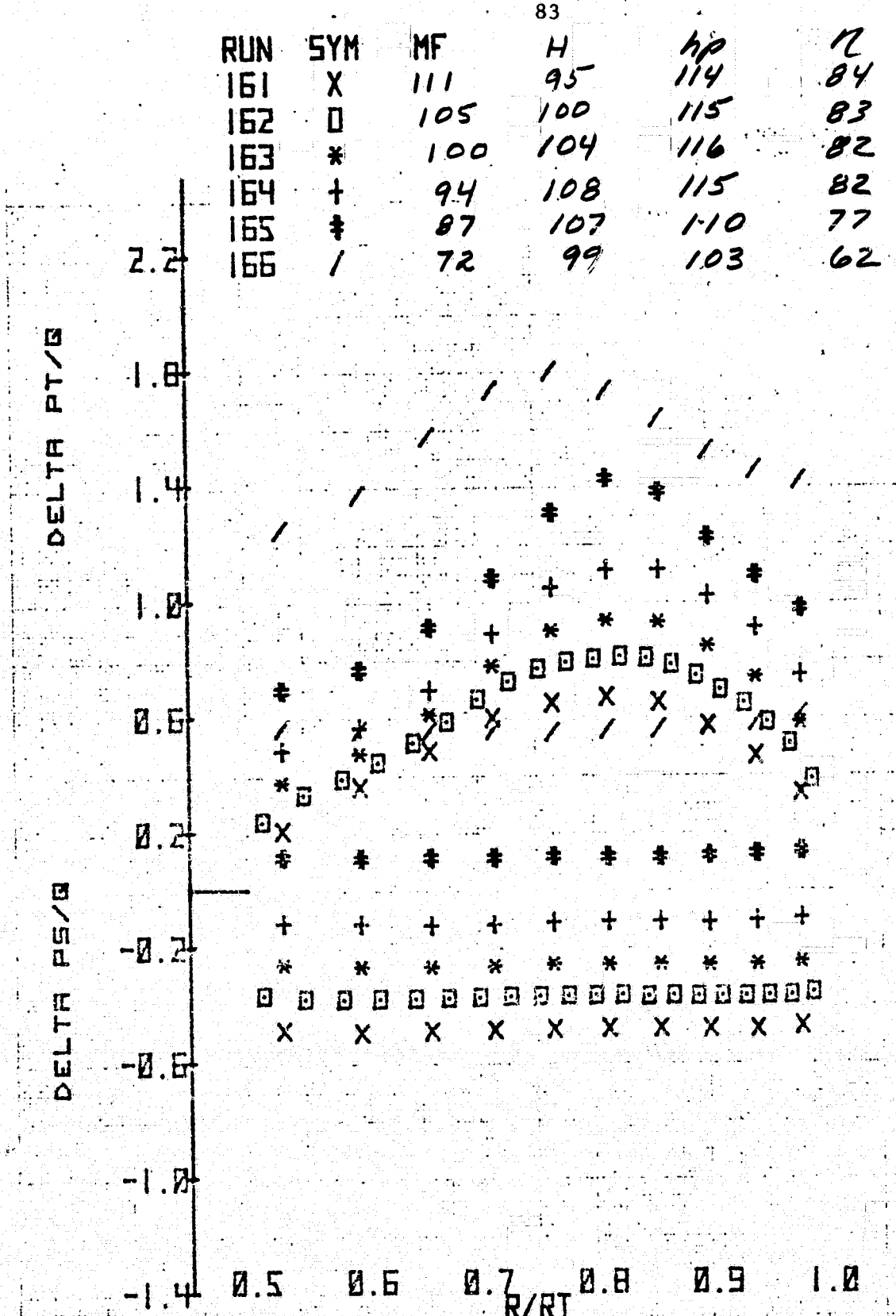

N = 100%

(a) Port azimuth - concluded.

Figure 9.- Continued.

RUN	SYM	MF	H	hp	n
167	X	111	95	114	84
168	□	106	100	116	85
169	*	95	95	111	83
170	+	74	102	104	66

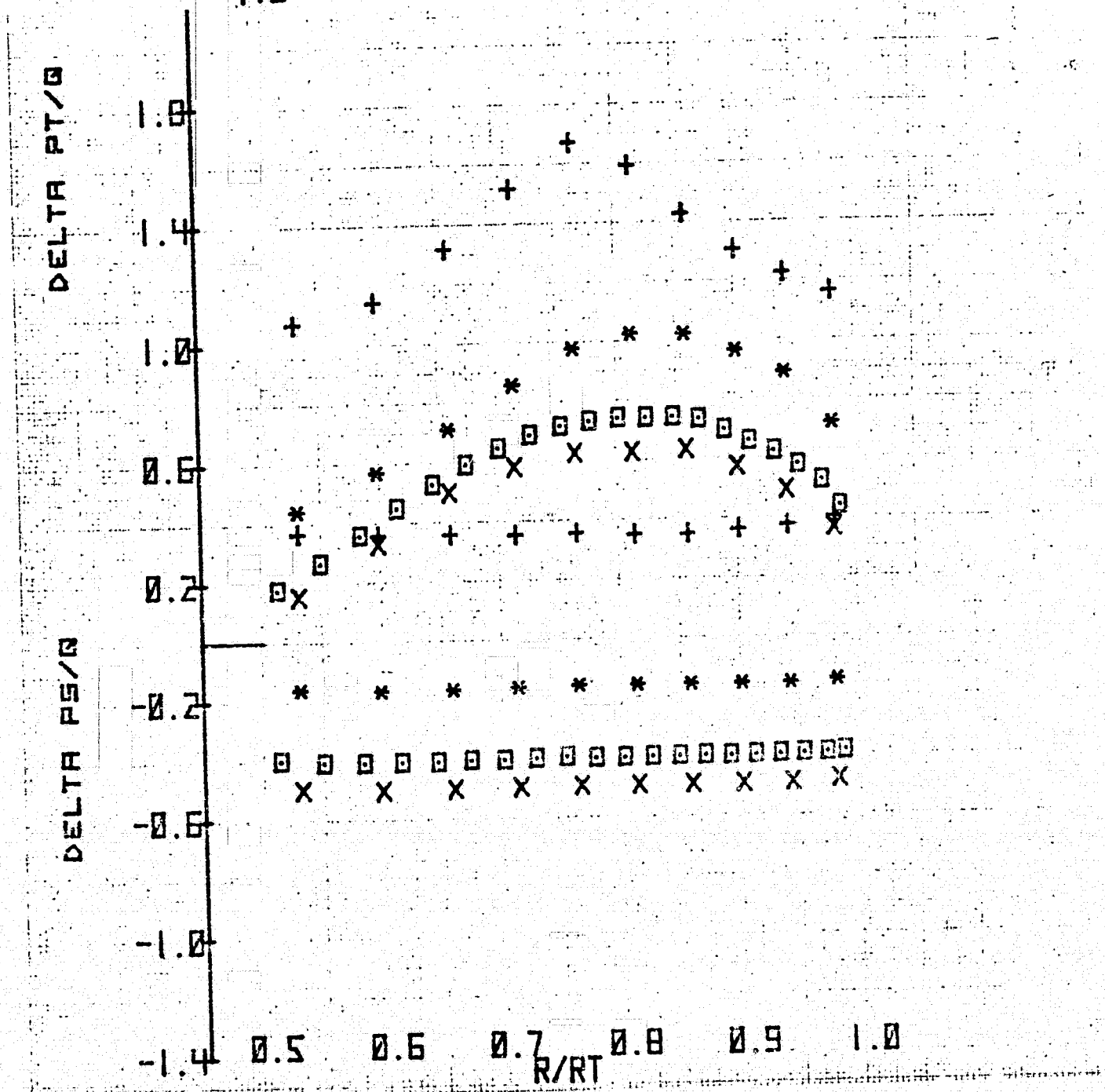

N = 100%

(b) Top azimuth.

Figure 9.- Continued.

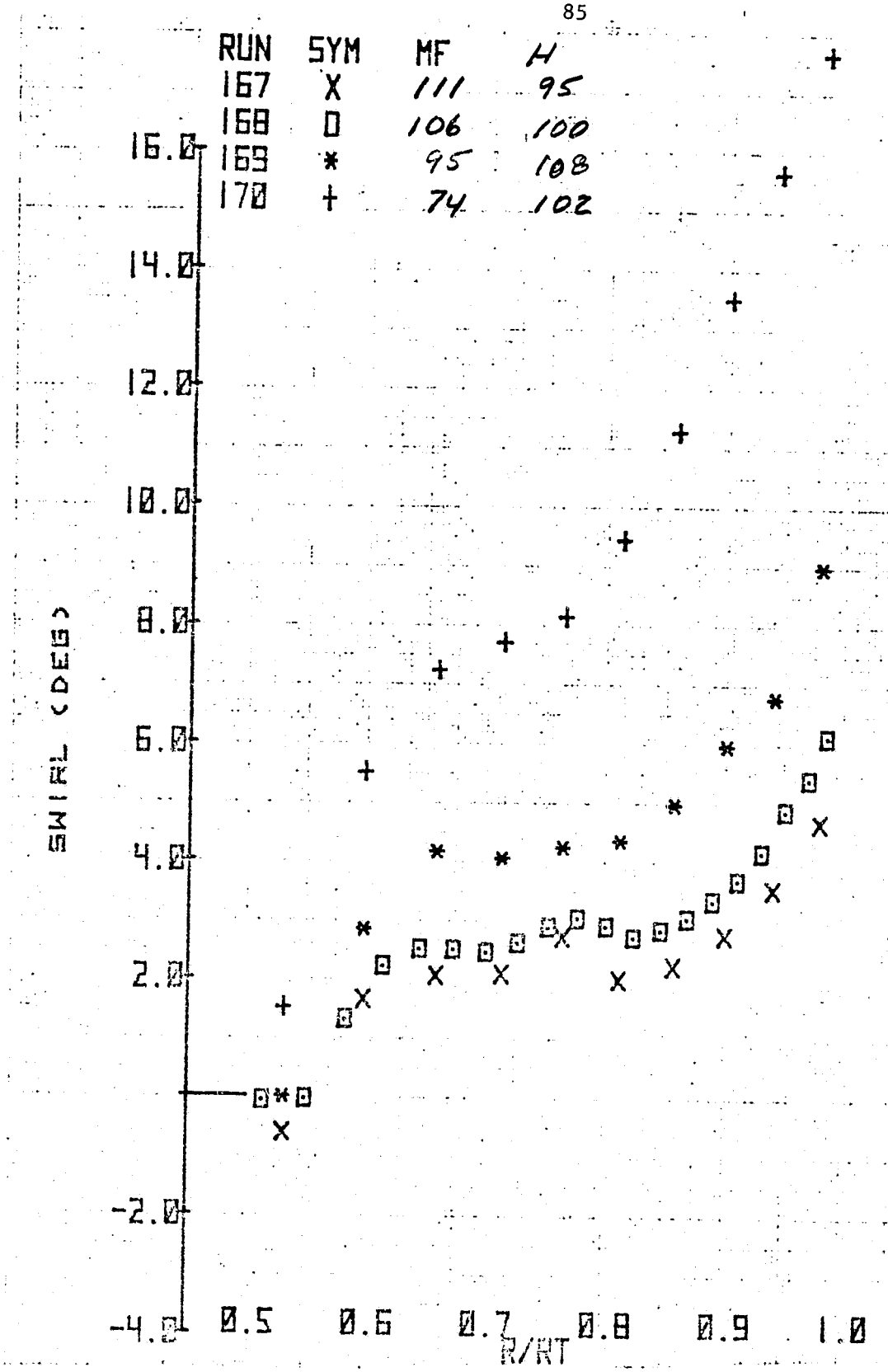

N - 100%

(b) Top azimuth - concluded.

Figure 9.- Continued.

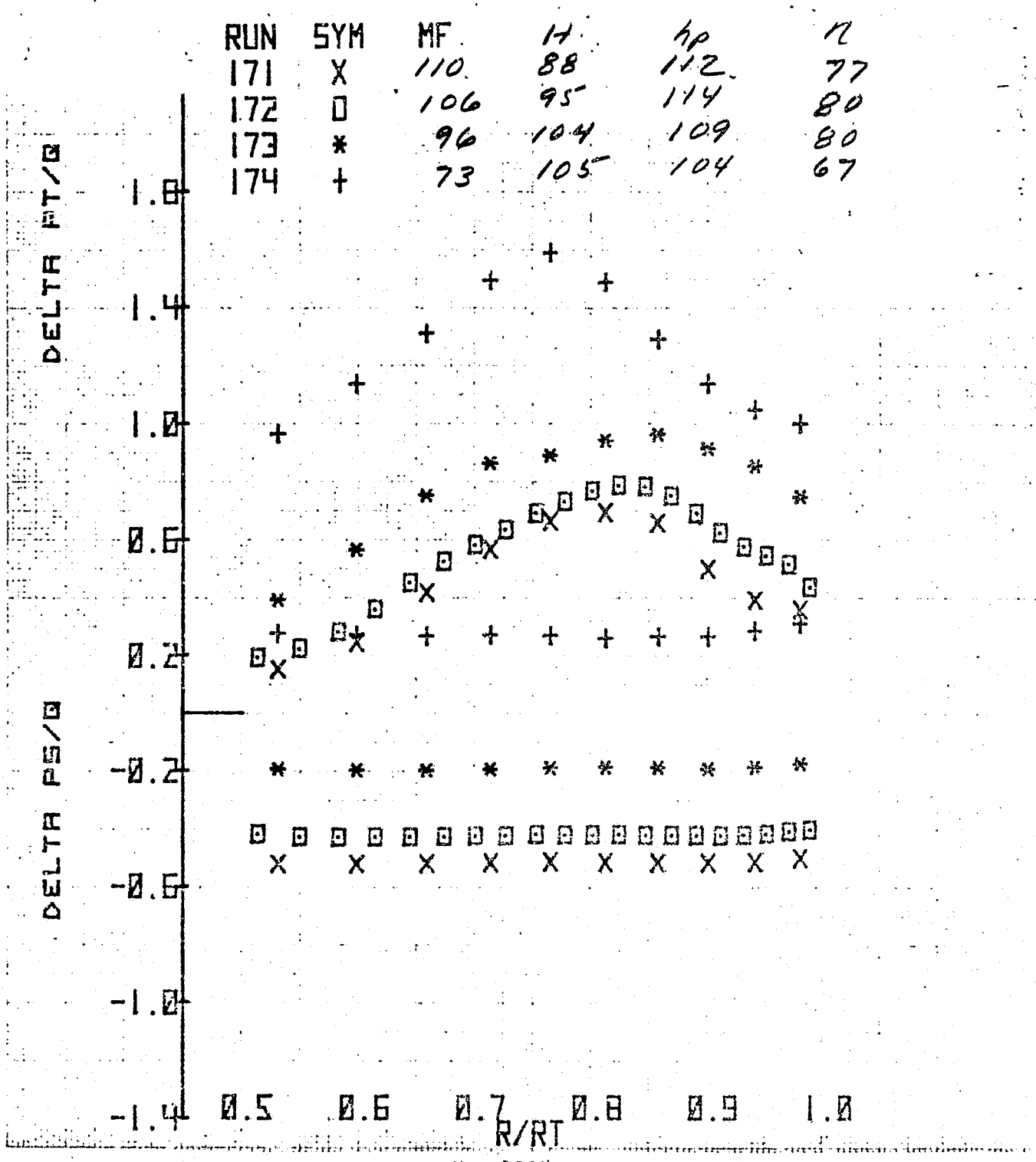

N = 100%

(c) Starboard azimuth.

Figure 9.- Continued.

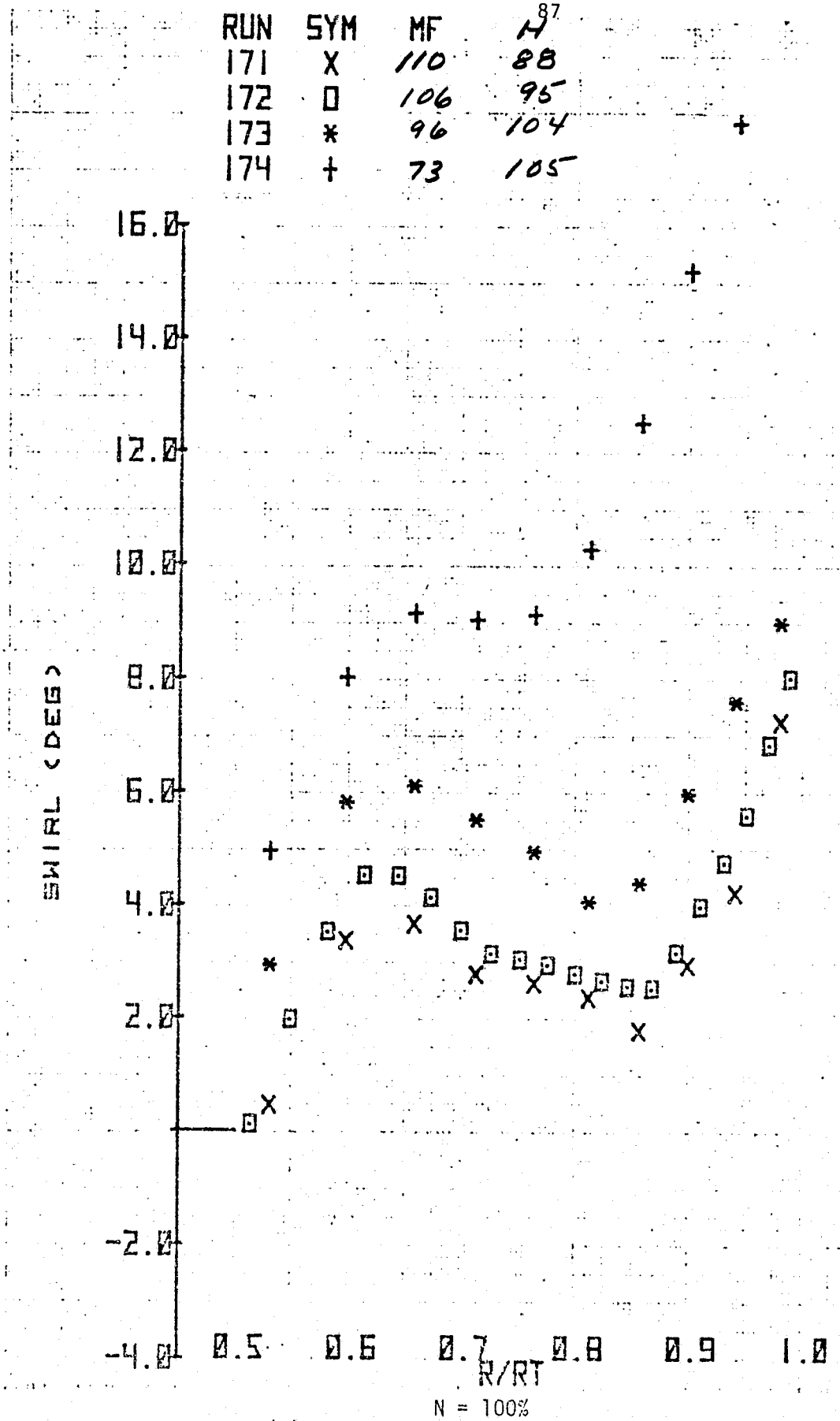

N = 100%

(c) Starboard azimuth - concluded.

Figure 9.- Continued.

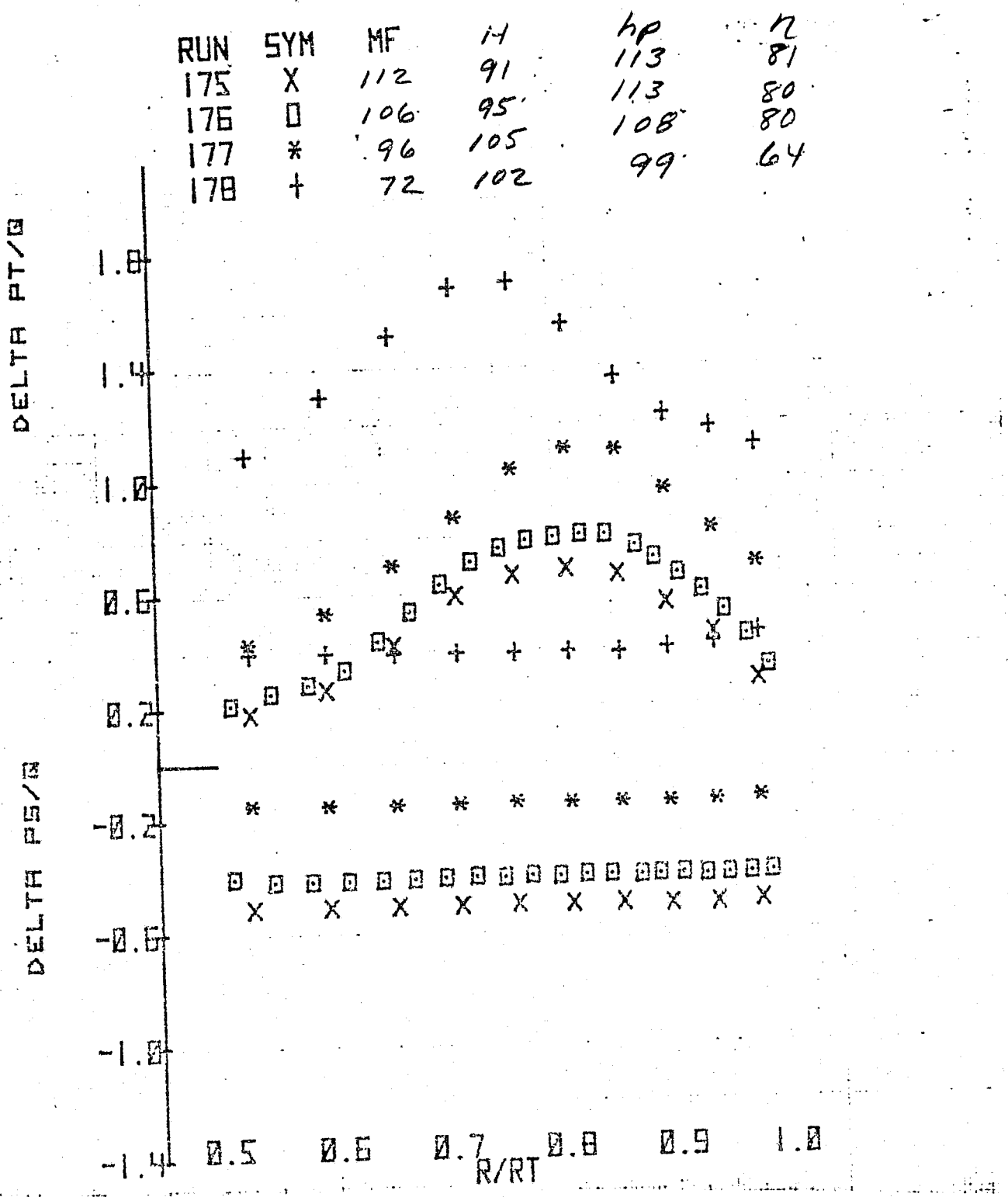

N = 100%

(d) Bottom azimuth.

Figure 9.- Continued.

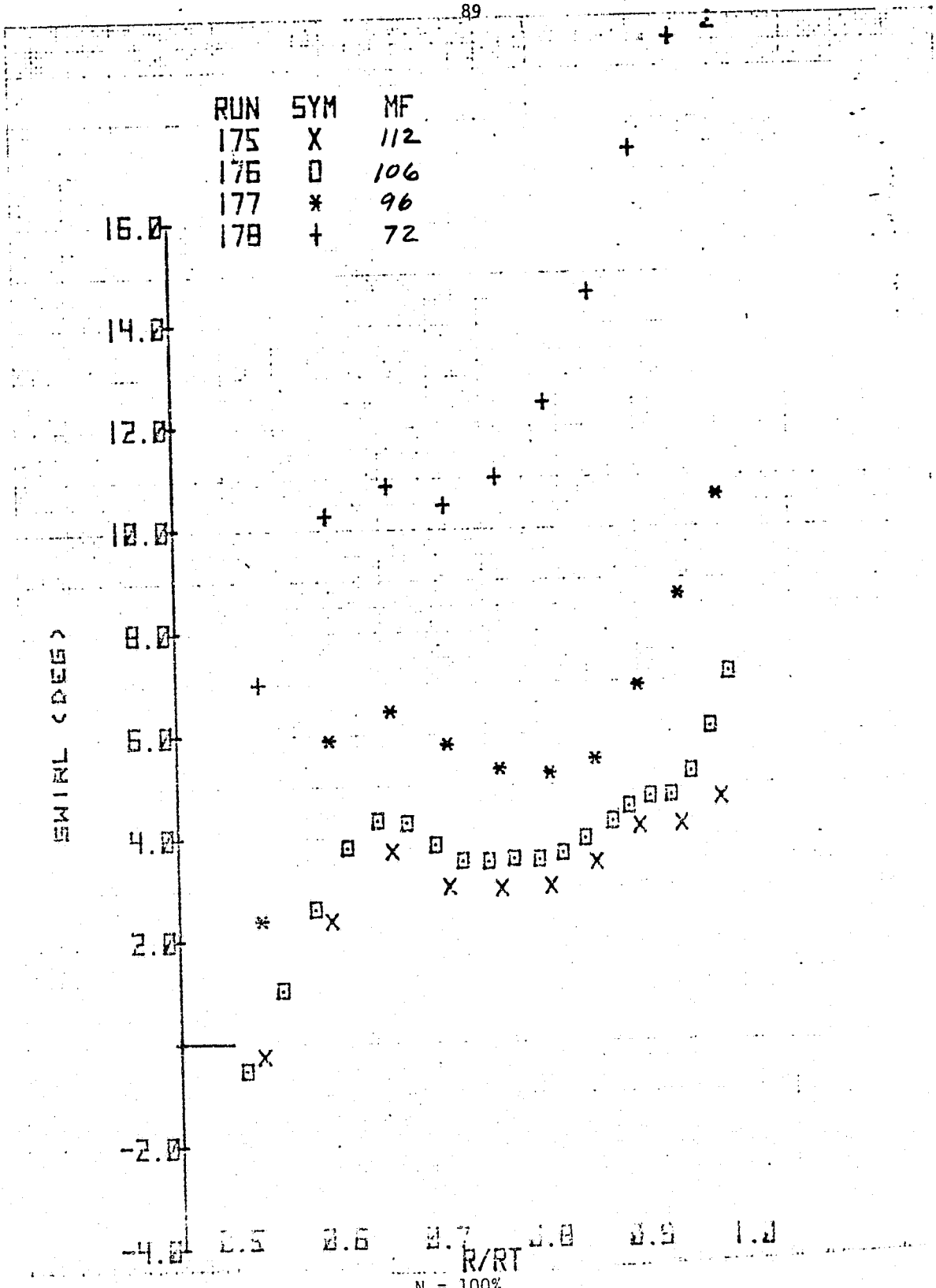

(d) Bottom azimuth - continued.

Figure 9.- Continued.

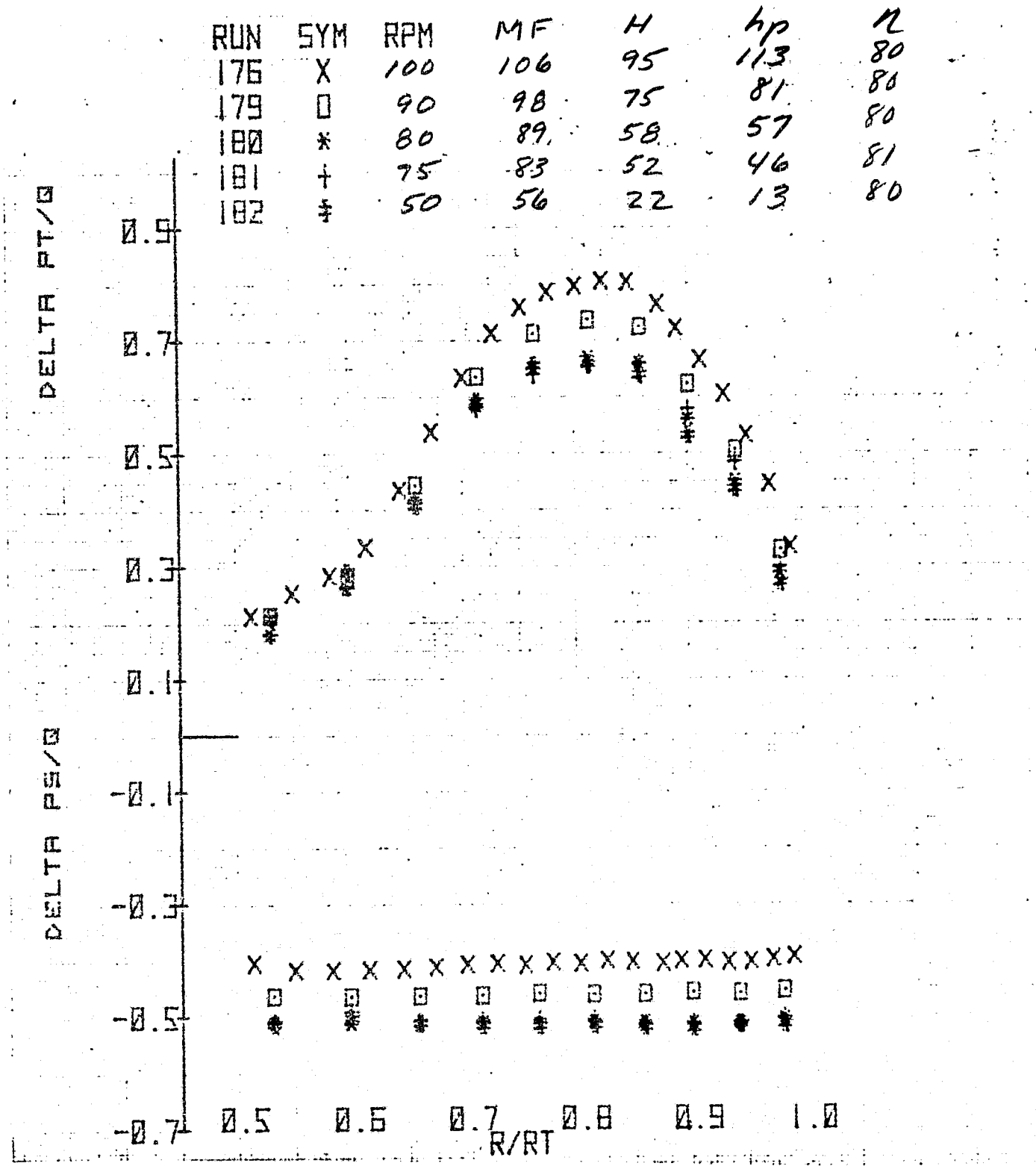

N = Various speeds.

(d) Bottom azimuth - continued.

Figure 9.- Continued

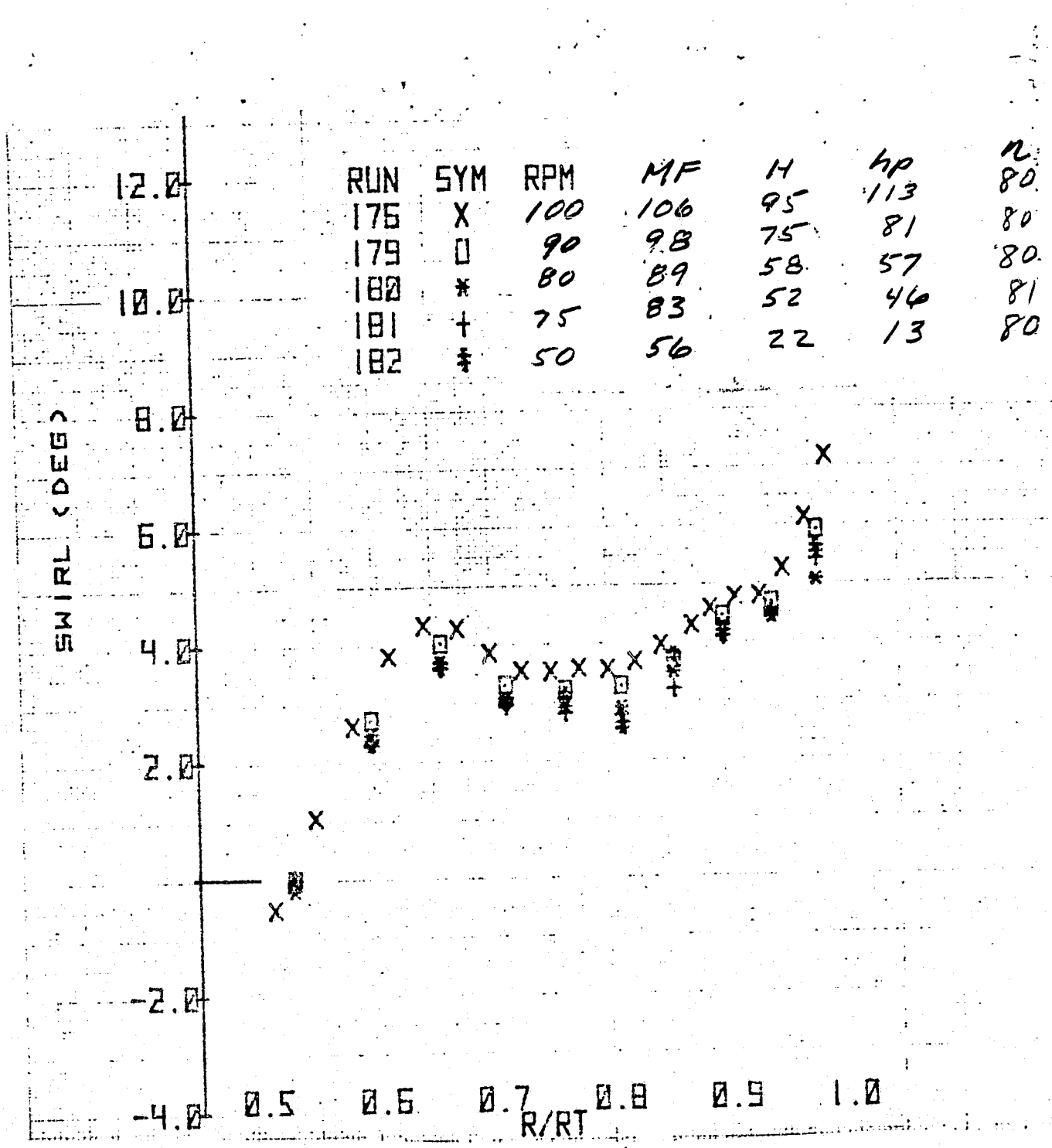

N = Various speeds.

(d) Bottom azimuth - concluded.

Figure 9.- Concluded.

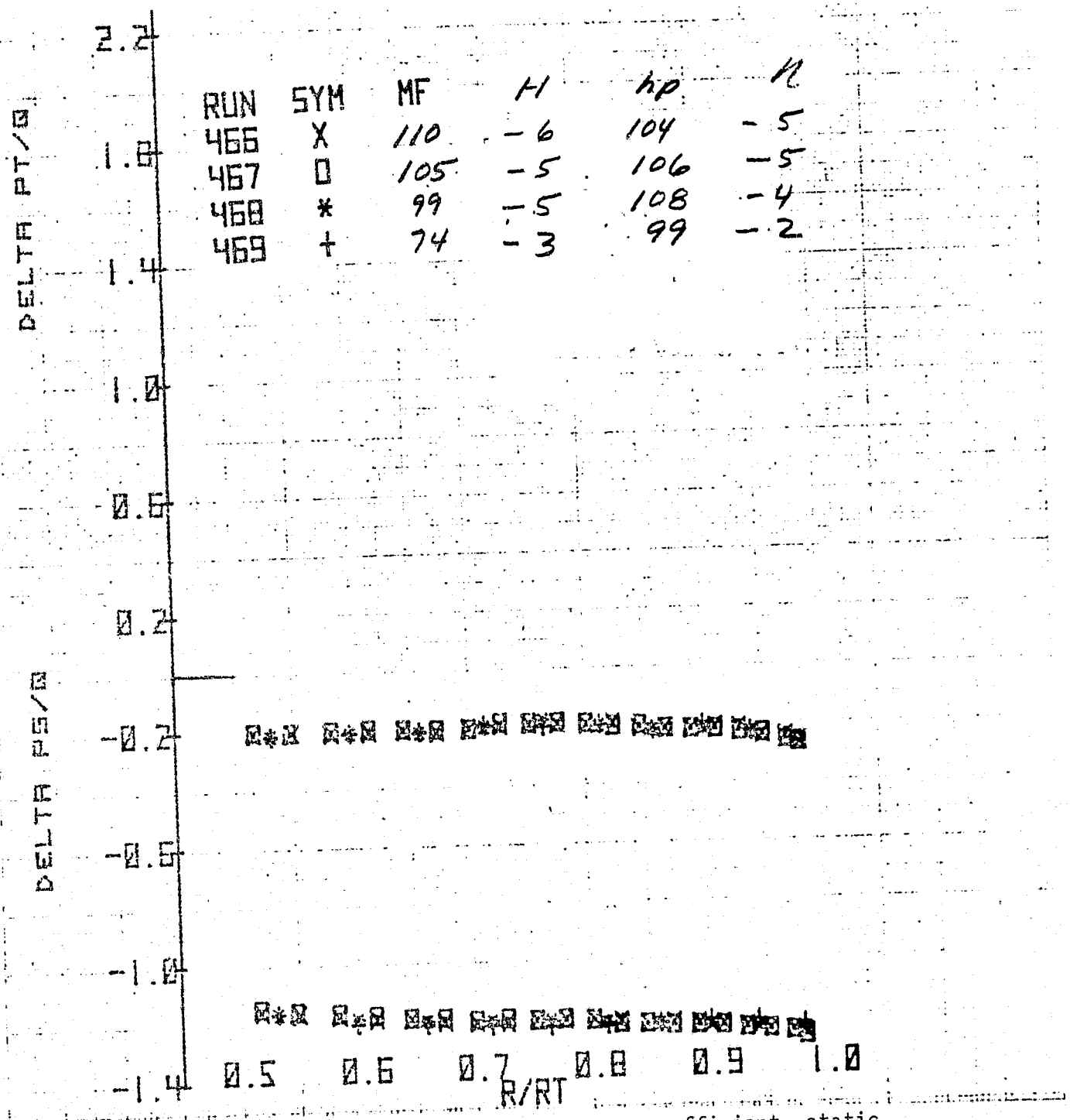

Figure 10.- Radial variation of total pressure coefficient, static pressure coefficient, and swirl angle upstream of rotor at the top azimuth at several mass flows; inlet honeycomb in, modified contraction, N = 100%, ξ = 38°.

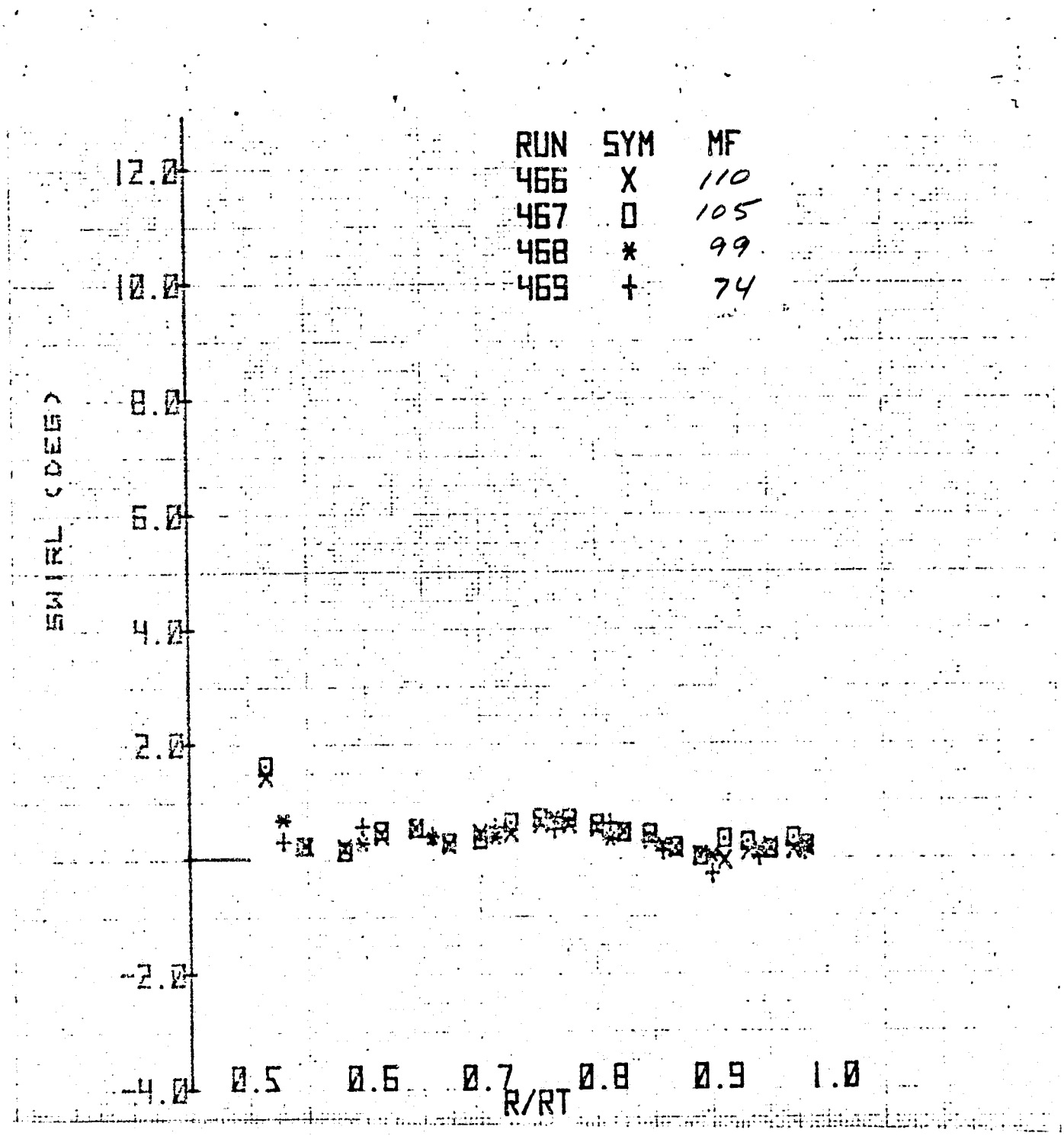

Figure 10.- Concluded.

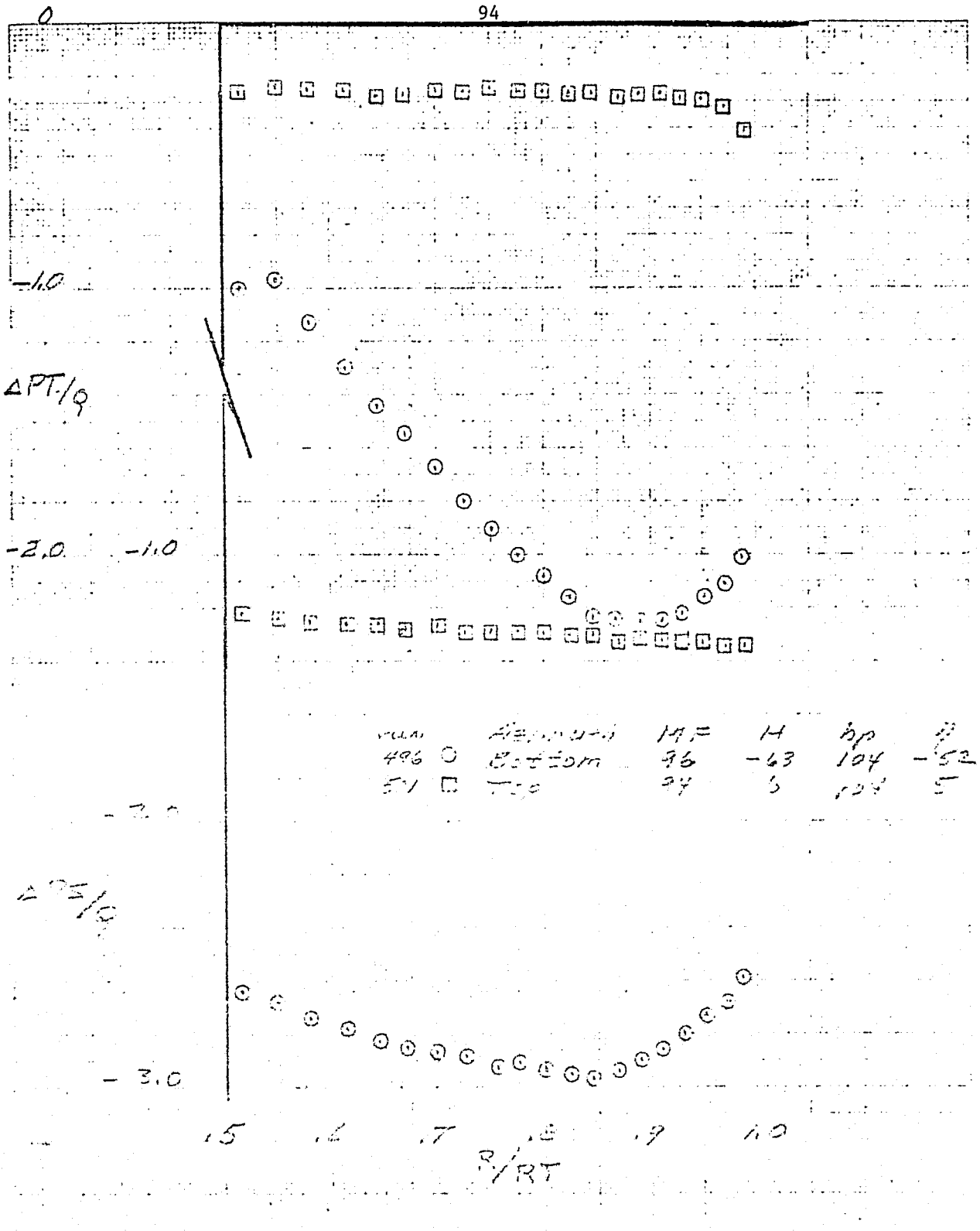

Figure 11.- [illegible] pressure coefficient, static pressure coefficient and swirl angle upstream of rotor for two azimuths, 95% mass flow; N = 100%, inlet honeycomb in, "D" inflow configuration, modified contraction, and F = 38°

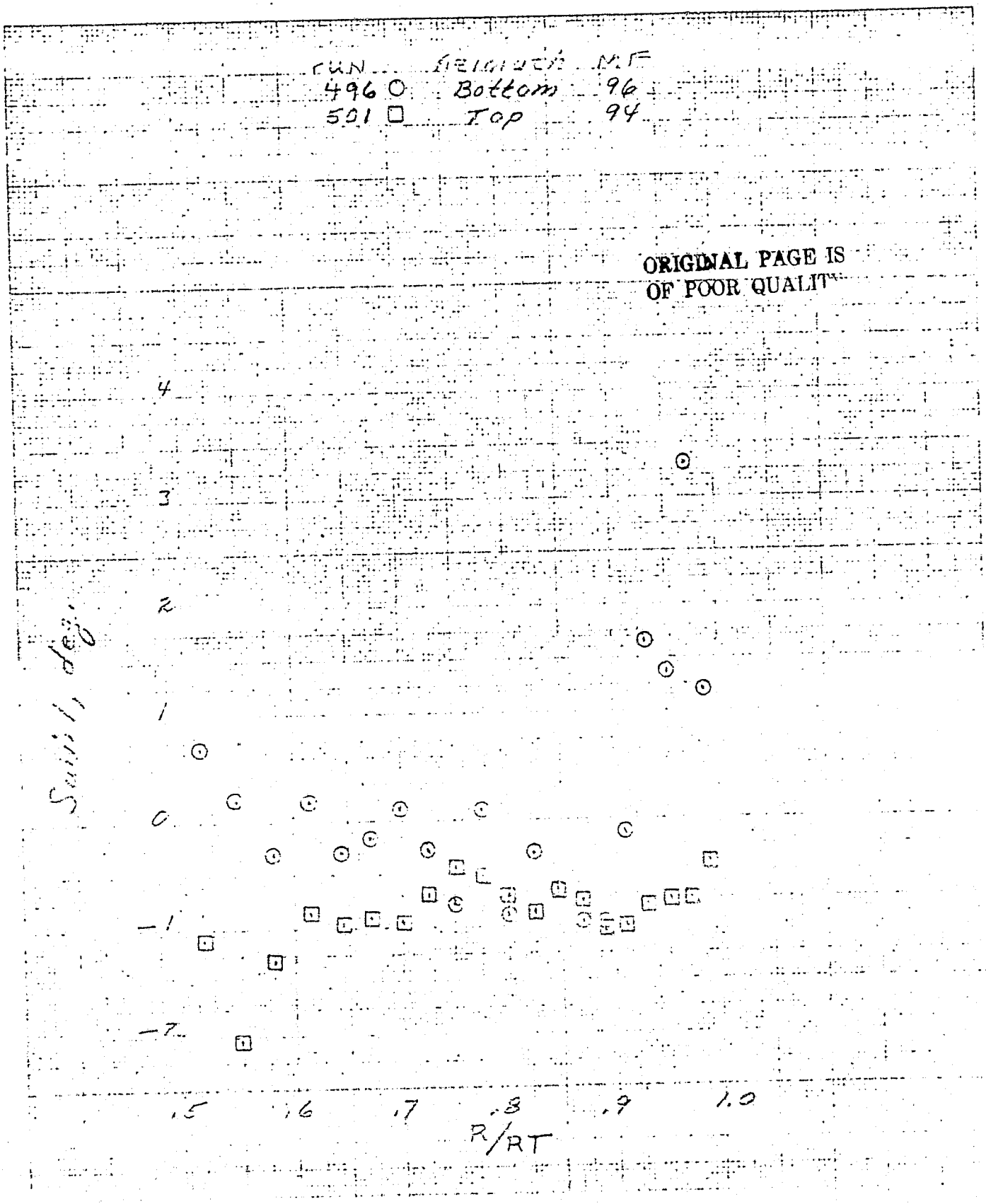

Figure 11.- Concluded.

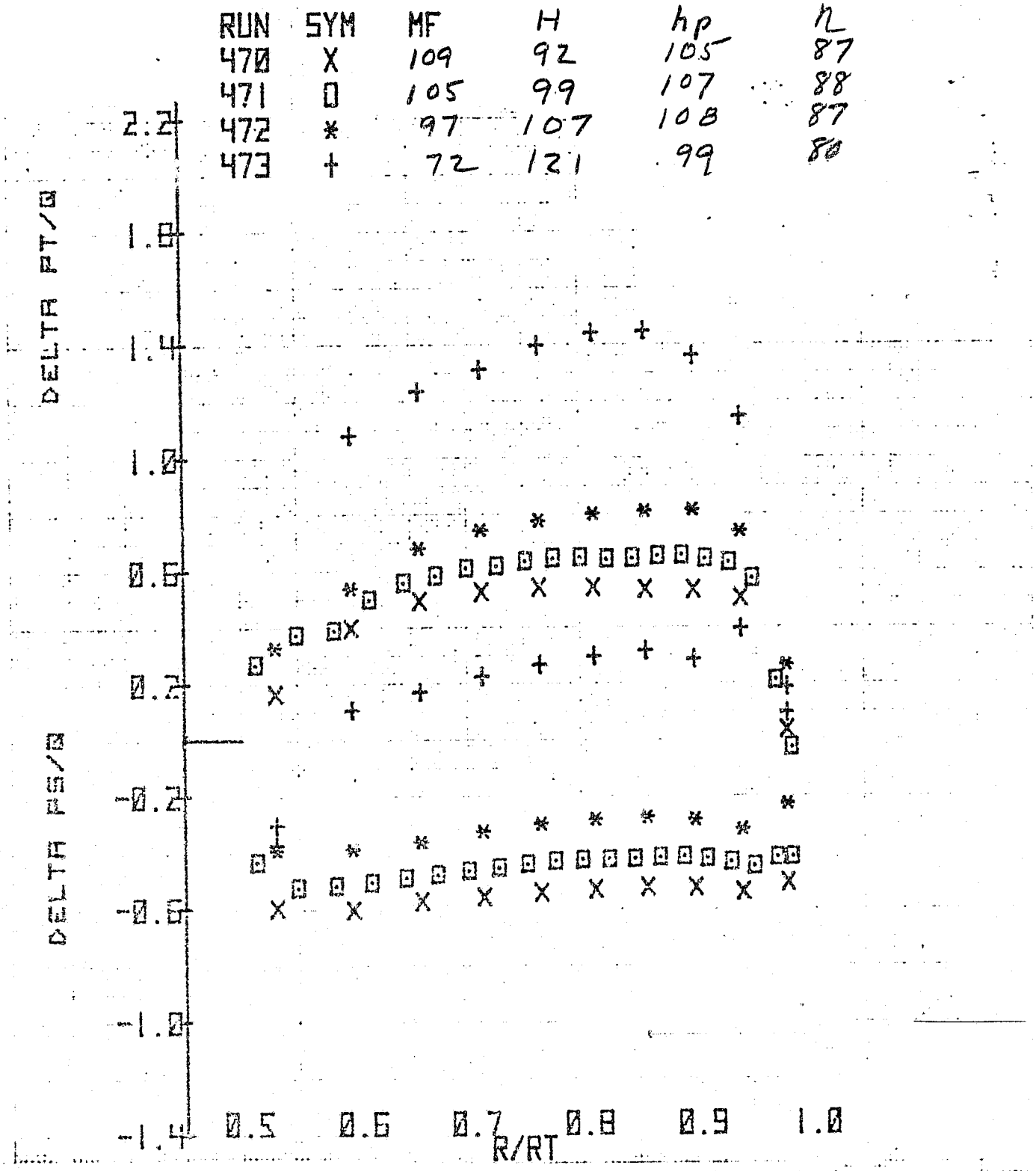

Figure 12.- Radial variation of total pressure coefficient, static pressure coefficient and swirl angle between the rotor and stator at the top azimuth; several mass flows, N = 100%, inlet honeycomb, modified contraction, and $\xi = 38°$.

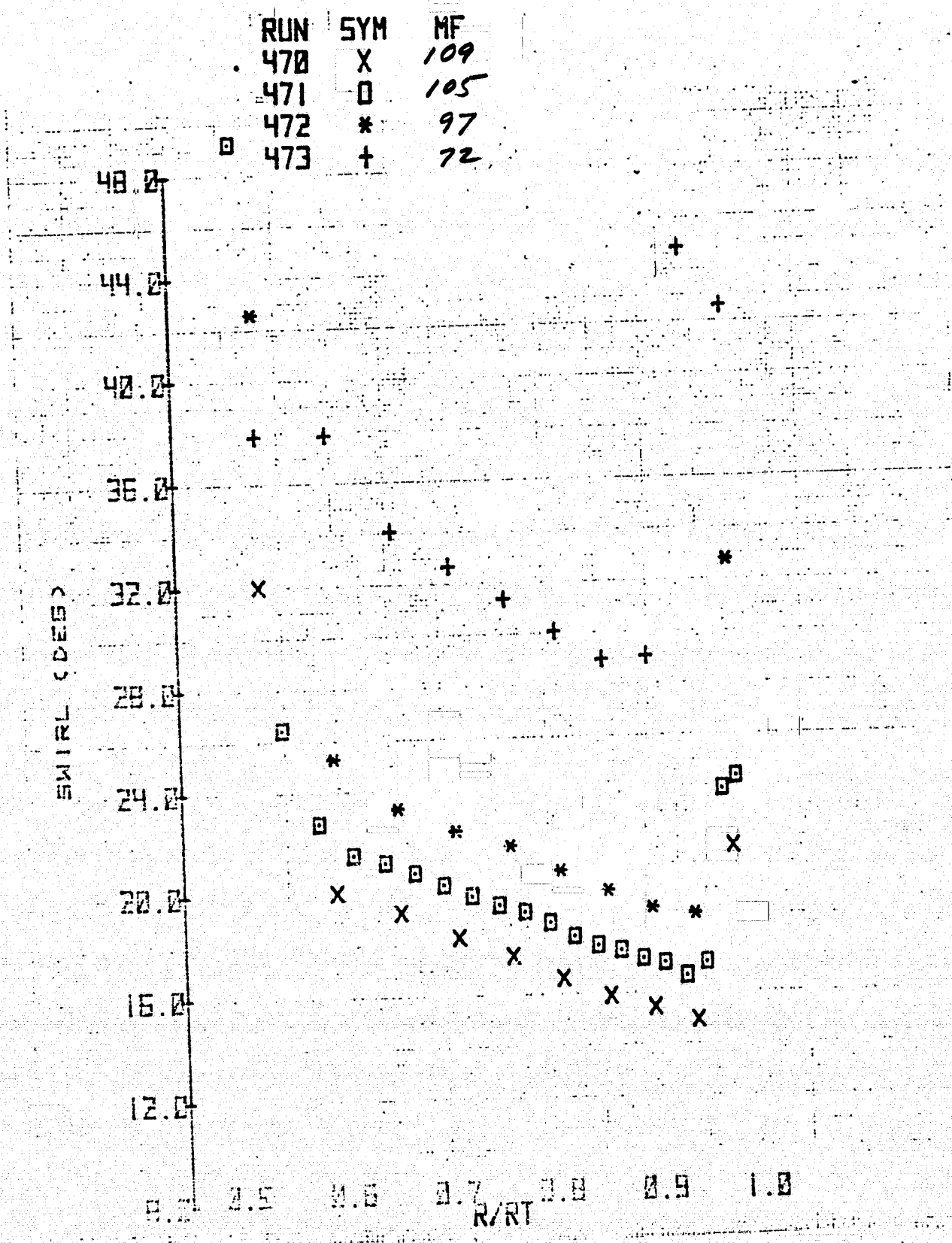

Figure 12.- Concluded.

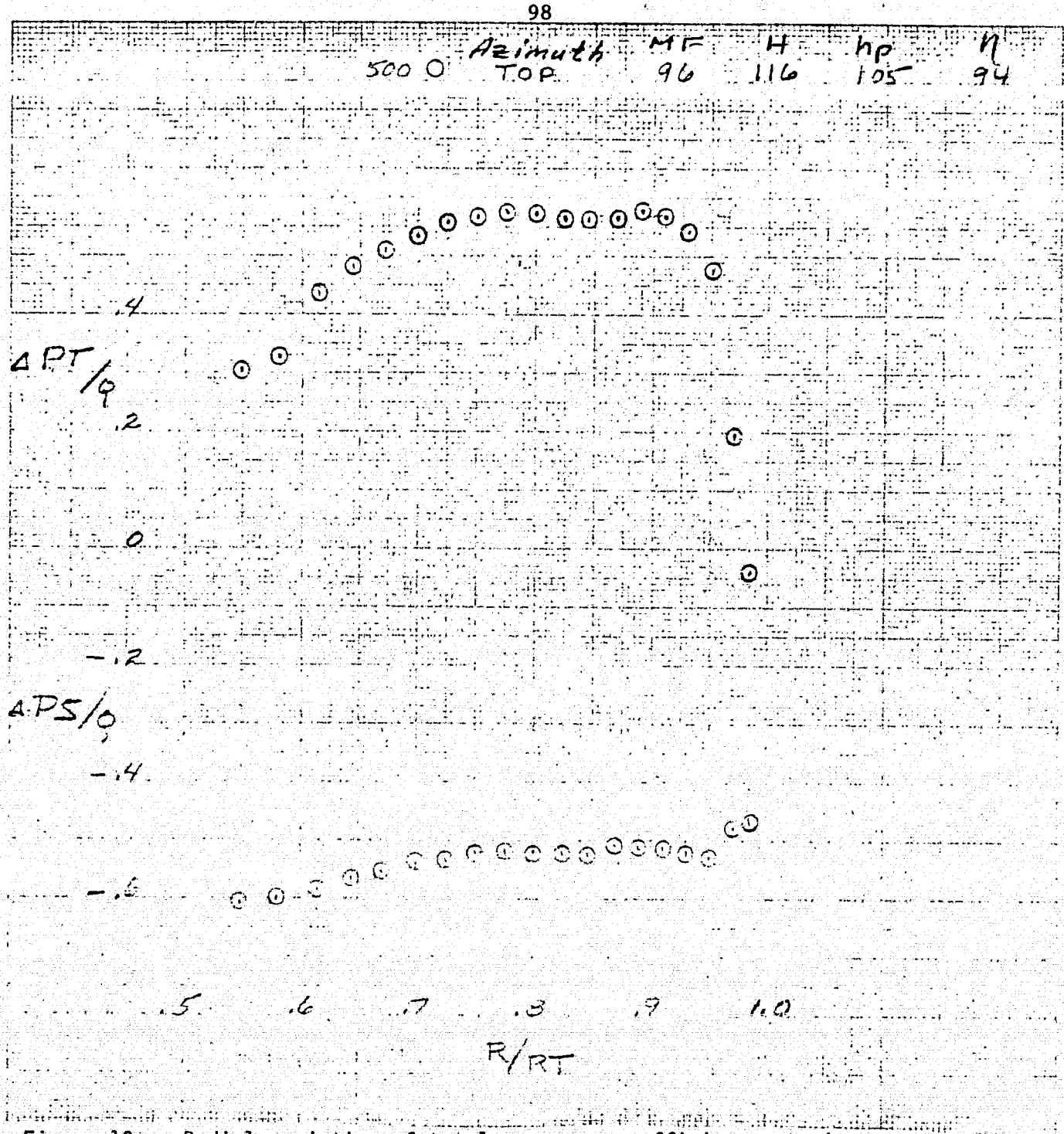

Figure 13.- Radial variation of total pressure coefficient, static pressure coefficient and swirl angle between the rotor and stator for two azimuths at 95% mass flow; N = 100%, "D" inflow configuration, inlet honeycomb, modified contraction, and $\xi = 38°$.

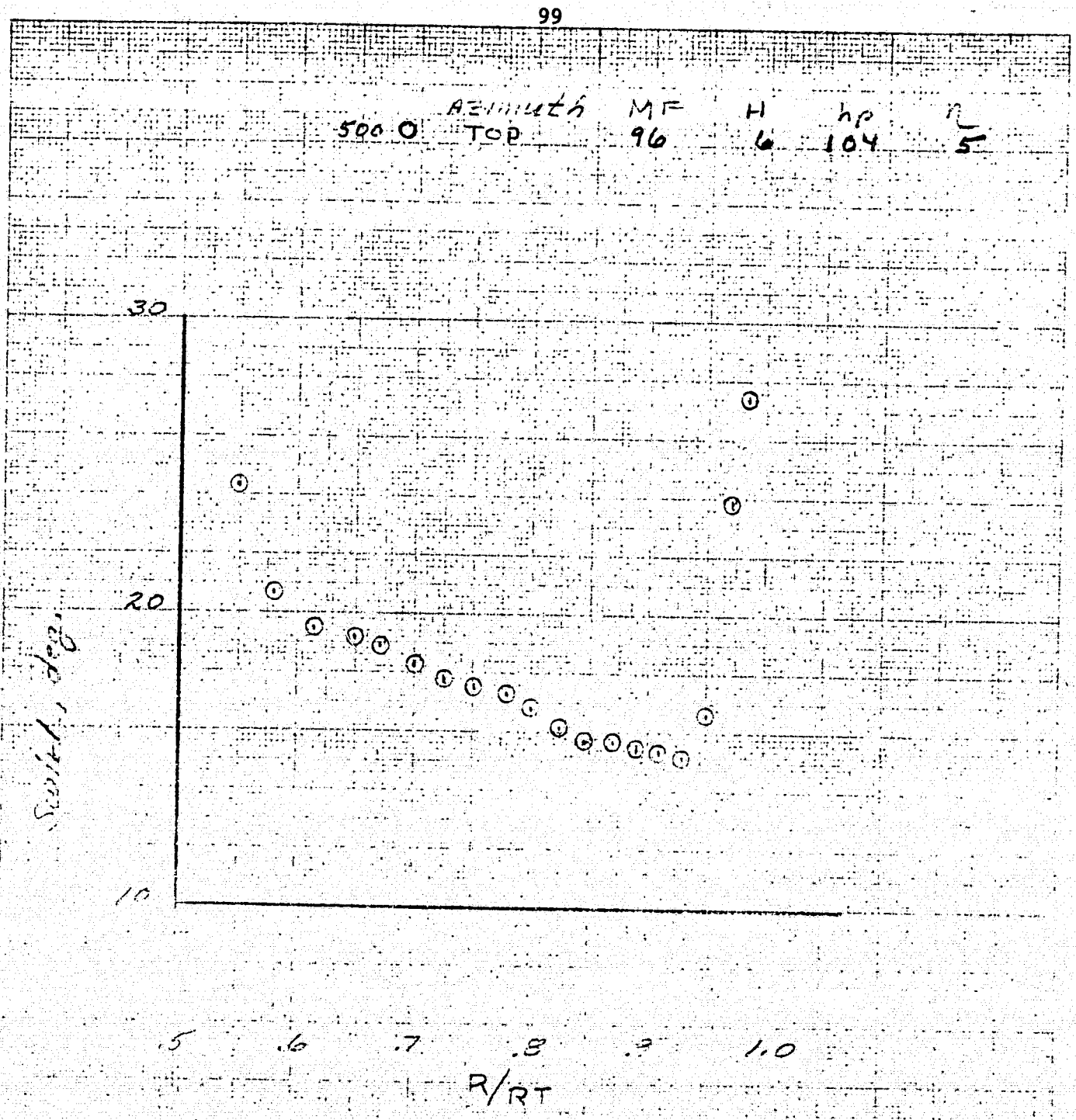

Figure 13.- Concluded.

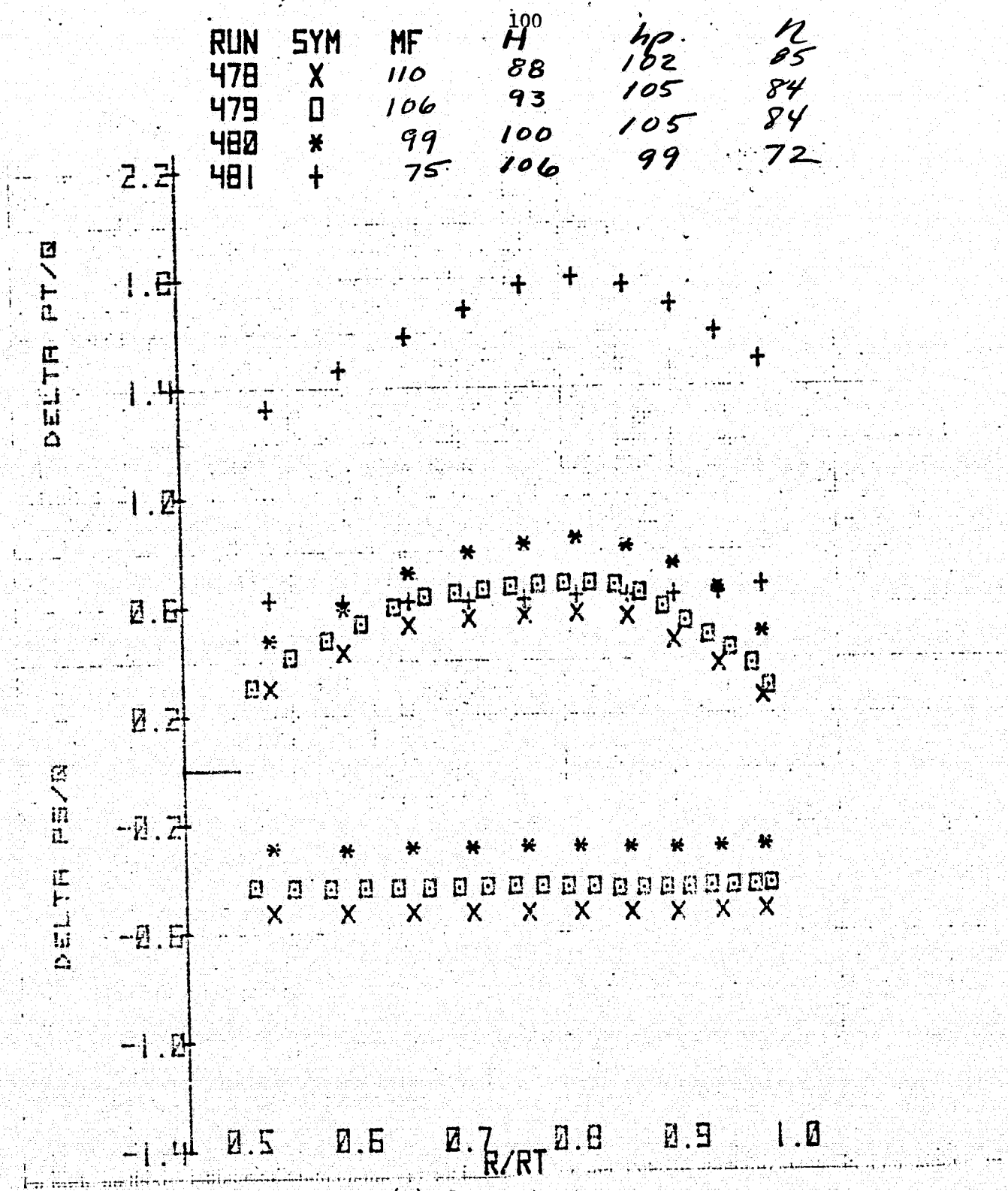

(a) Port azimuth.

Figure 14.- Radial variation of total pressure coefficient, static pressure coefficient, and swirl angle upstream of rotor for several azimuths, and mass flows; N = 100%, modified contraction, inlet honeycomb, and ξ = 38°.

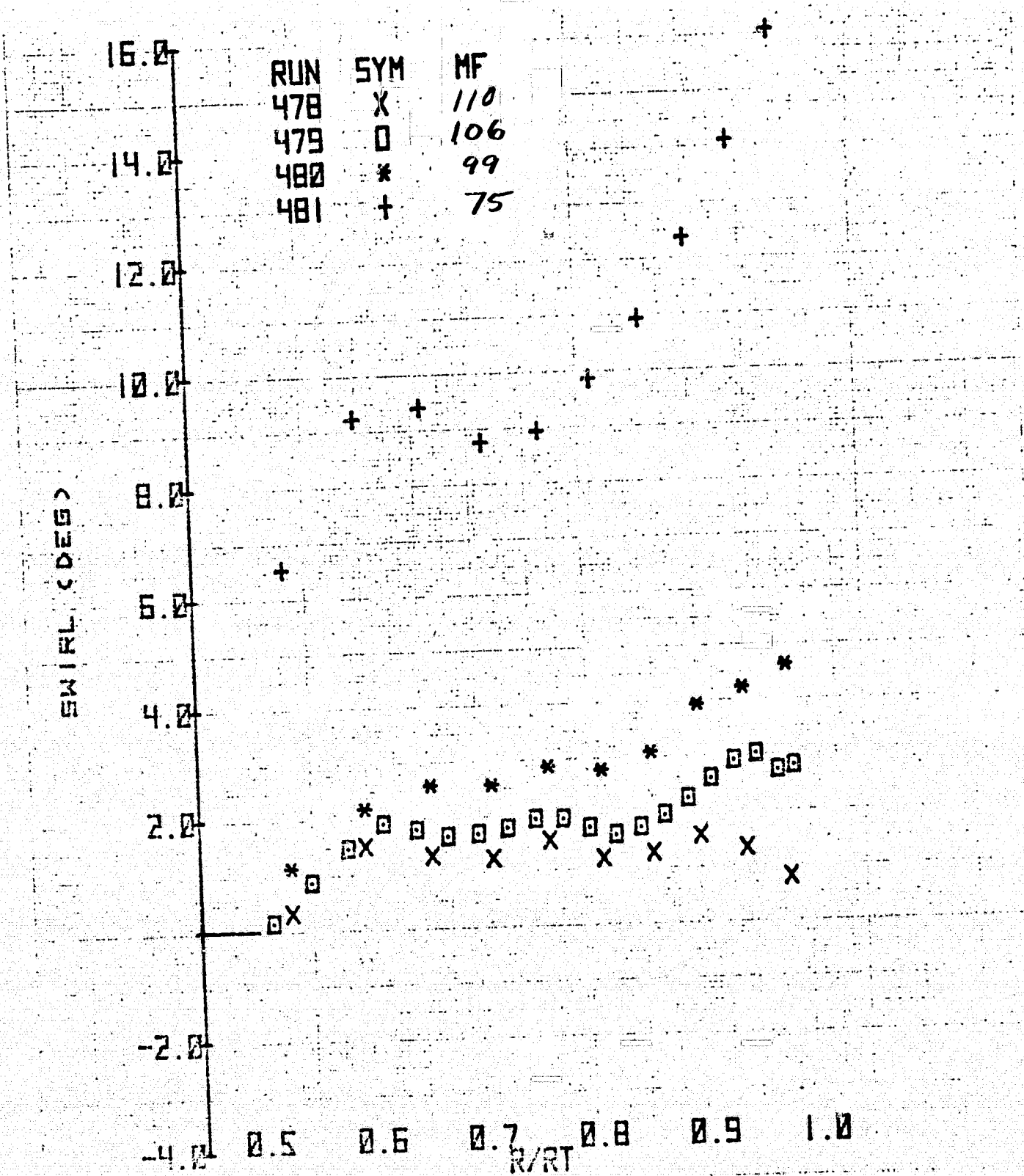

(a) Port azimuth - concluded.

Figure 14.- Continued.

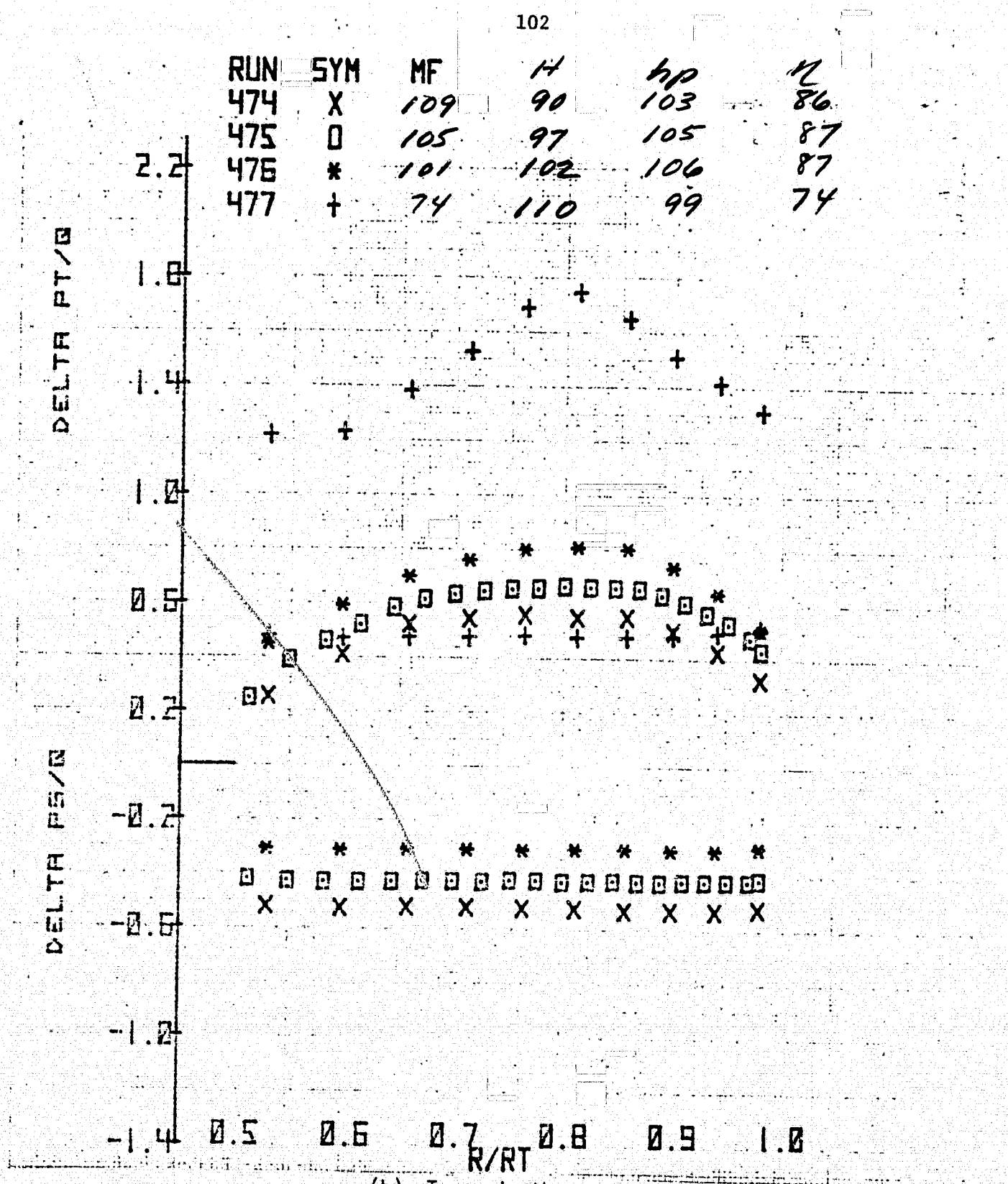

(b) Top azimuth.

Figure 14.- Continued.

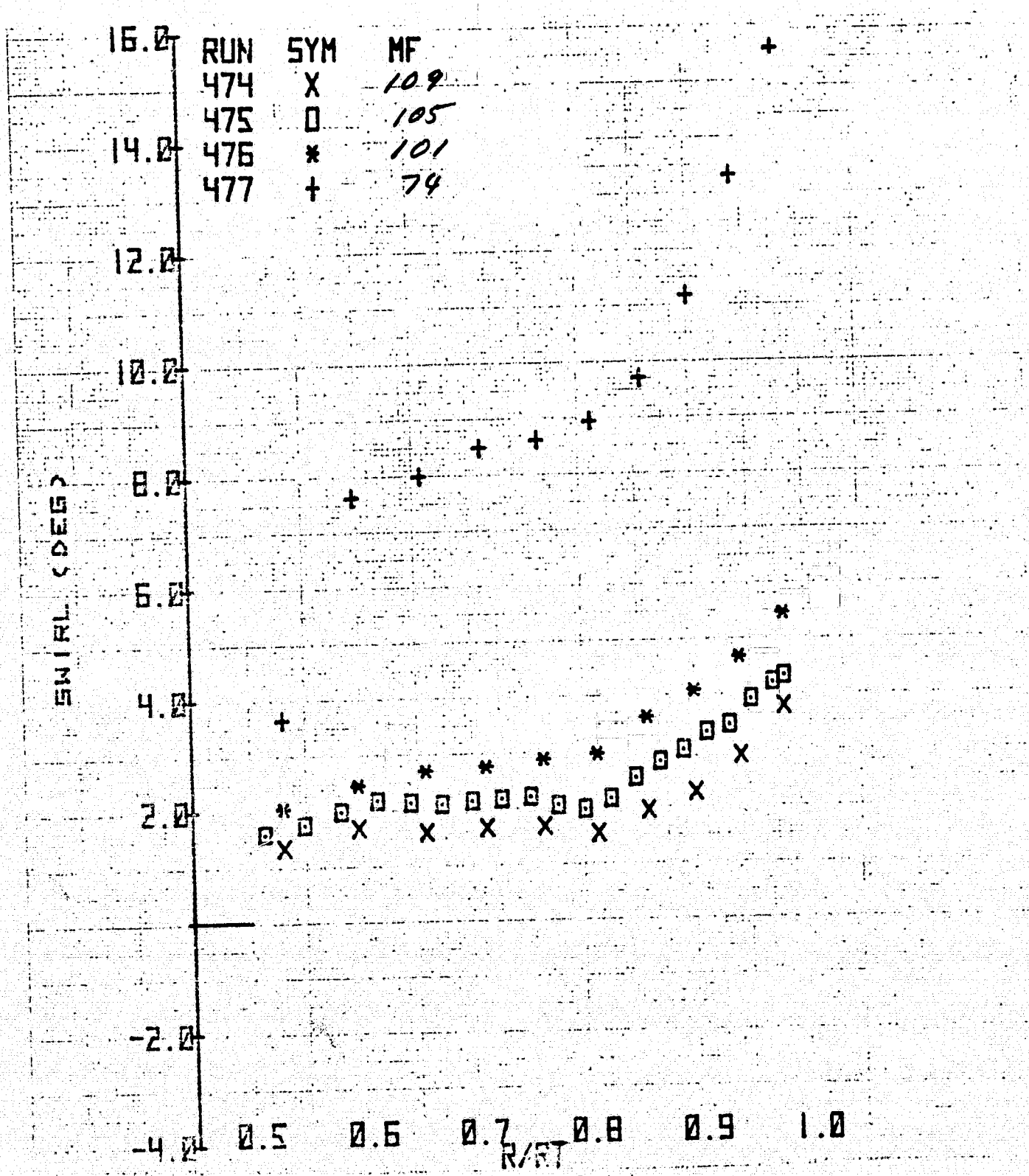

(b) Top azimuth - concluded.

Figure 14.- Continued.

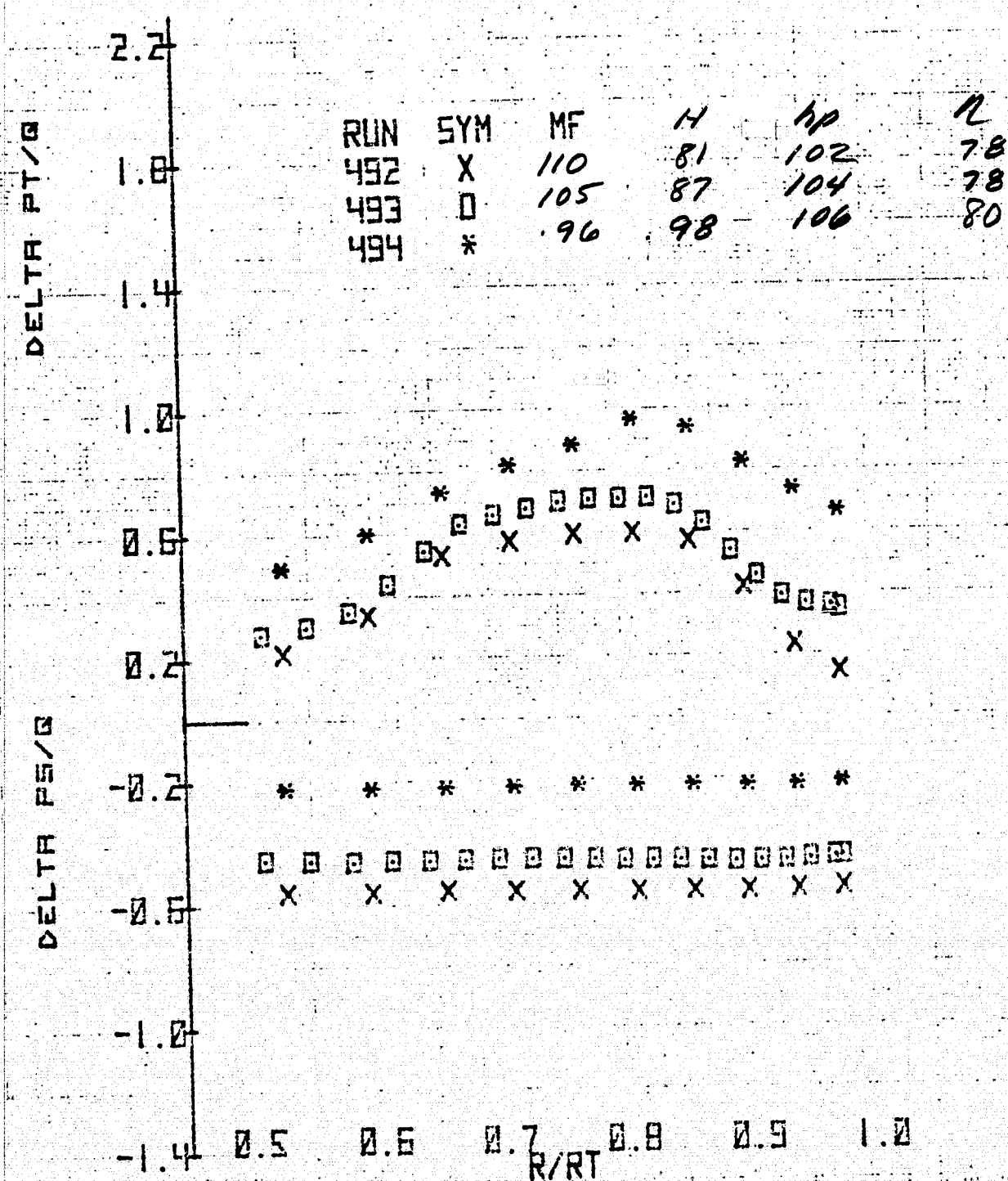

(c) Starboard azimuth.

Figure 14.- Continued.

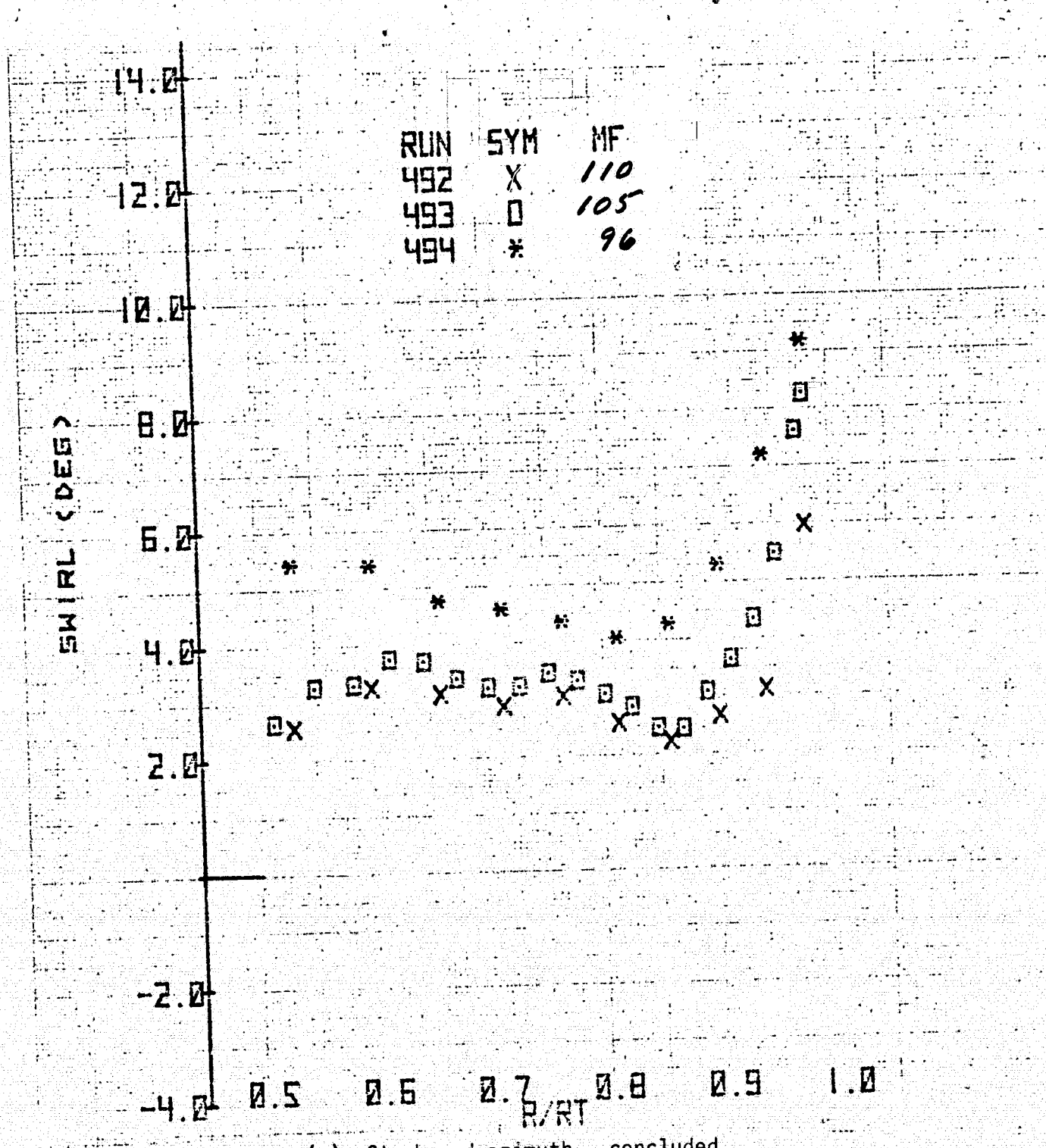

(c) Starboard azimuth - concluded.

Figure 14.- Continued.

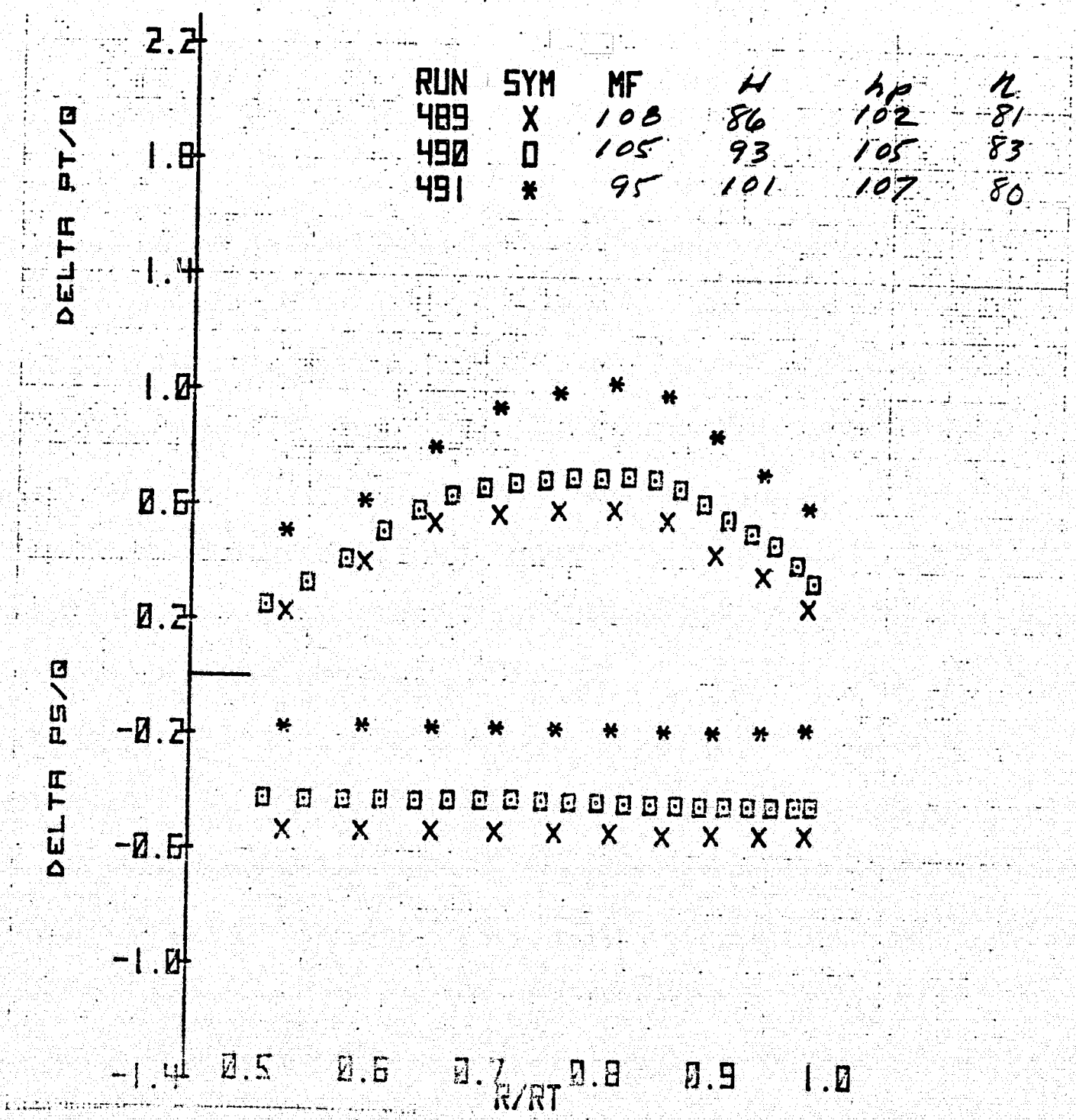

(d) Bottom azimuth.

Figure 14.- Continued.

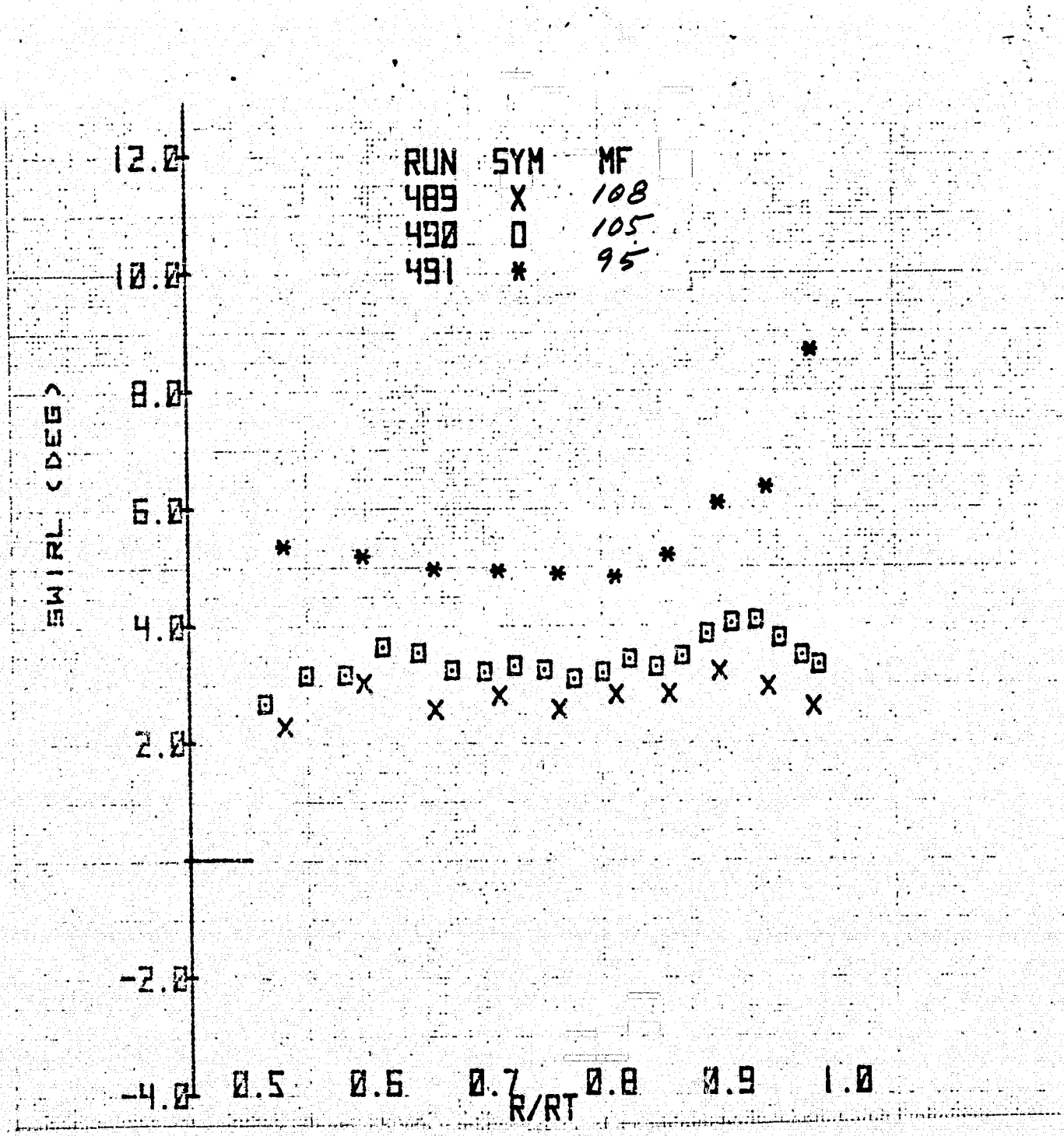

(d) Bottom azimuth - concluded.

Figure 14.- Concluded.

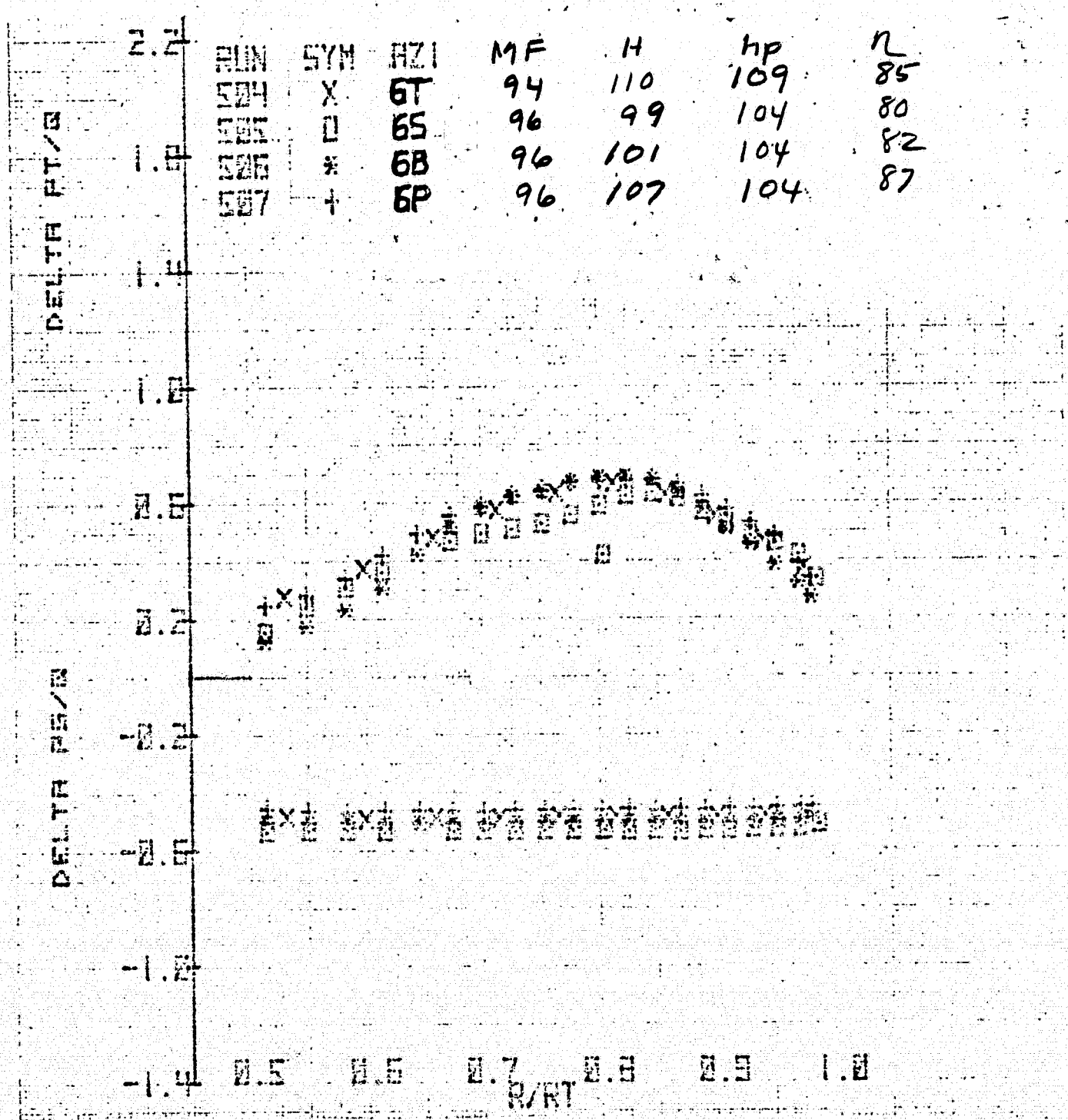

Figure 15.- Radial variation of total pressure coefficient, static pressure coefficient, and swirl angle upstream of rotor for several azimuths; 90% mass flow at N = 100%, inlet screen in, inlet honeycomb, modified contraction, and ϵ = 38°.

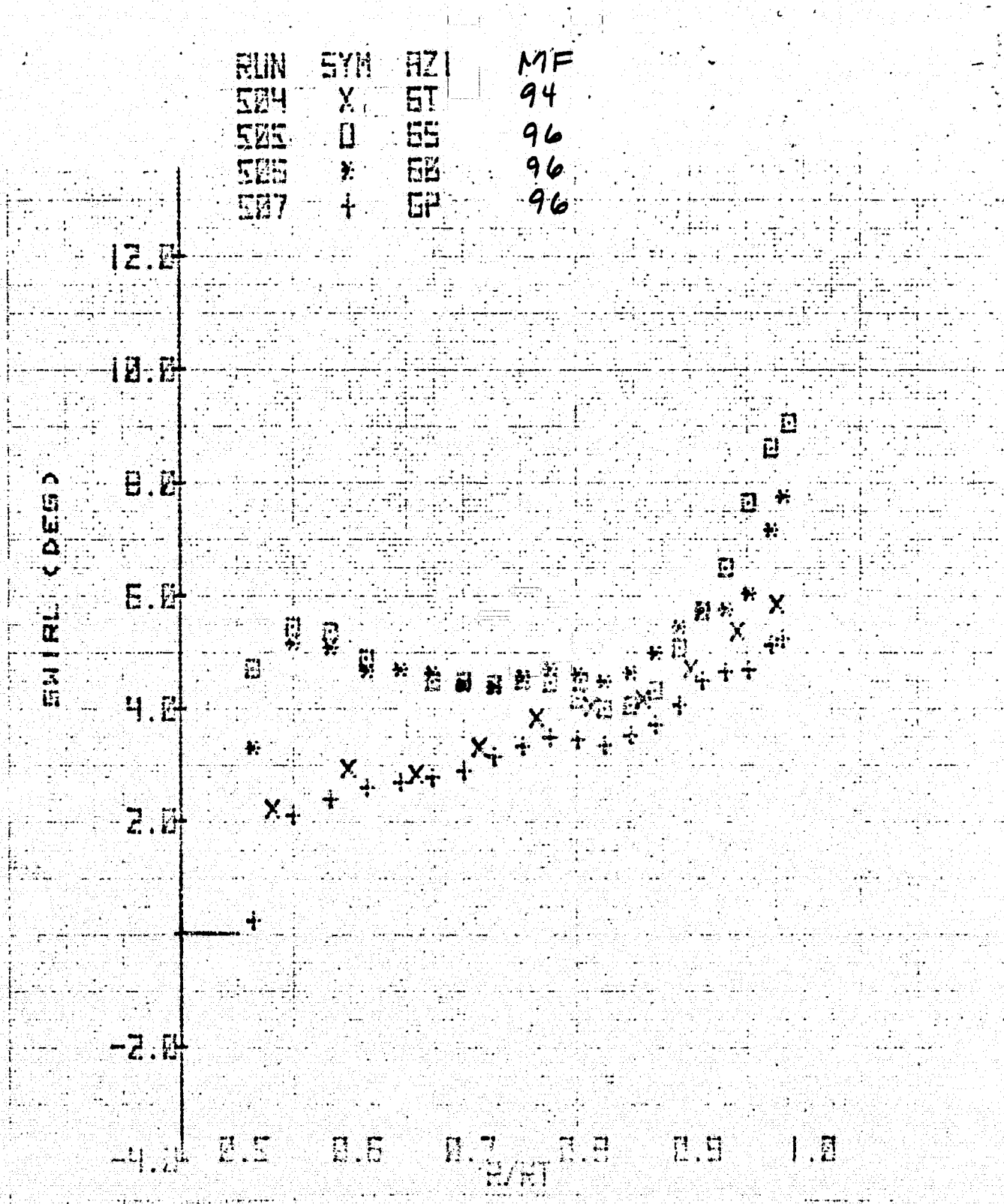

Figure 15.- Concluded.

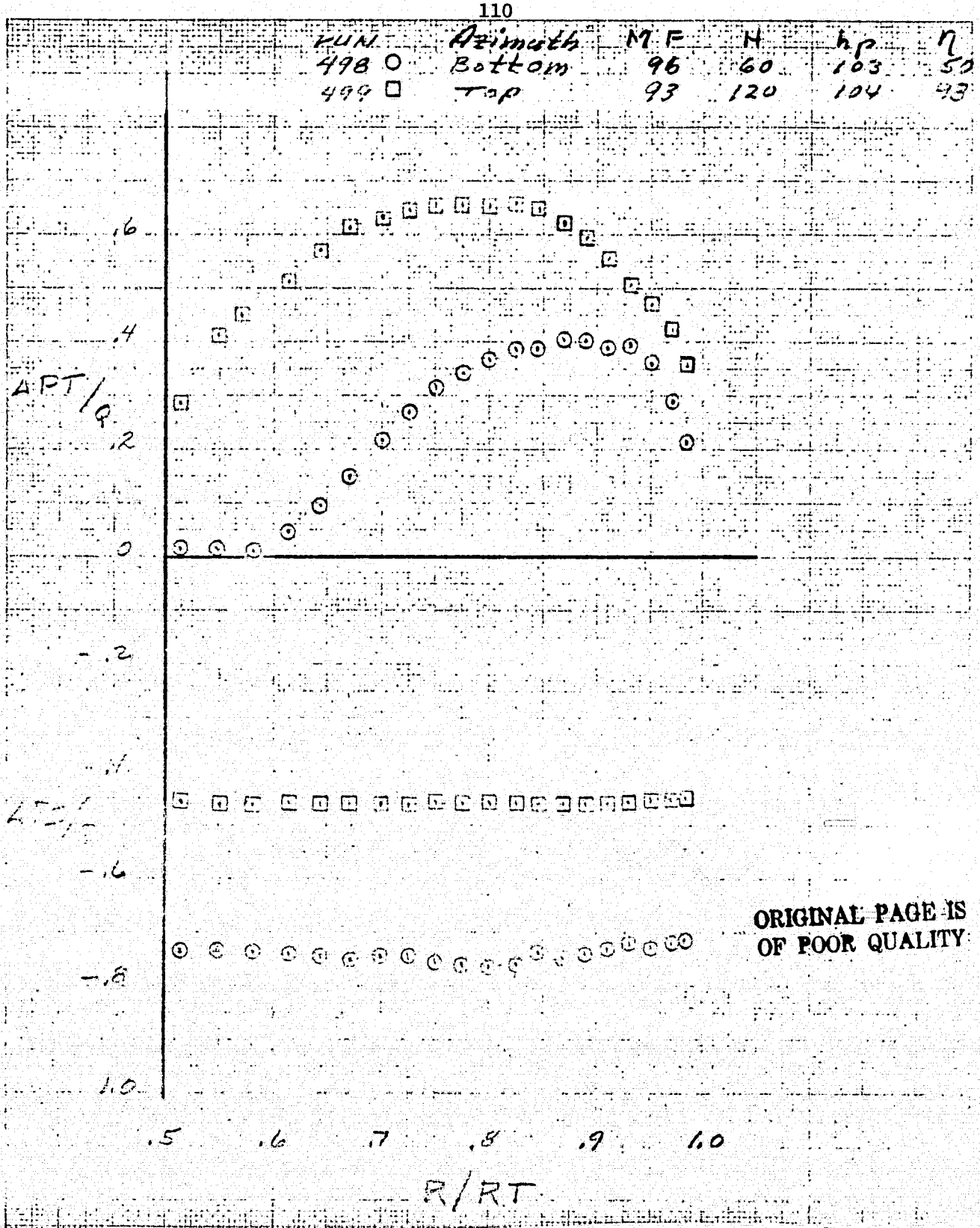

Figure 16.- Radial variation of total pressure coefficient, static pressure coefficient, and swirl angle downstream of stators for two azimuths; 95% mass flow at N = 100%, "D" inflow configuration, inlet honeycomb, modified contraction, and $\xi = 38°$.

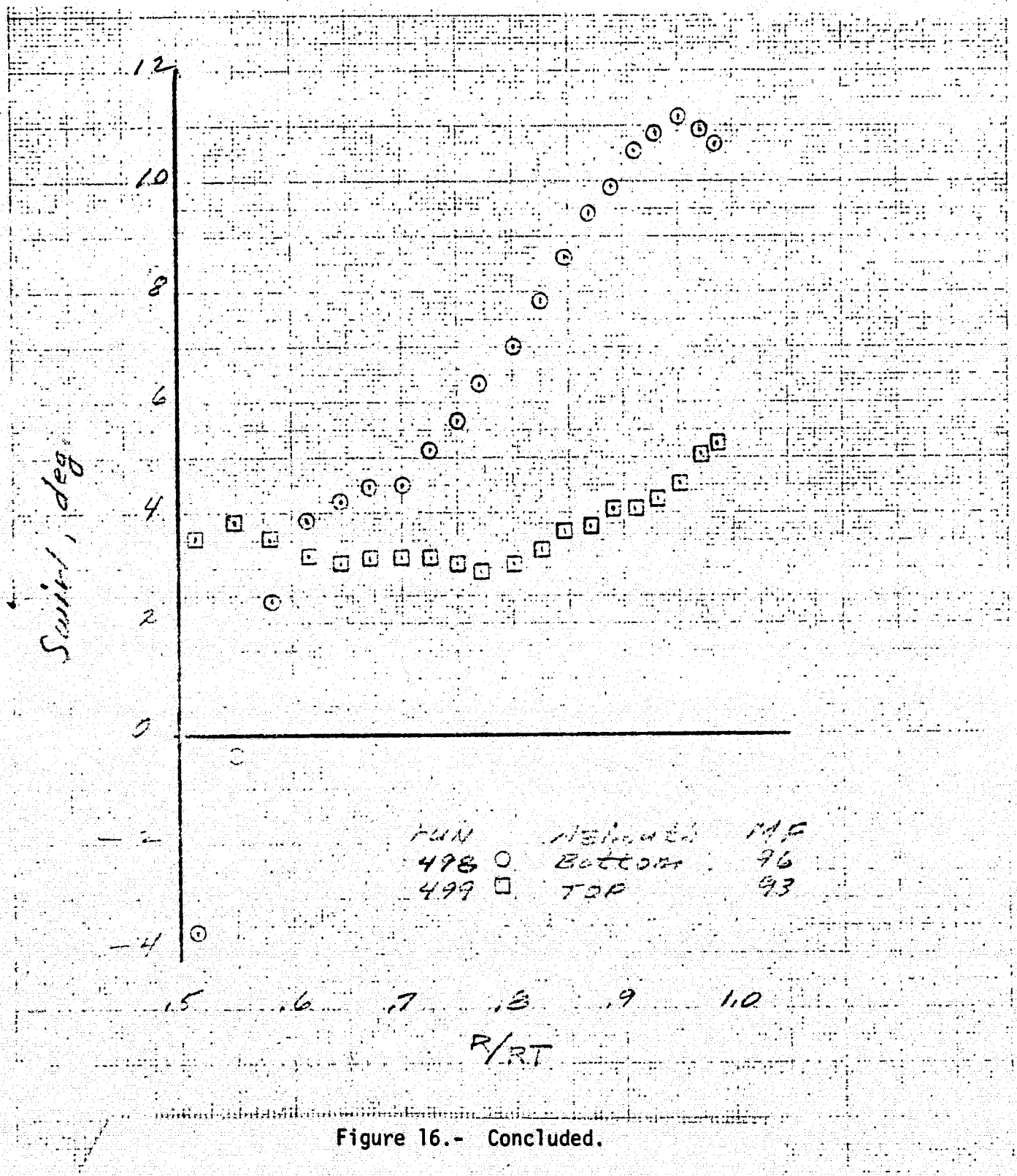

Figure 16.- Concluded.

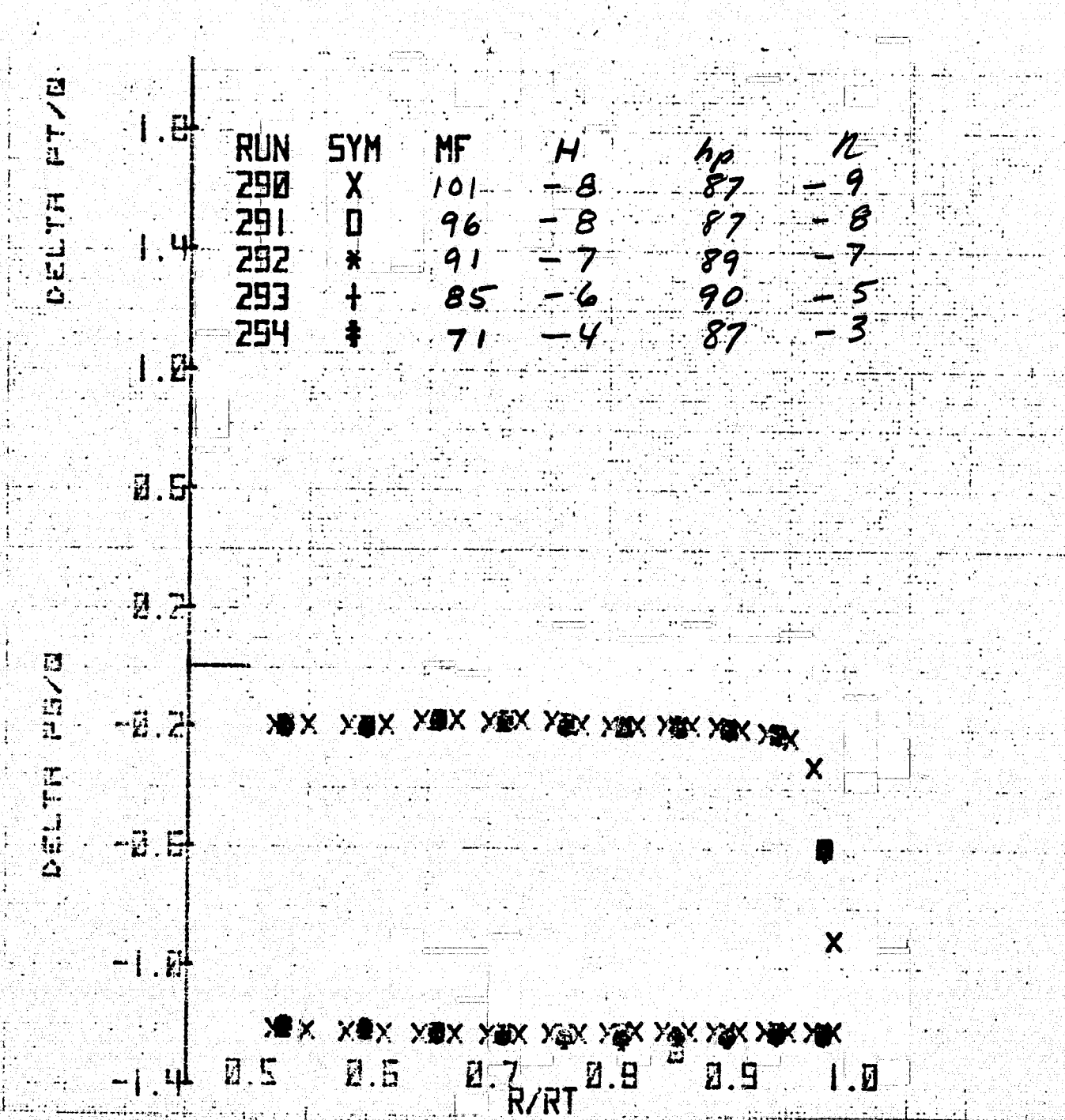

Figure 17.- Radial variation of total pressure coefficient, static pressure coefficient, and swirl angle upstream of rotor at the port azimuth for several mass flows; inlet honeycomb, original contraction, N = 100% and ξ = 40.8°.

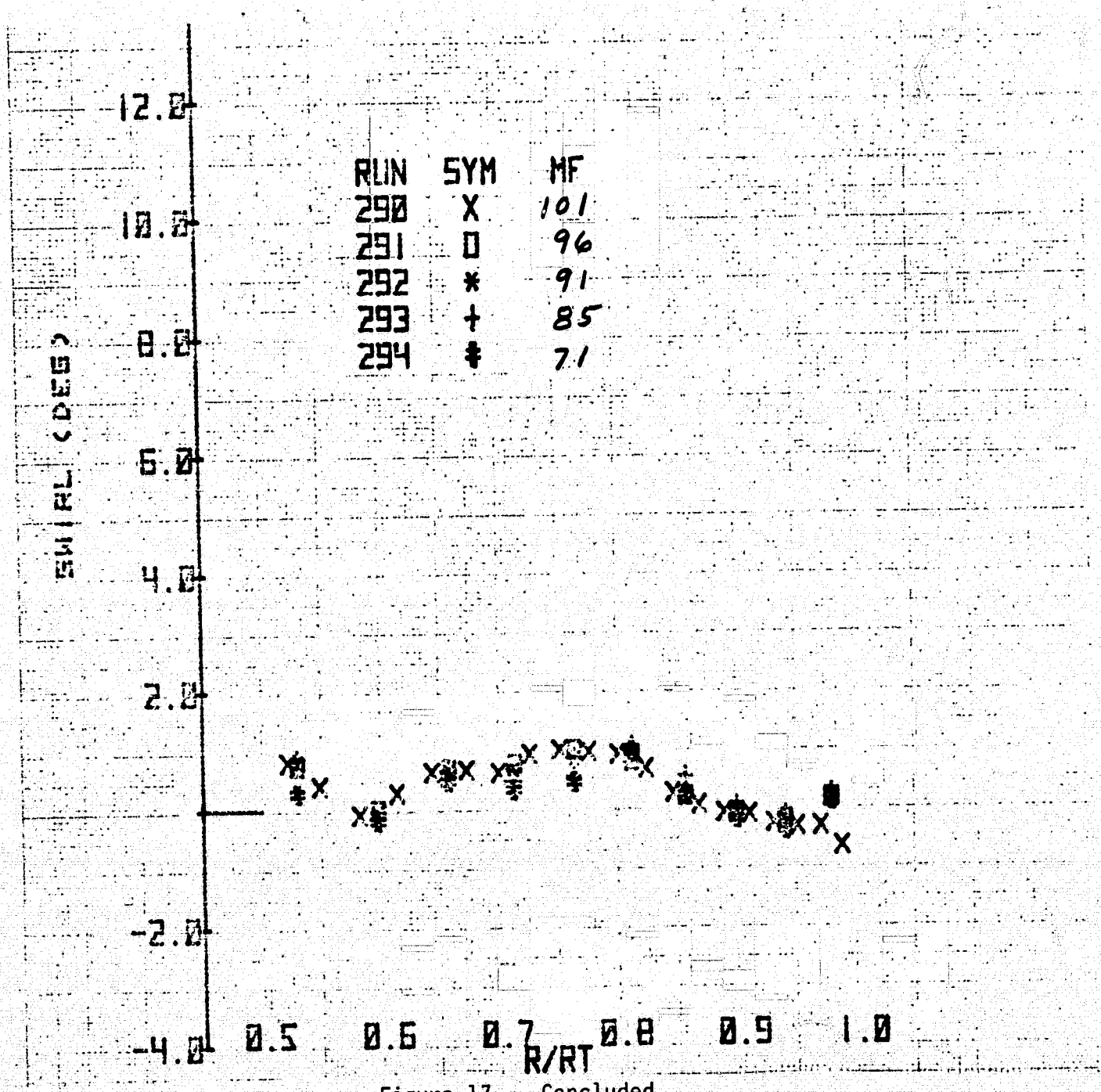

Figure 17.- Concluded.

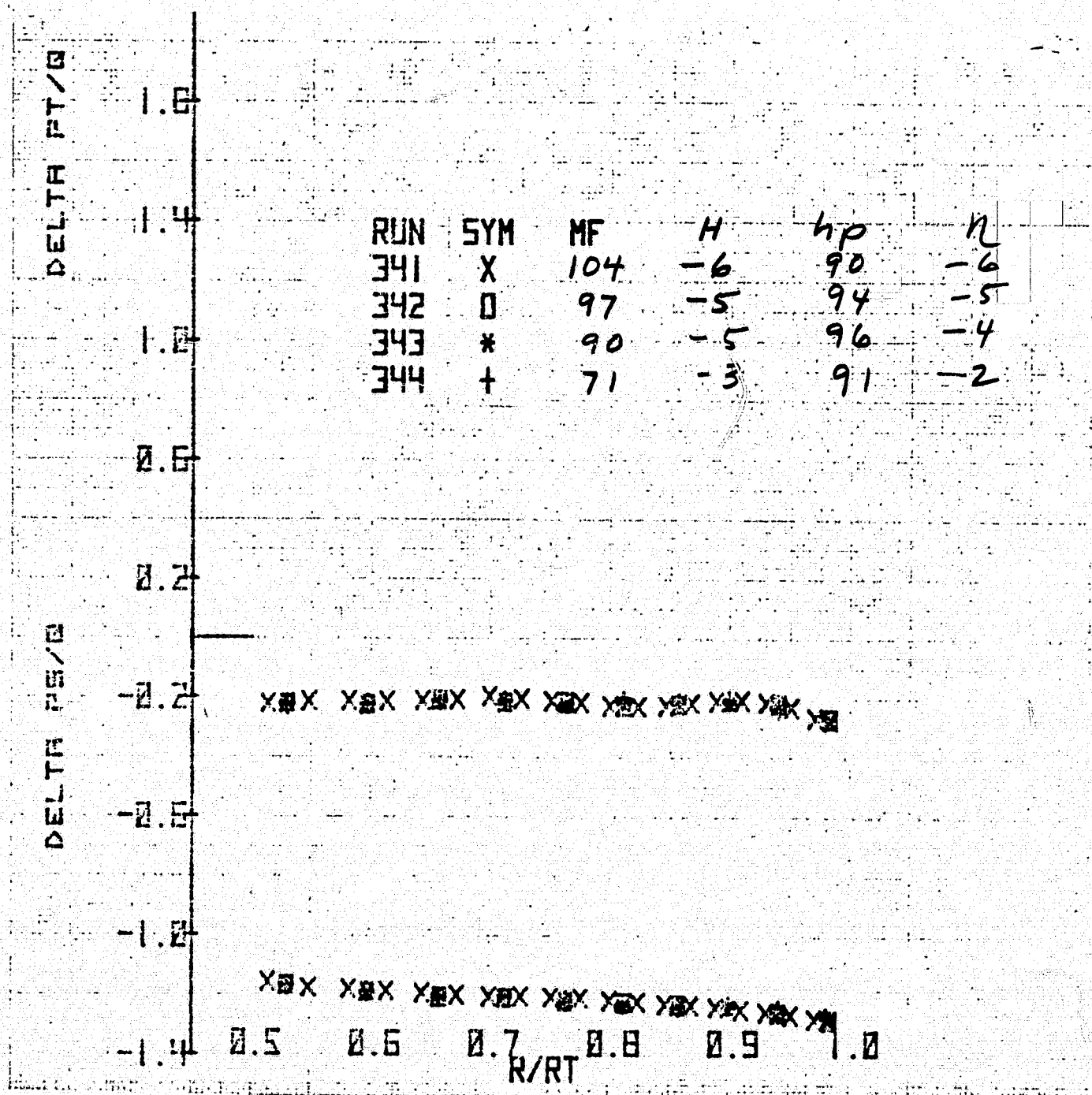

N = 100%

(a) Port azimuth.

Figure 18.- Radial variation of total pressure coefficient, static pressure coefficient, and swirl angle upstream of rotor for several azimuths; modified contraction, inlet honeycomb in and $\xi = 40.8°$.

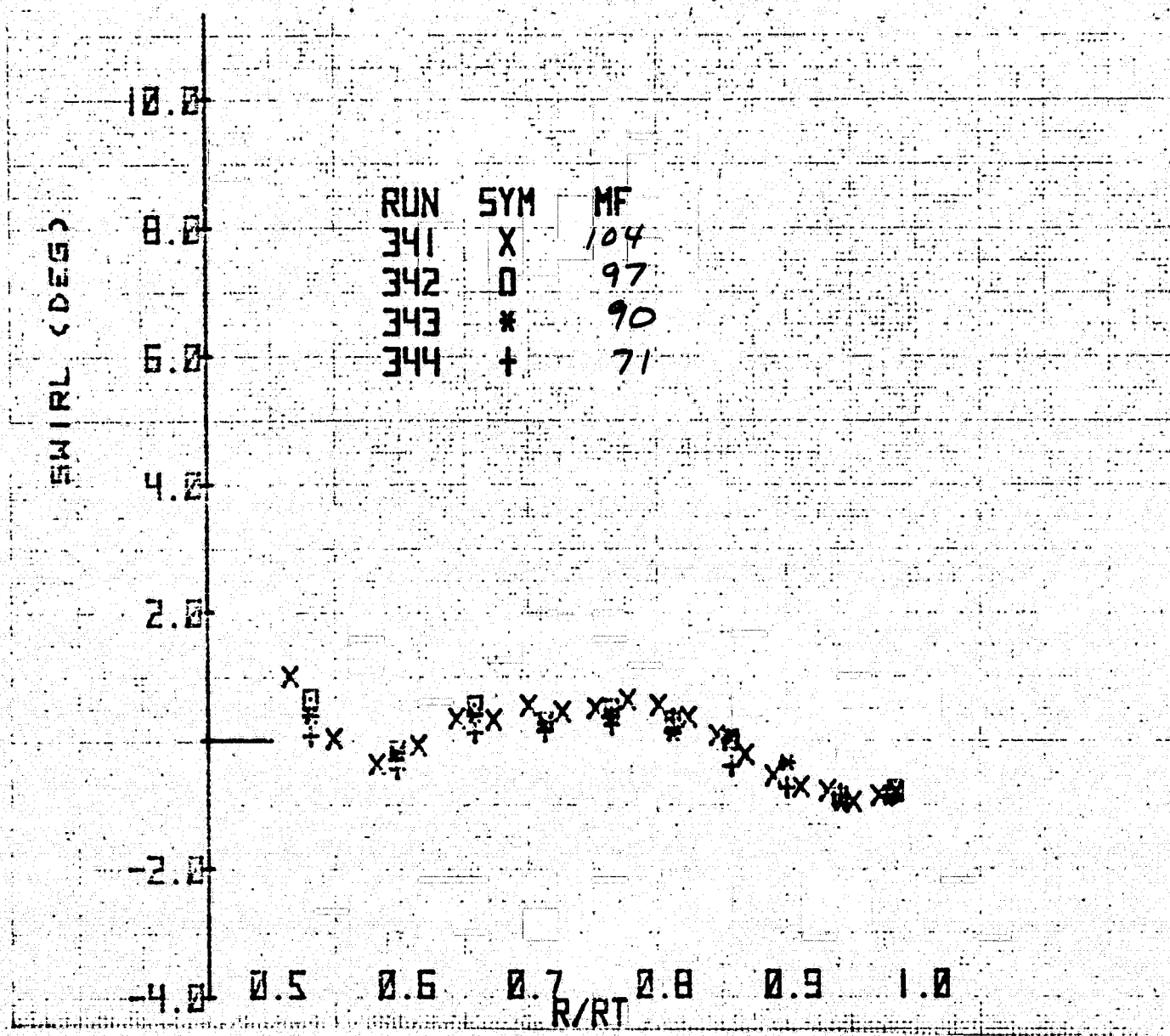

N = 100%

(a) Port azimuth - continued.

Figure 18.- Continued.

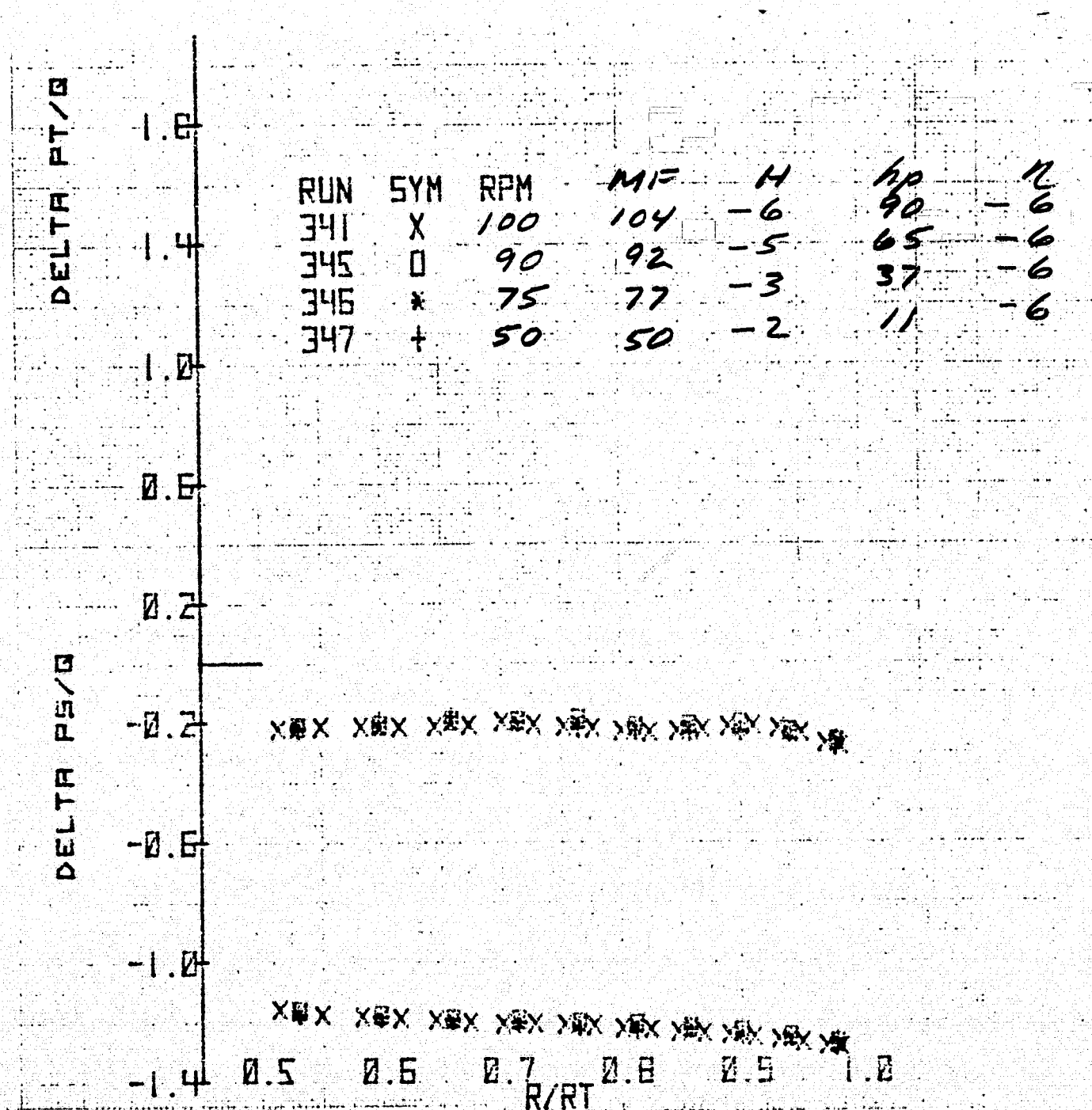

N = Various speeds.
(a) Port azimuth - continued.

Figure 18.- Continued.

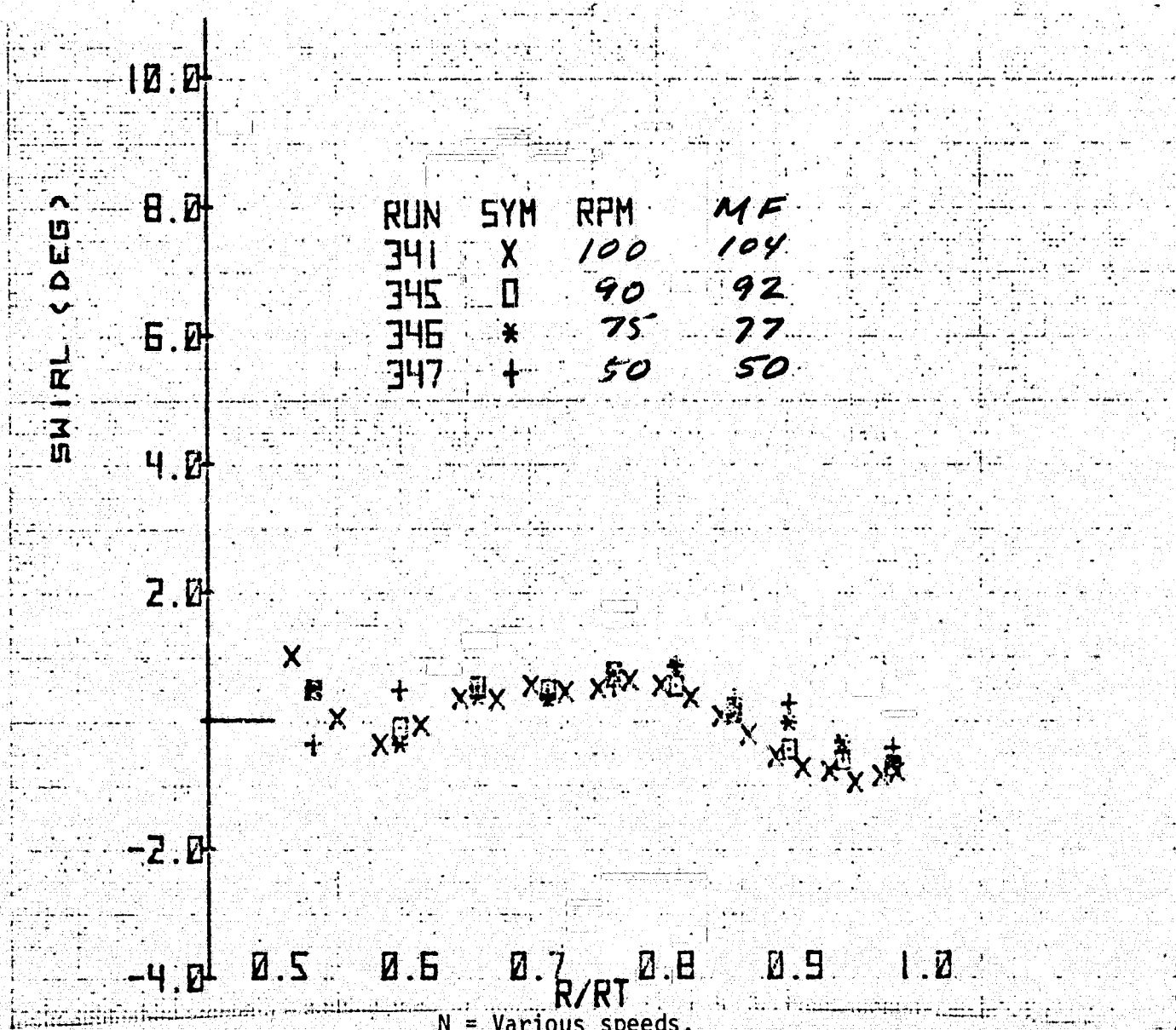

N = Various speeds.

(a) Port azimuth - concluded.

Figure 18.- Continued.

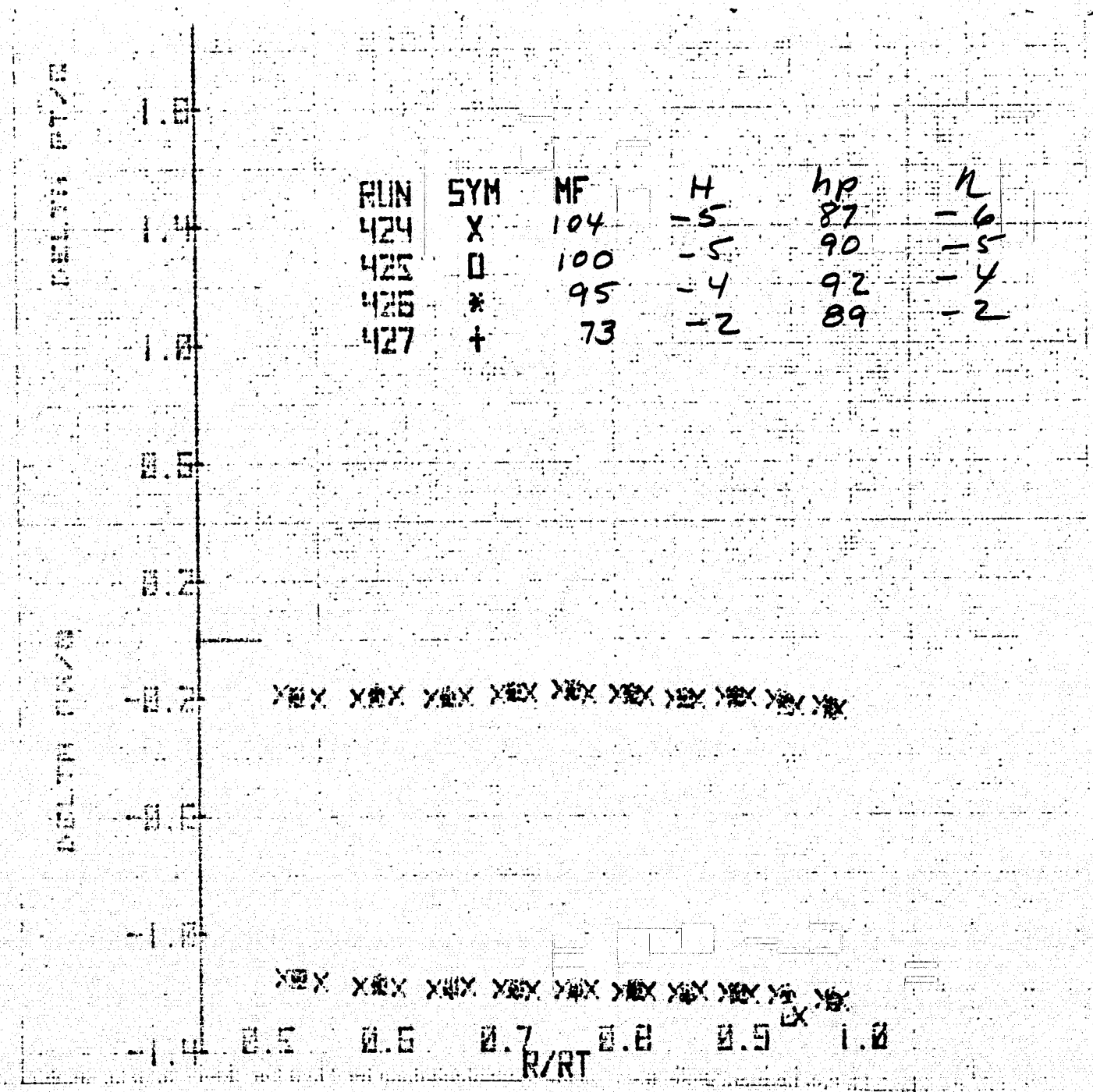

N = 100%
(b) Top azimuth.

Figure 18.- Continued.

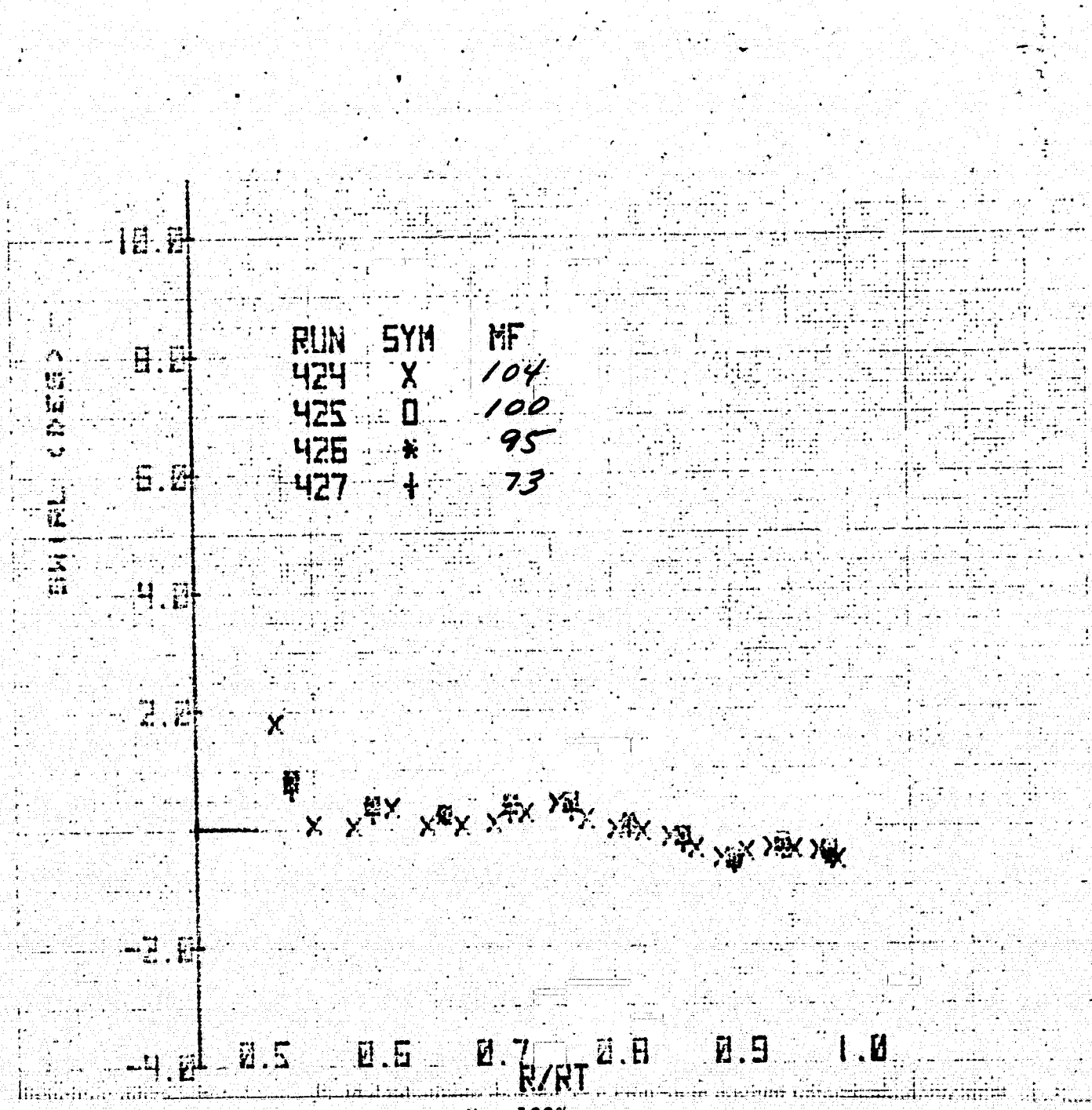

N = 100%

(b) Top azimuth - concluded.

Figure 18.- Continued.

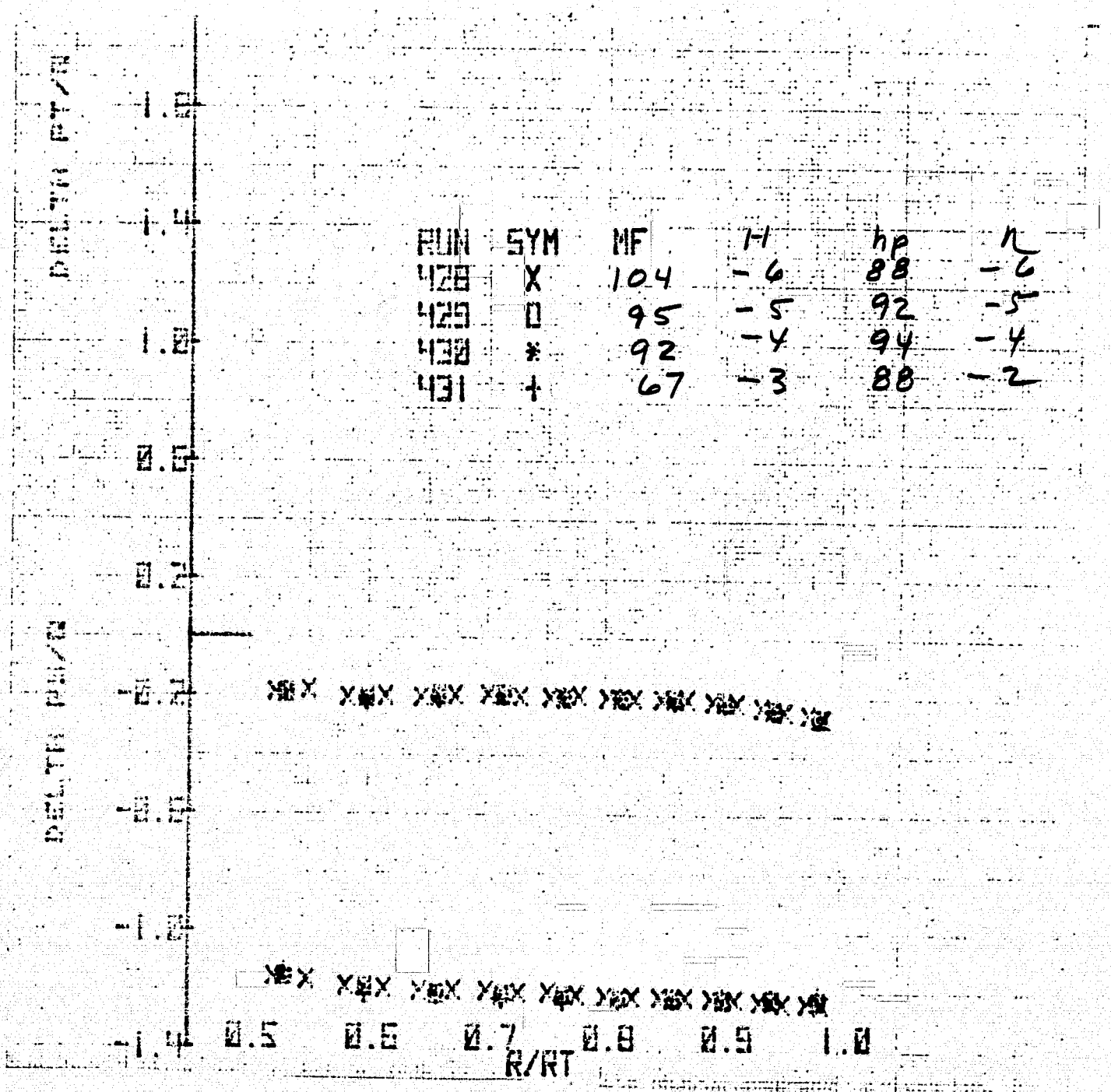

N = 100%

(c) Starboard azimuth.

Figure 18.- Continued.

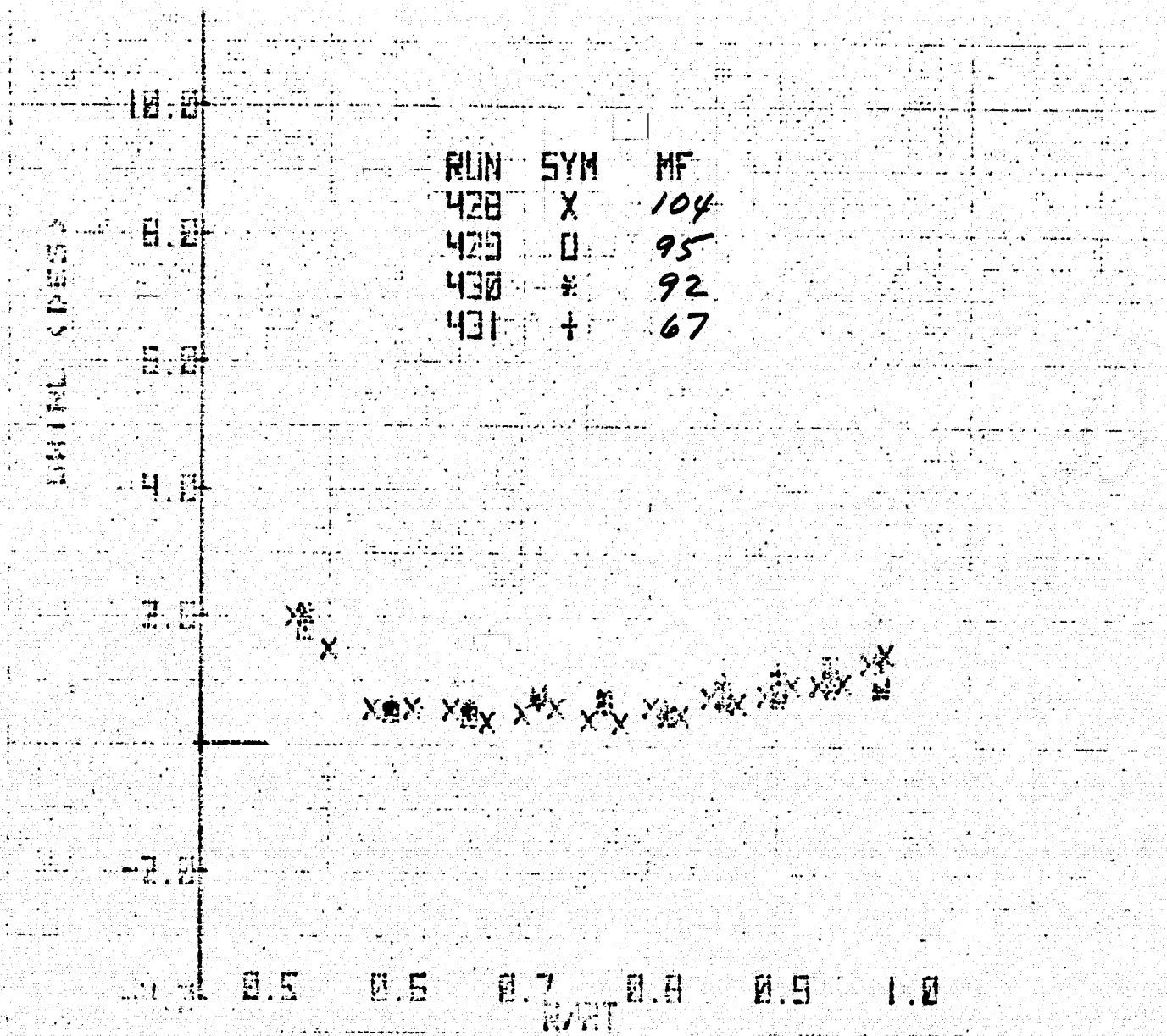

N = 100%

(c) Starboard azimuth - concluded.

Figure 18.- Concluded.

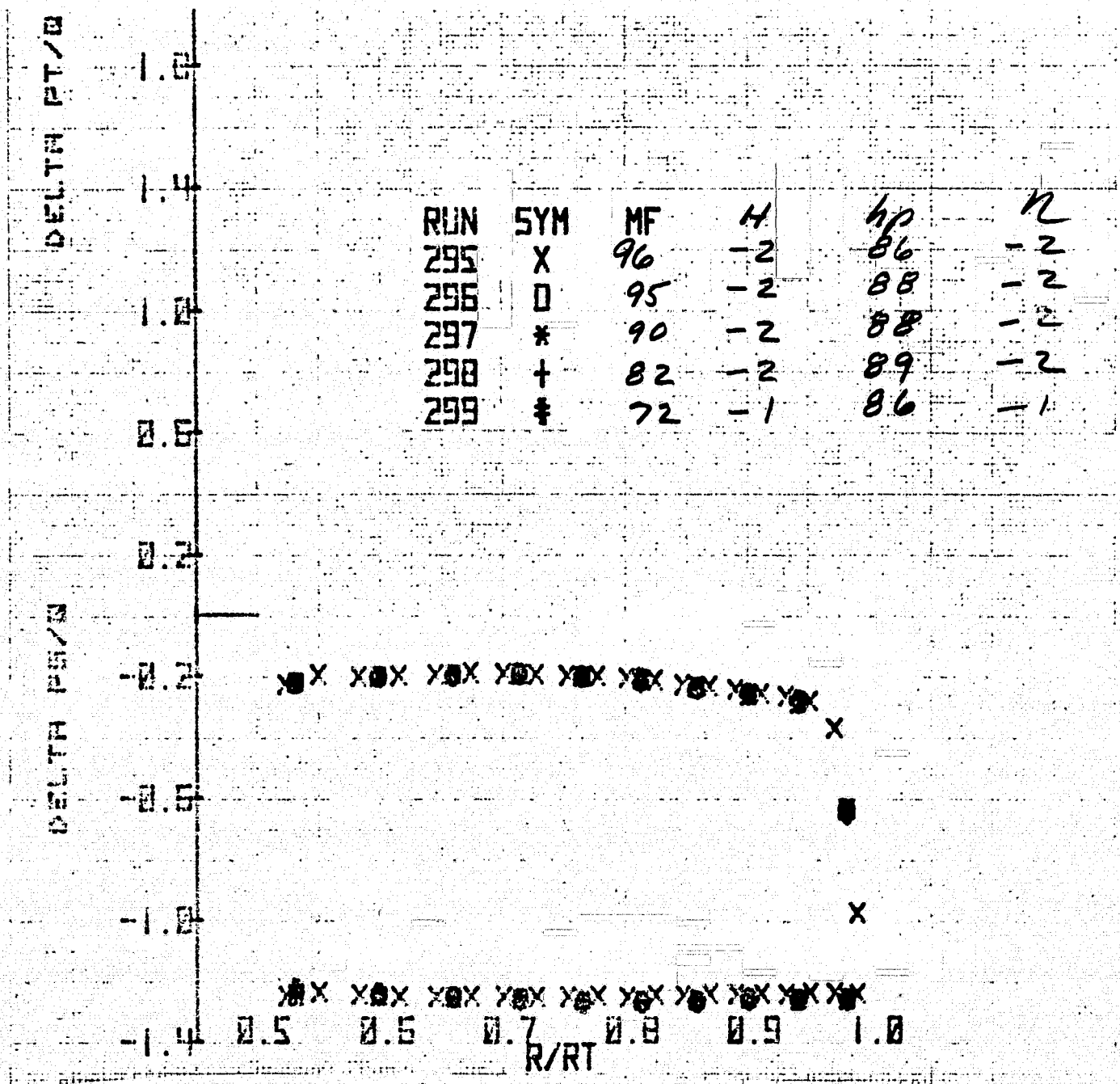

(a) Port azimuth.

Figure 19.- Radial variation of total pressure coefficient, static pressure coefficient, and swirl angle upstream of rotor for several azimuths and mass flows at N = 100%; "H" inflow configuration, inlet honeycomb, original contraction, and ξ = 40.8°.

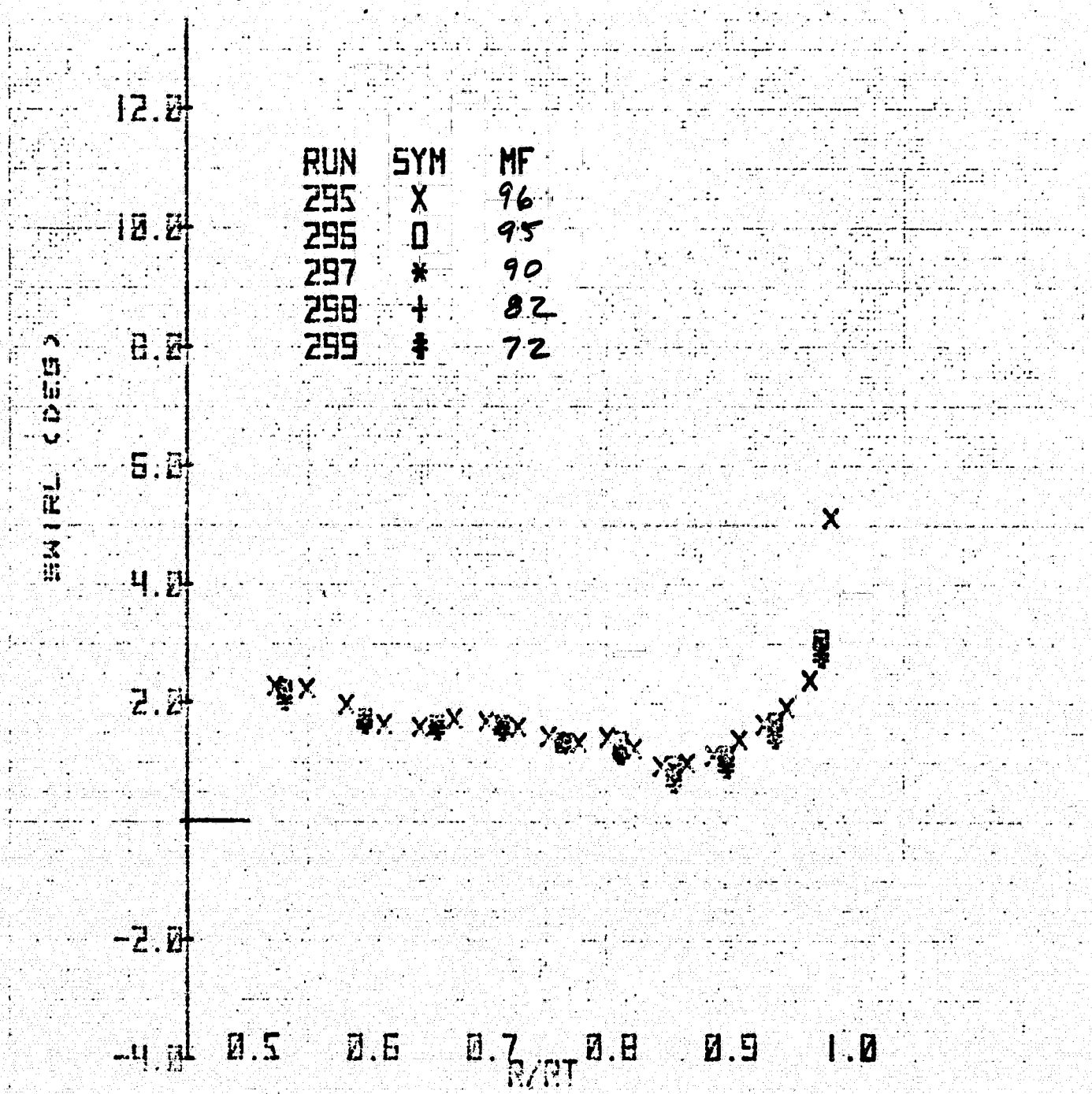

(a) Port azimuth - concluded.

Figure 19.- Continued.

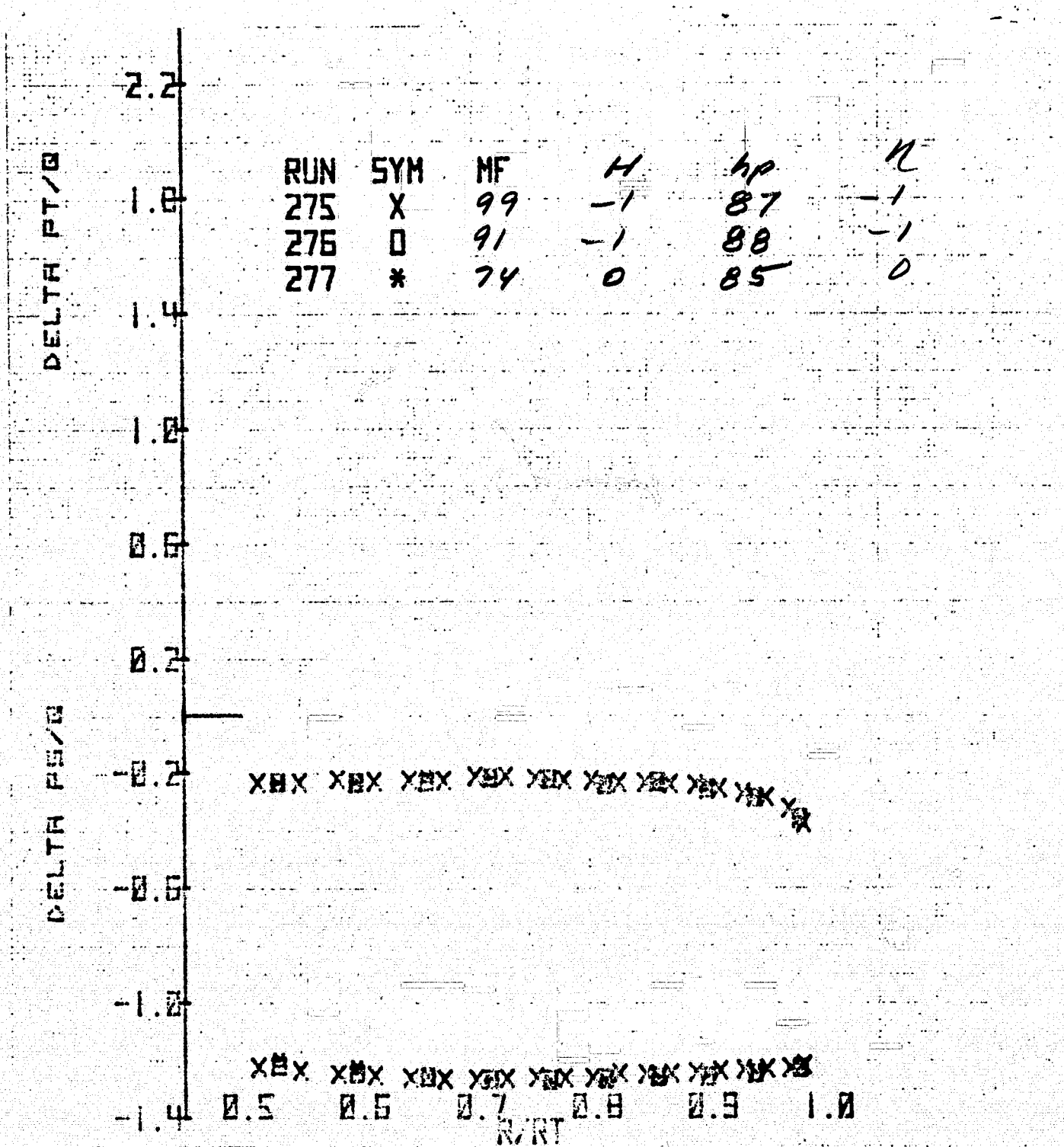

(b) Top azimuth.

Figure 19.- Continued.

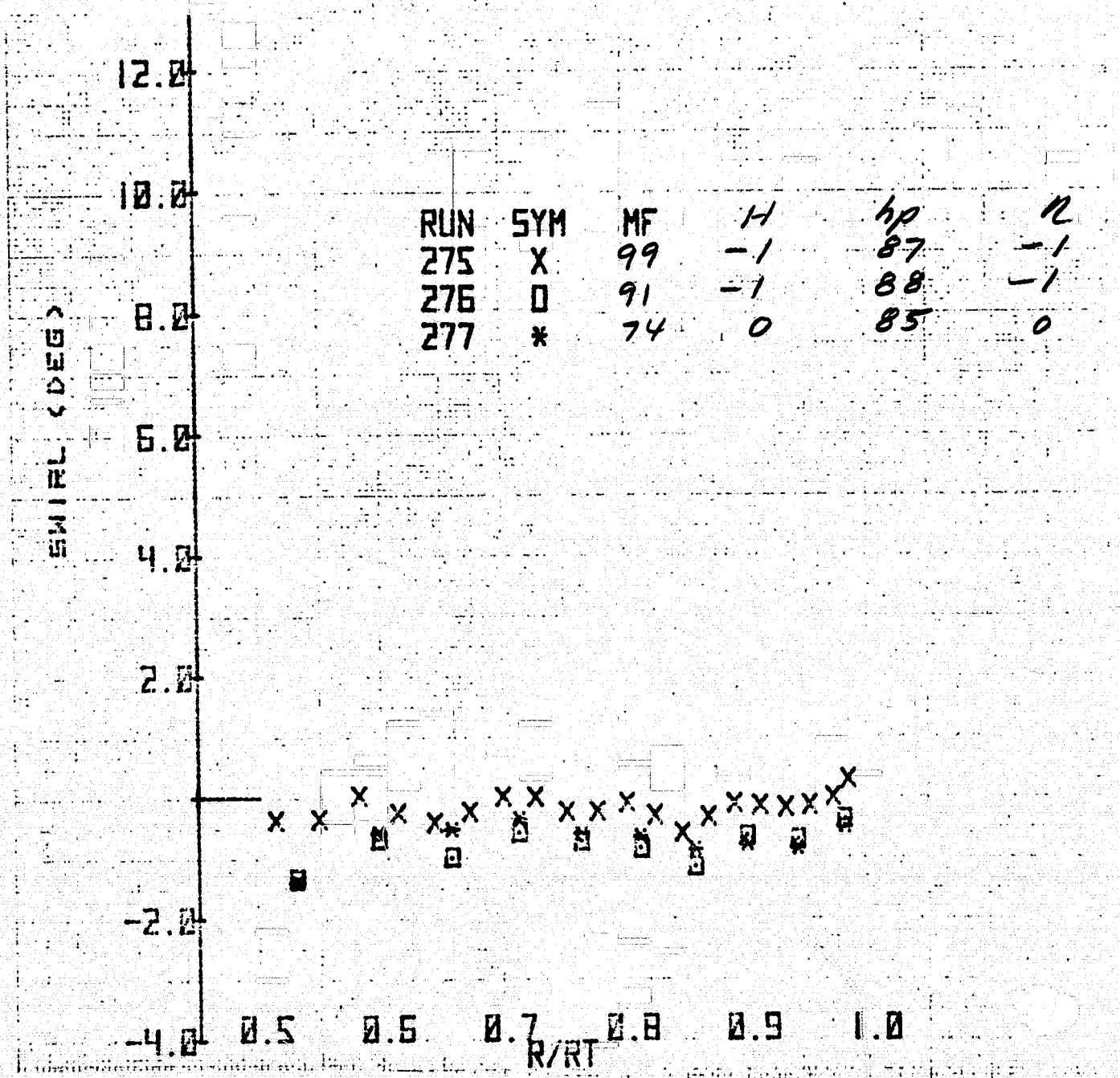

(b) Top azimuth - concluded.

Figure 19.- Continued.

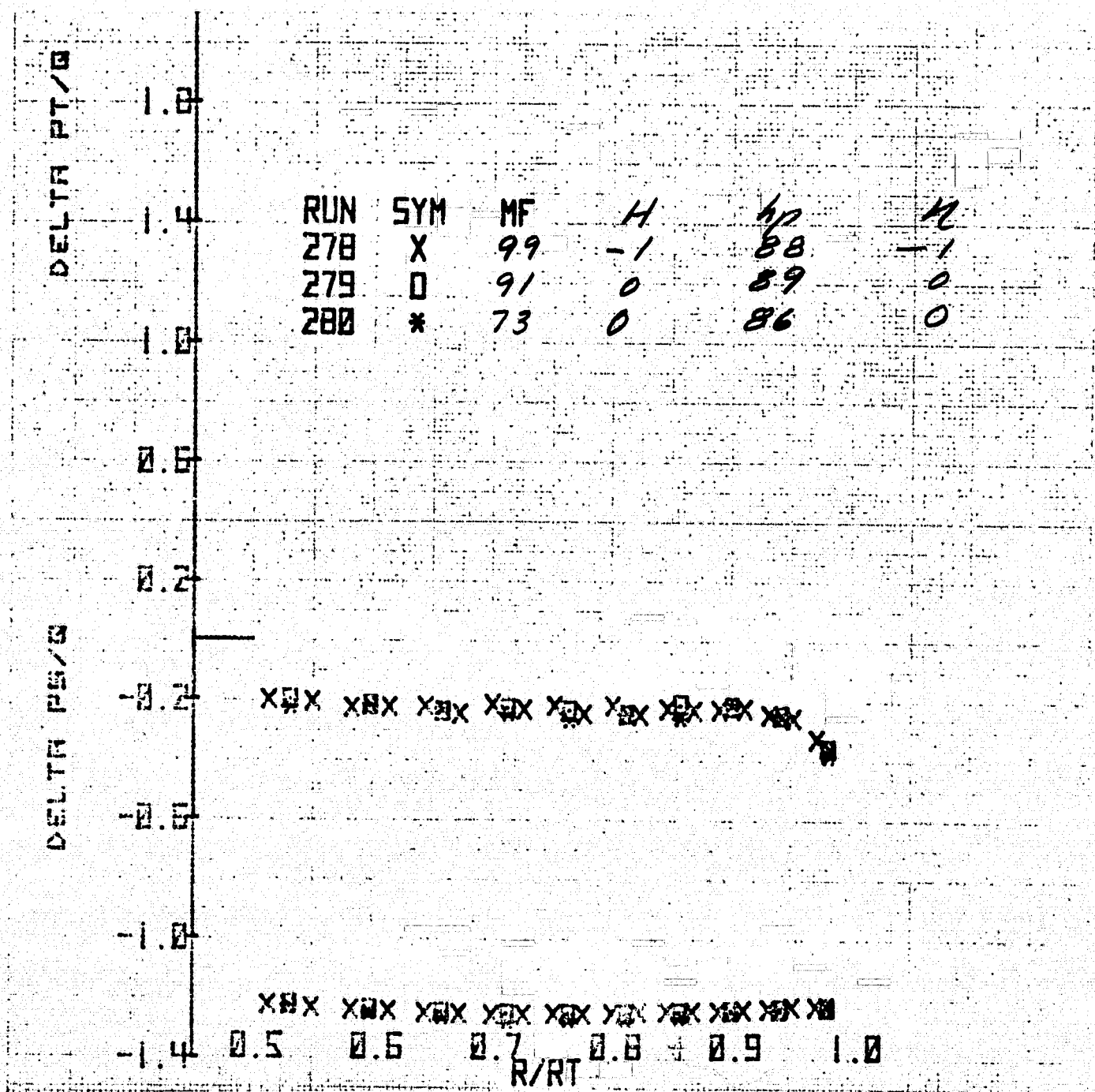

(c) Starboard.

Figure 19.- Continued.

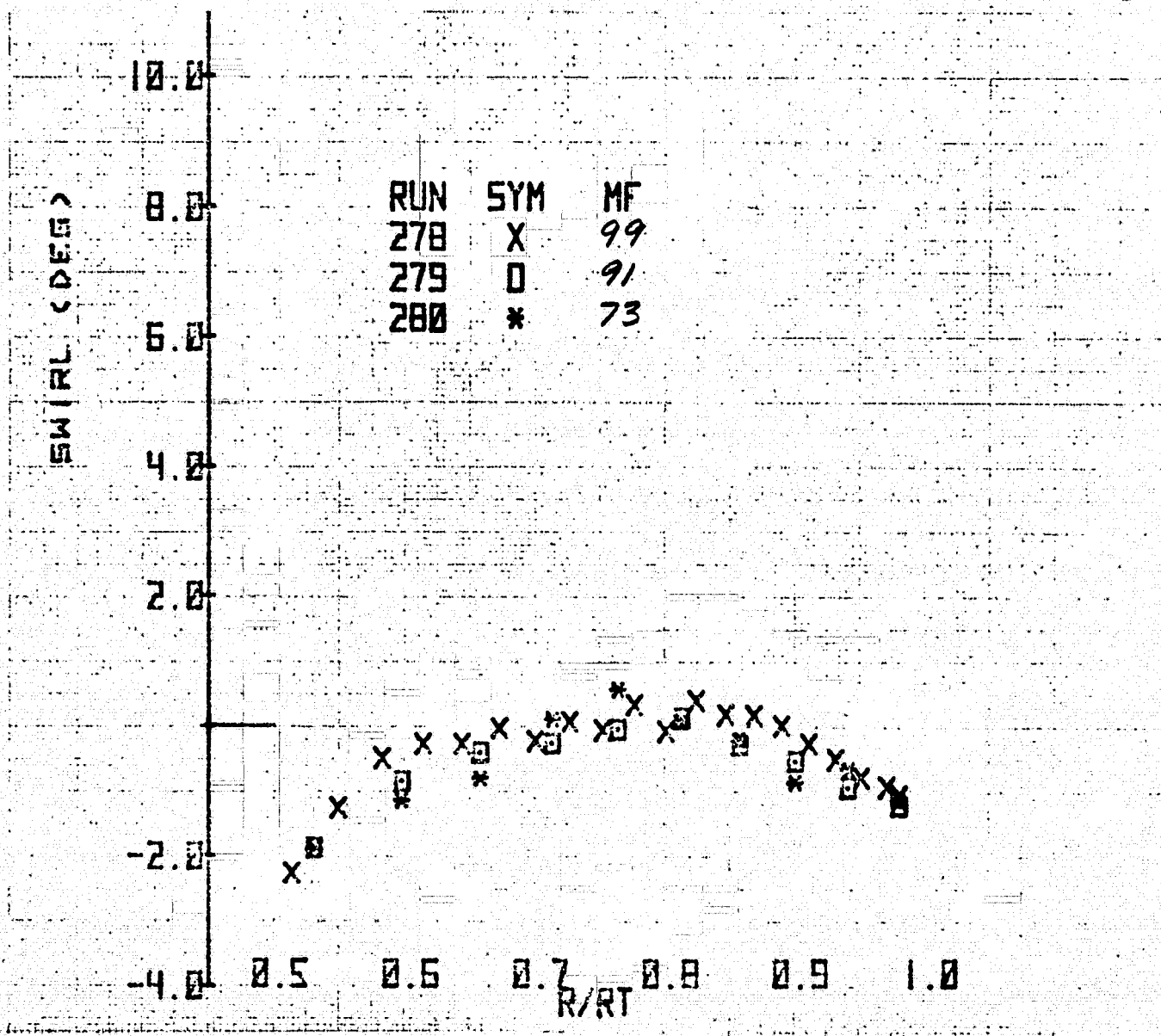

(c) Starboard - concluded.

Figure 19.- Continued.

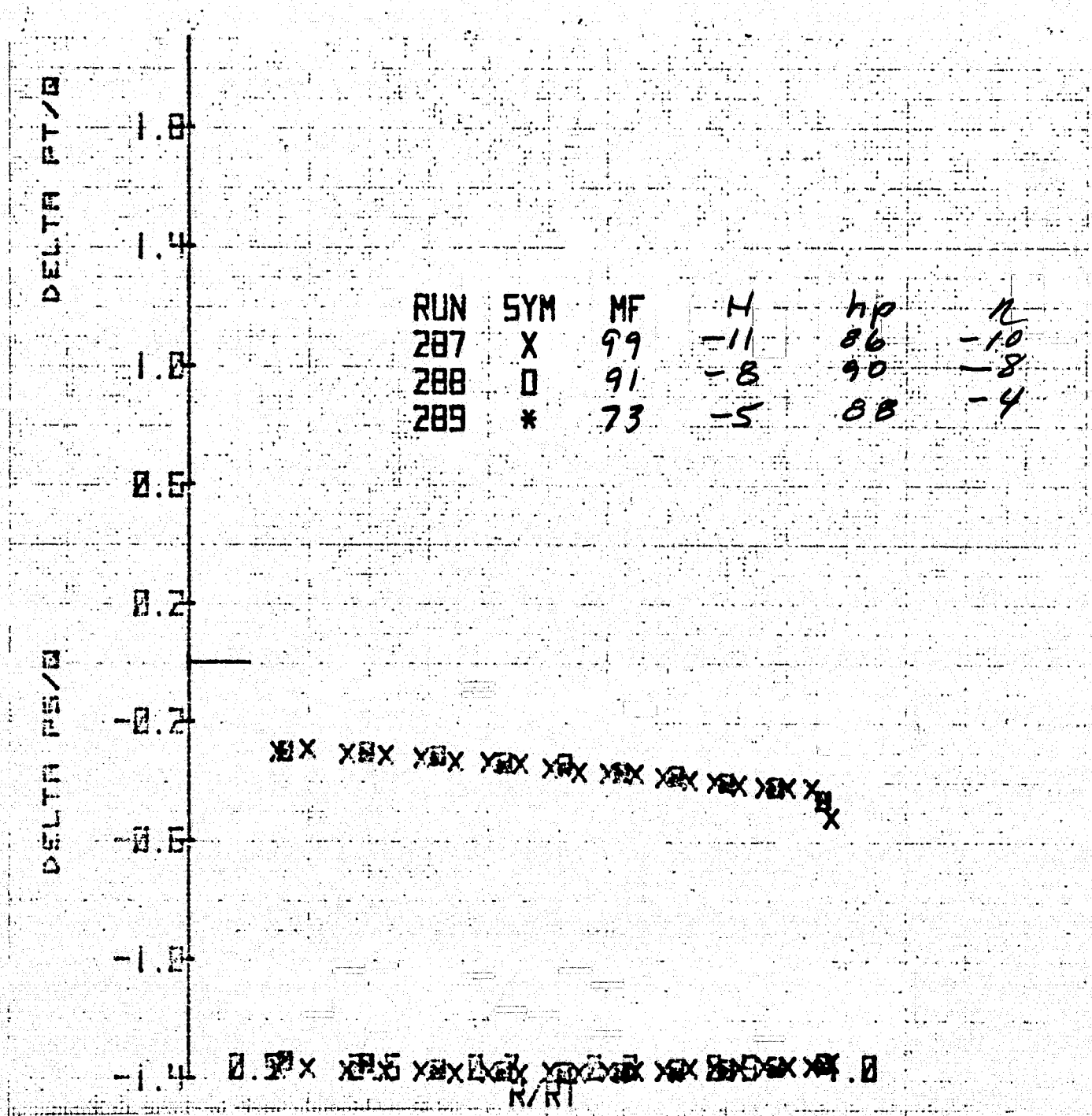

(d) Bottom azimuth.

Figure 19.- Continued.

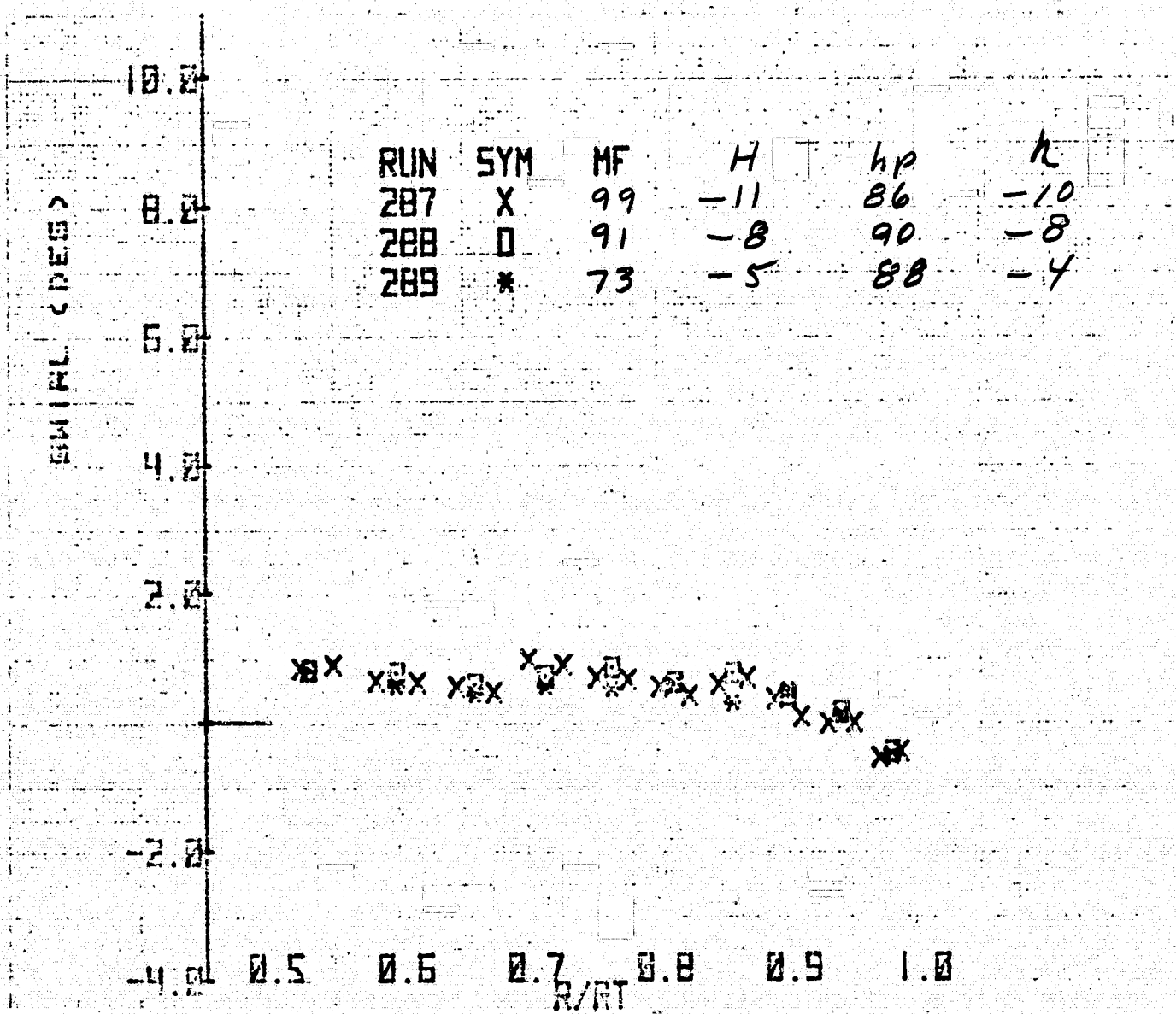

(d) Bottom azimuth - concluded.

Figure 19.- Concluded.

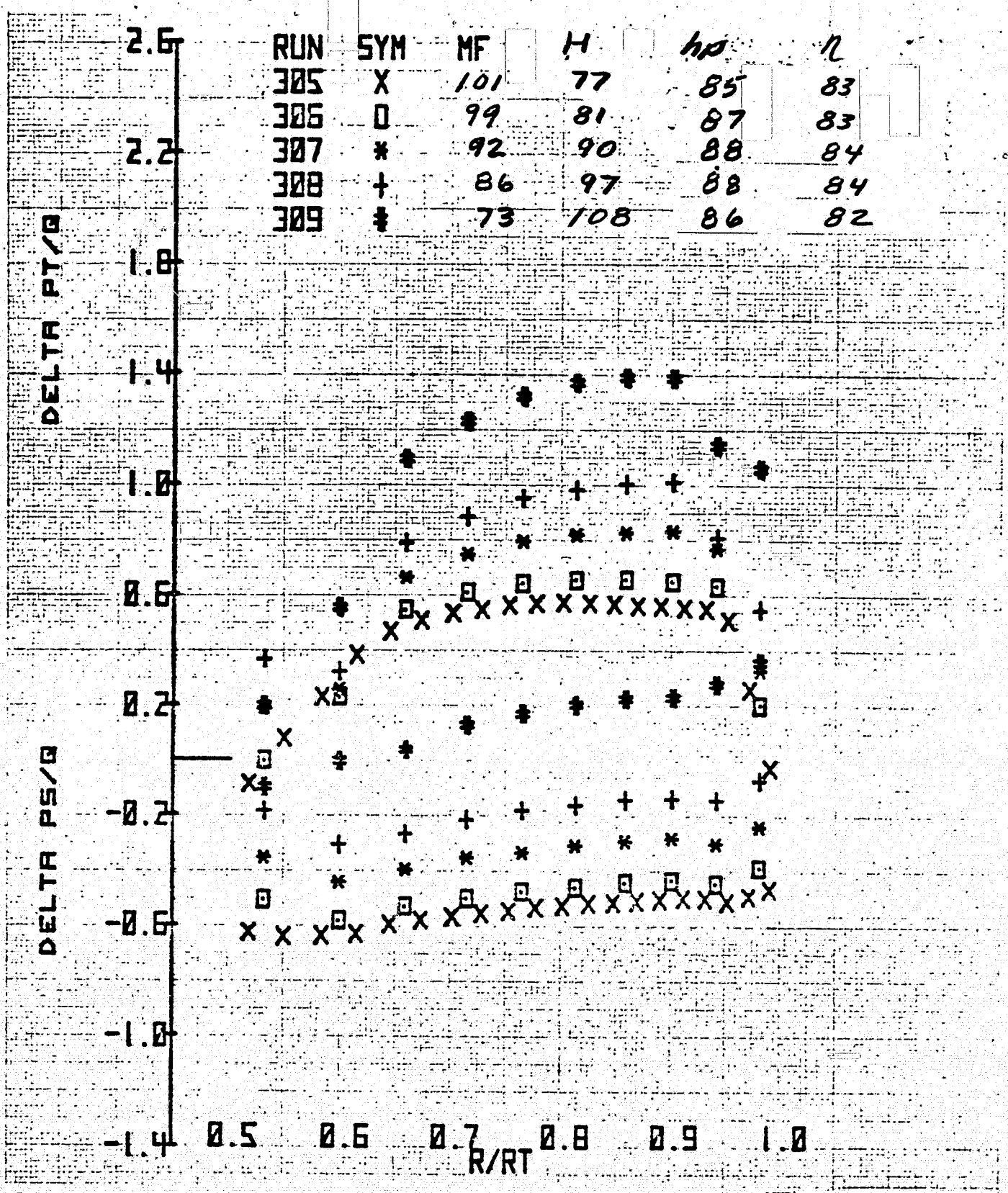

Figure 20.- Radial variation of total pressure coefficient, static pressure coefficient, and swirl angle between stator and rotor at the port azimuth at several mass flows; inlet honeycomb in. N = 100% and ξ = 40.8°.

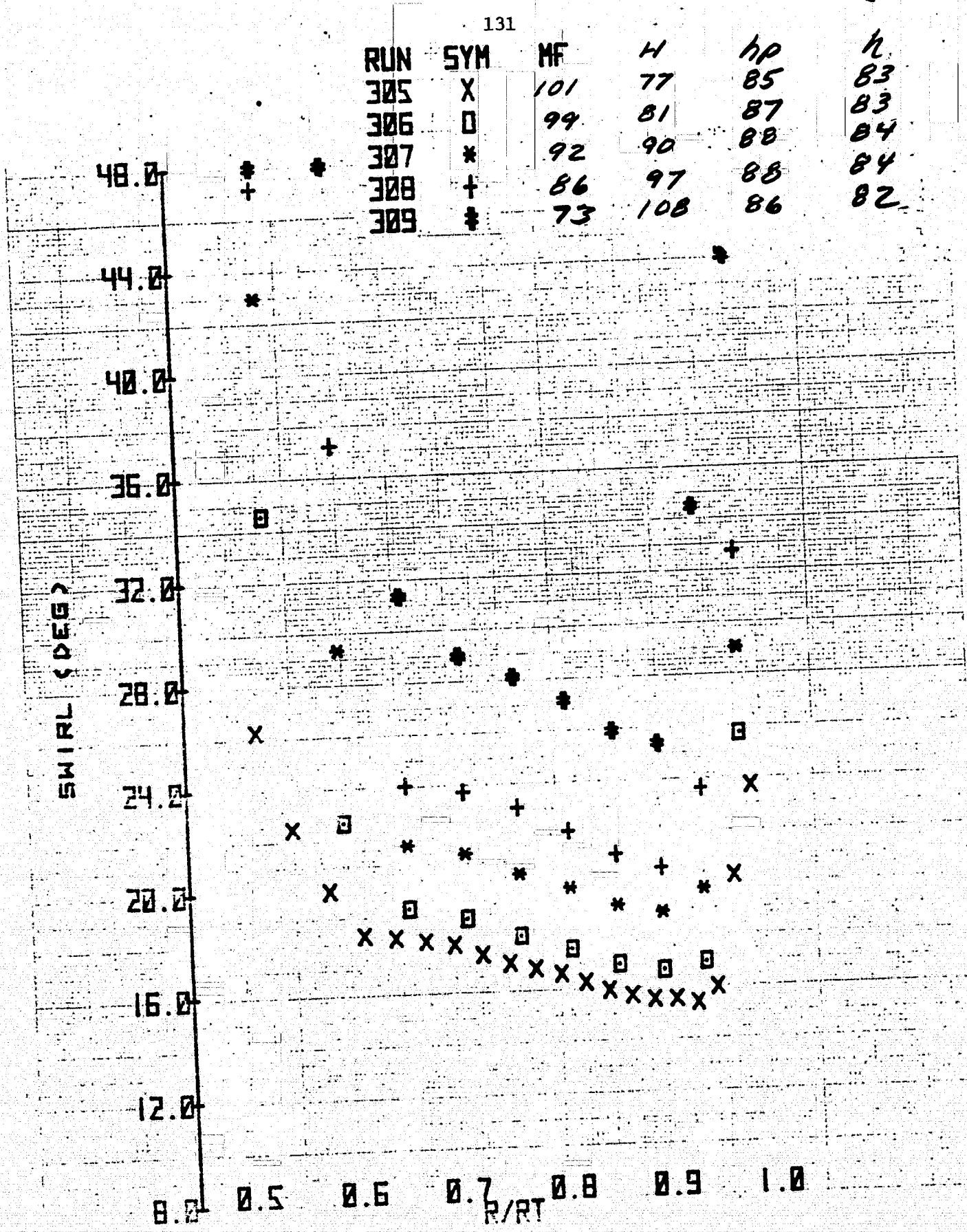

Figure 20.- Concluded.

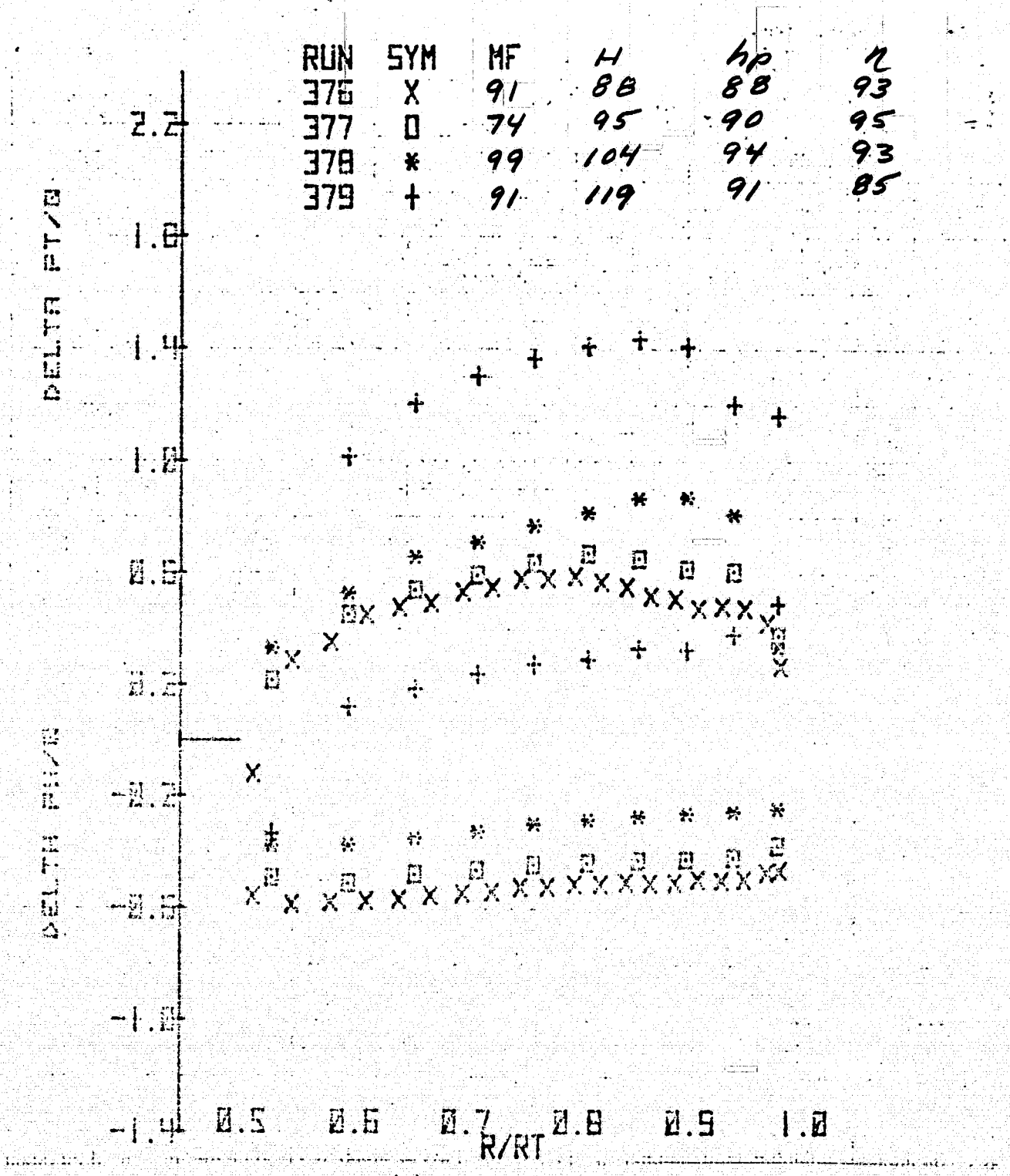

(a) Port azimuth.

Figure 21.- Radial variation of total pressure coefficient, static pressure coefficient, and swirl angle between rotor and stators for several azimuths and mass flows; modified contraction, inlet honeycomb, N = 100%, and ξ = 40.8°.

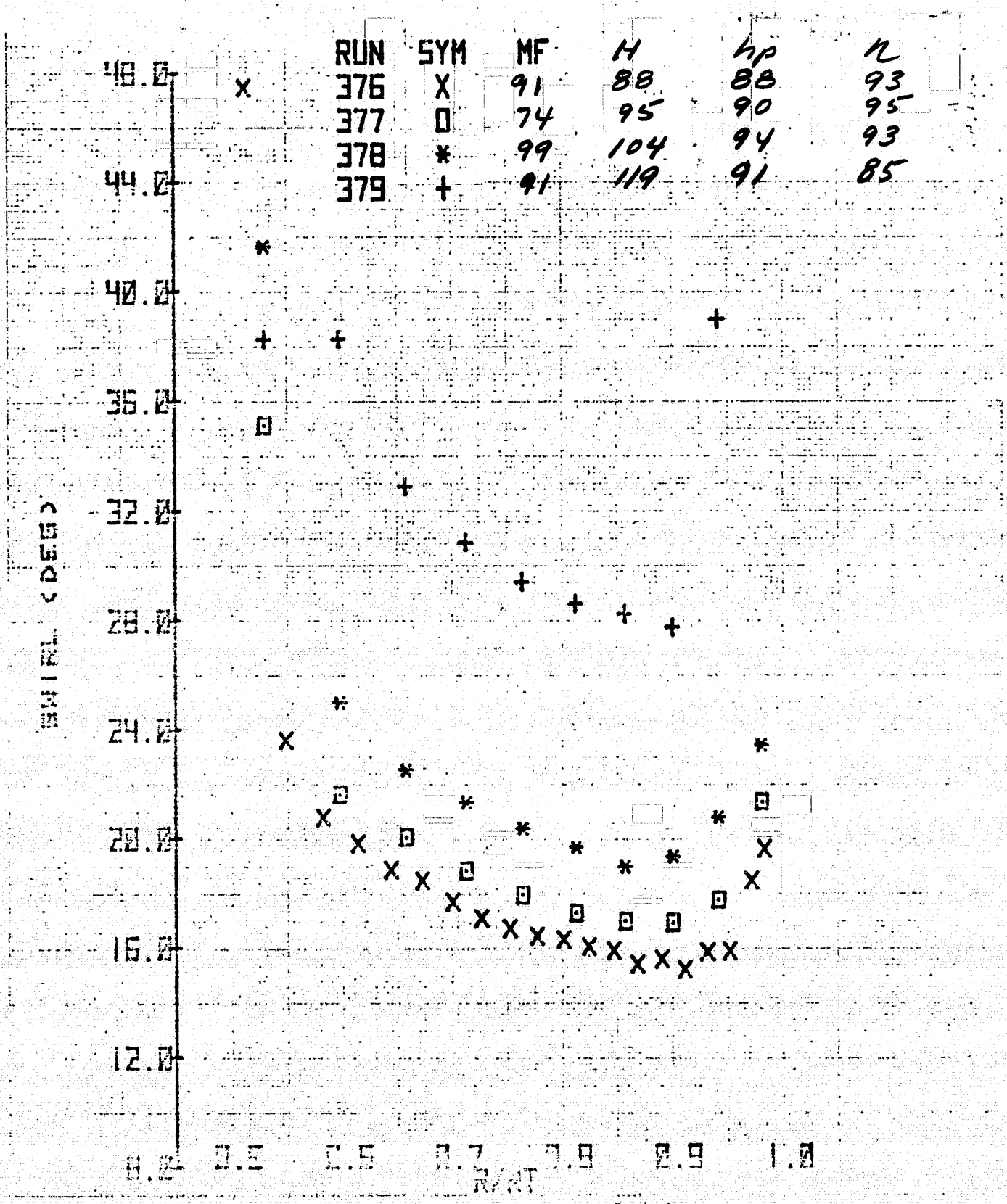

(a) Port azimuth - concluded.

Figure 21.- Continued.

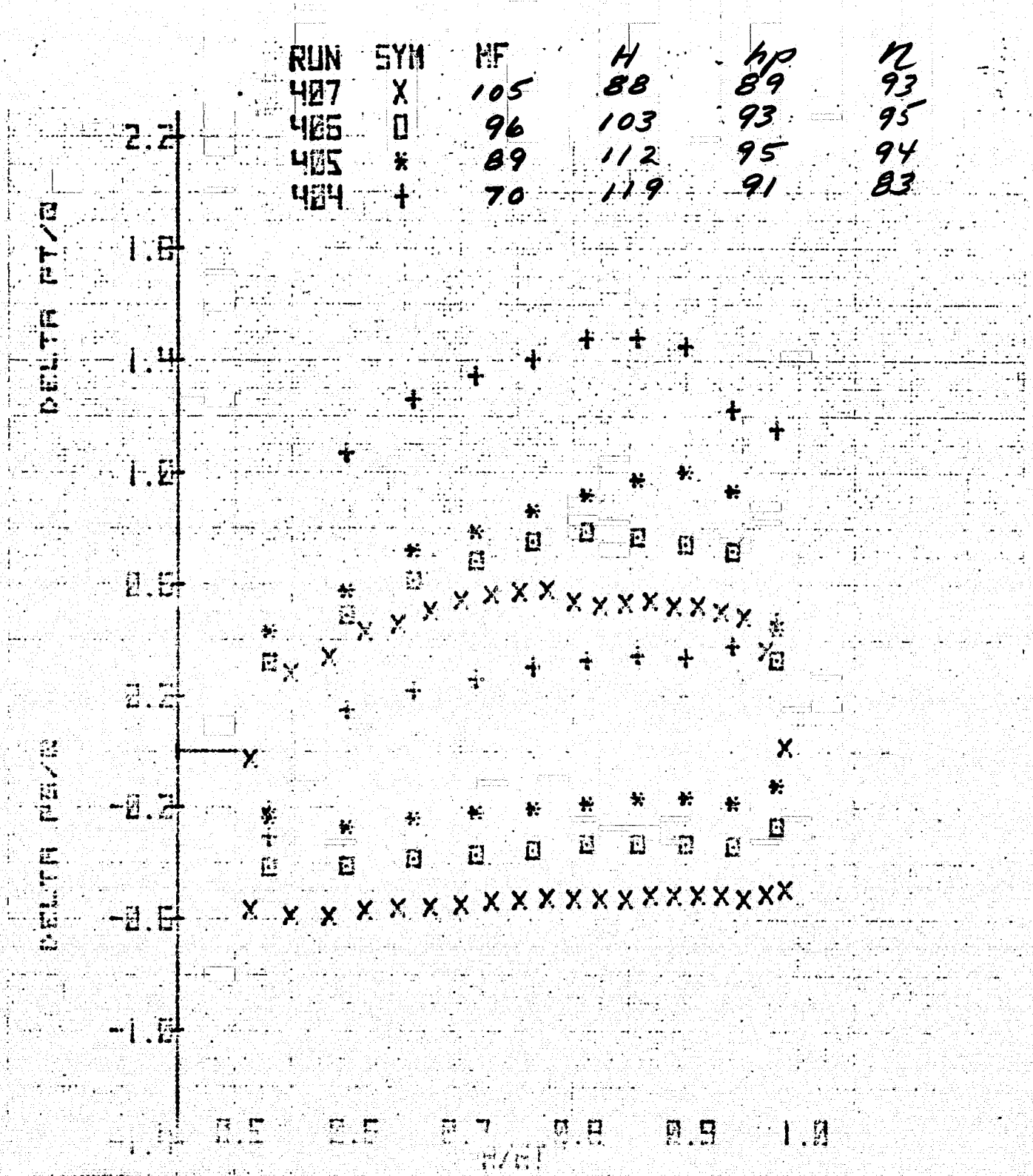

(b) Top azimuth.

Figure 21.- Continued.

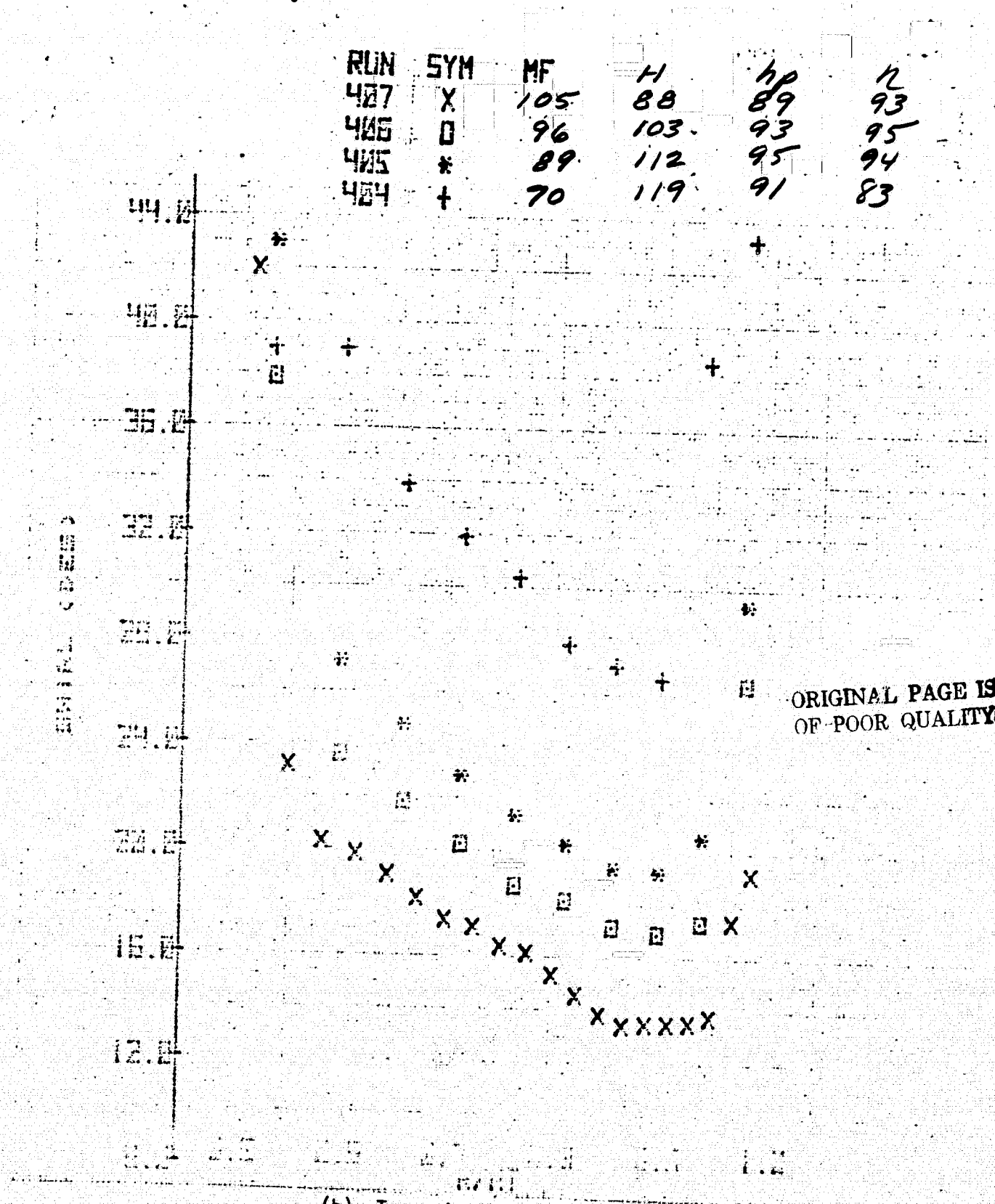

(b) Top azimuth - concluded.

Figure 21.- Continued.

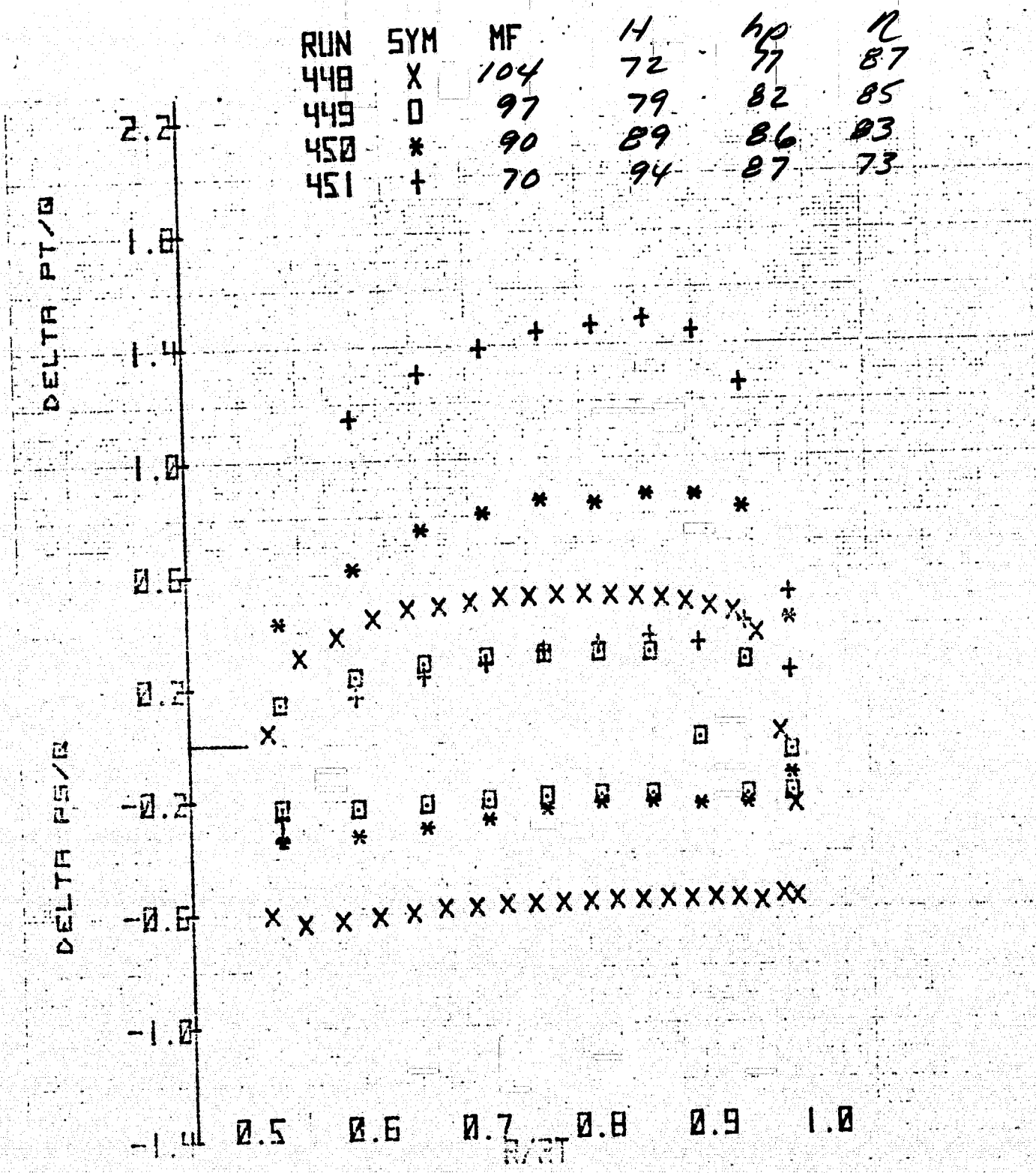

(c) Starboard azimuth.

Figure 21.- Continued.

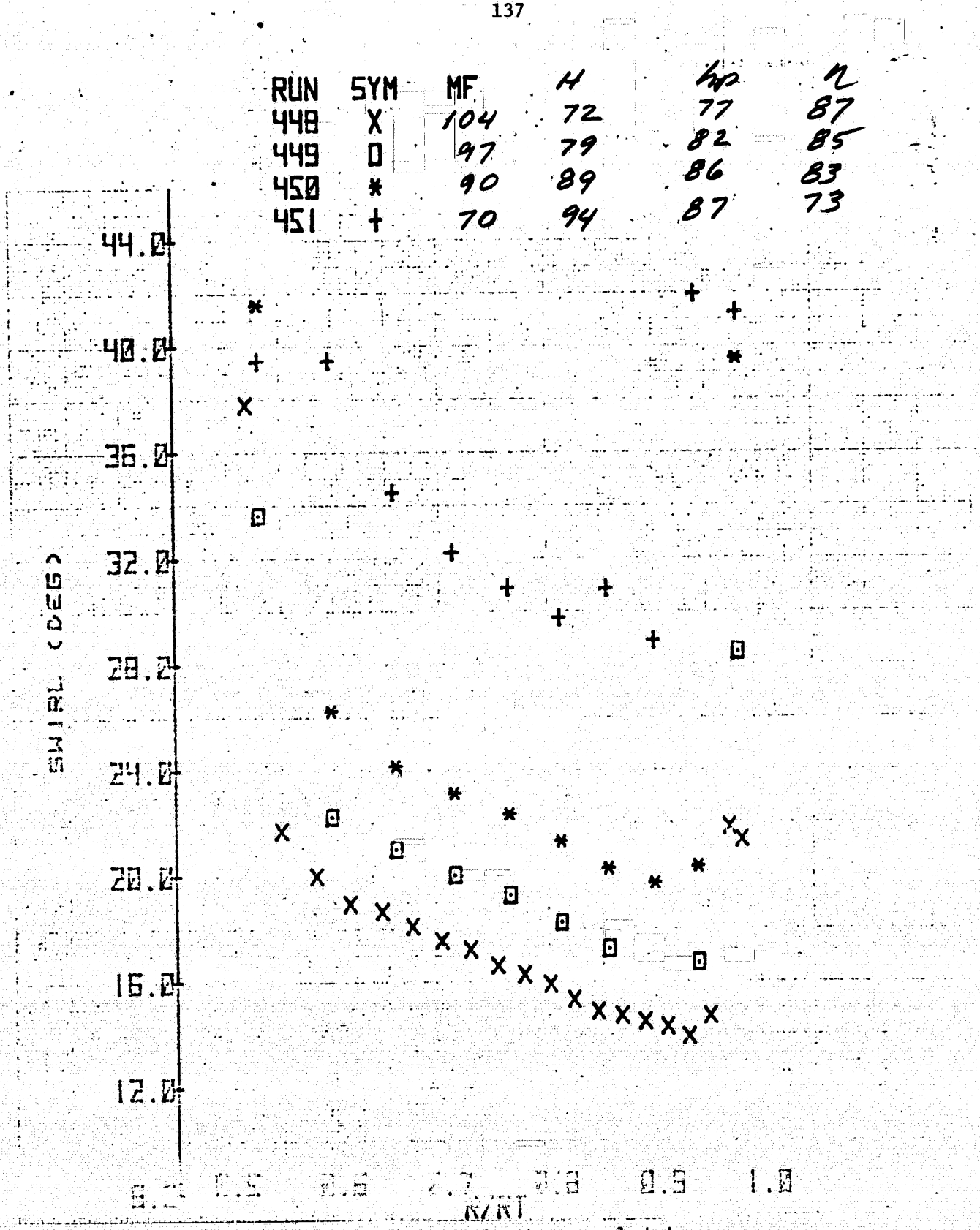

(c) Starboard azimuth - concluded.

Figure 21.- Concluded.

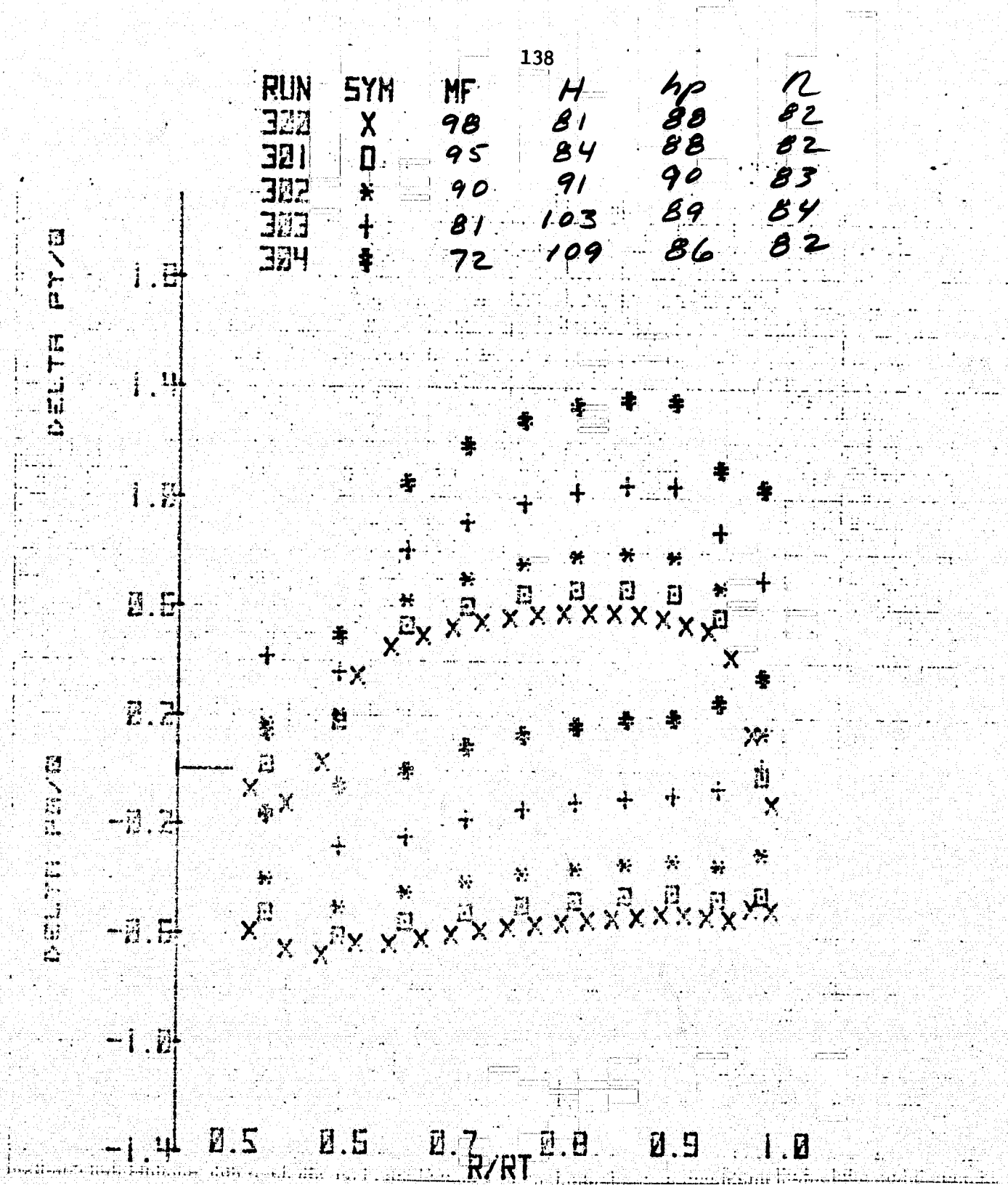

(a) Port azimuth.

Figure 22.- Radial variation of total pressure coefficient, static pressure coefficient, and swirl angle between rotor and stator for two azimuths and several mass flows; inlet honeycomb, original contraction, "H" inflow configuration, N = 100%, and ξ = 40.8°.

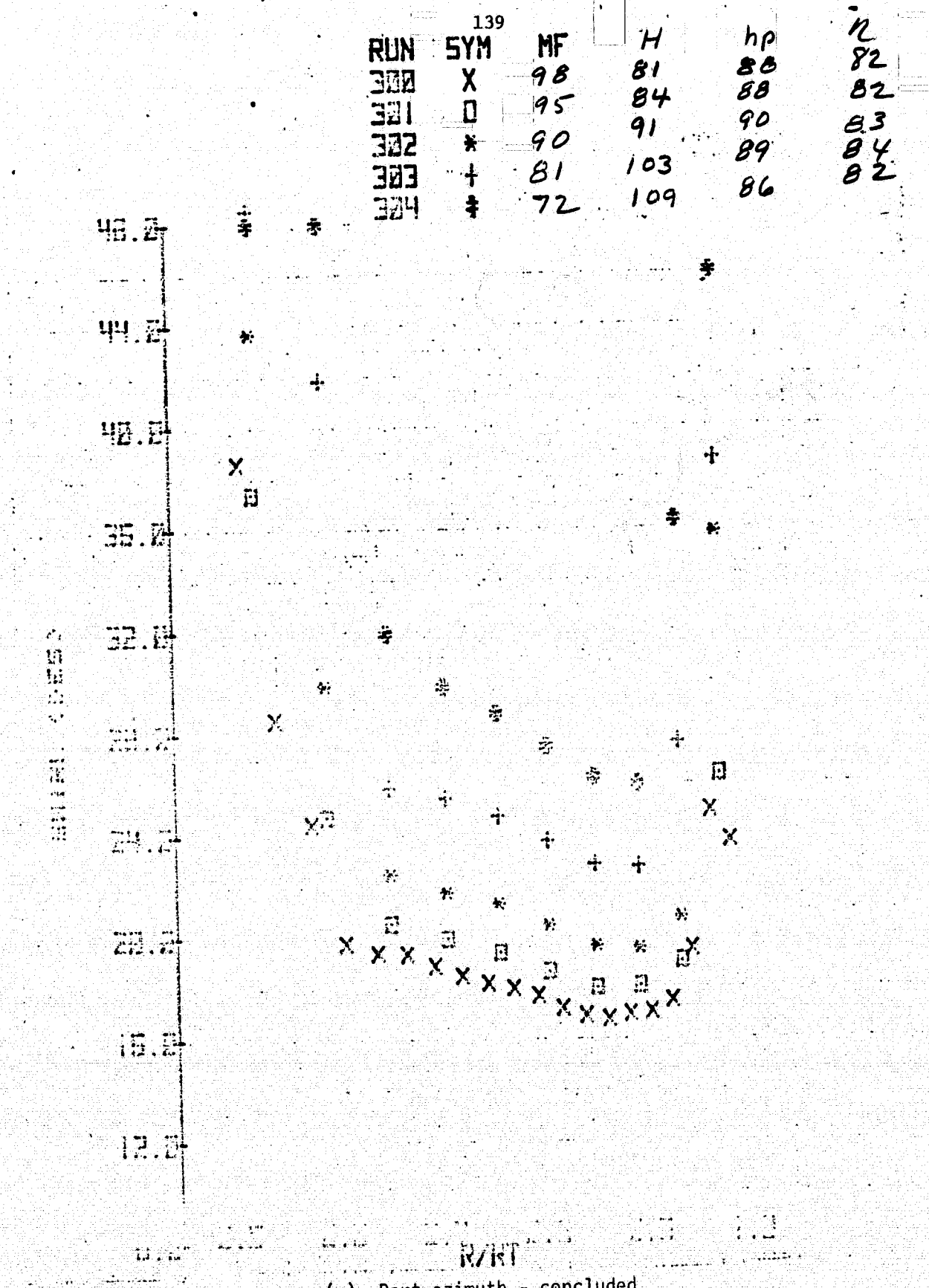

(a) Port azimuth - concluded.

Figure 22.- Continued.

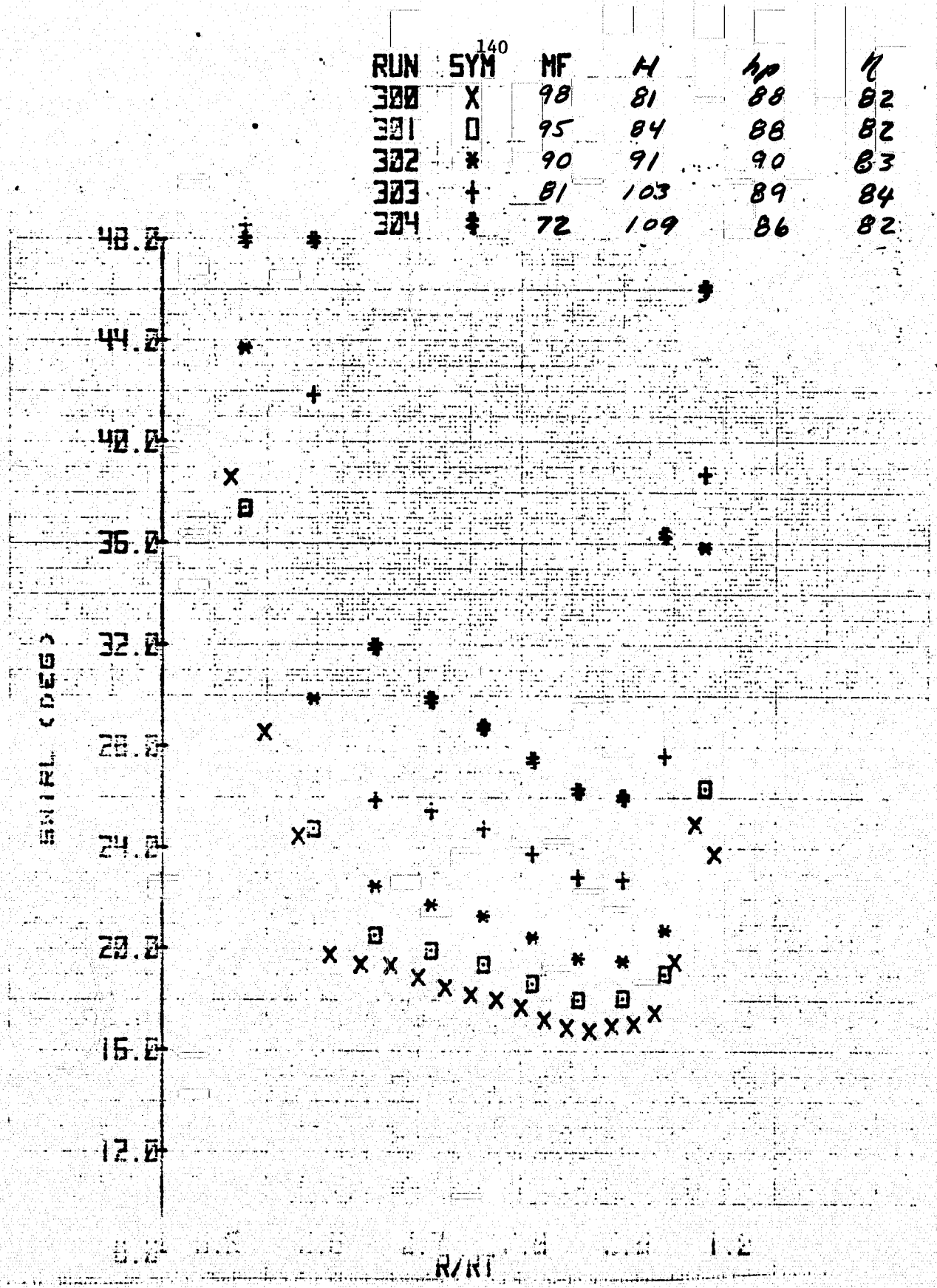

(a) Port azimuth - concluded.

Figure 22.- Continued.

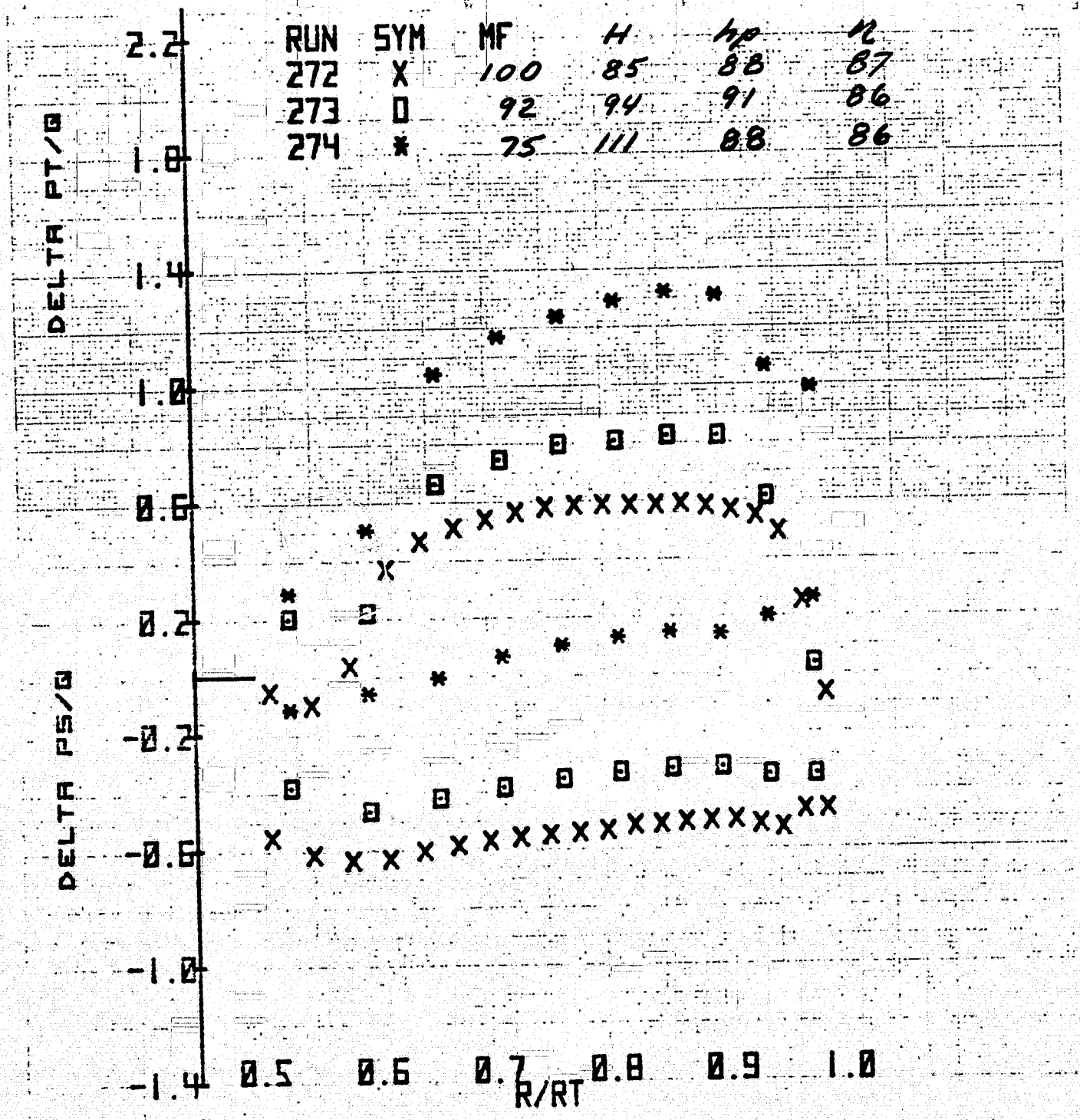

(b) Top azimuth.

Figure 22.- Continued.

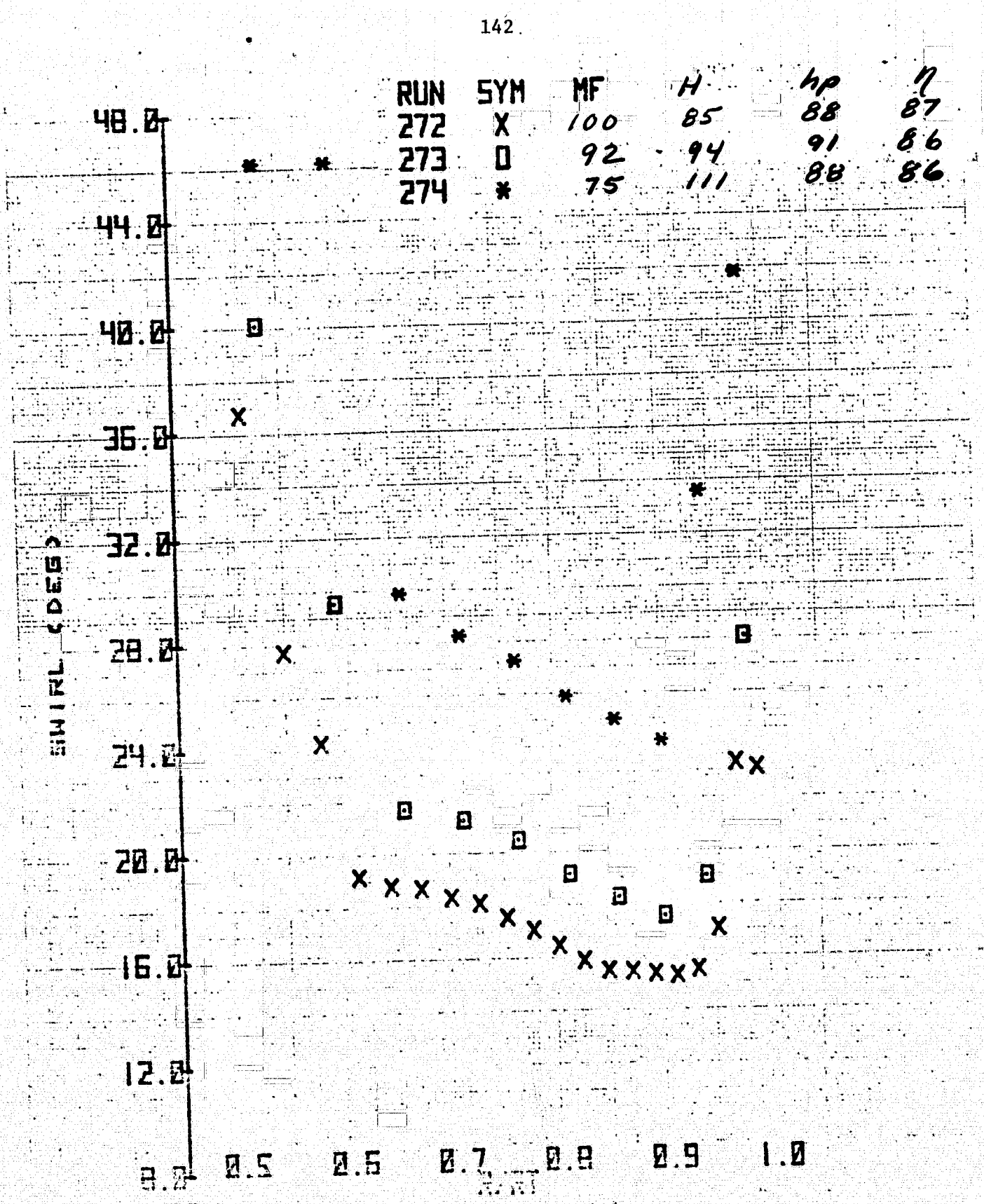

(b) Top azimuth - concluded.

Figure 22.- Continued.

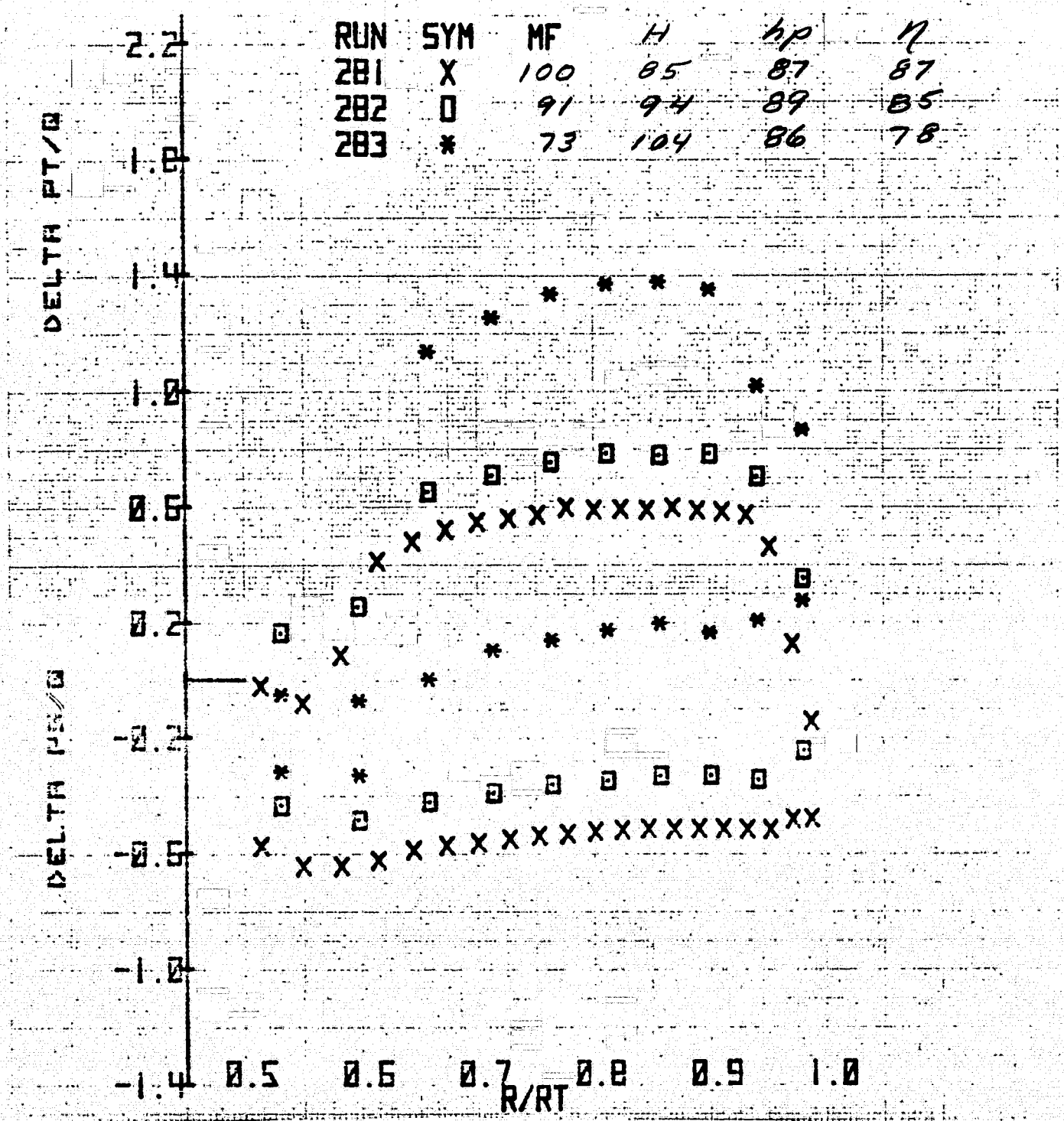

(c) Starboard azimuth.

Figure 22.- Continued.

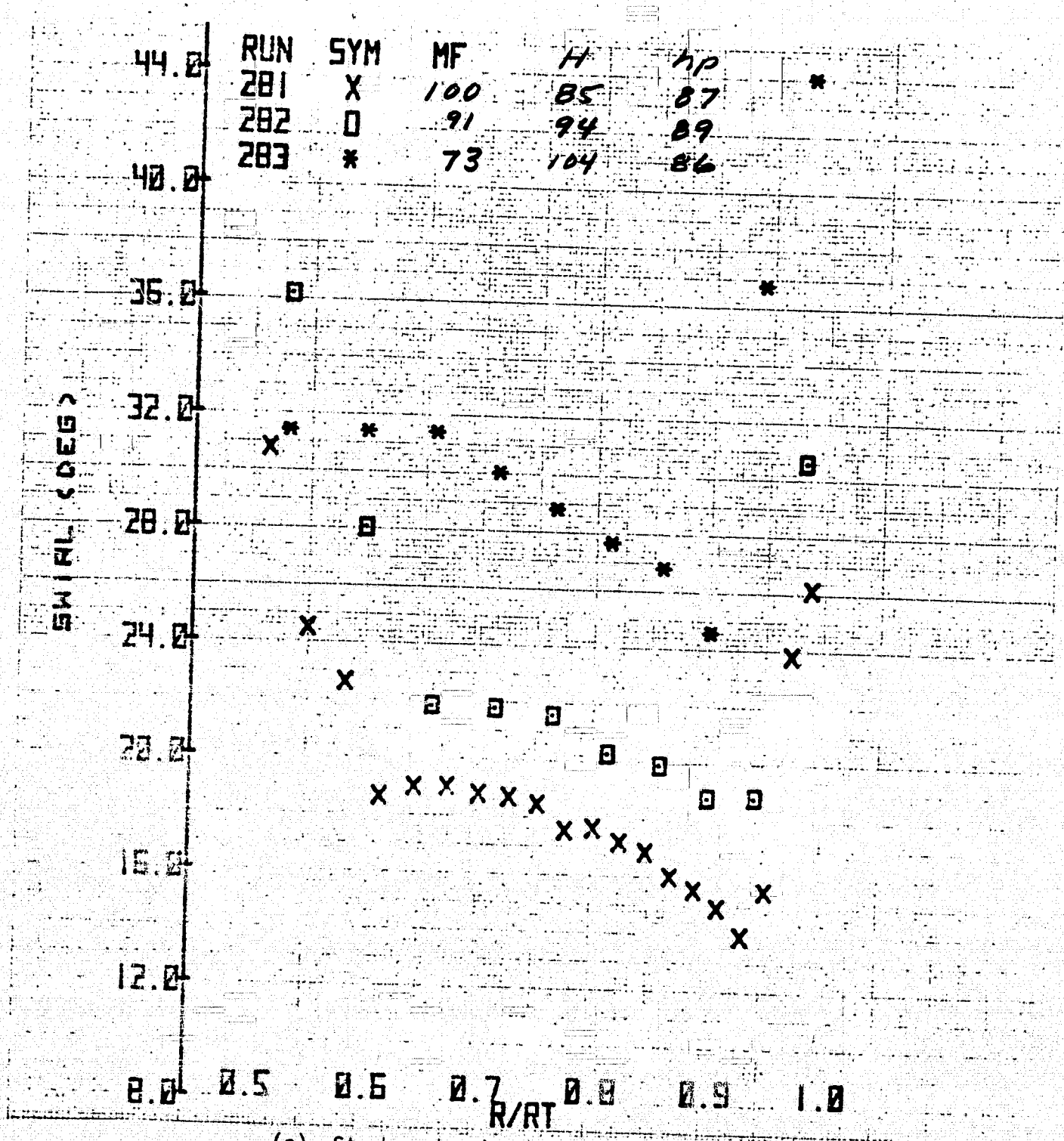

(c) Starboard azimuth - concluded.

Figure 22.- Continued.

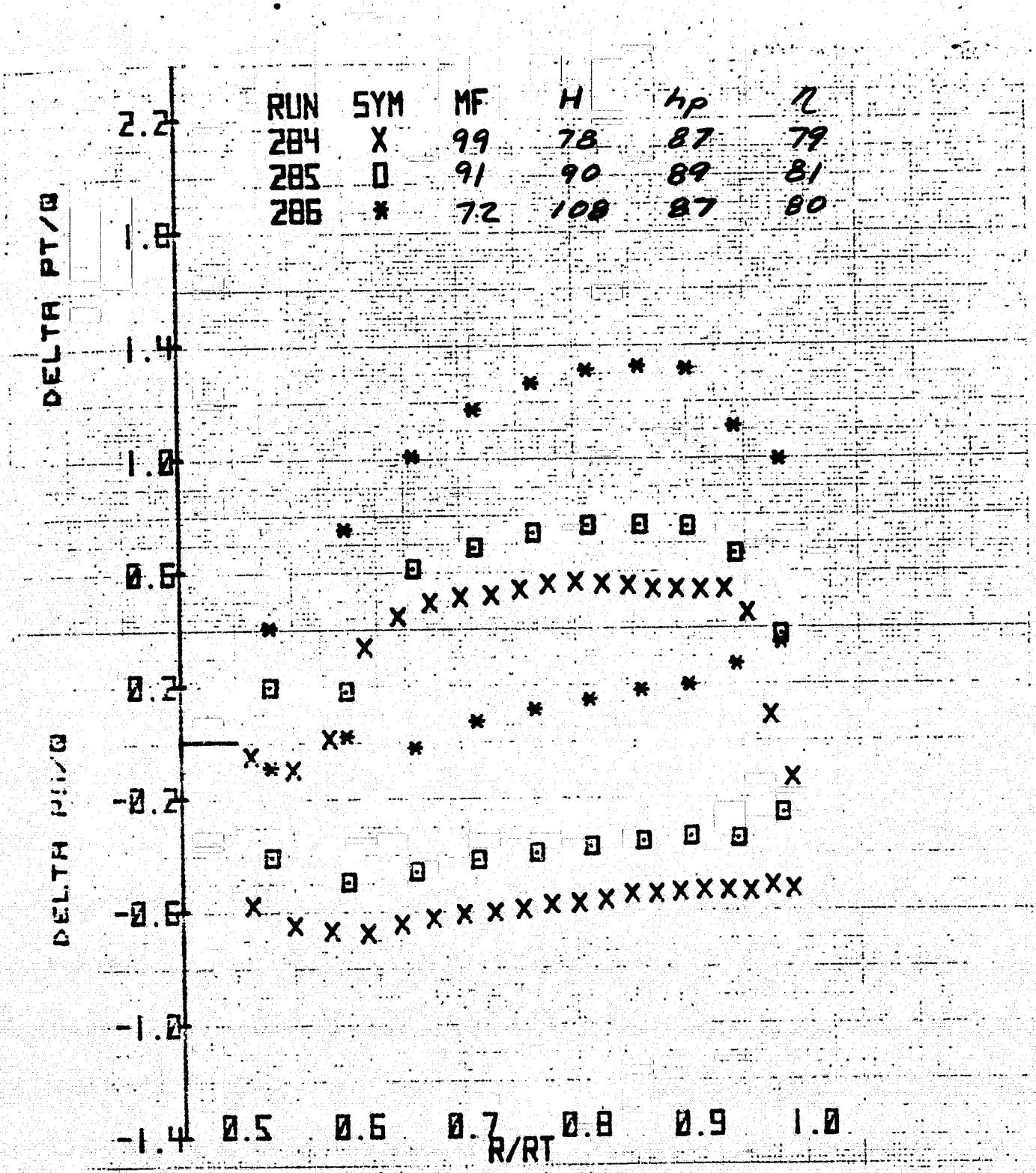

(d) Bottom azimuth.

Figure 22.- Continued.

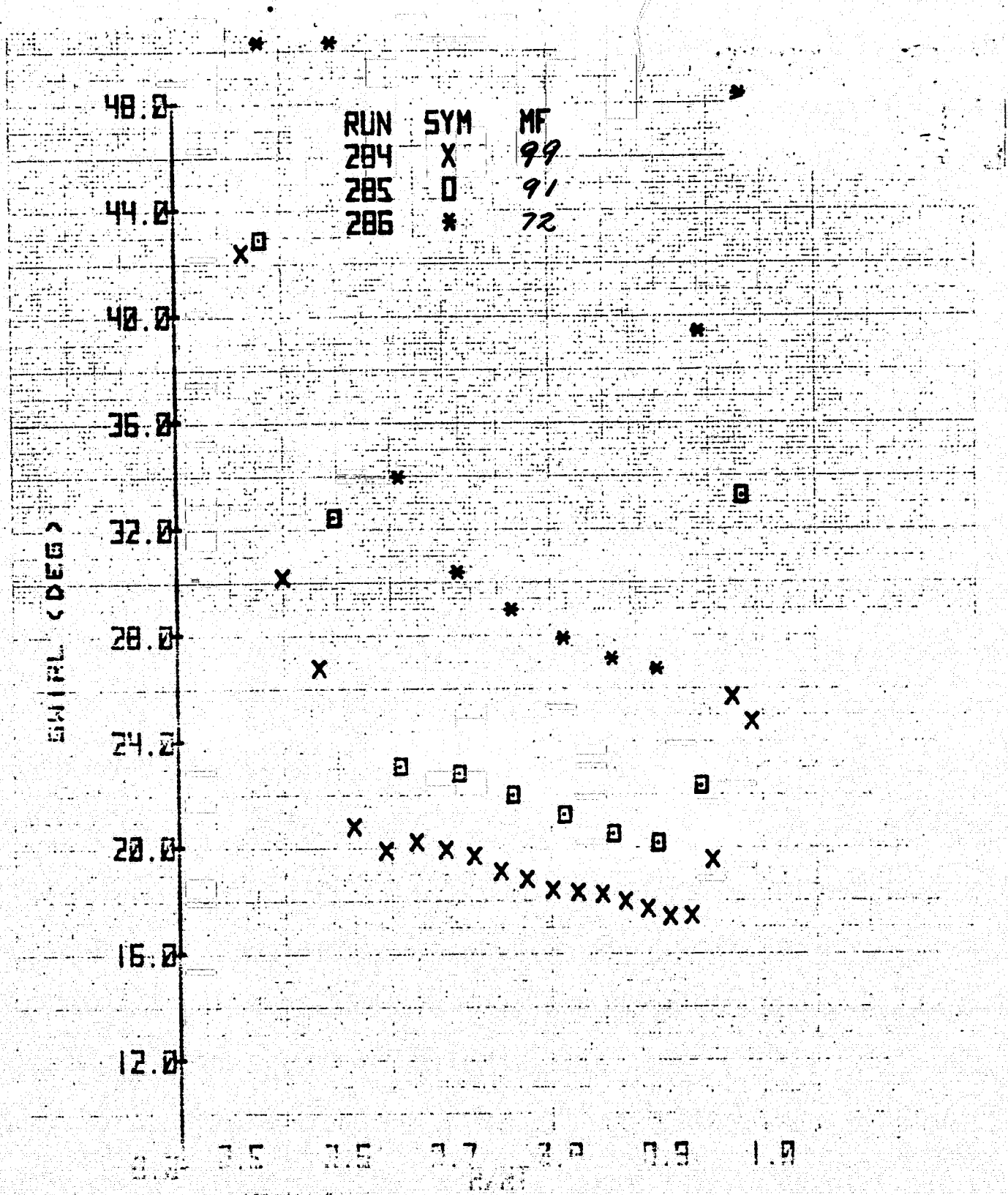

(d) Bottom azimuth - concluded.

Figure 22.- Concluded.

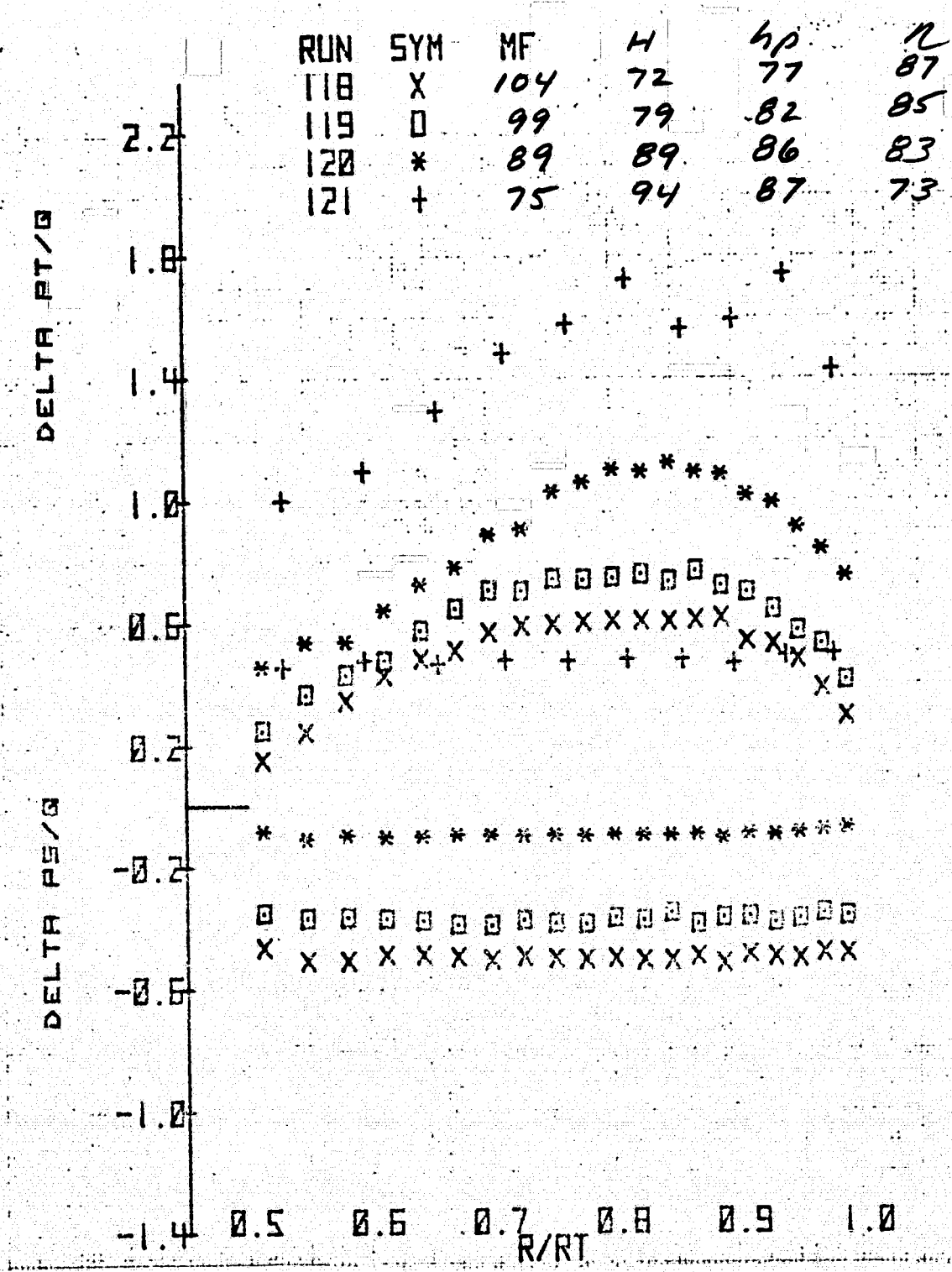

(a) Port azimuth.

Figure 23.- Radial variation of total pressure coefficient, static pressure coefficient, and swirl angle downstream of stators for several azimuths and mass flows; original contraction, N = 100% and ξ = 40.8°.

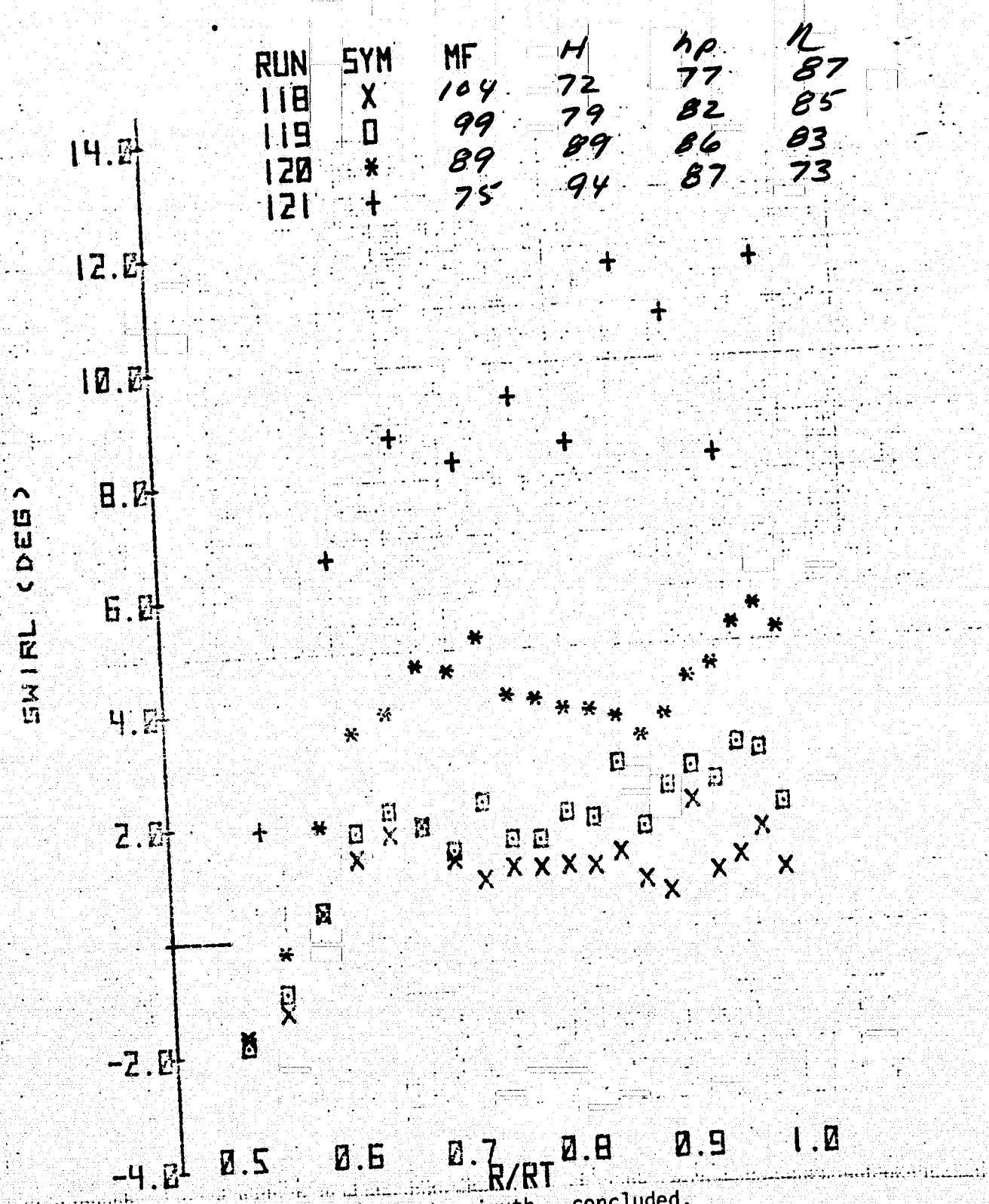

(a) Port azimuth - concluded.

Figure 23.- Continued.

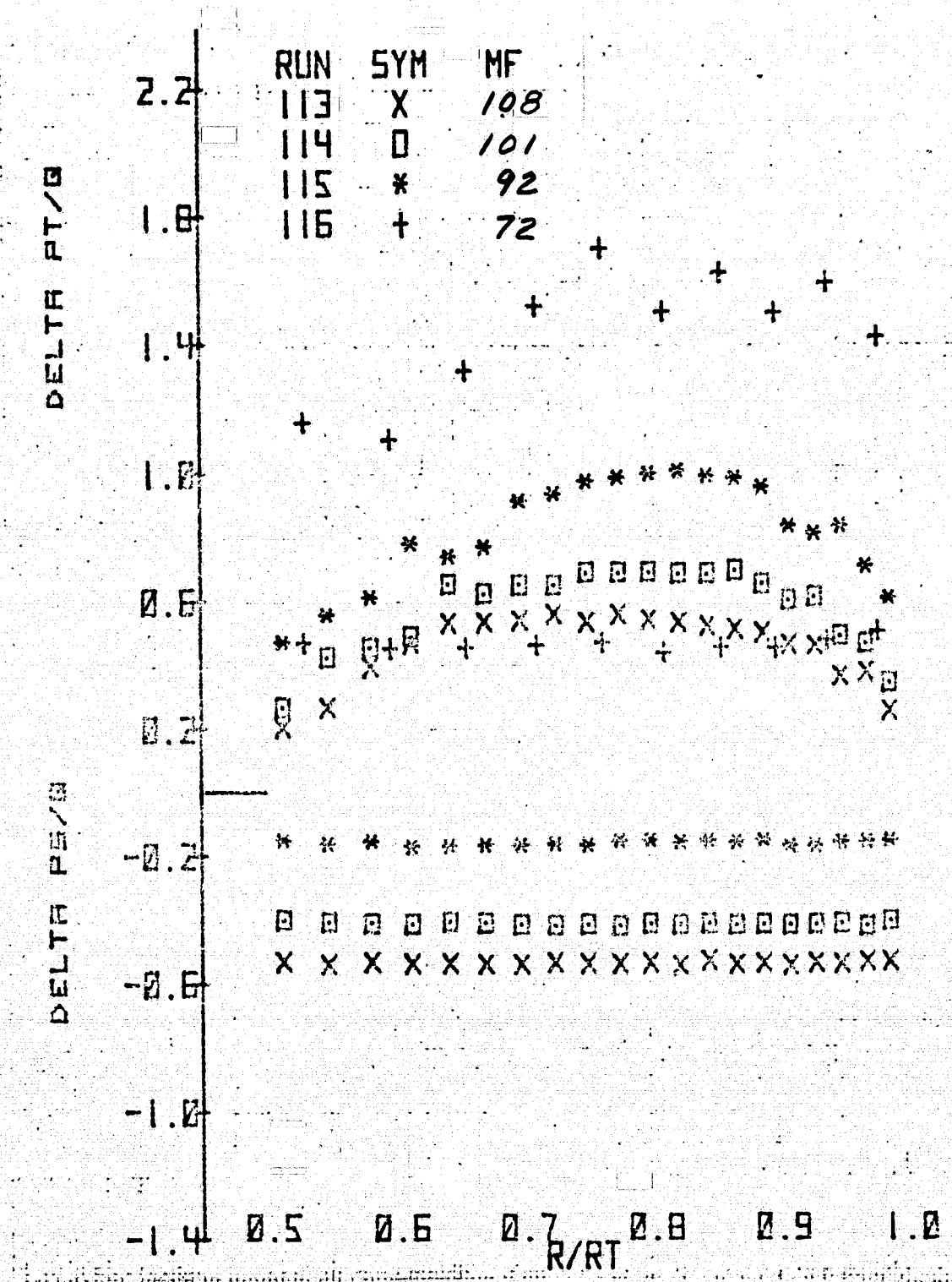

(b) Top azimuth.

Figure 23.- Continued.

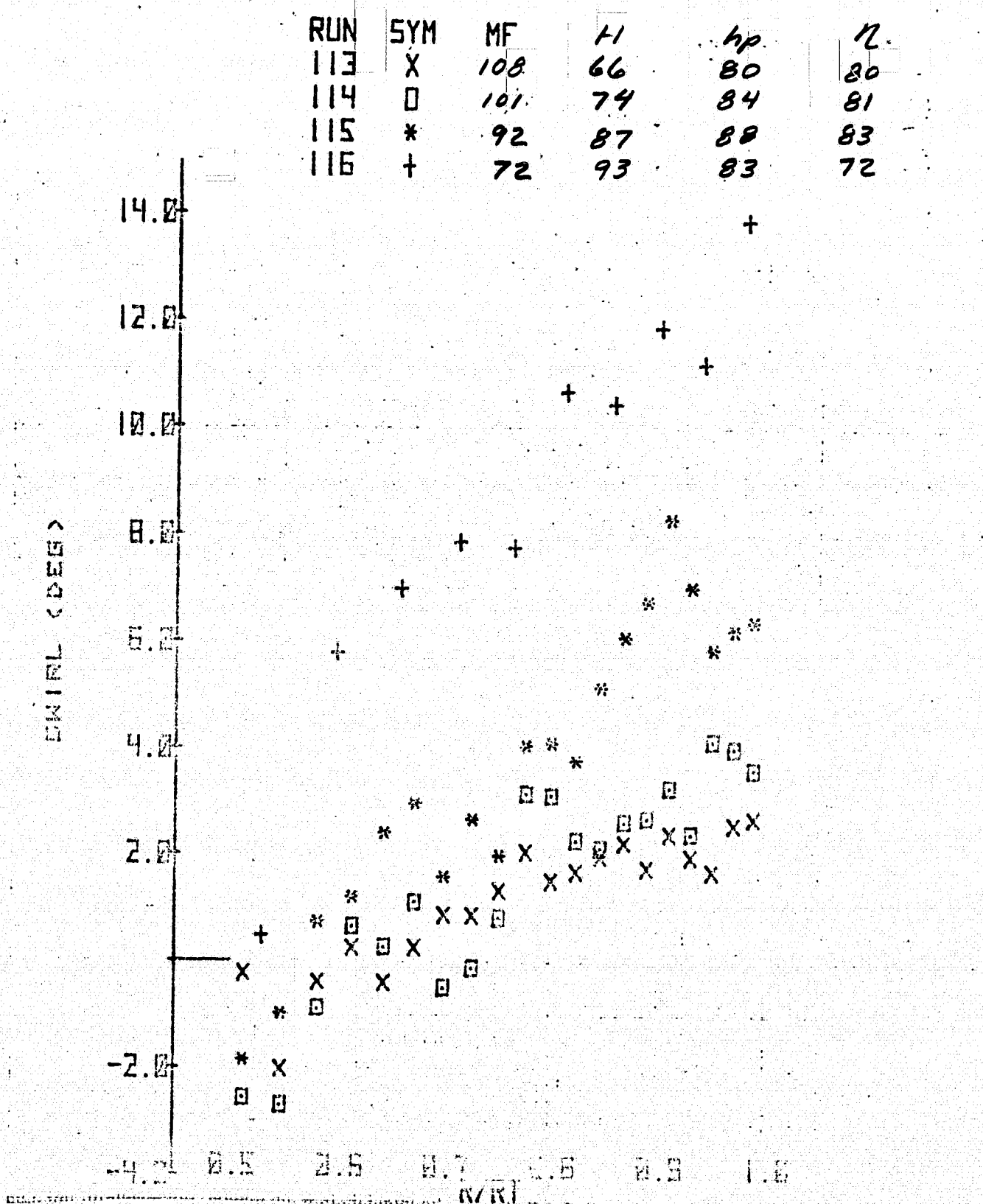

(b) Top azimuth - concluded.

Figure 23.- Continued.

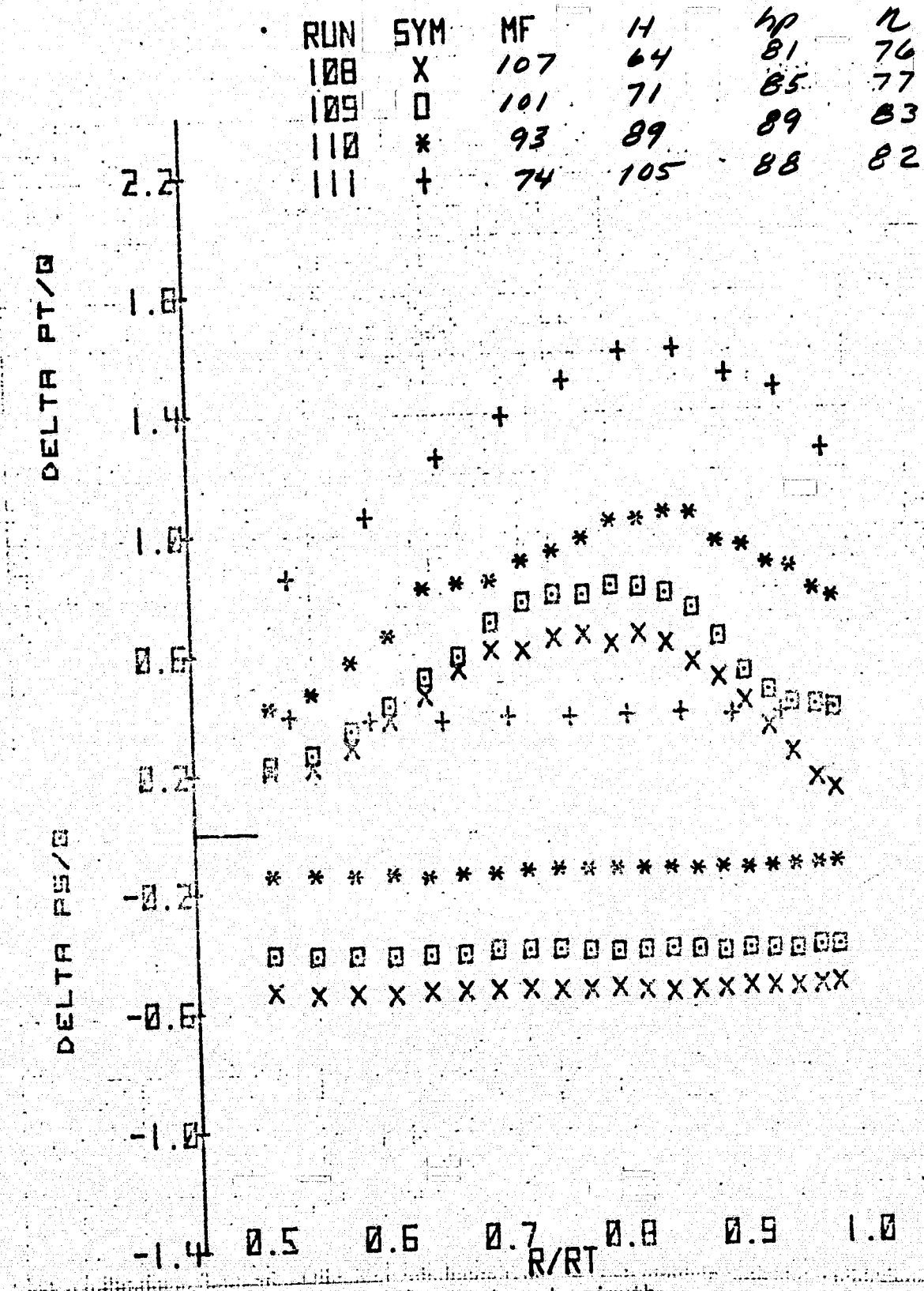

(c) Starboard azimuth.

Figure 23.- Continued.

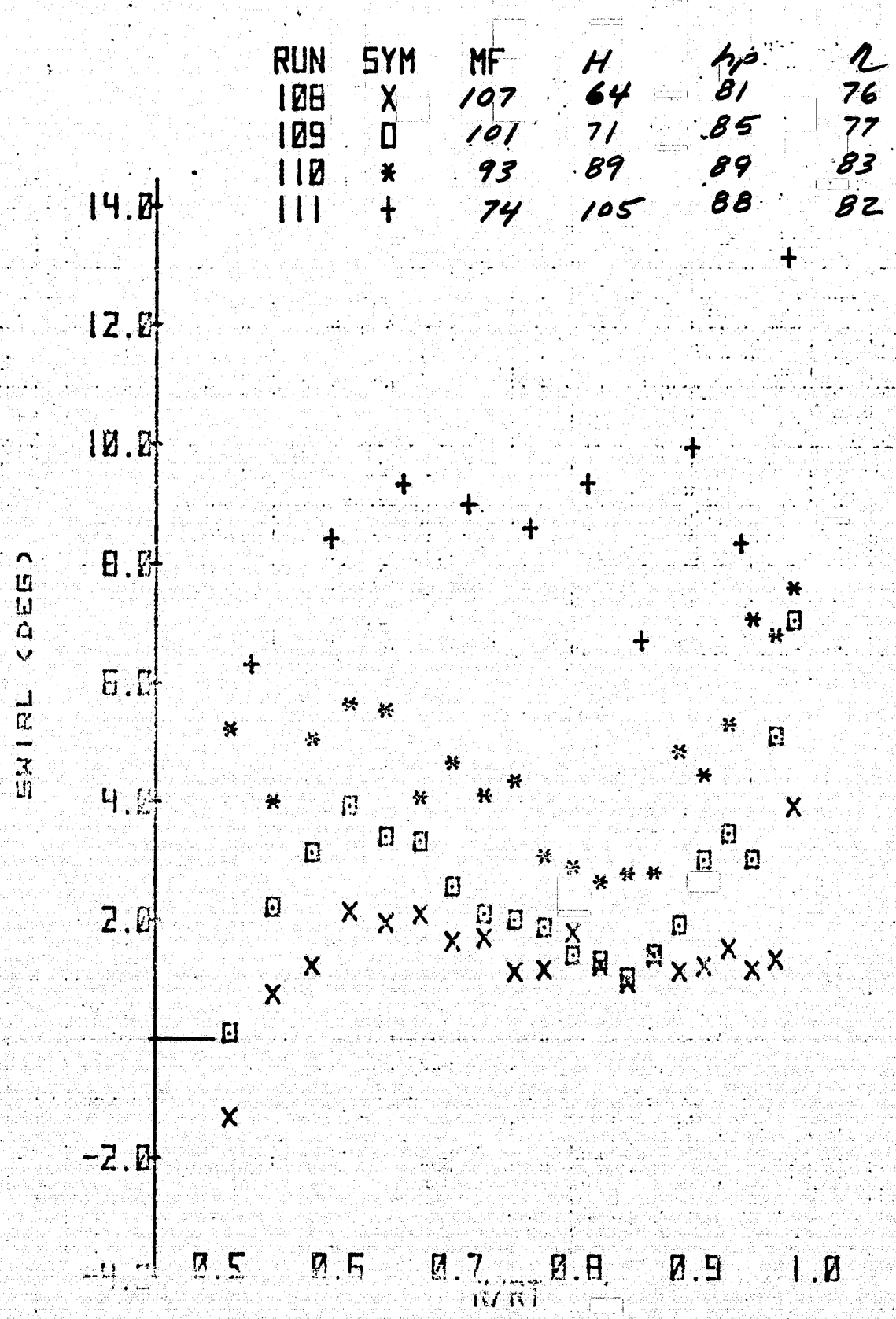

(c) Starboard azimuth - concluded.

Figure 23.- Continued.

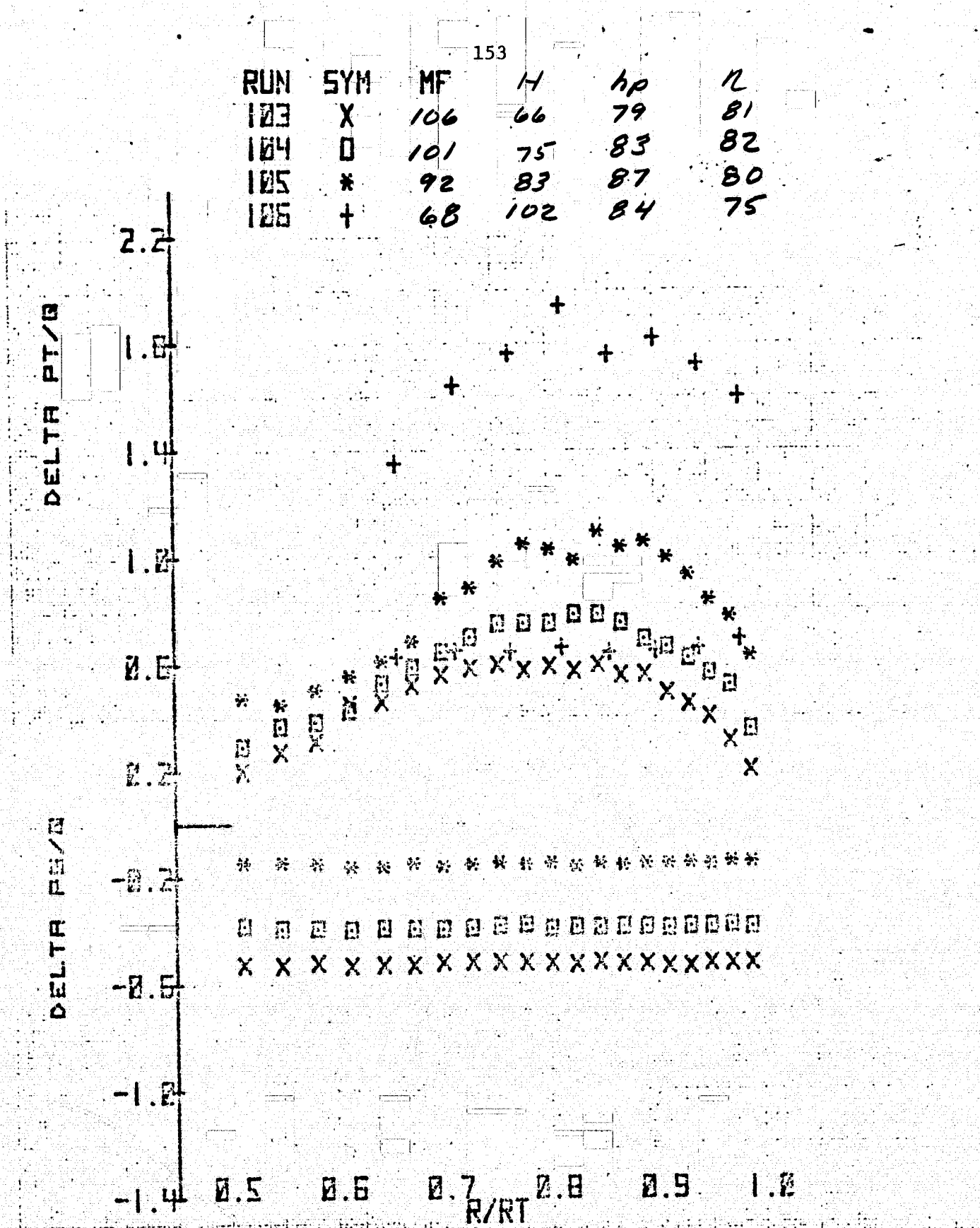

(d) Bottom azimuth.

Figure 23.- Continued.

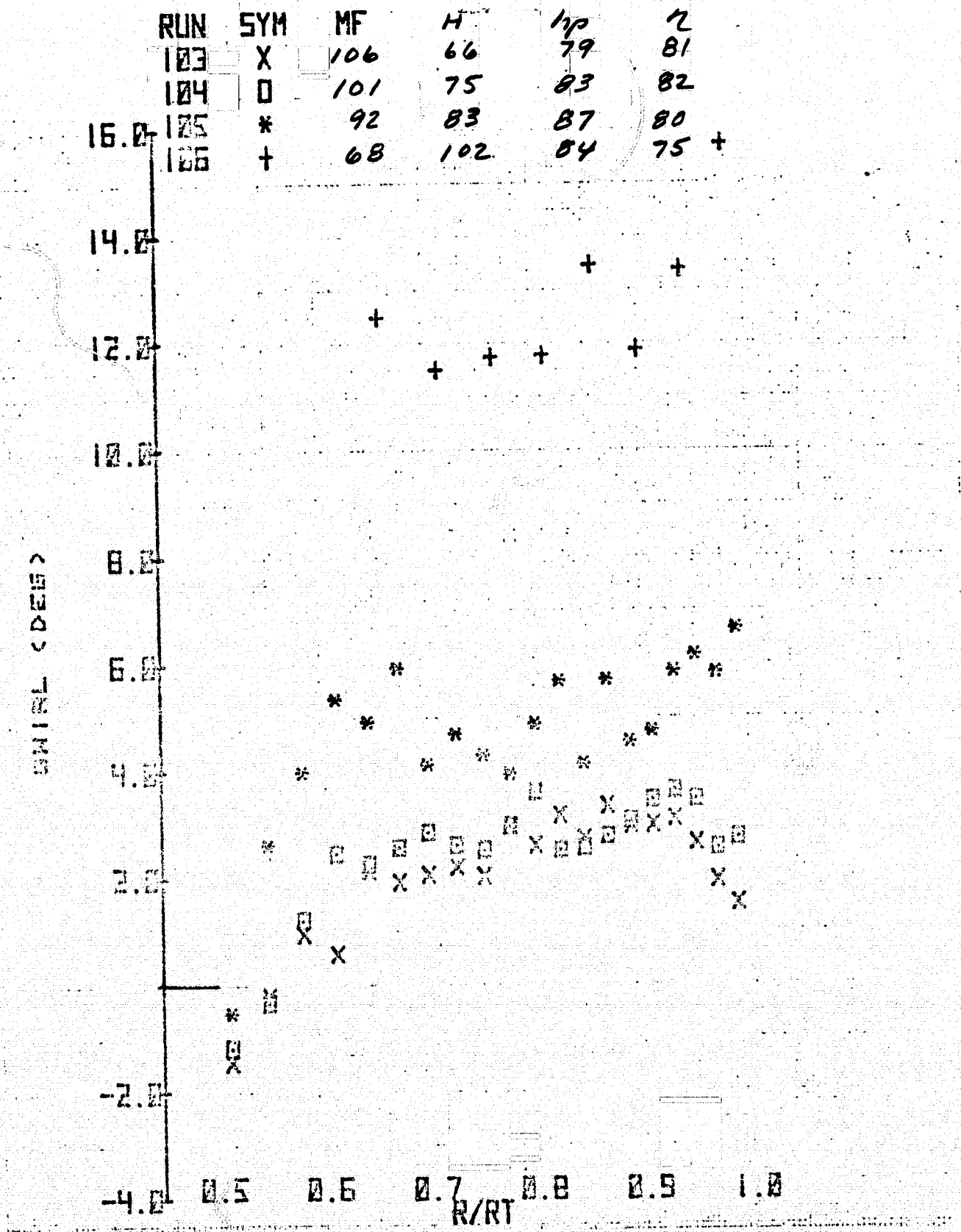

(d) Bottom azimuth - concluded.

Figure 23.- Concluded.

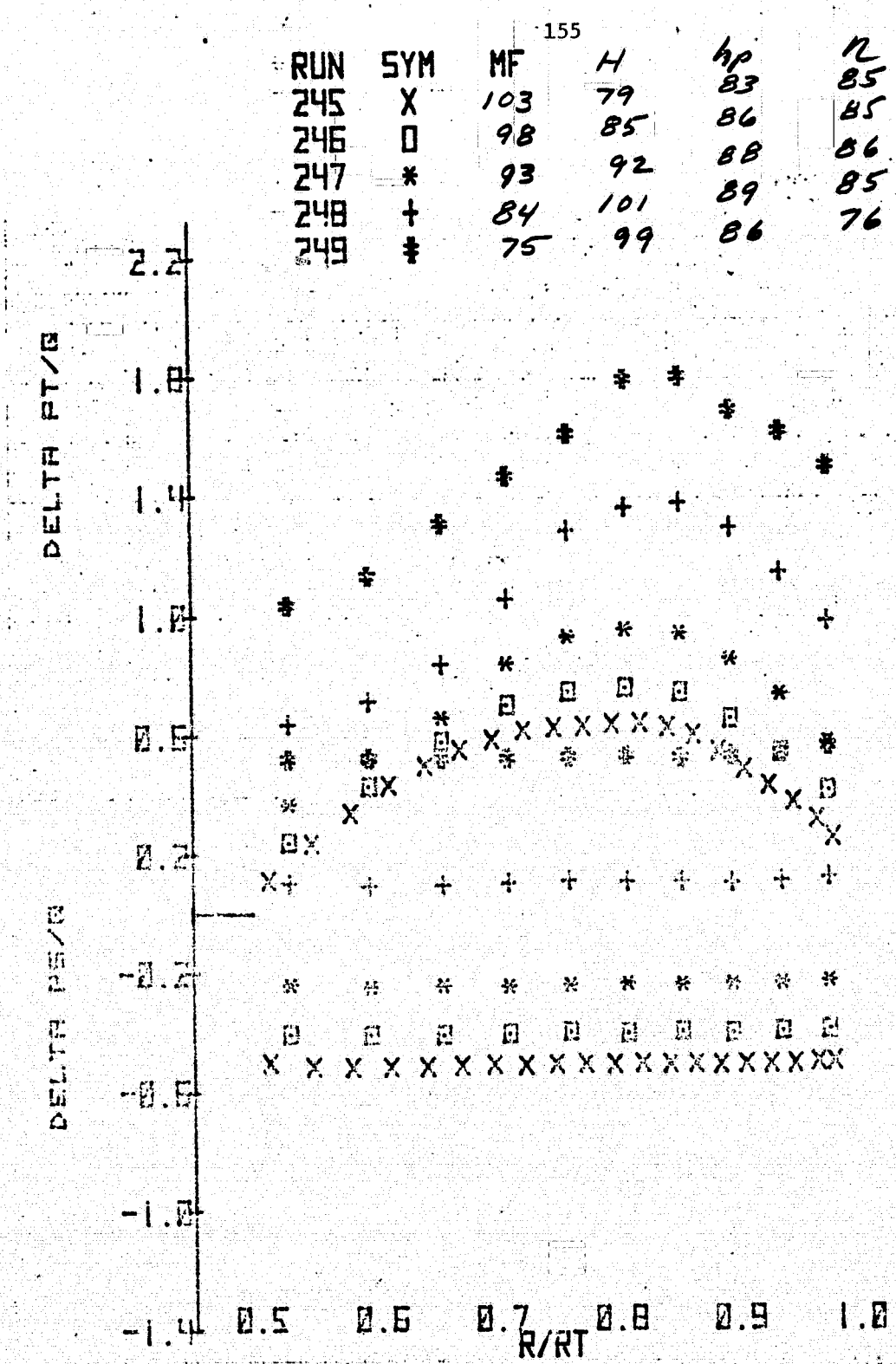

Exit doors on.
(a) Port azimuth.

Figure 24.- Radial variation of total pressure coefficient, static pressure coefficient and swirl angle downstream of stators for several azimuths and mass flows: inlet honeycomb in, original contraction, exit doors on and off, N = 100%, and ξ = 40.8°.

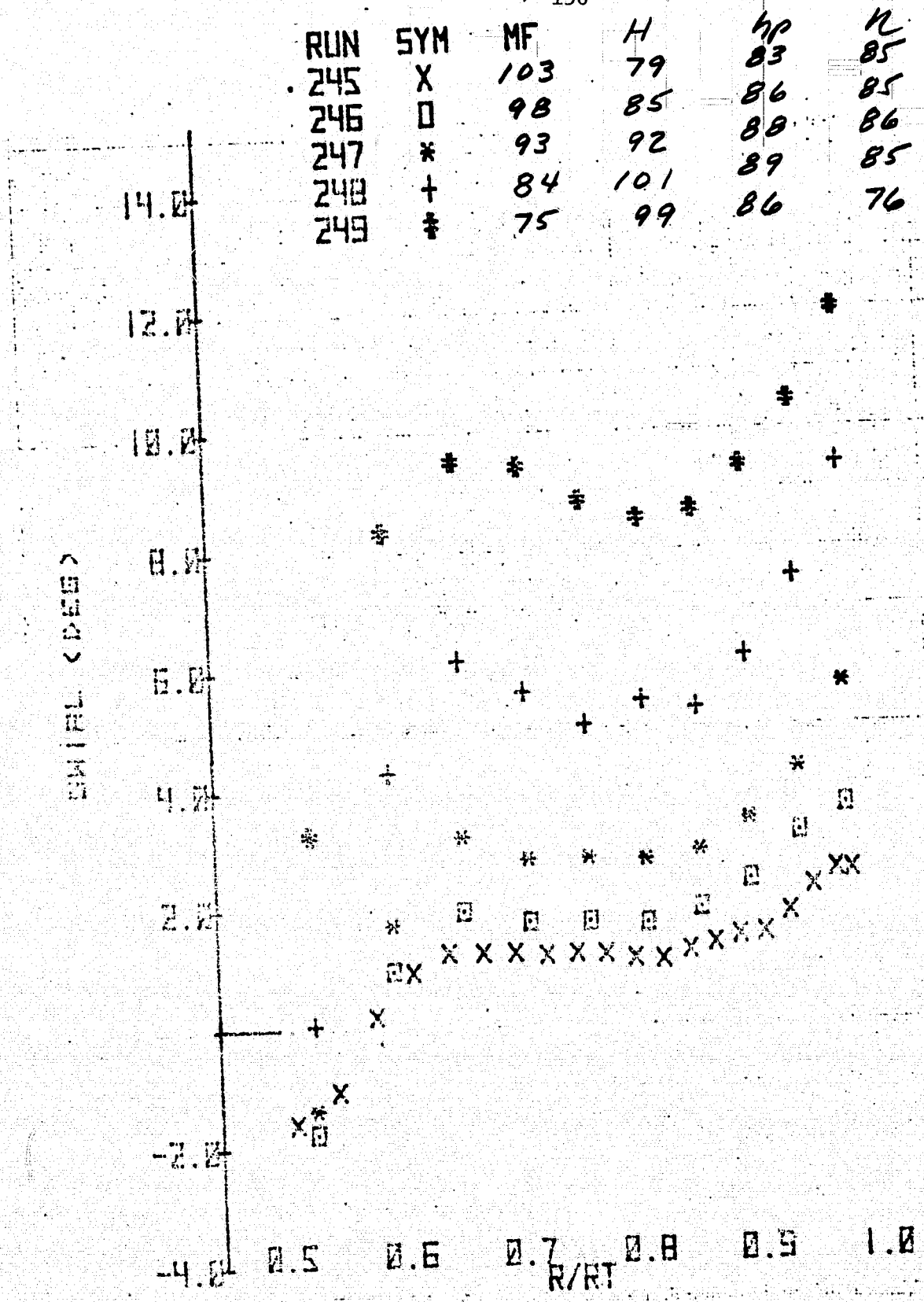

Exit doors on.
(a) Port azimuth - continued.

Figure 24.- Continued.

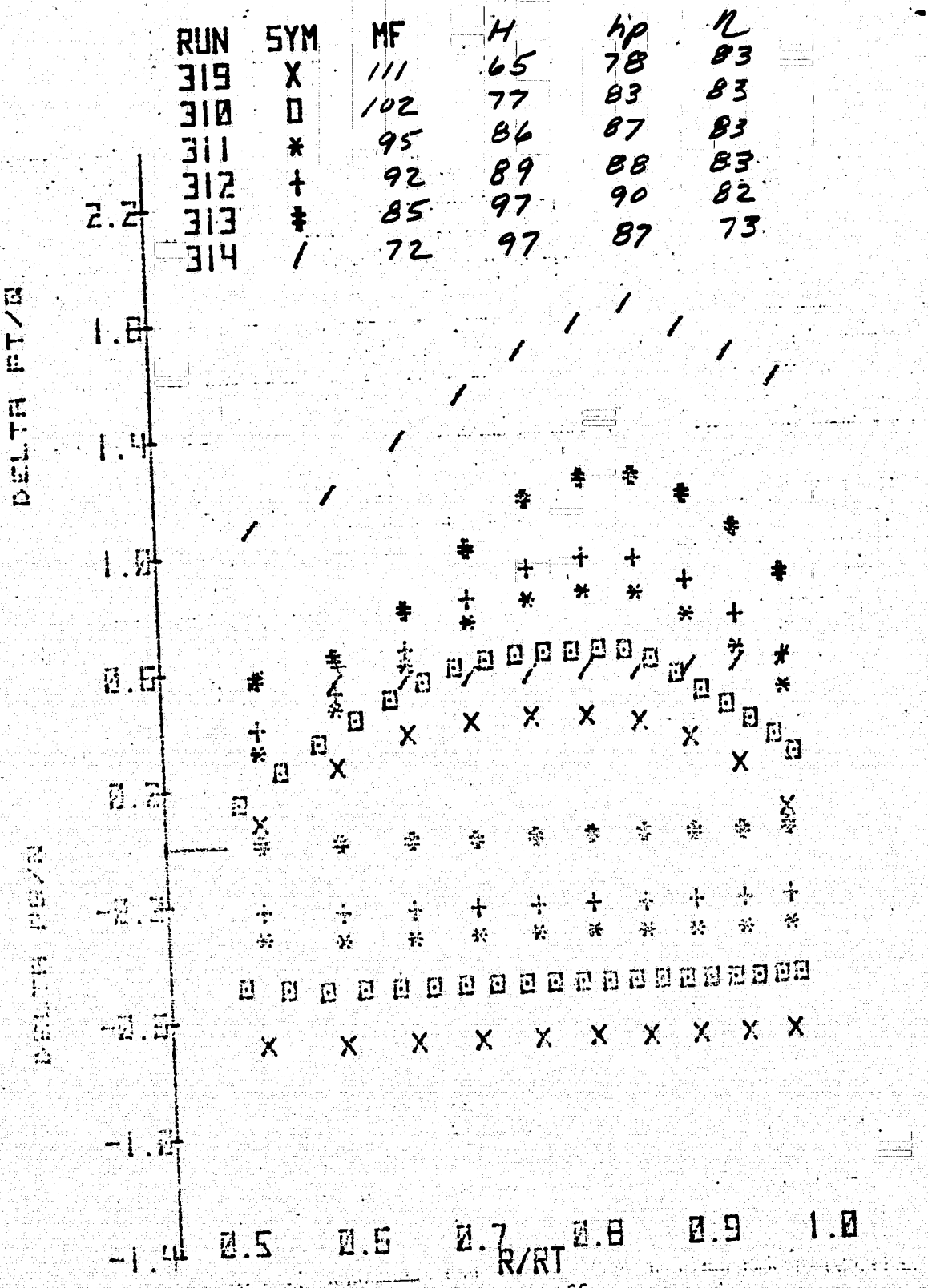

Exit doors off.

(a) Port azimuth - continued.

Figure 24.- Continued.

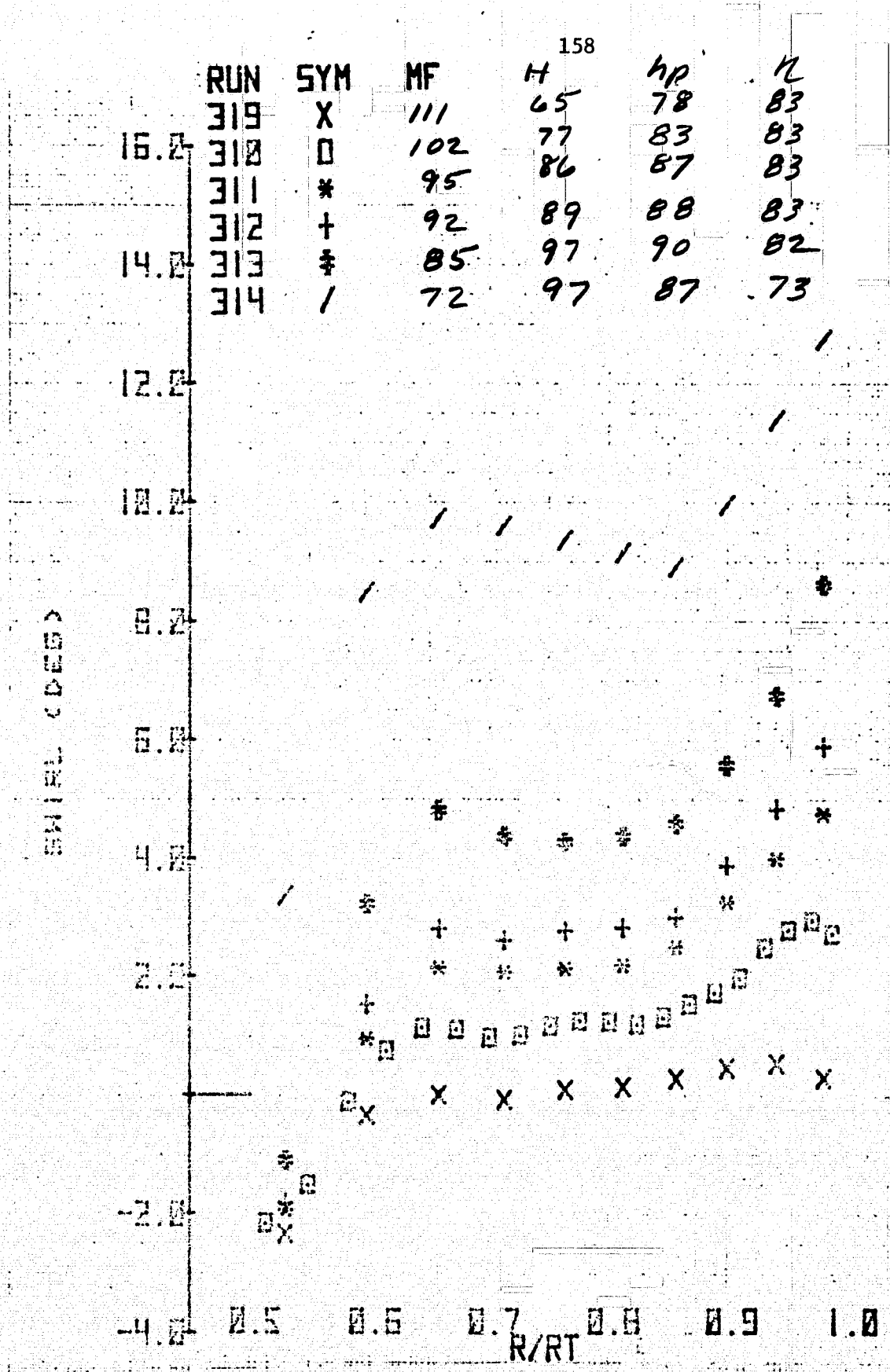

Exit doors off.
(a) Port azimuth - continued.

Figure 24.- Continued.

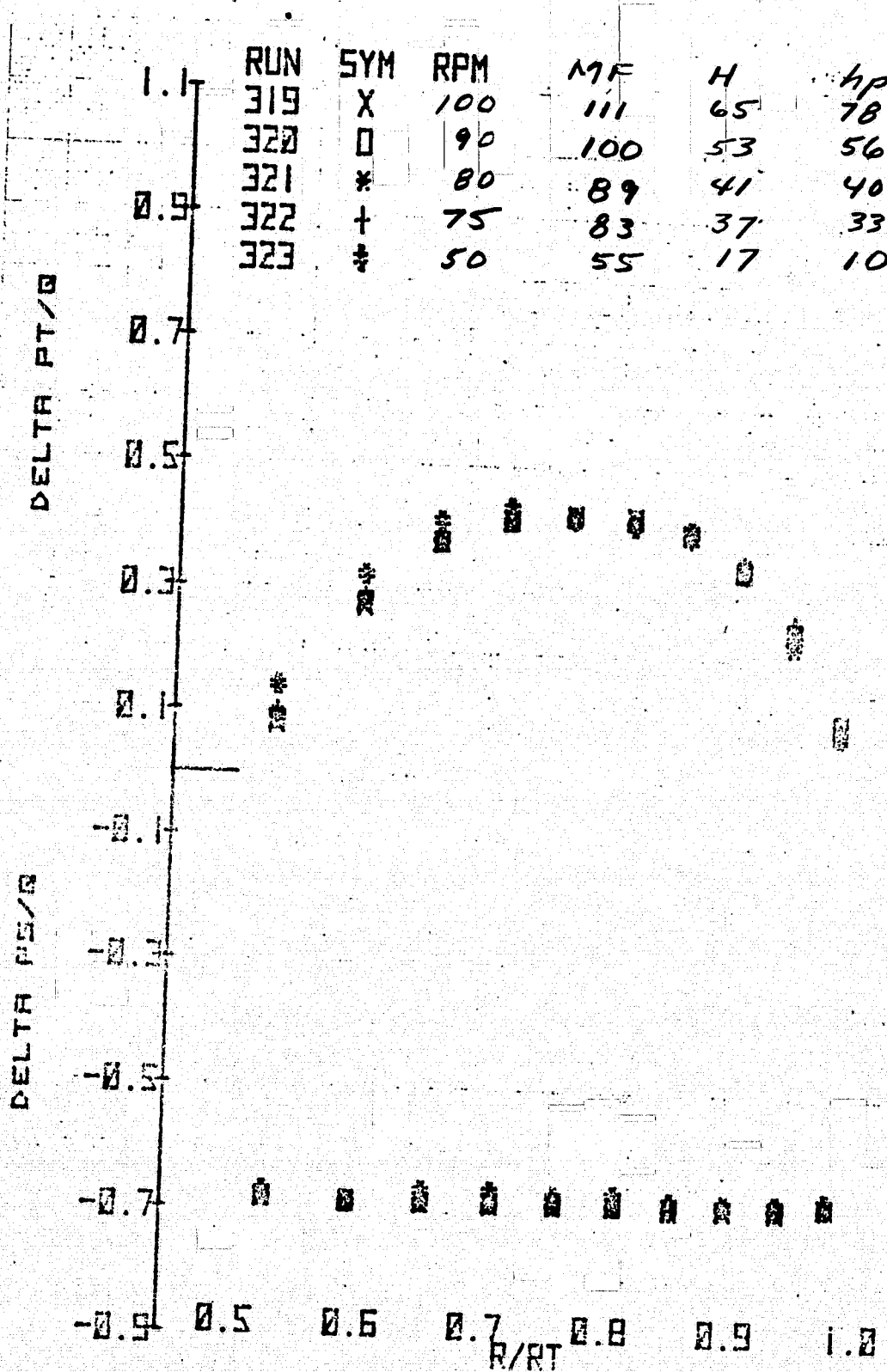

Exit doors off, 110% mass flow.
(a) Port azimuth - continued.

Figure 24.- Continued.

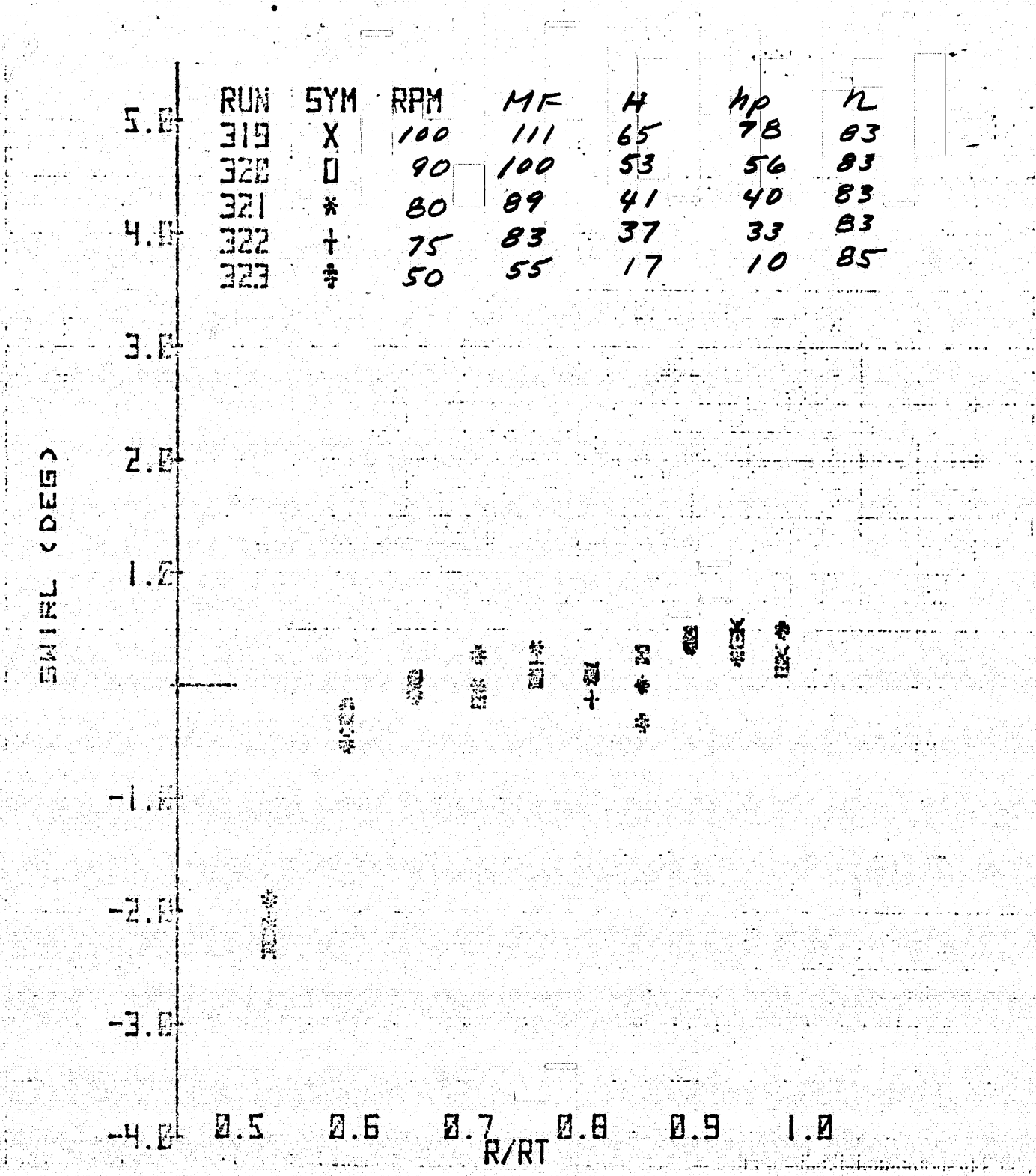

Exit doors off, 110% mass flow.
(a) Port azimuth - concluded.

Figure 24.- Continued.

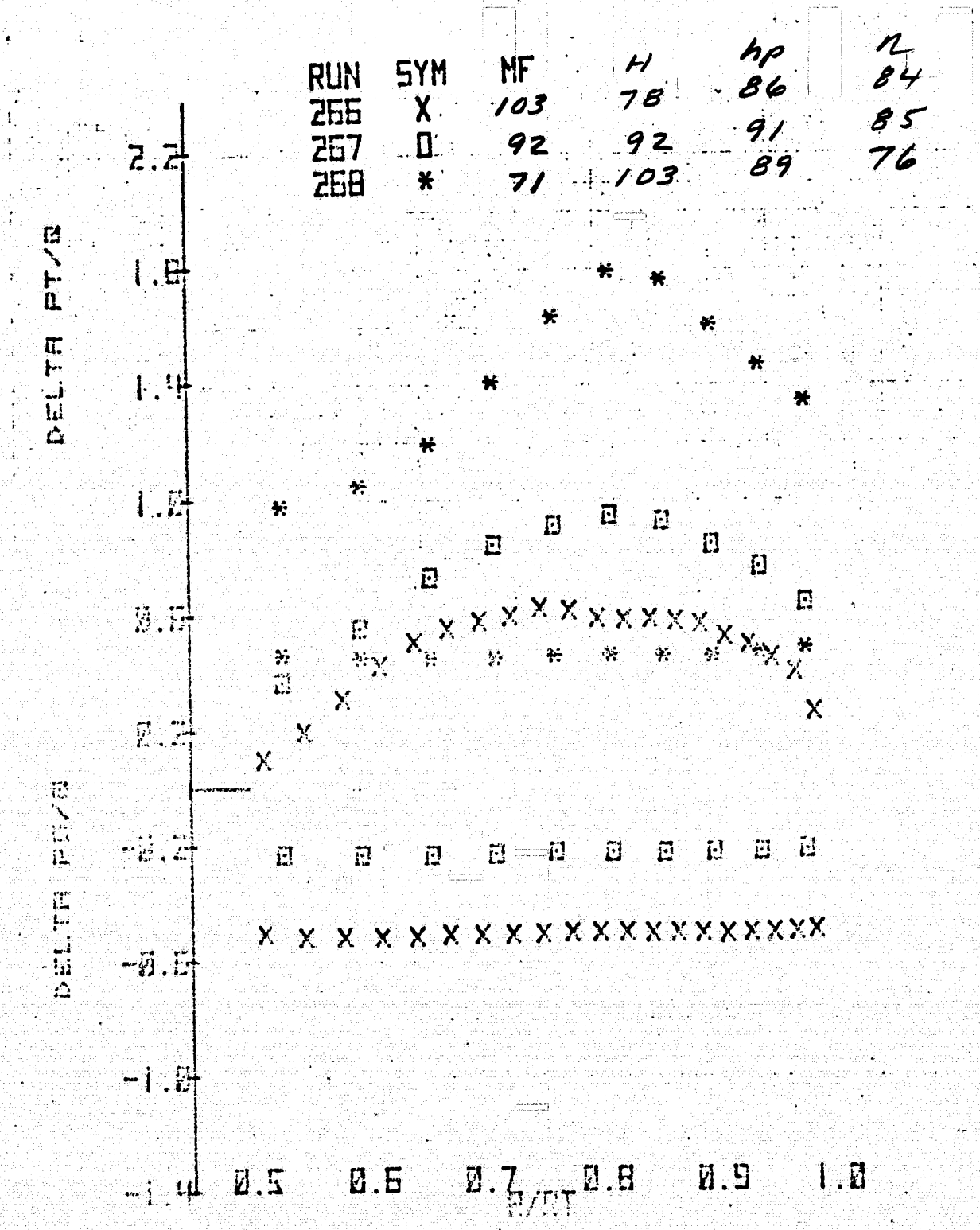

Exit doors on.
(b) Top azimuth.

Figure 24.- Continued.

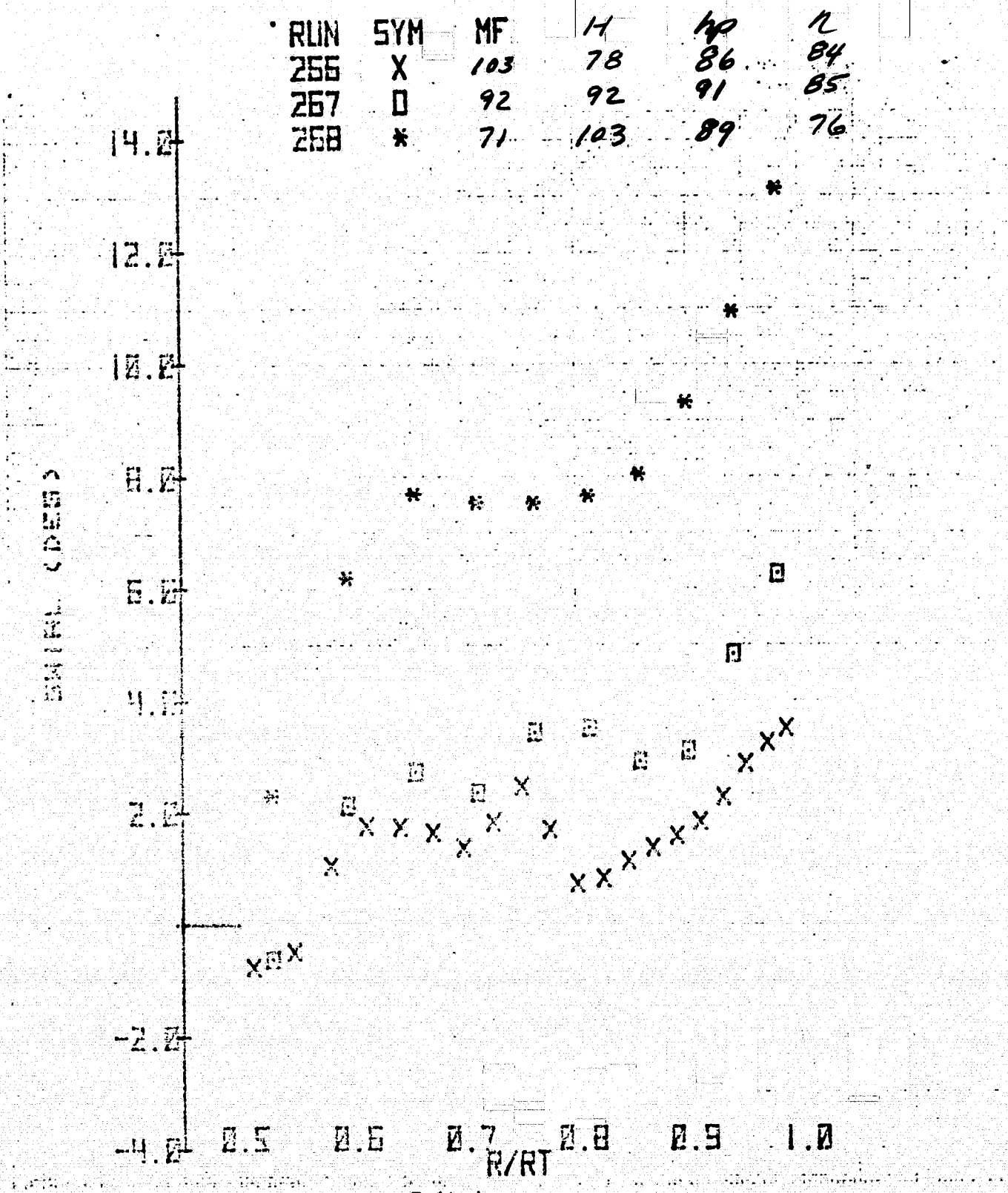

Exit doors on.

(b) Top azimuth - concluded.

Figure 24.- Continued.

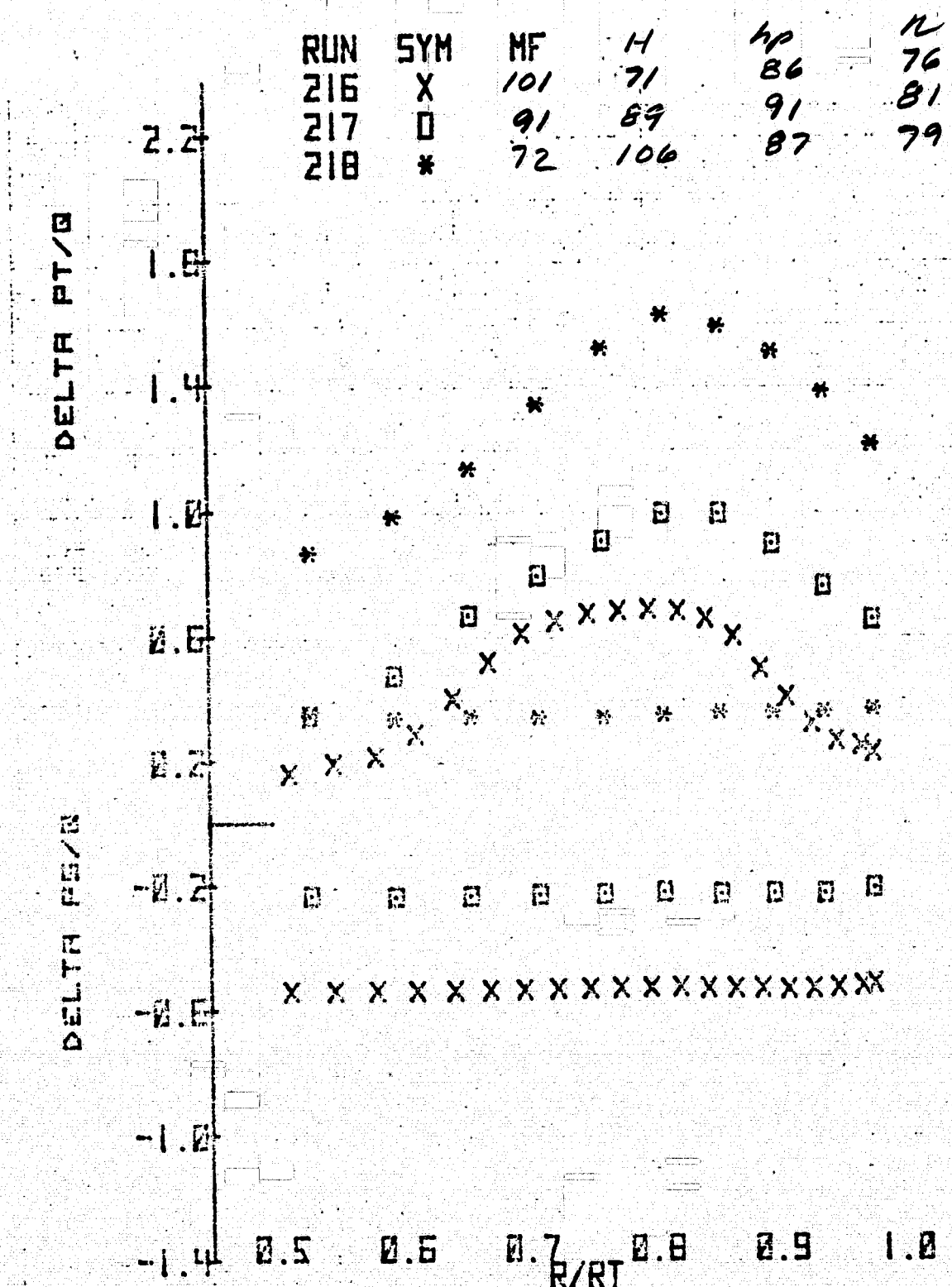

Exit doors on.

(c) Starboard azimuth.

Figure 24.- Continued.

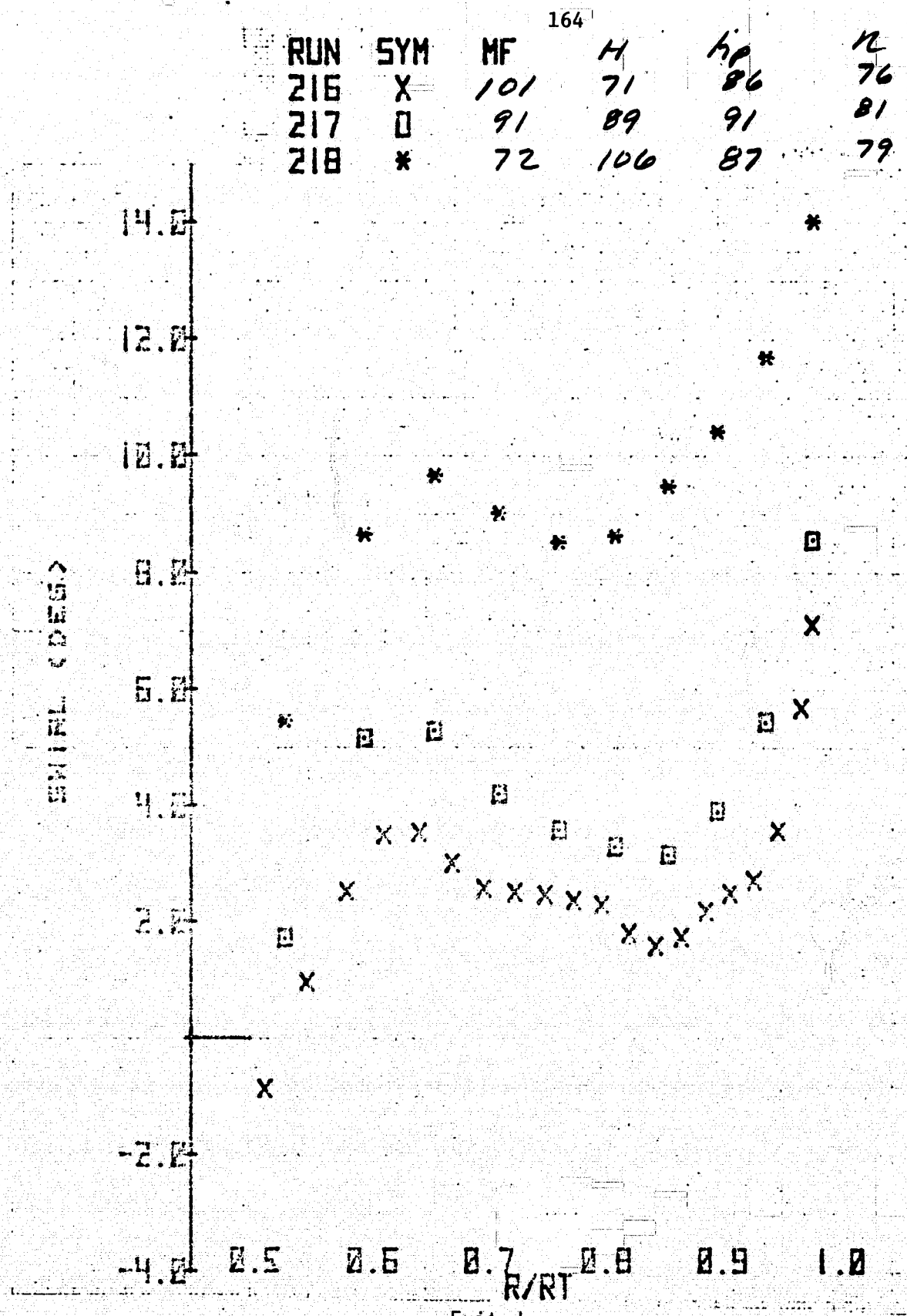

Exit doors on.

(c) Starboard azimuth - concluded.

Figure 24.- Continued.

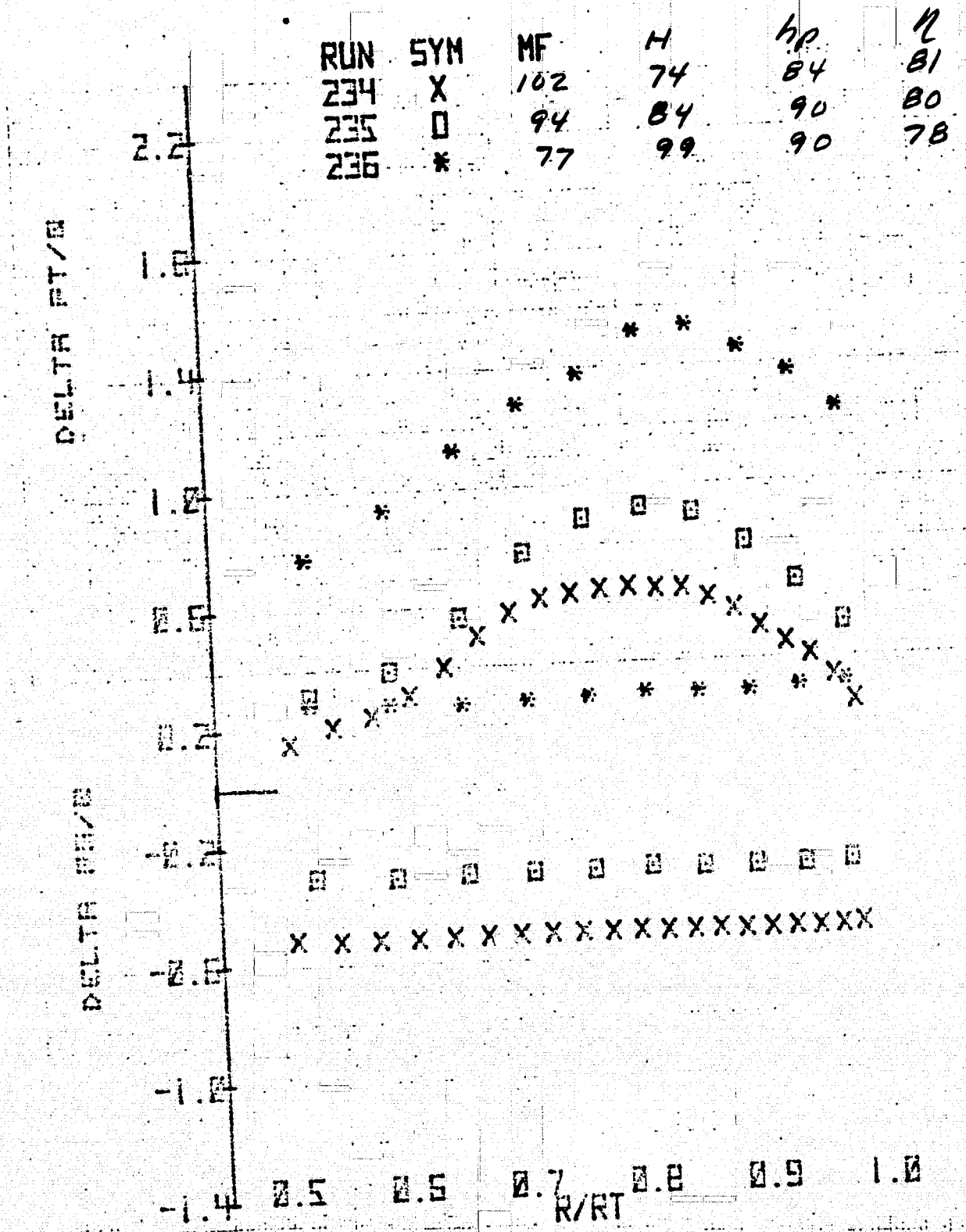

Exit doors on.

(d) Bottom azimuth.

Figure 24.- Continued.

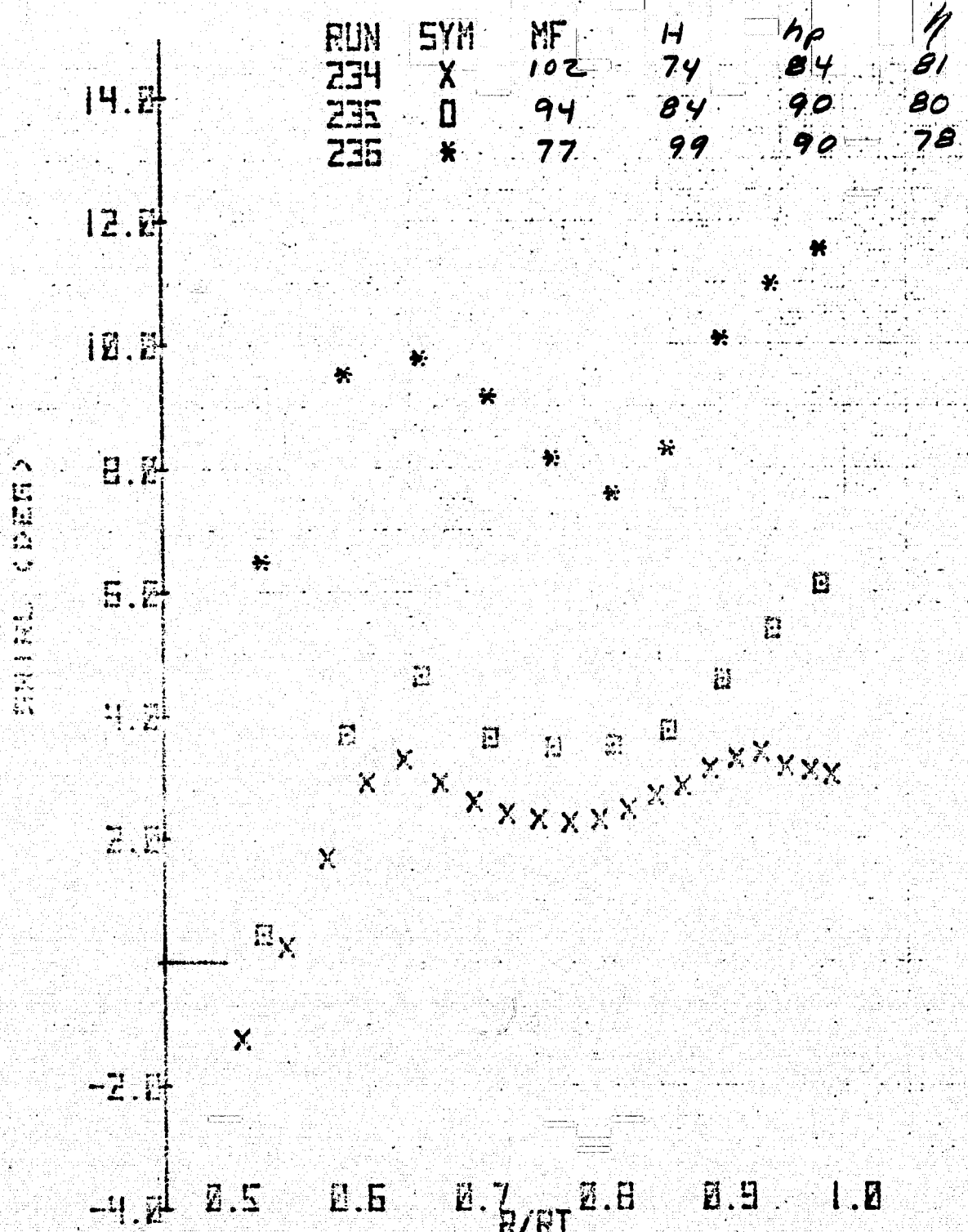

Exit doors on.

(d) Bottom azimuth - concluded.

Figure 24.- Concluded.

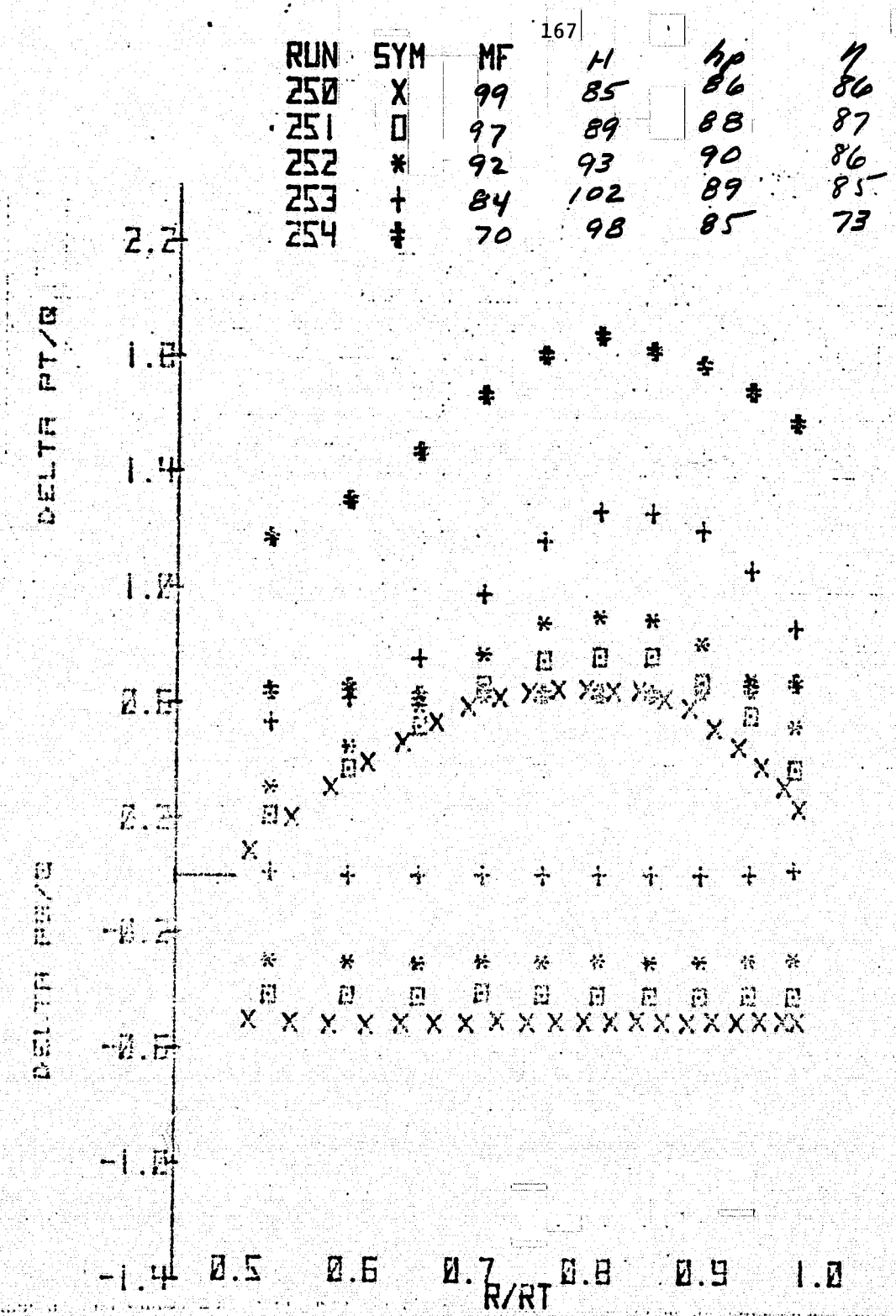

(a) Port azimuth.

Figure 25.- Radial variation of total pressure coefficient, static pressure coefficient and swirl angle downstream of stators for several azimuths and mass flows; "H" inflow configuration, inlet honeycomb, original contraction, N = 100%, and ξ = 40.8°.

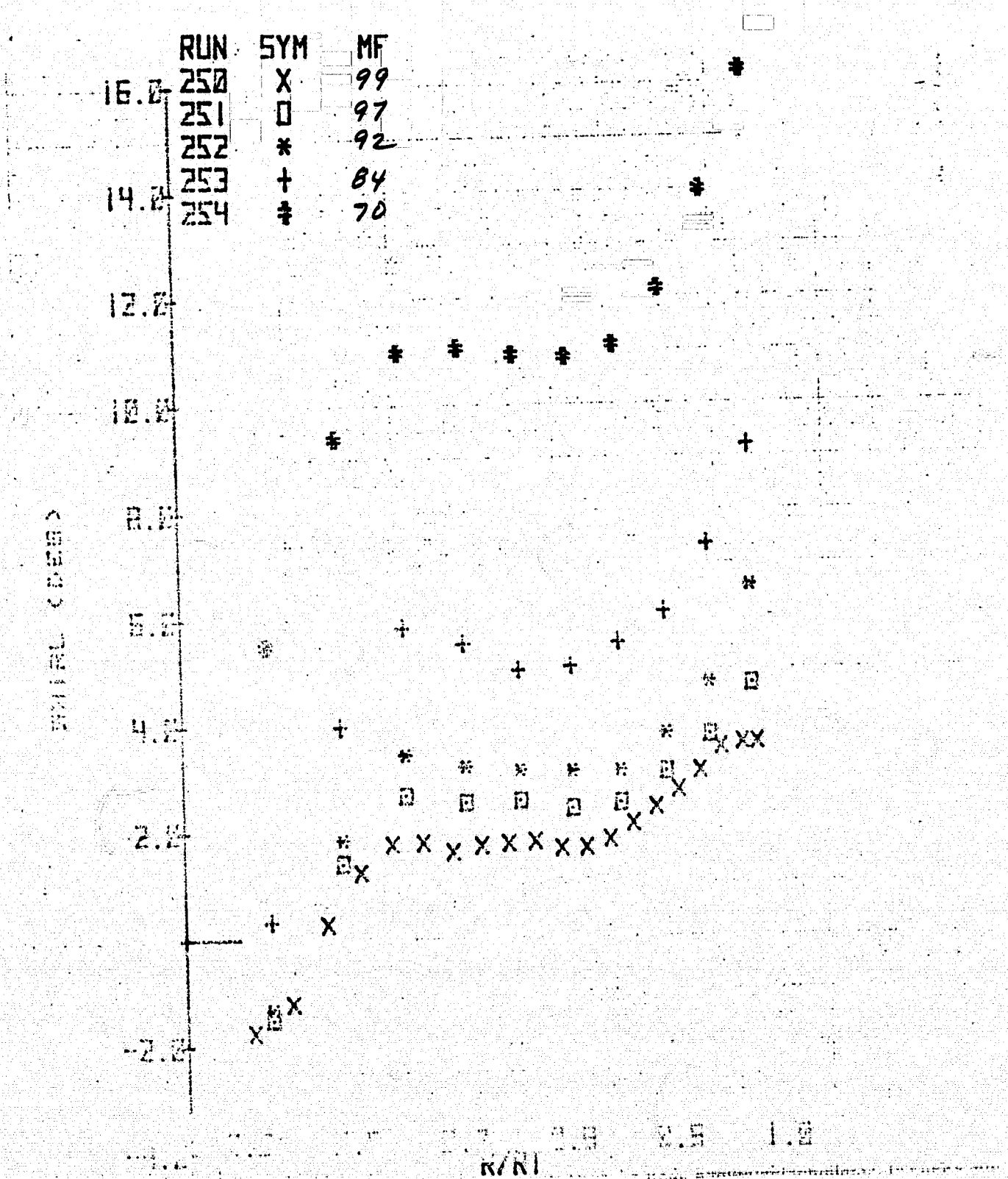

(a) Port azimuth - concluded.

Figure 25.- Continued.

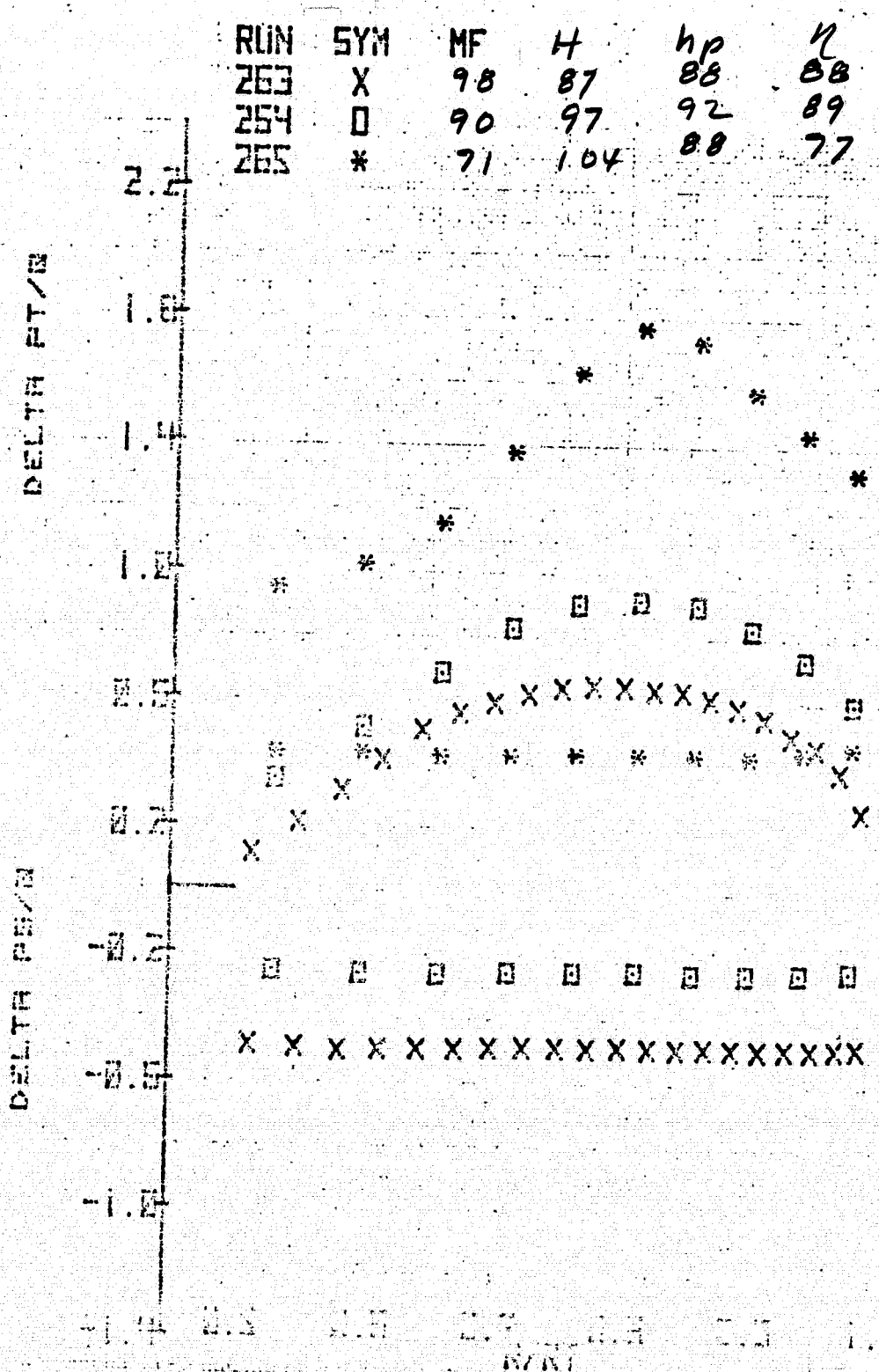

(b) Top azimuth.

Figure 25.- Continued.

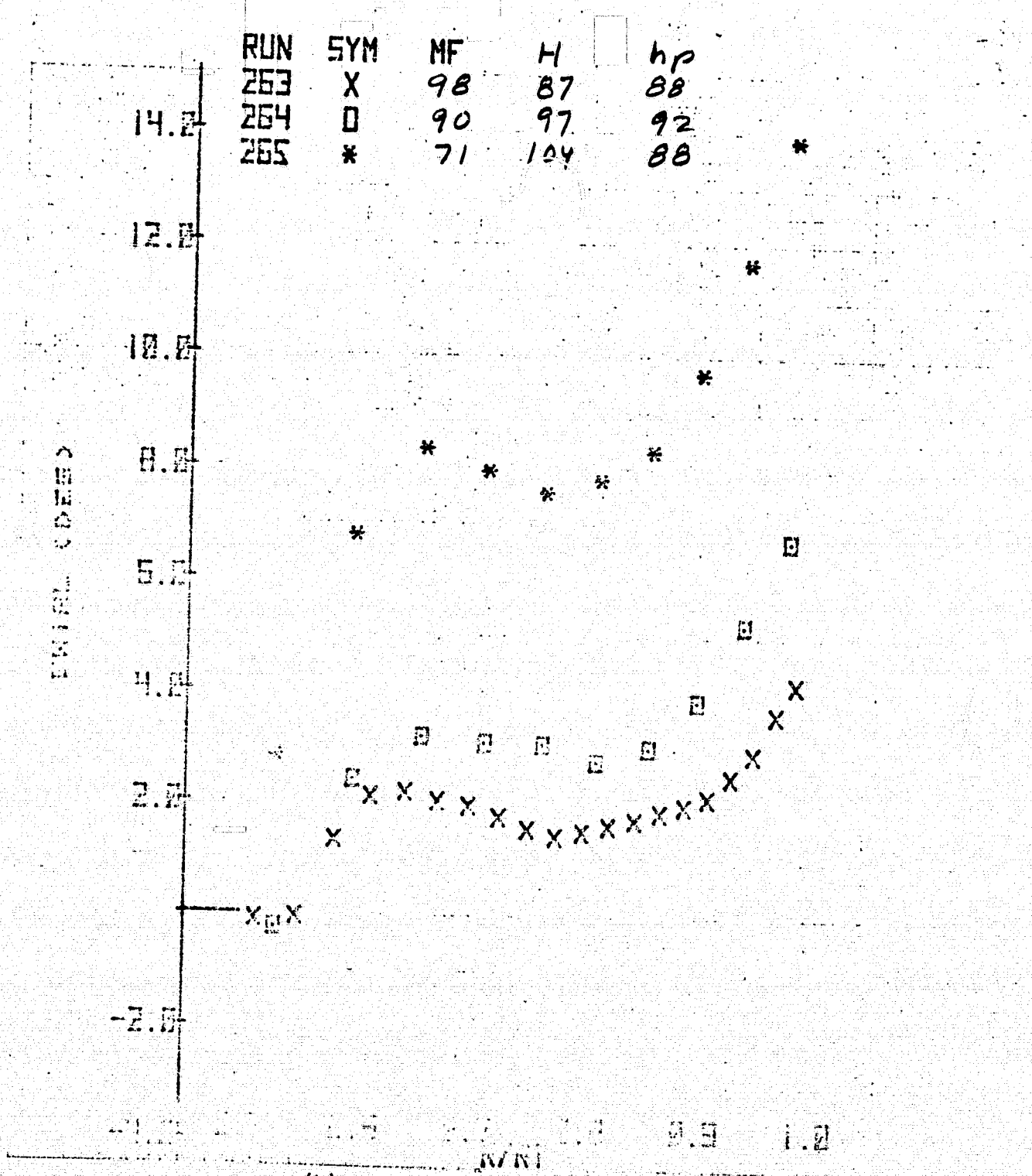

(b) Top azimuth - concluded.

Figure 25.- Continued.

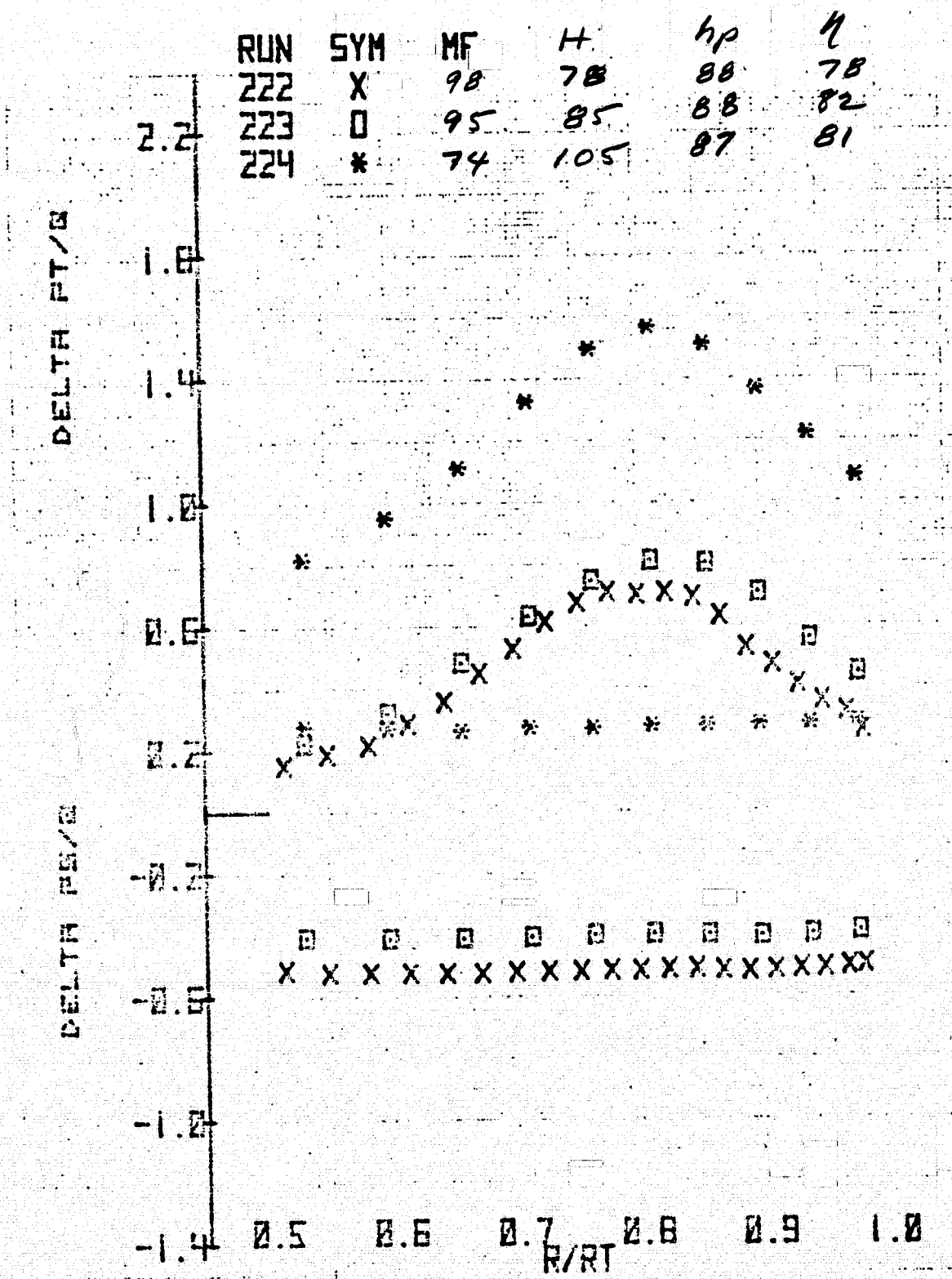

(c) Starboard azimuth.

Figure 25.- Continued.

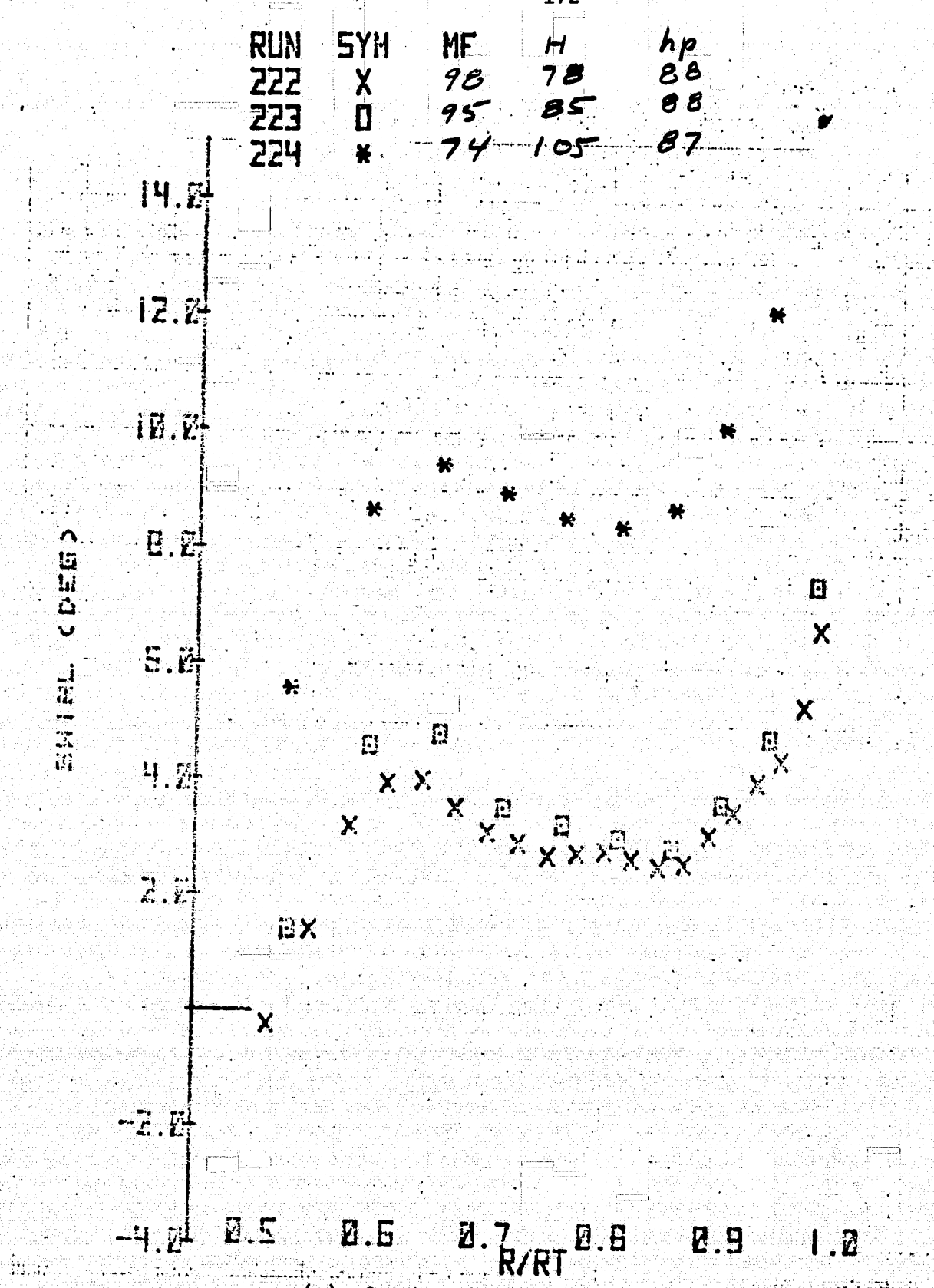

(c) Starboard azimuth - concluded.

Figure 25.- Continued.

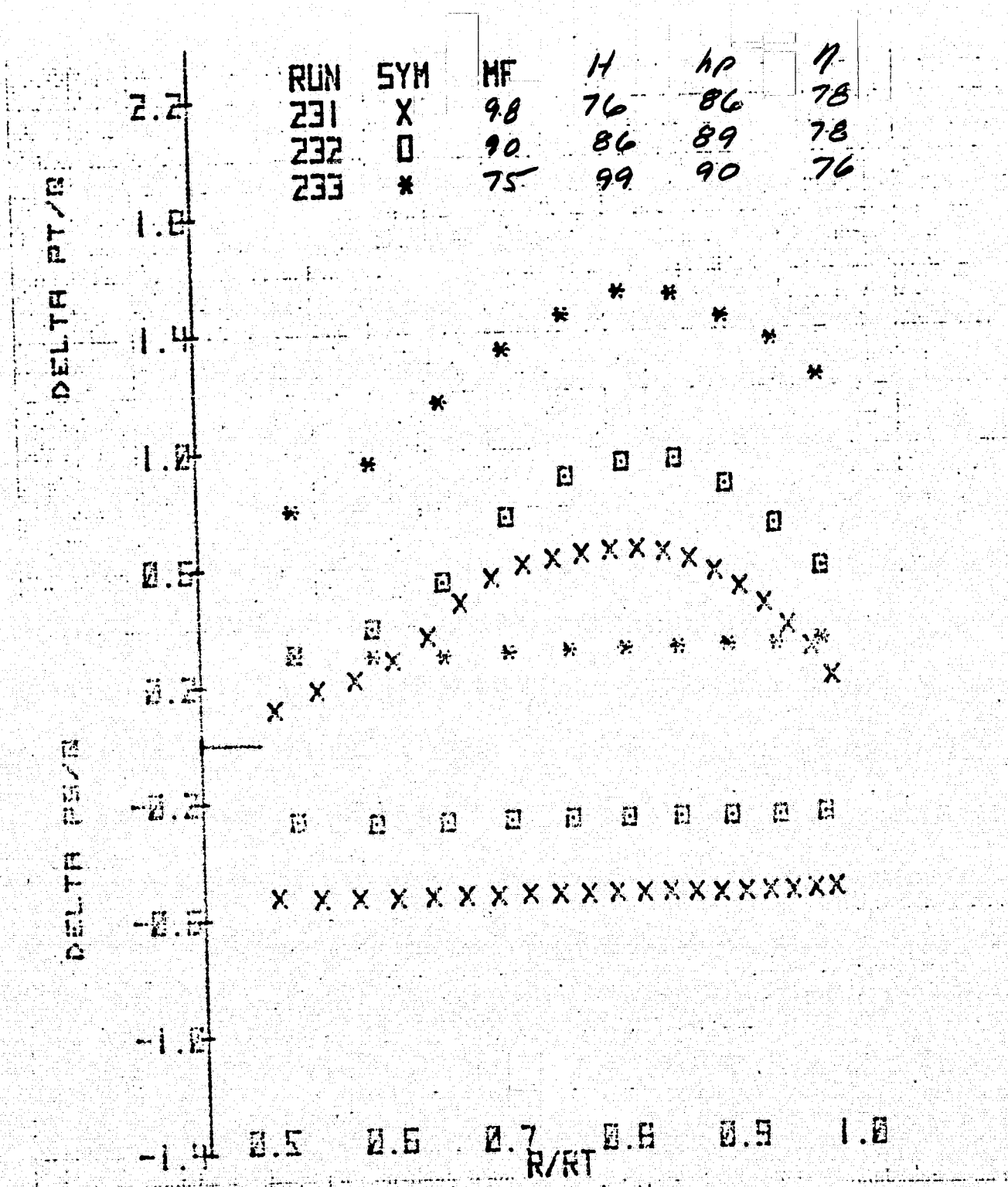

(d) Bottom azimuth.

Figure 25.- Continued.

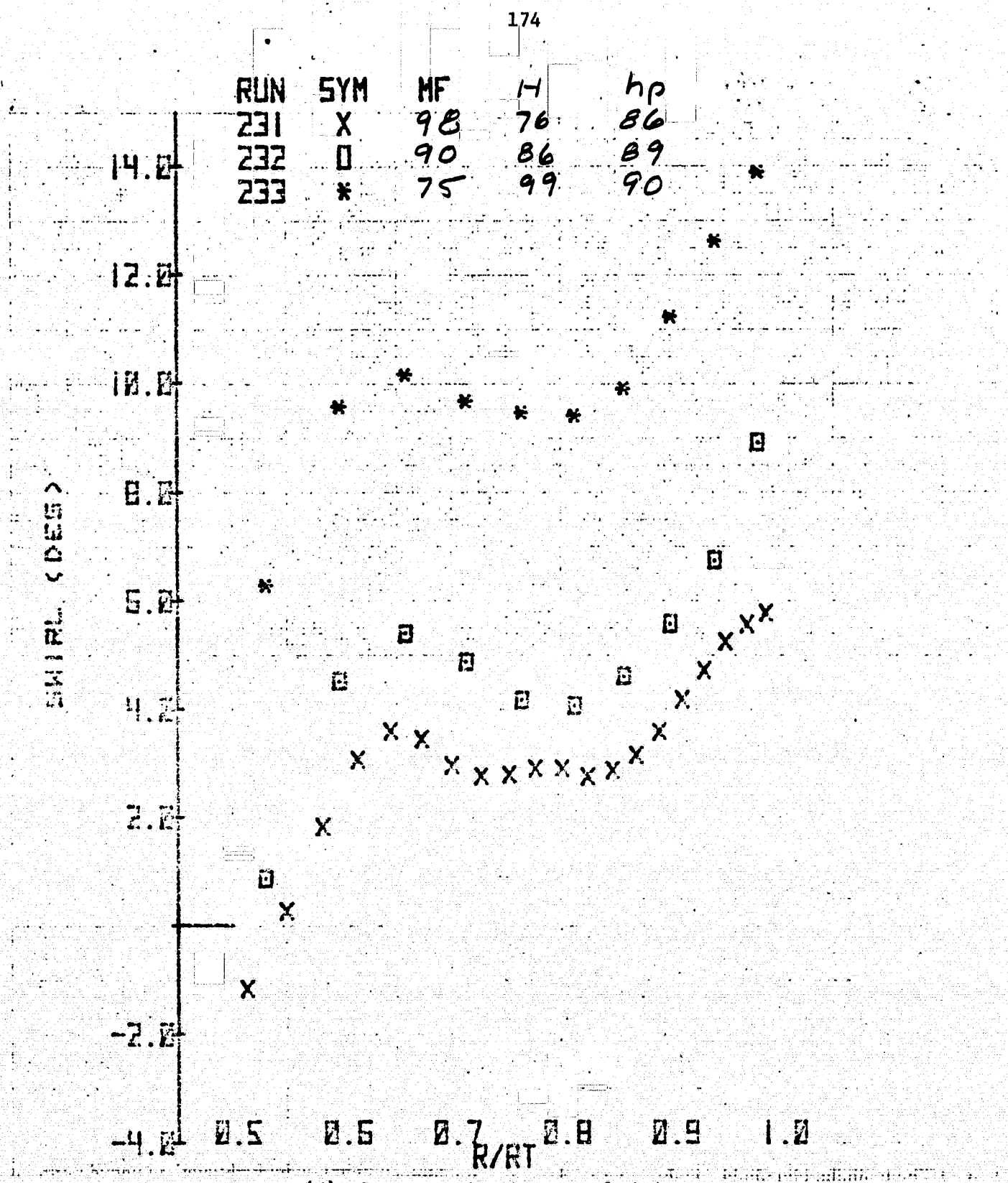

(d) Bottom azimuth - concluded.

Figure 25.- Concluded.

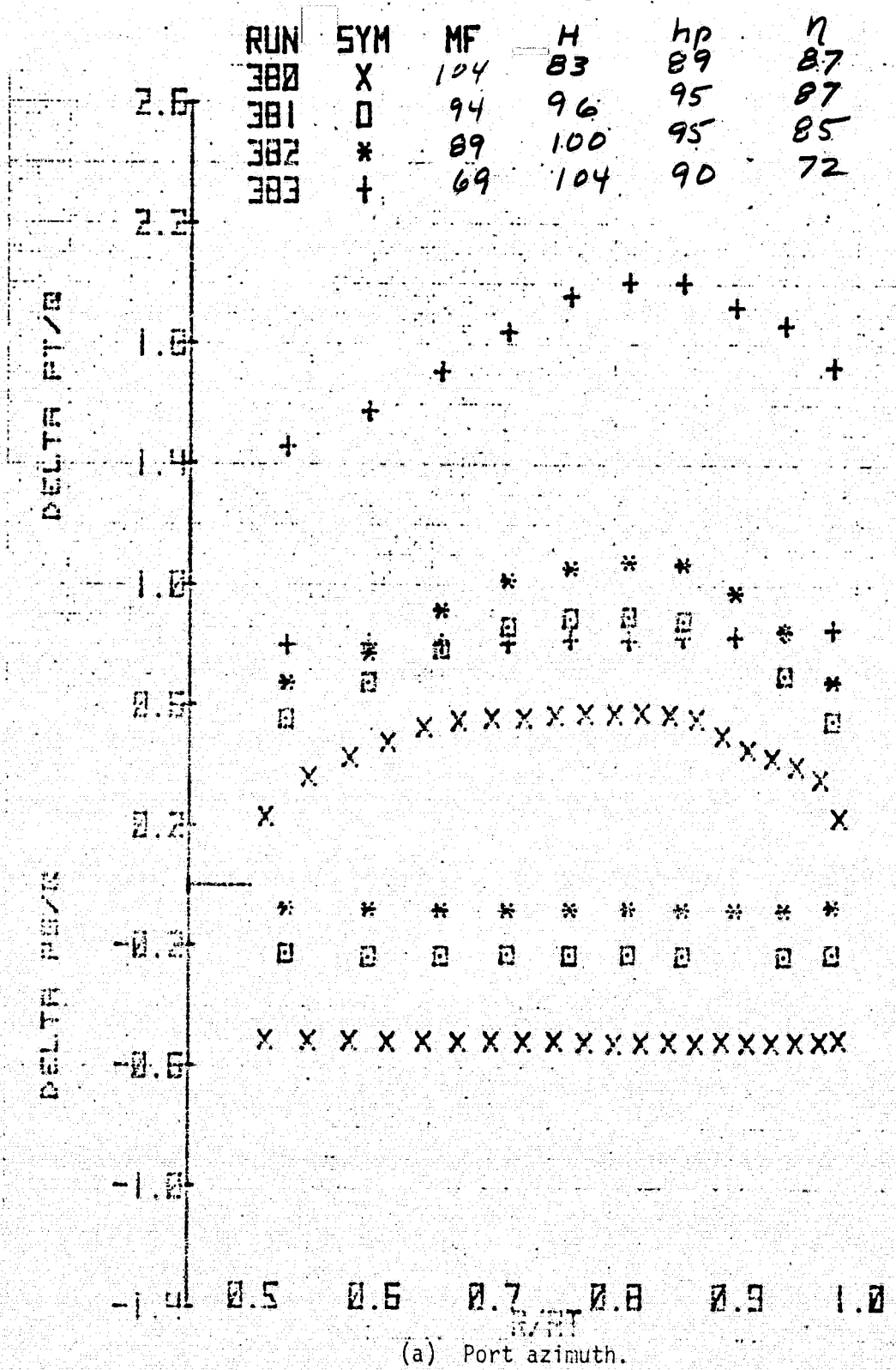

(a) Port azimuth.

Figure 26.- Radial variation of total pressure coefficient, static pressure coefficient, and swirl angle downstream of stators for two azimuths and several mass flows; N = 100%, and ξ = 40.8°.

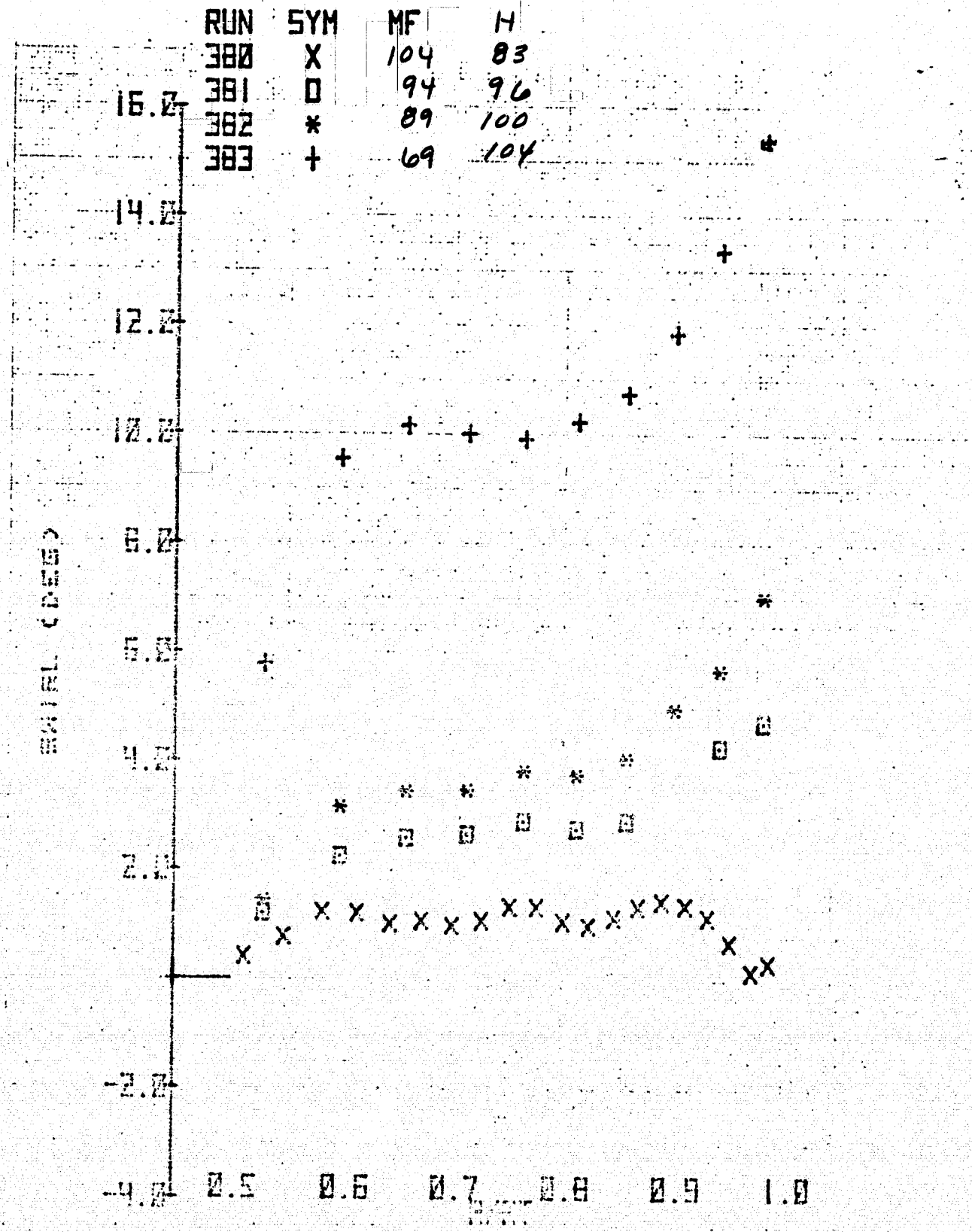

(a) Port azimuth - concluded.

Figure 26.- Continued.

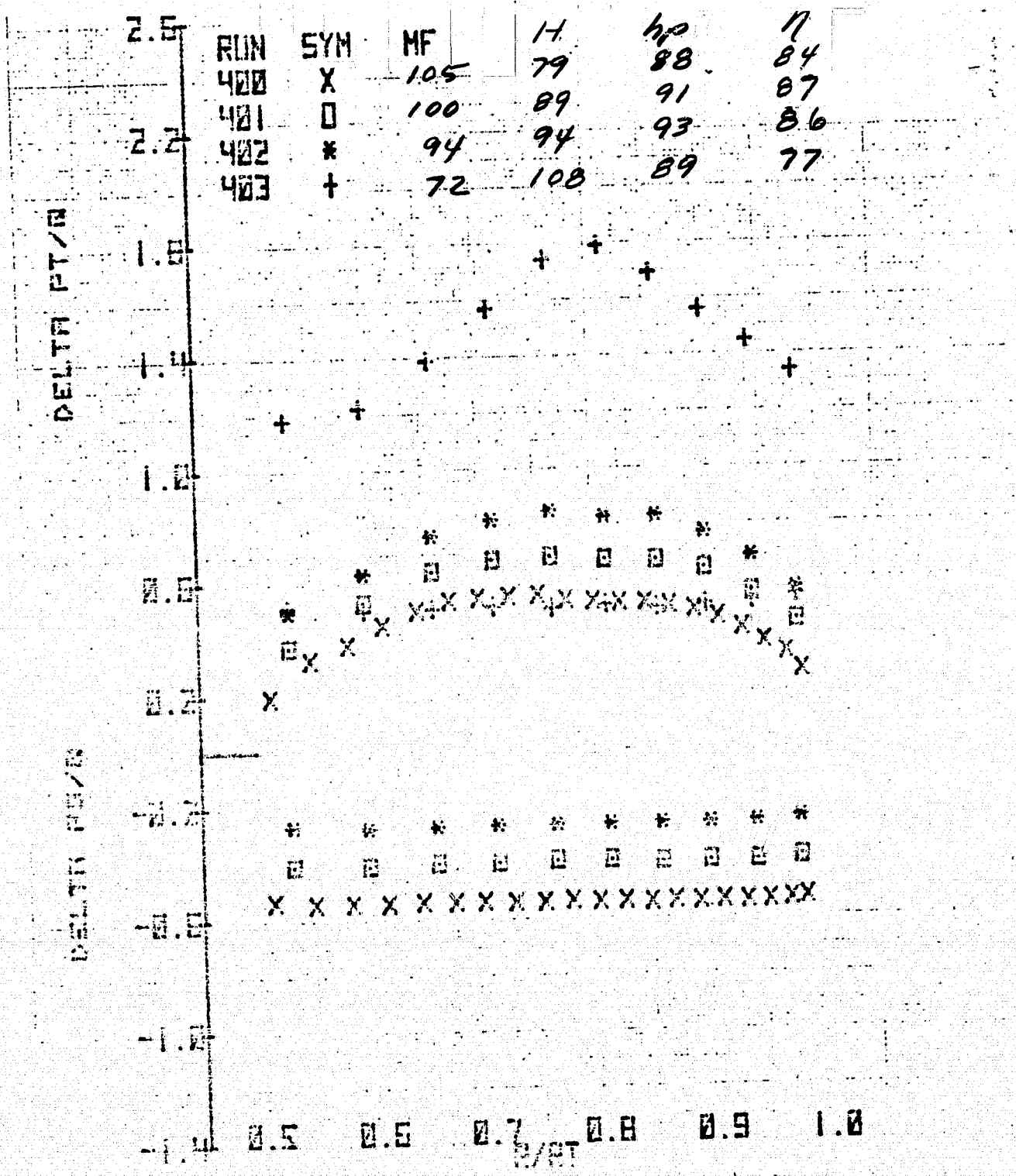

(b) Top azimuth.

Figure 26.- Continued.

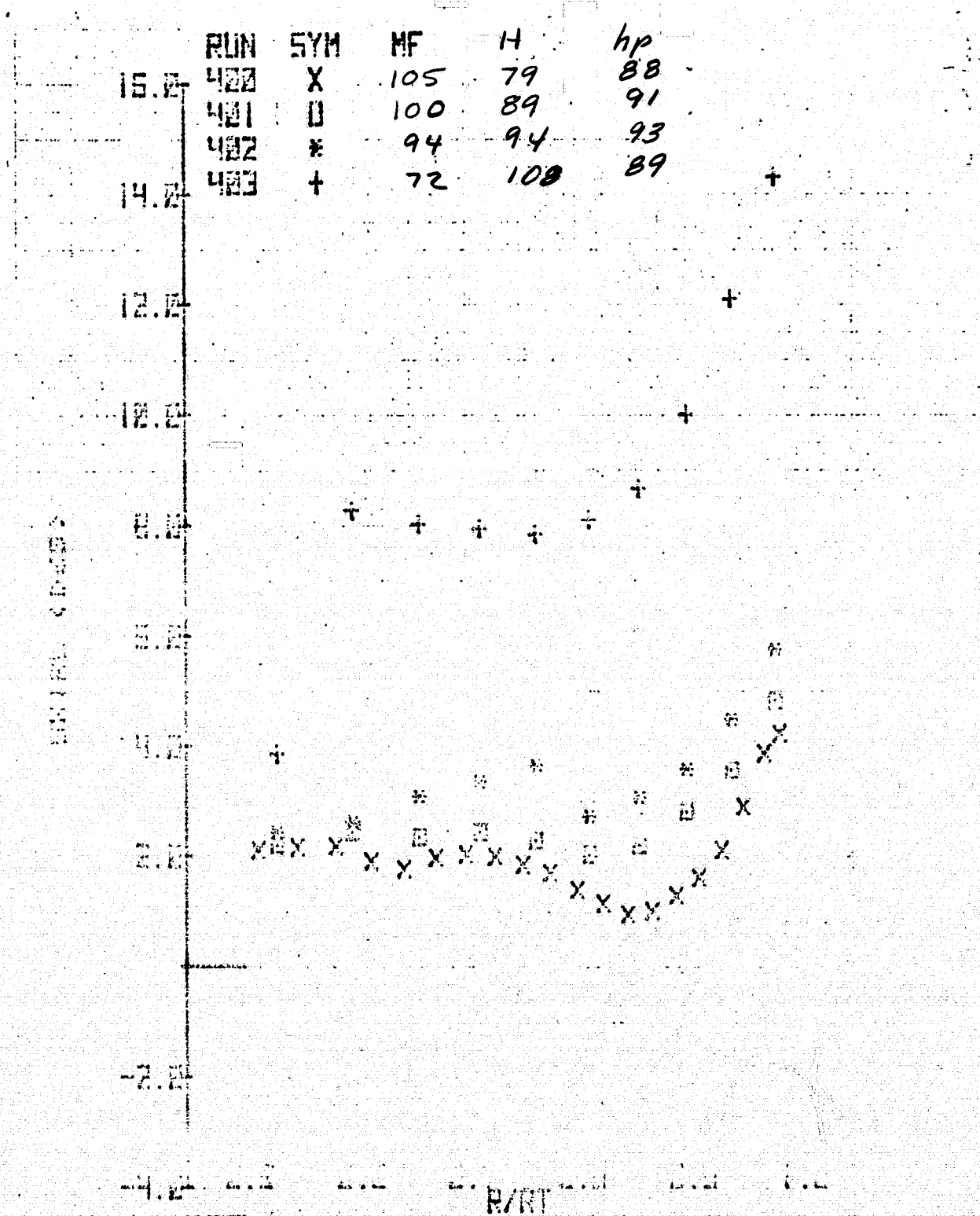

(b) Top azimuth - concluded.

Figure 26.- Concluded.

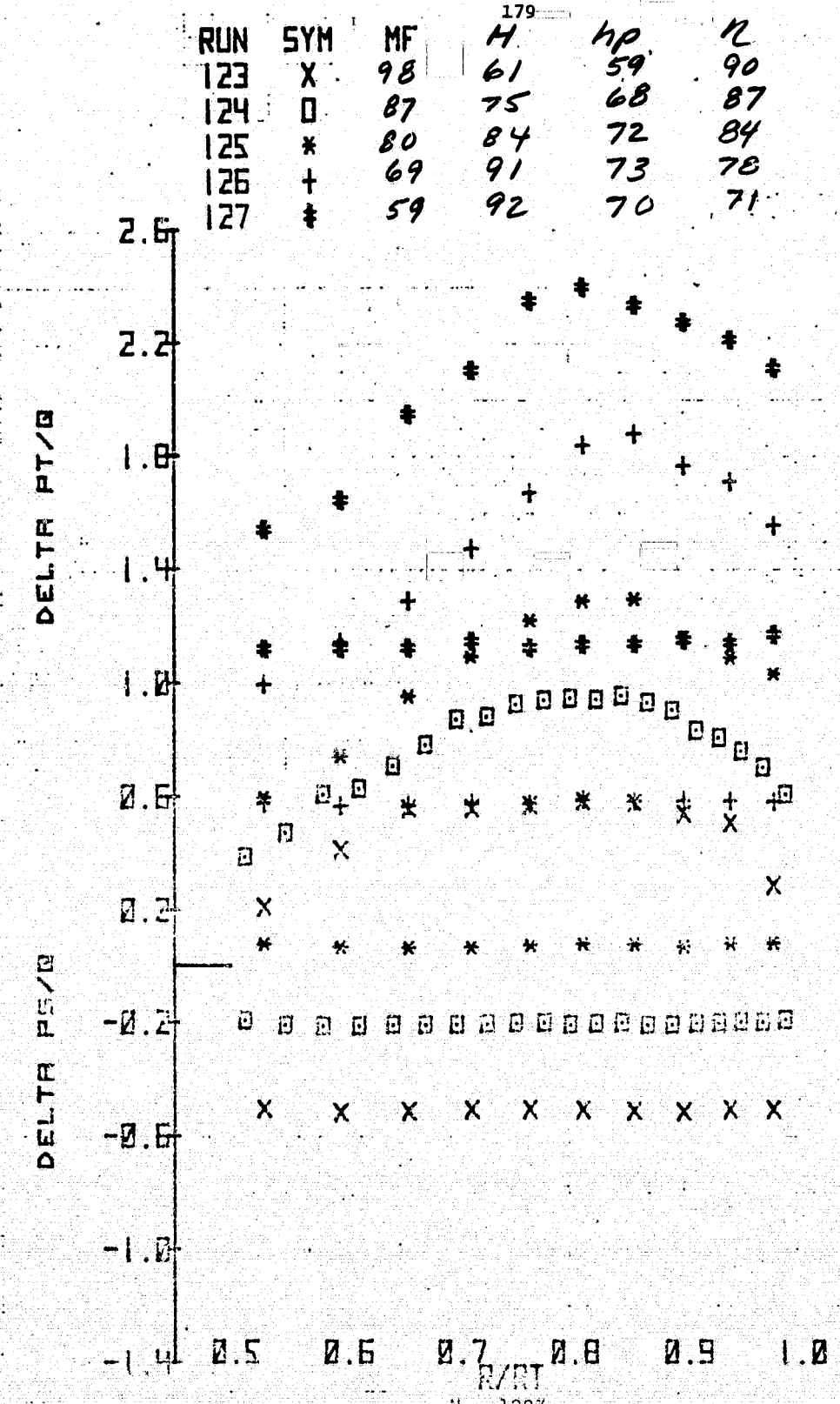

(a) Port azimuth.

Figure 27.- Radial variation of total pressure coefficient, static pressure coefficient, and swirl angle downstream of stators for several azimuths and mass flows; exit honeycomb out, original contraction, and $\xi = 45.2°$.

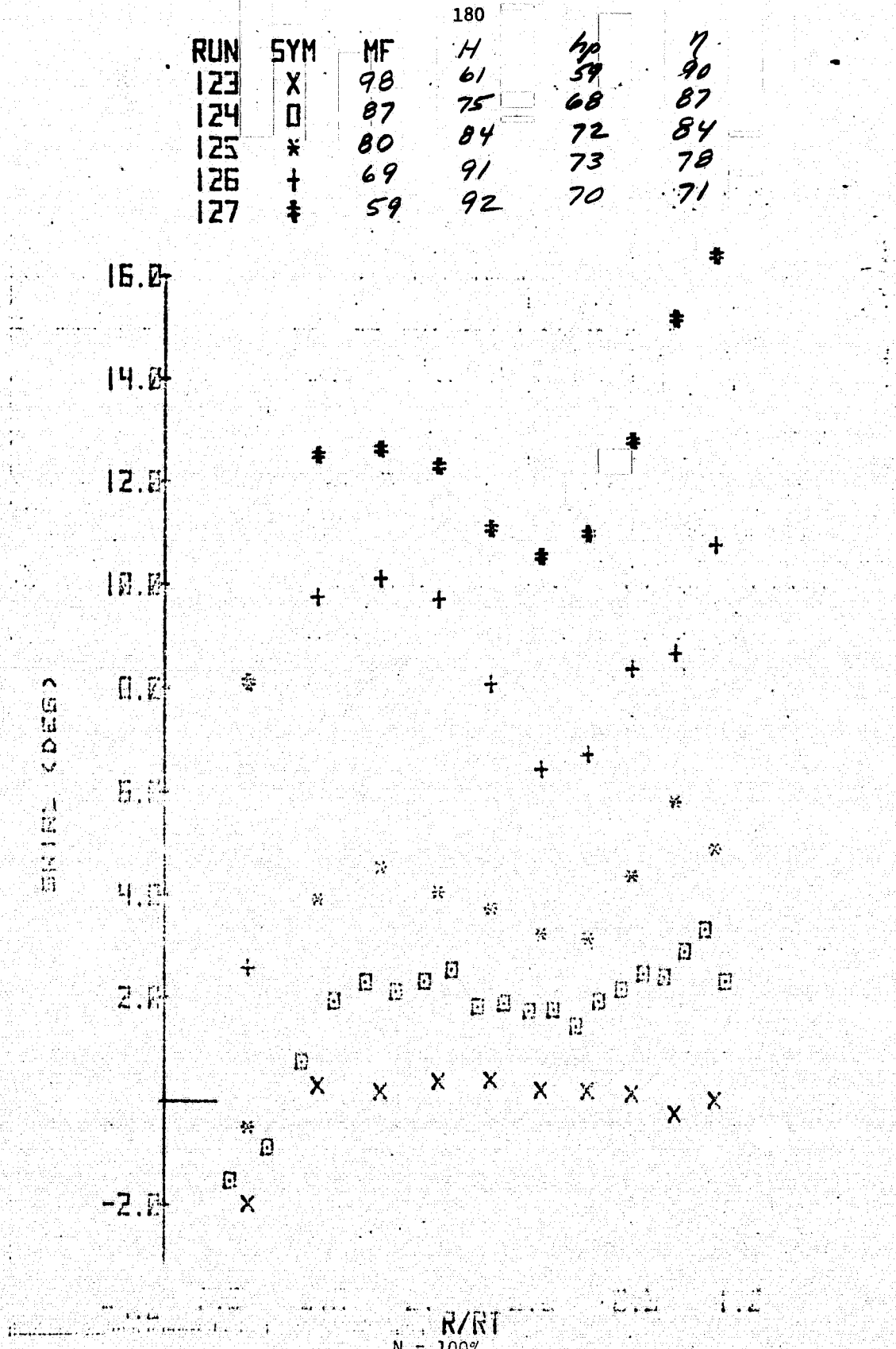

(a) Port azimuth - continued.

Figure 27.- Continued.

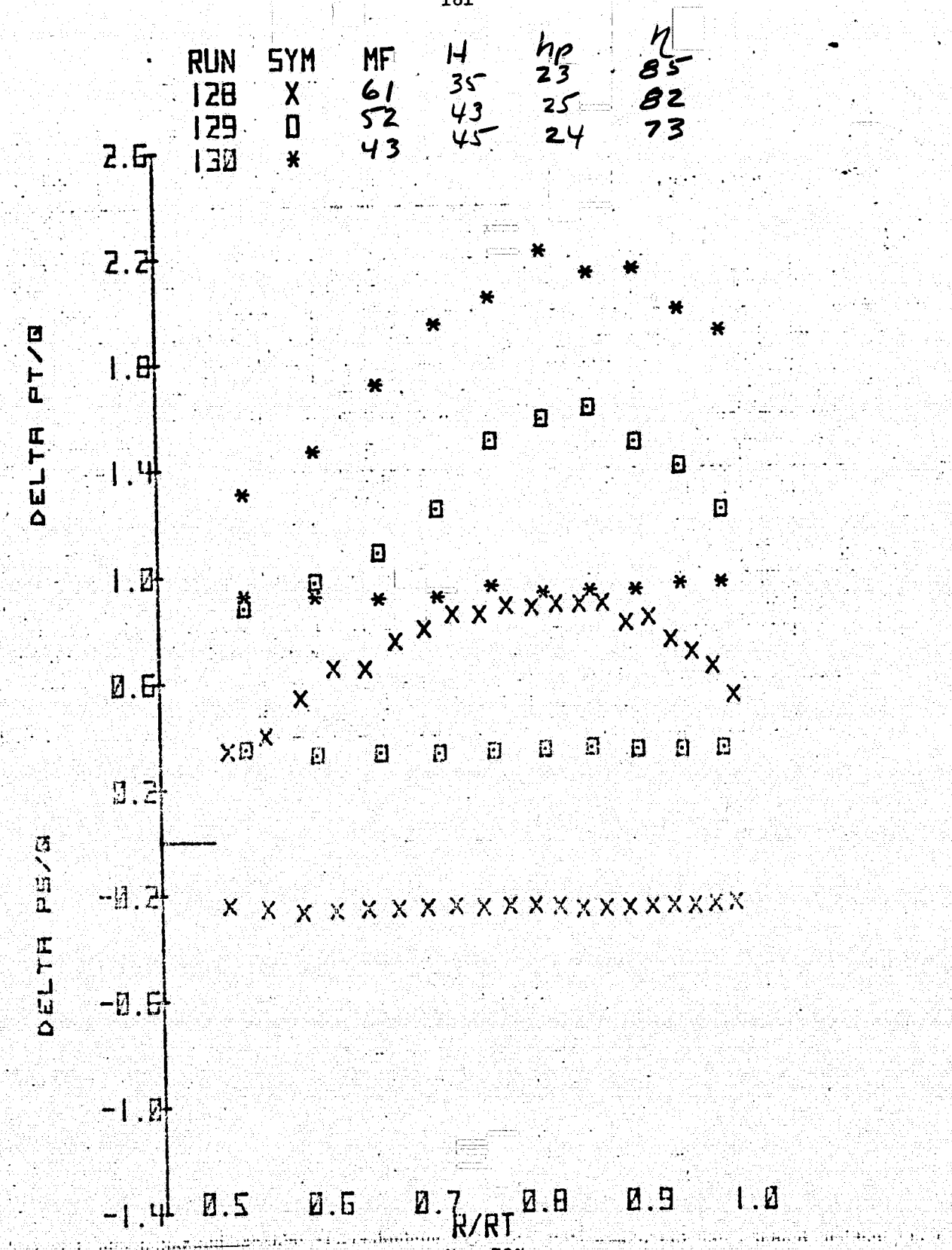

N = 70%

(a) Port azimuth - continued.

Figure 27.- Continued.

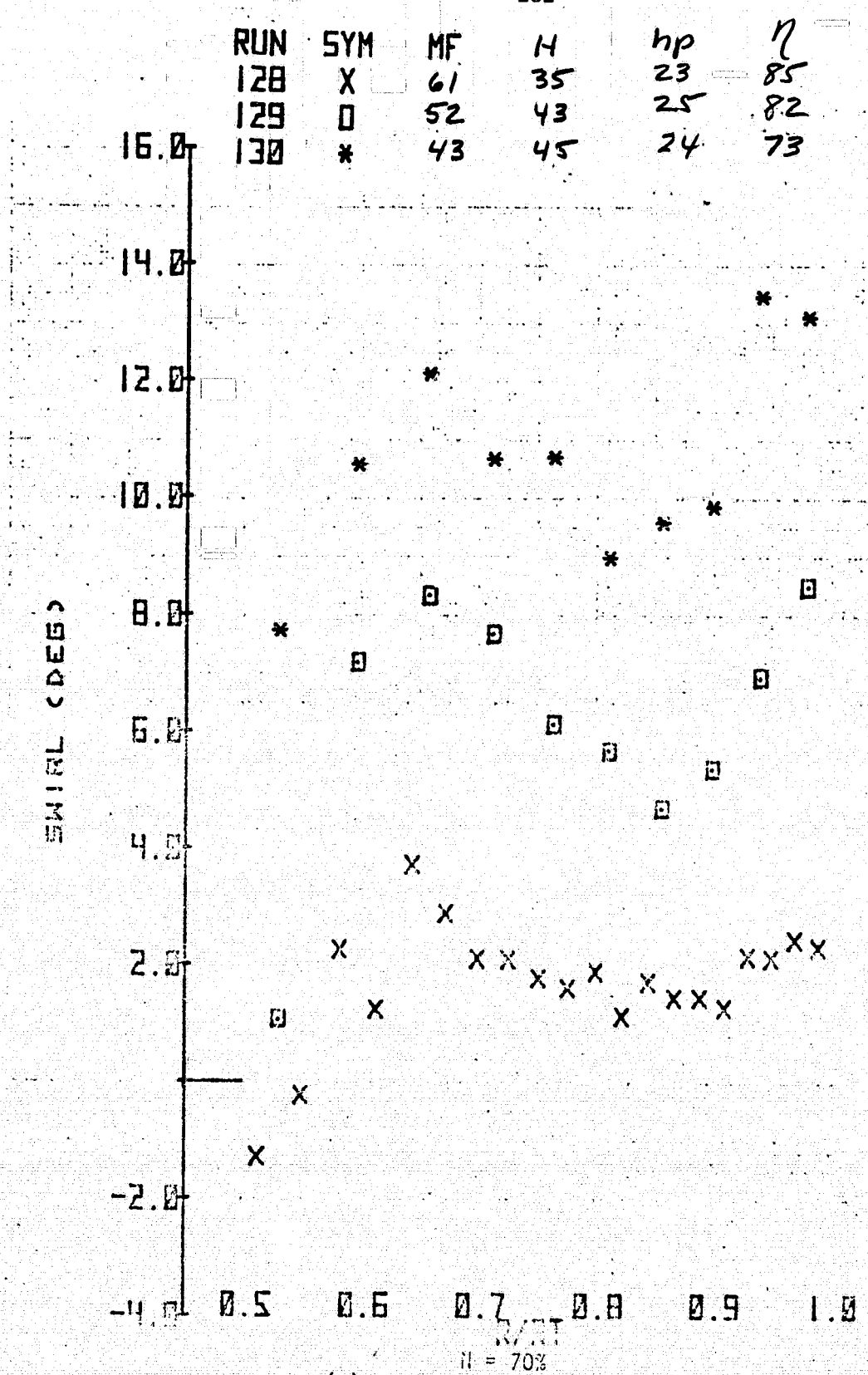

(a) Port azimuth - concluded.

Figure 27.- Continued.

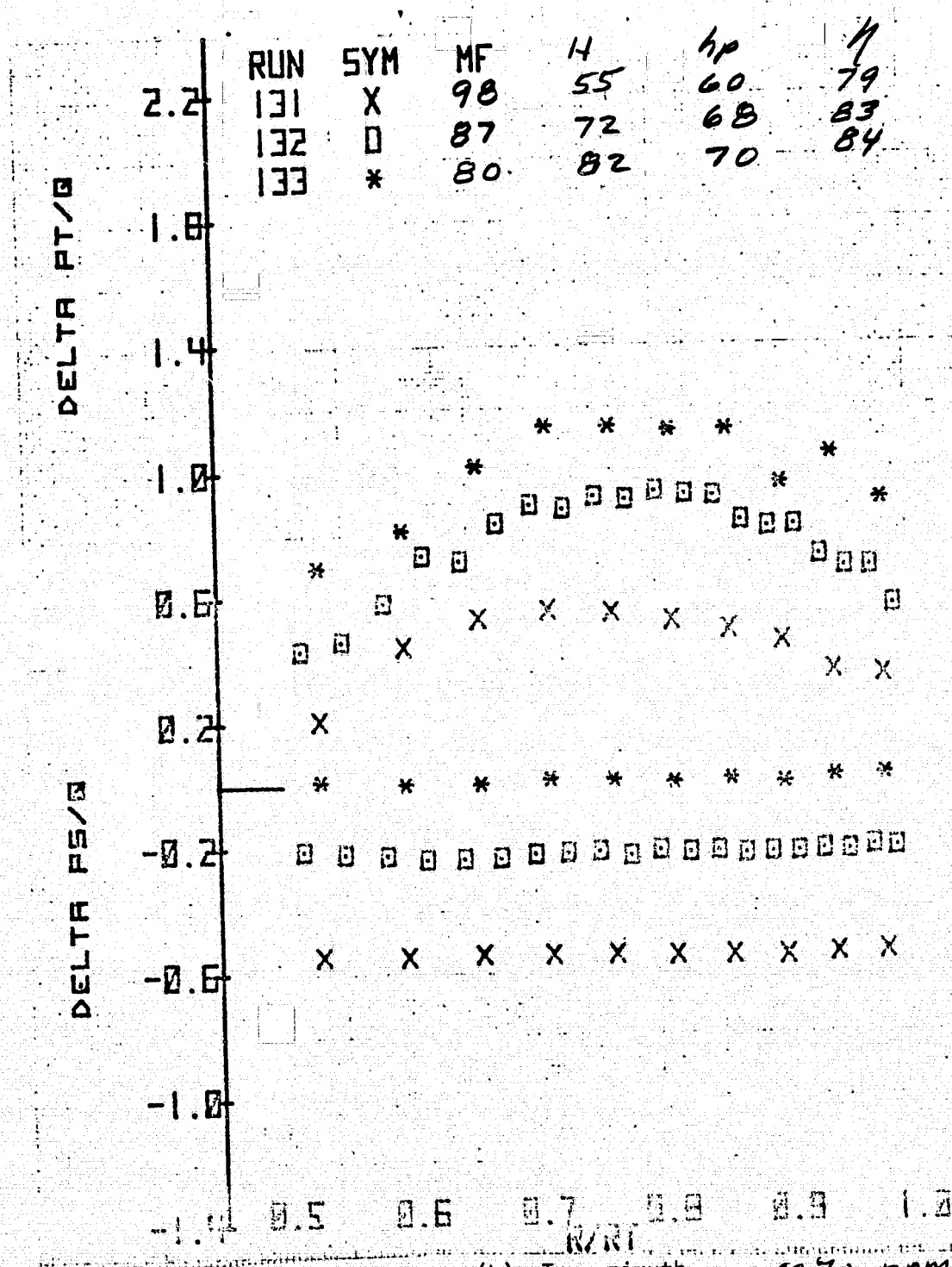

(b) Top azimuth. 1600 70 rpm

Figure 27.- Continued.

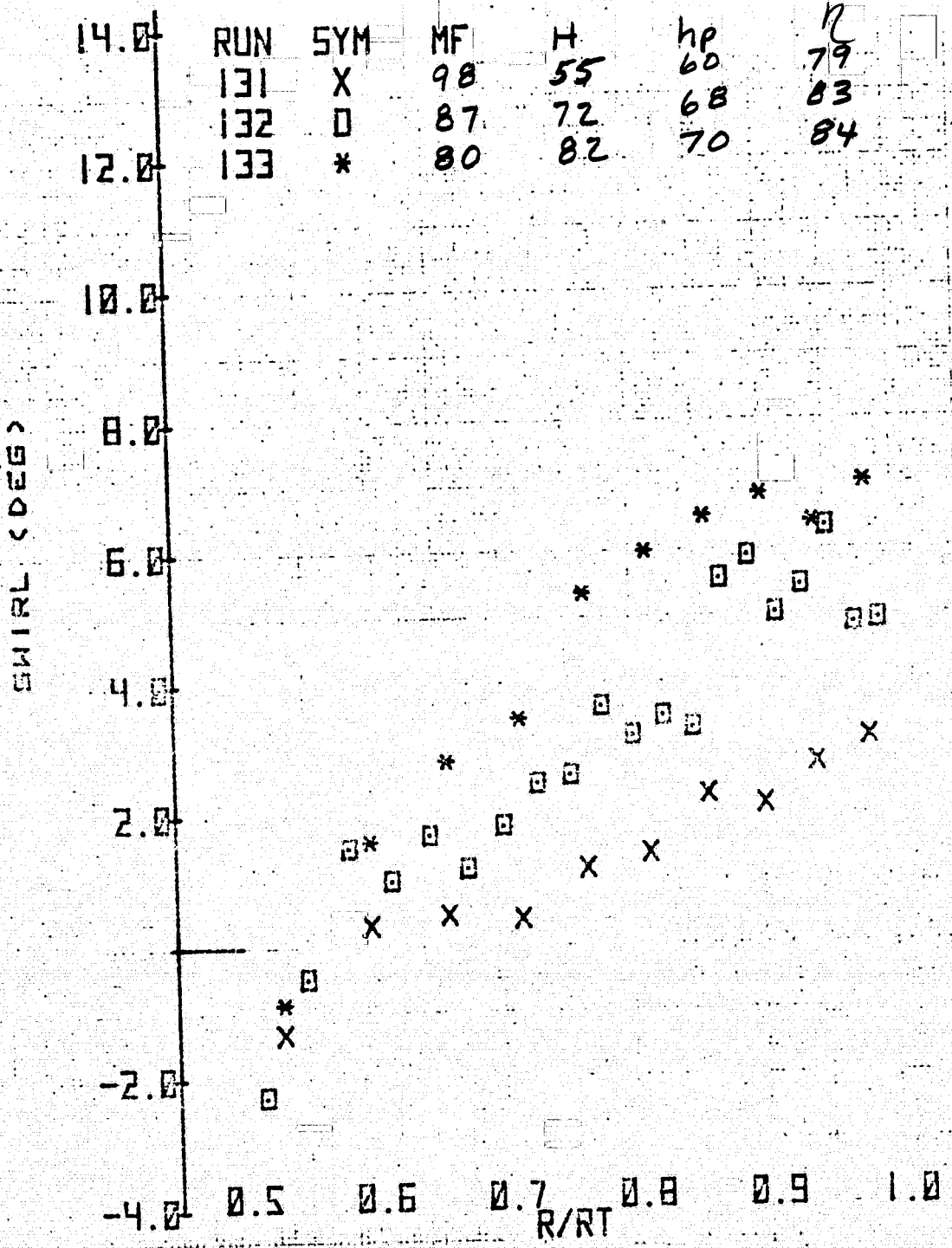

(b) Top azimuth - concluded.

Figure 27.- Continued.

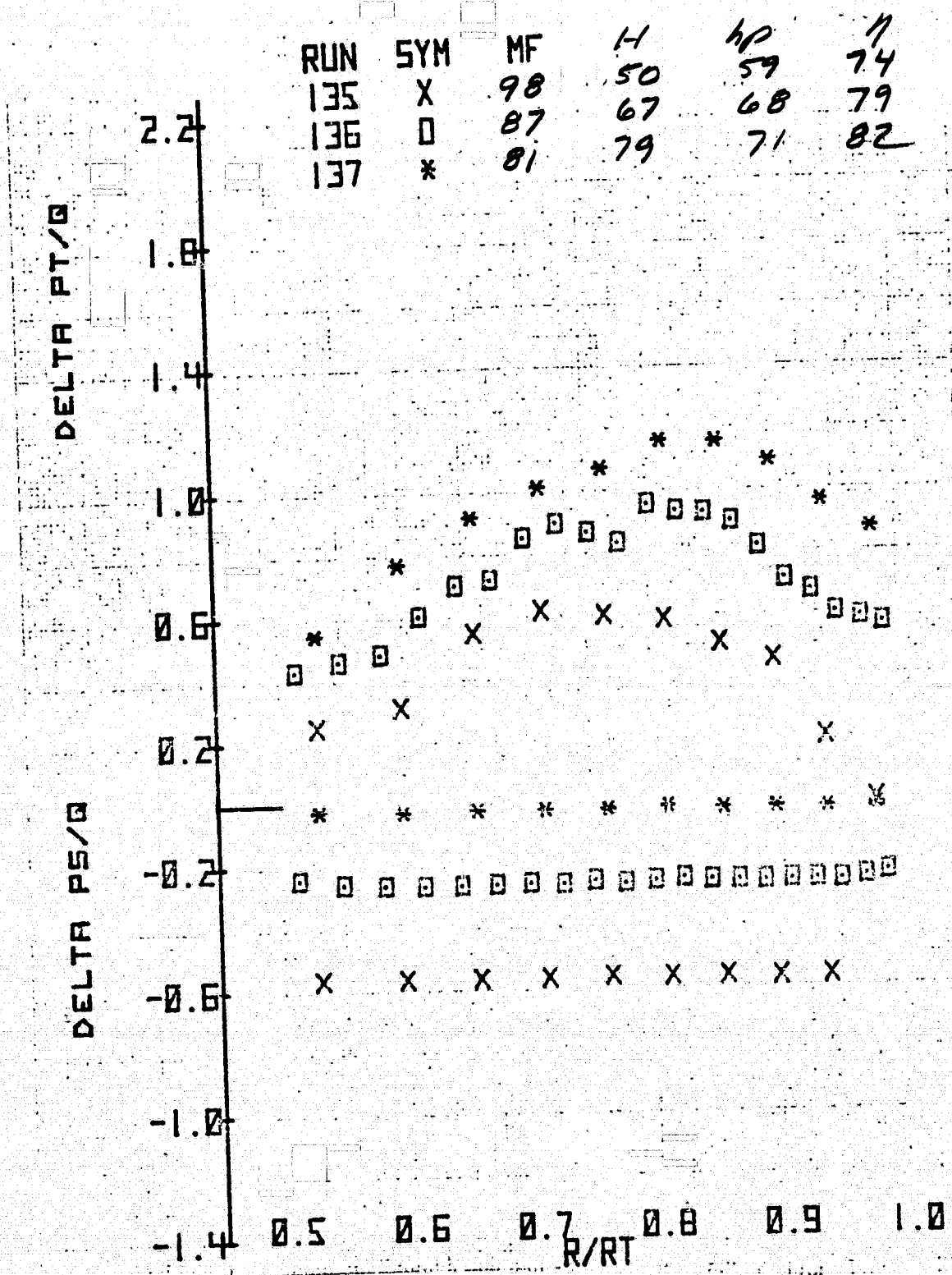

(c) Starboard azimuth.

Figure 27.- Continued.

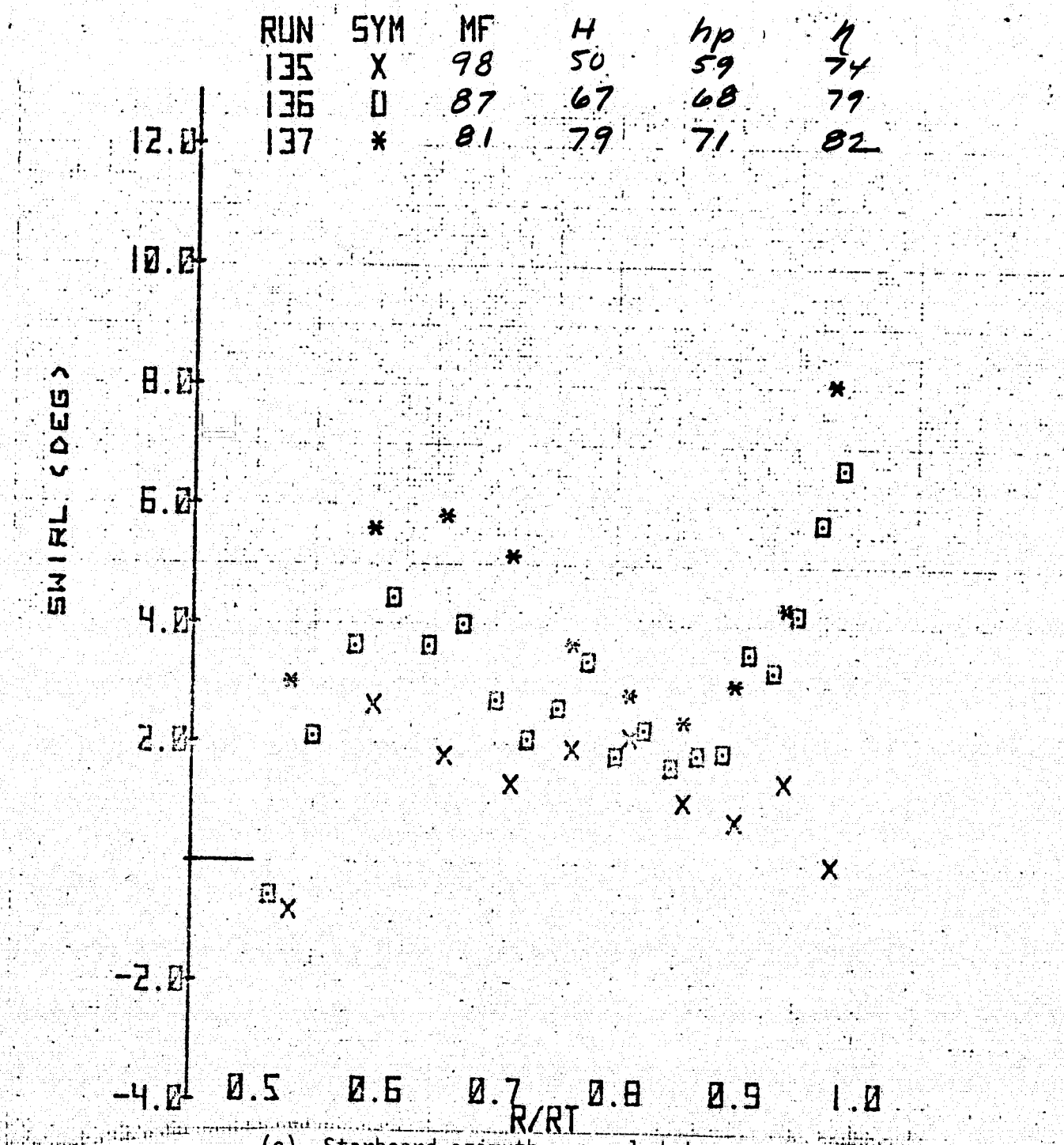

(c) Starboard azimuth - concluded.

Figure 27.- Continued.

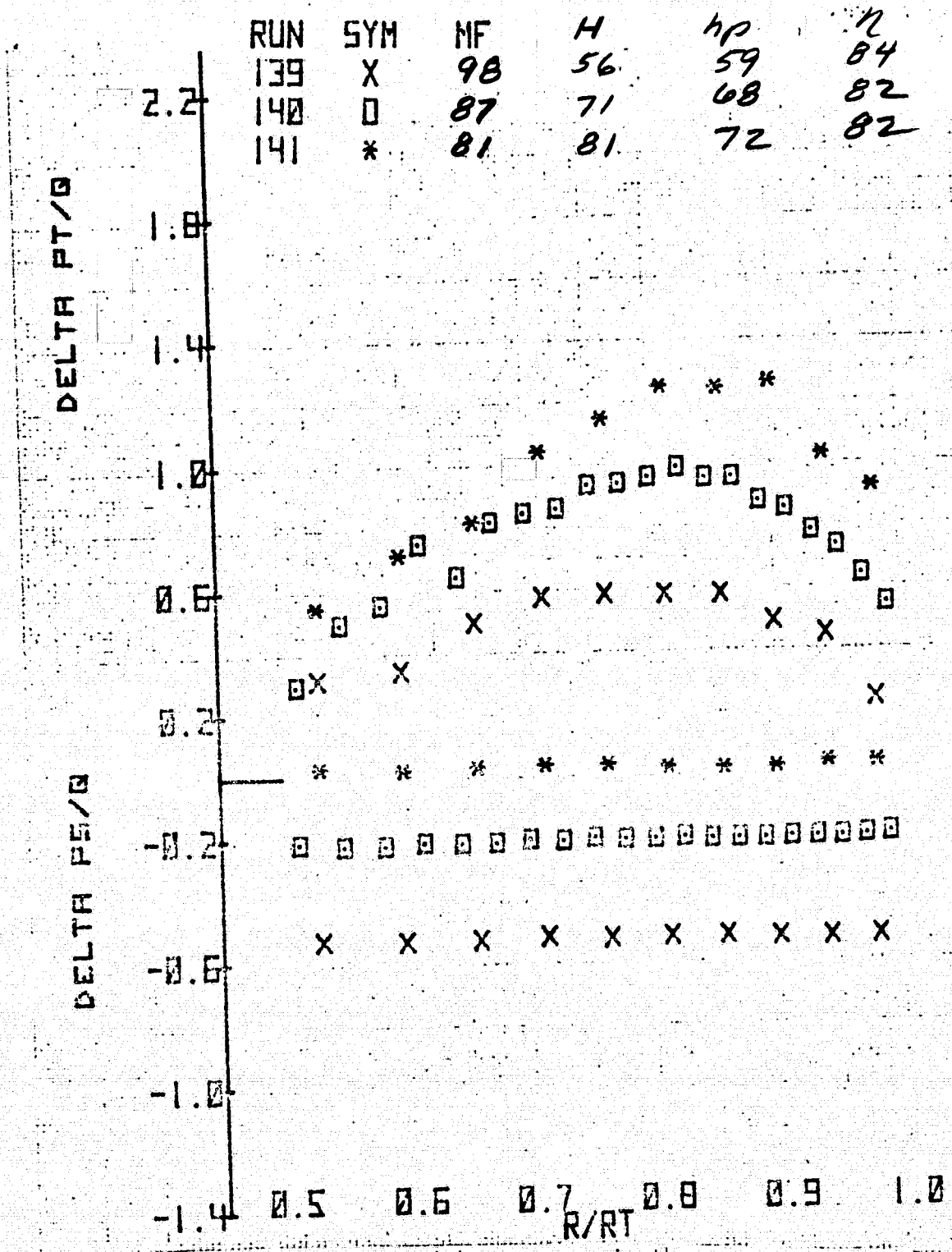

(d) Bottom azimuth.

Figure 27.- Continued.

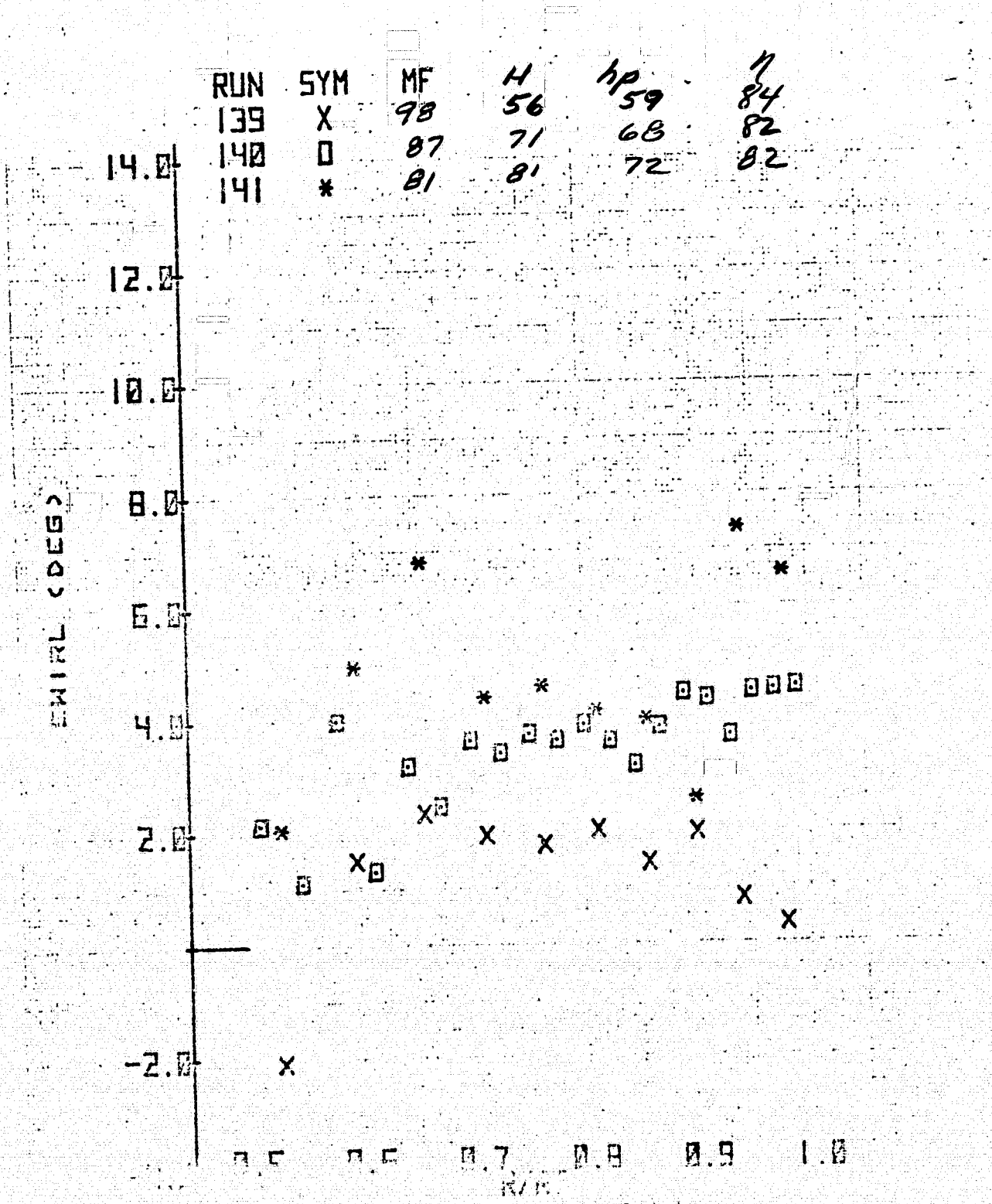

(d) Bottom azimuth - concluded.

Figure 27.- Concluded.

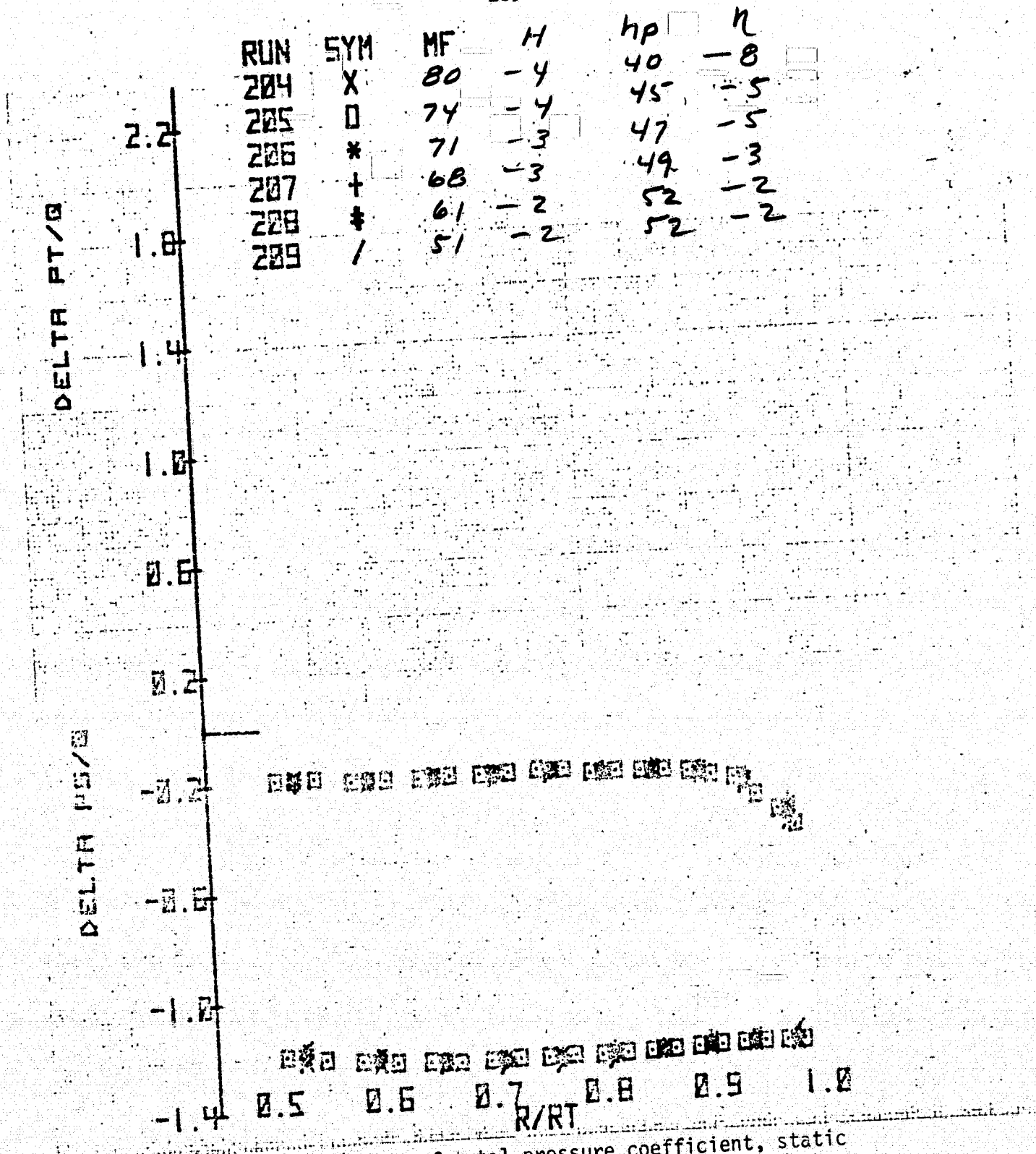

Figure 28.- Radial variation of total pressure coefficient, static pressure coefficient, and swirl angle upstream of the rotor at the starboard azimuth and several mass flows; N = 100% inlet honeycomb, original contraction, and $\xi = 52.8°$.

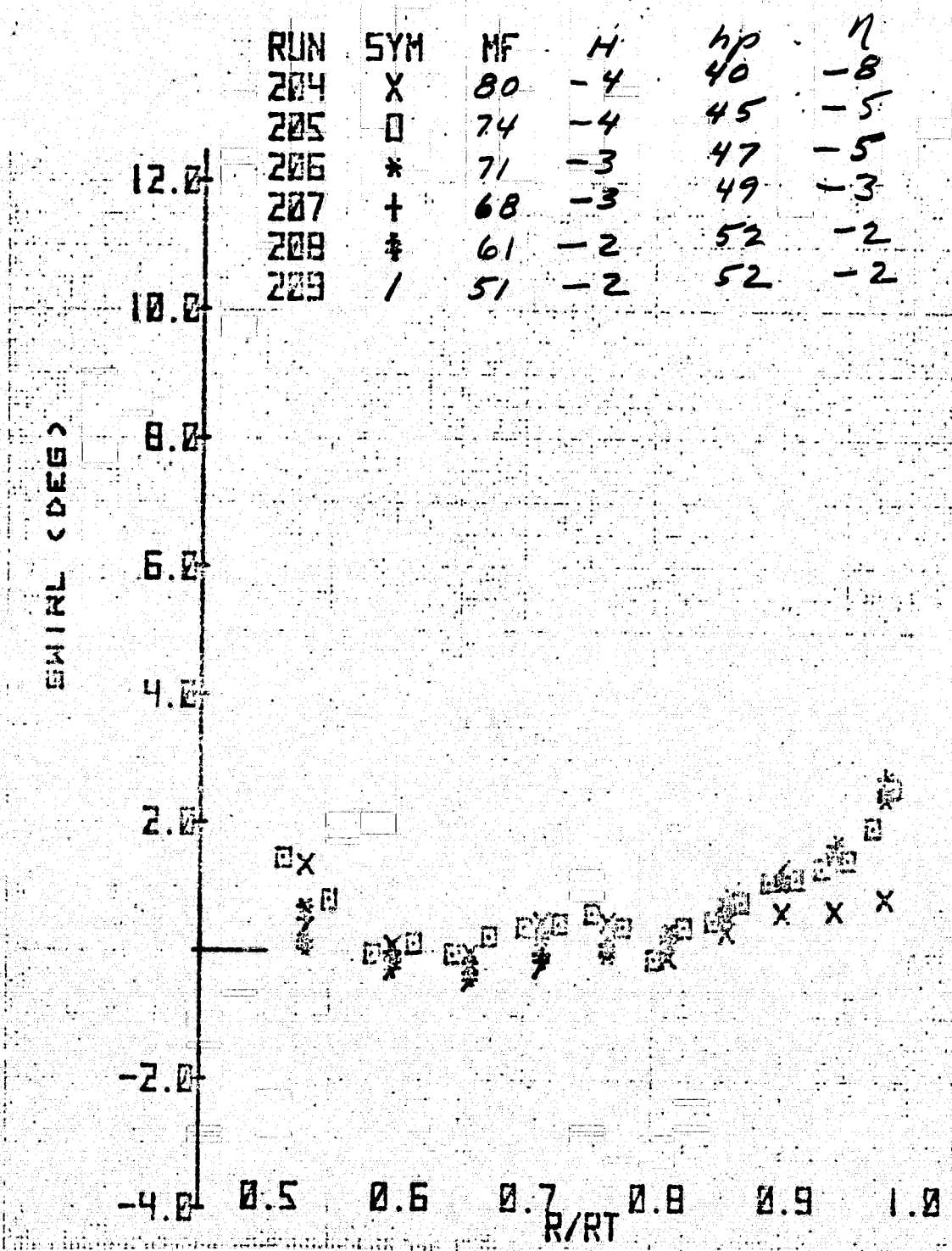

Figure 28.- Concluded.

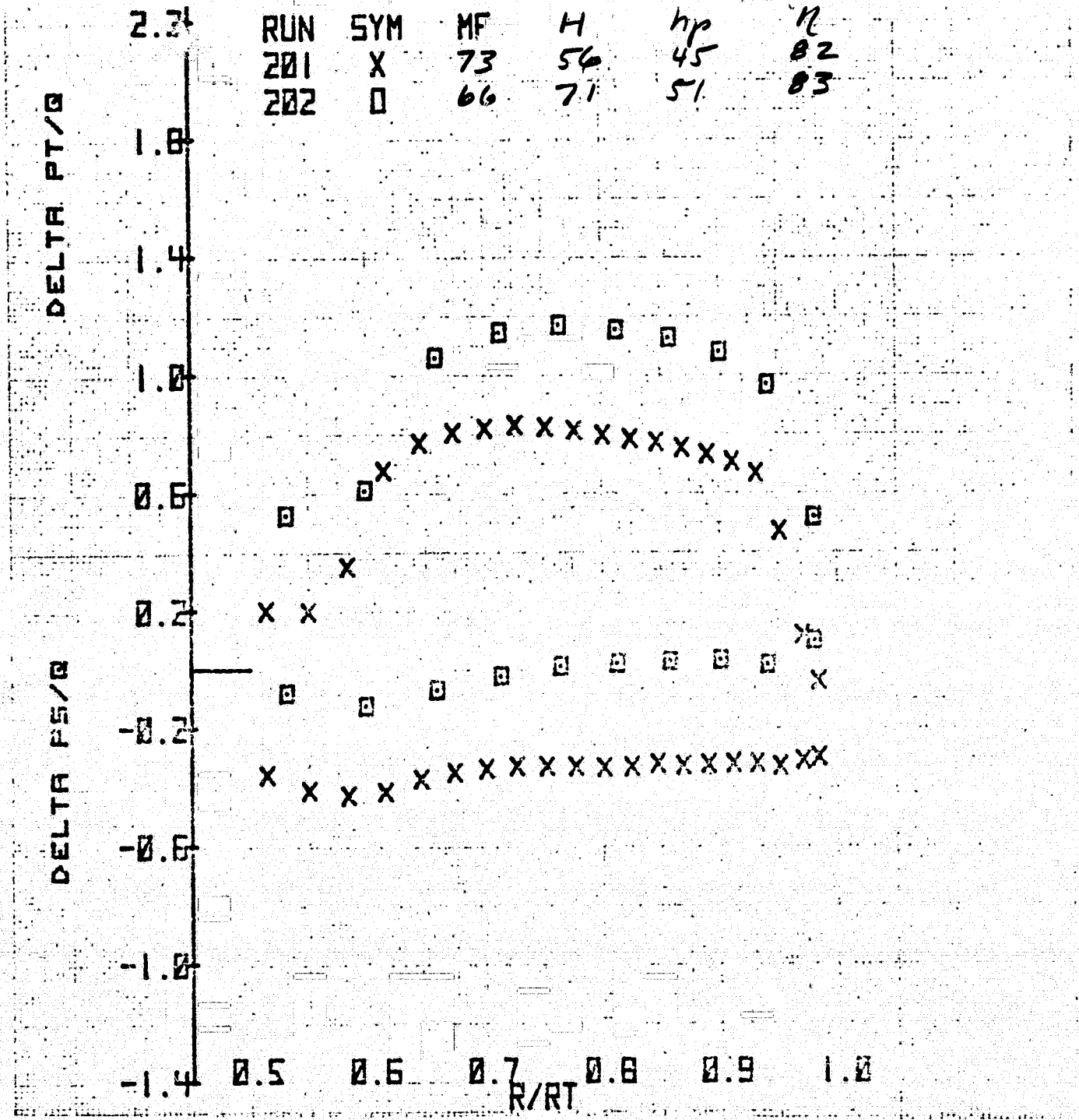

Figure 29.- Radial variation of total pressure coefficient, static pressure coefficient, and swirl angle between rotor and stator at the starboard azimuth, and several mass flows; inlet honeycomb in, original contraction, N = 100%, and ξ = 52.8°.

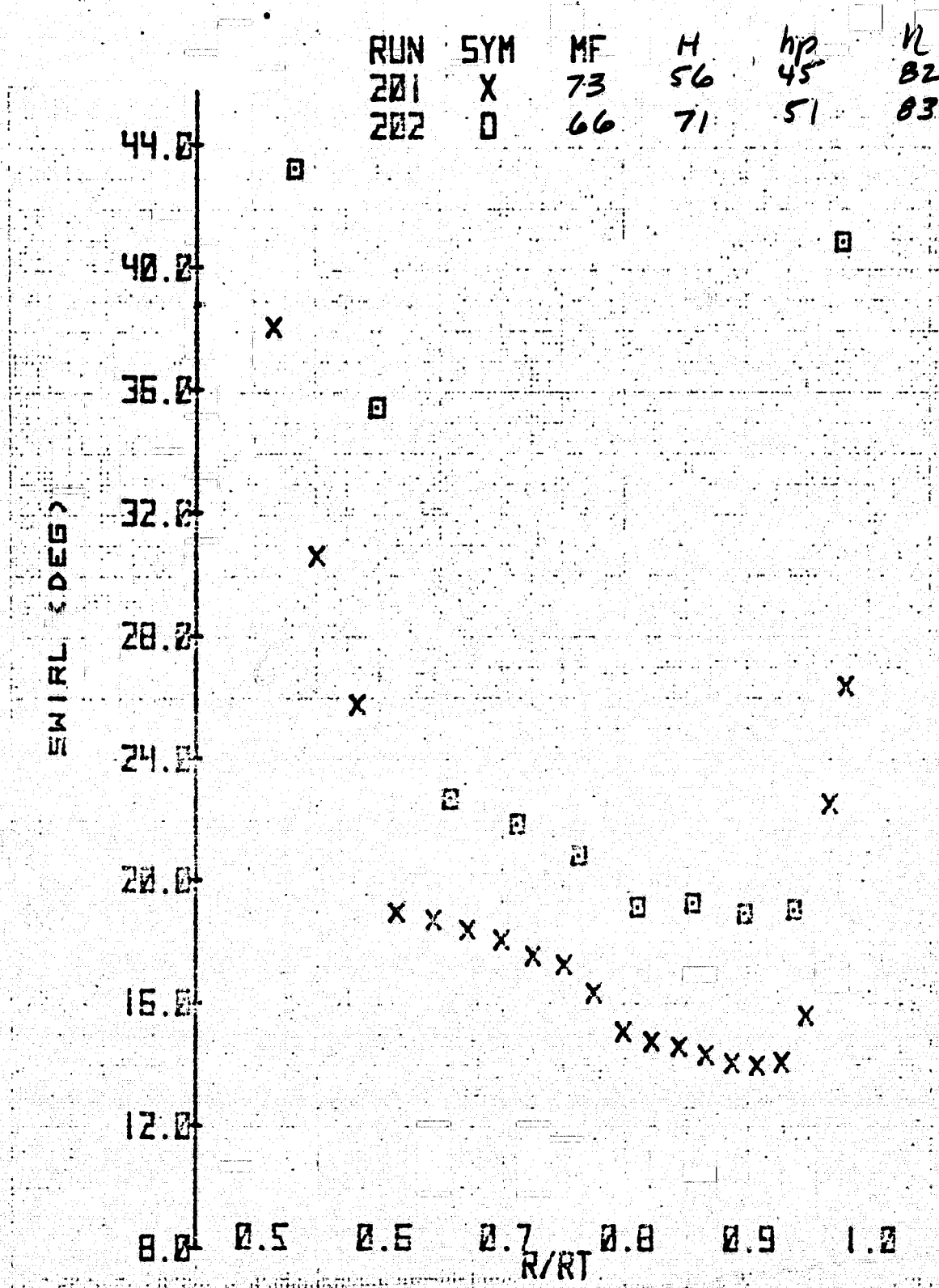

Figure 29. Concluded.

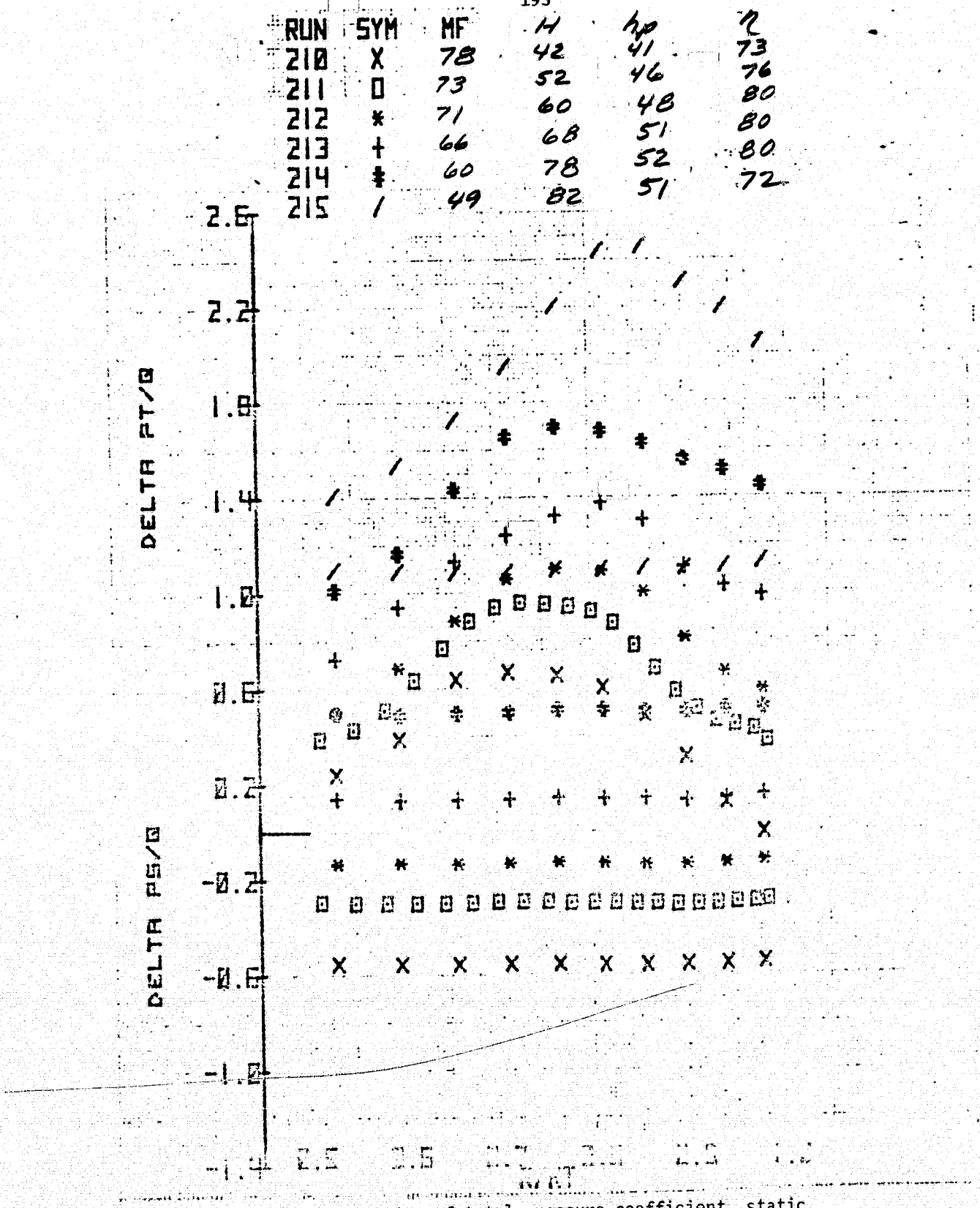

Figure 30.- Radial variation of total pressure coefficient, static pressure coefficient, and swirl angle downstream of stator at the starboard azimuth and several mass flows; inlet honeycomb in, original contraction, N = 100%, and $\xi = 52.8°$.

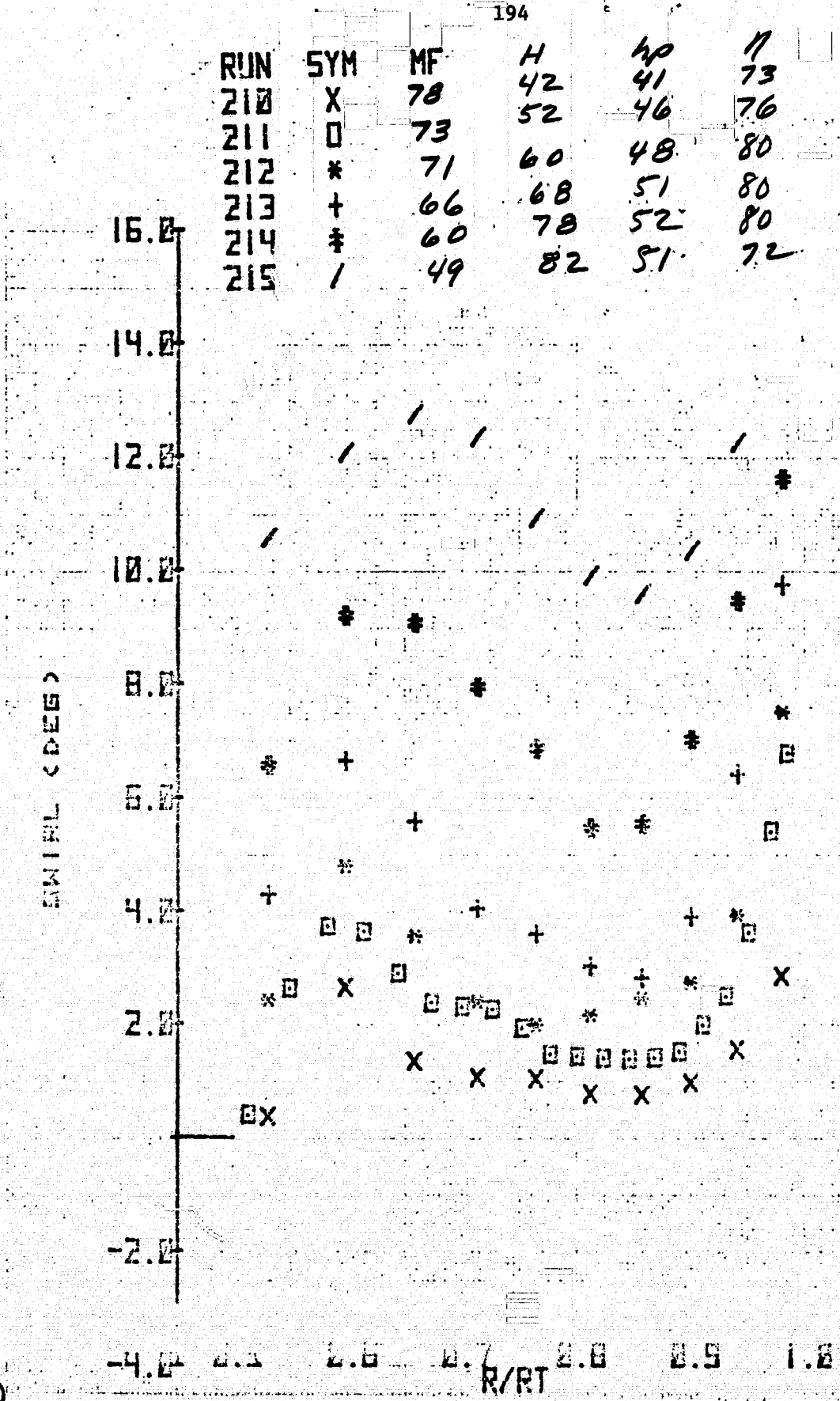

Figure 30.- Concluded.

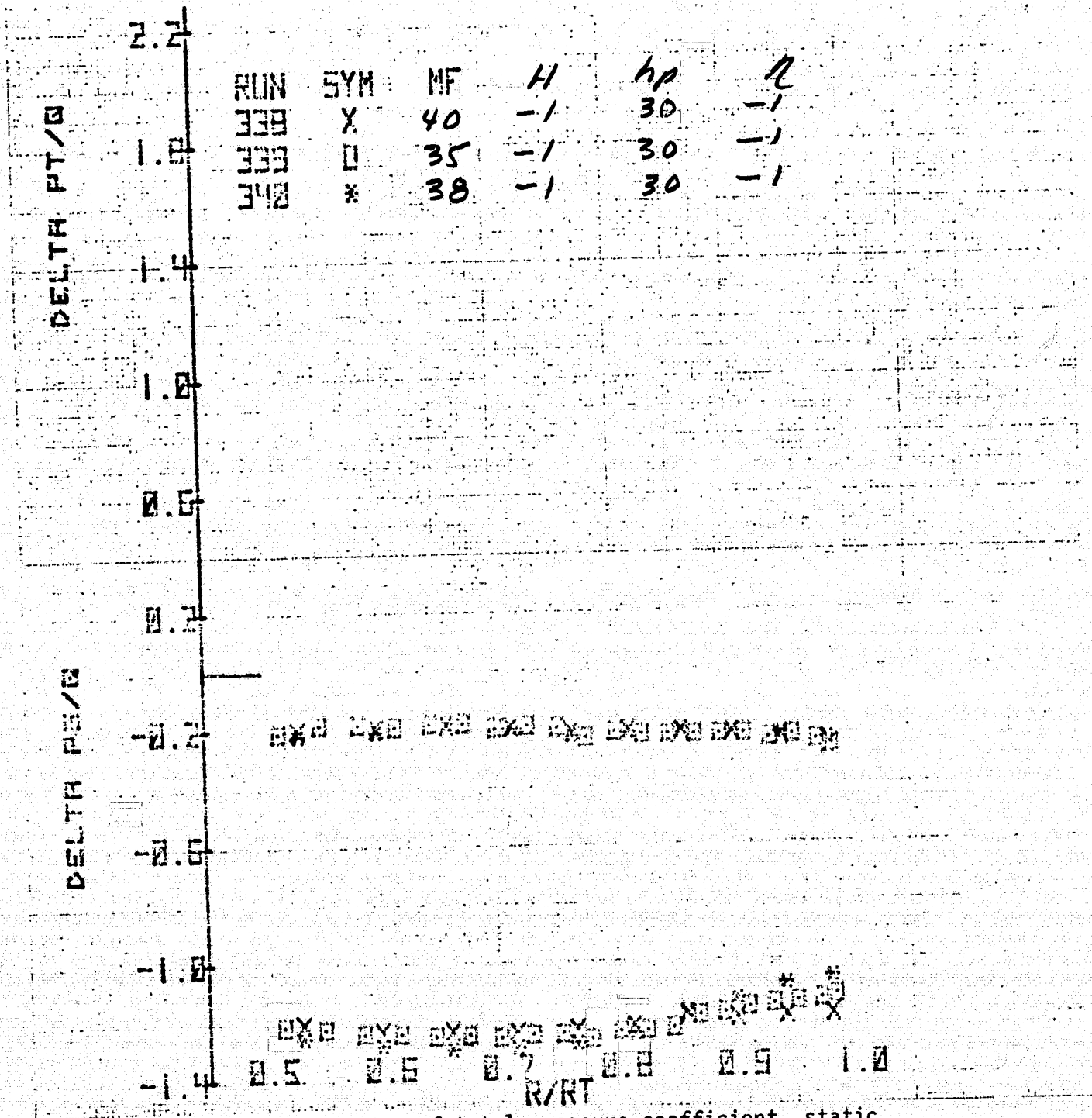

Figure 31.- Radial variation of total pressure coefficient, static pressure coefficient and swirl angle upstream of rotor at the port azimuth and for several mass flows; inlet honeycomb in, original contraction, N = 100%, and ξ = 62.9°.

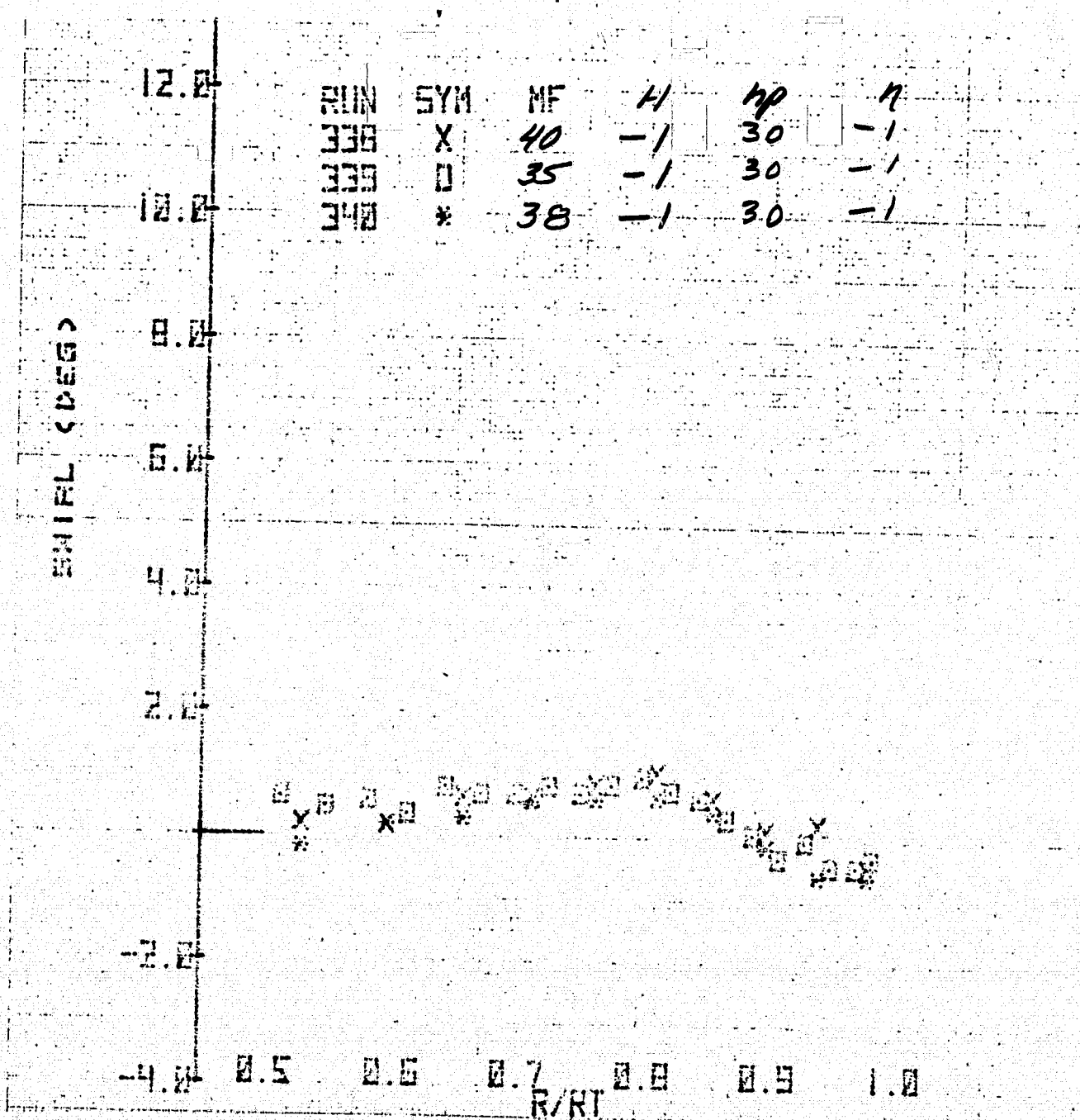

Figure 31.- Concluded.

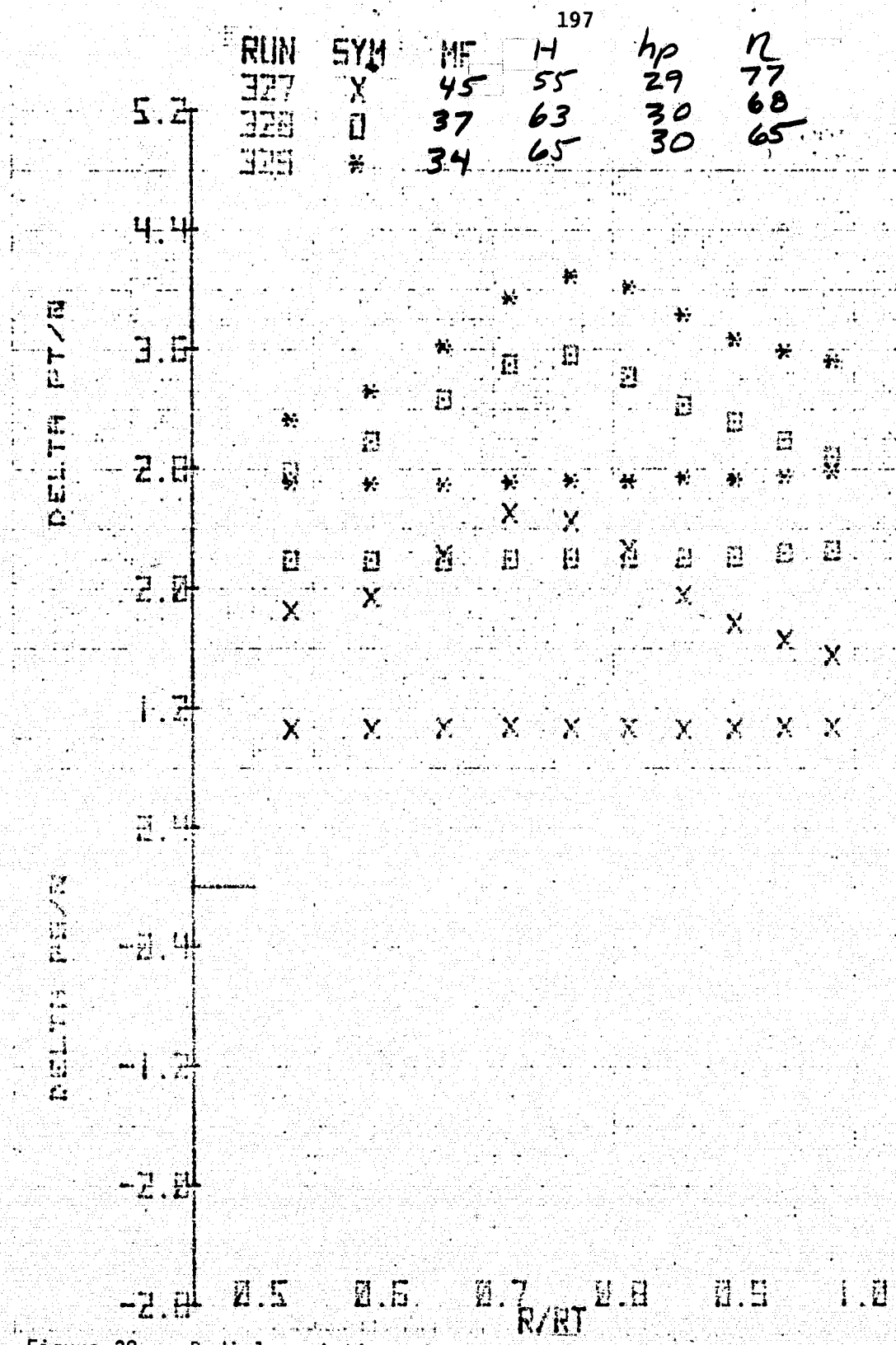

Figure 32.- Radial variation of total pressure coefficient, static pressure coefficient, and swirl angle downstream of the stators at the port azimuth for several mass flows; original contraction, N = 100%, and ξ = 62.9°.

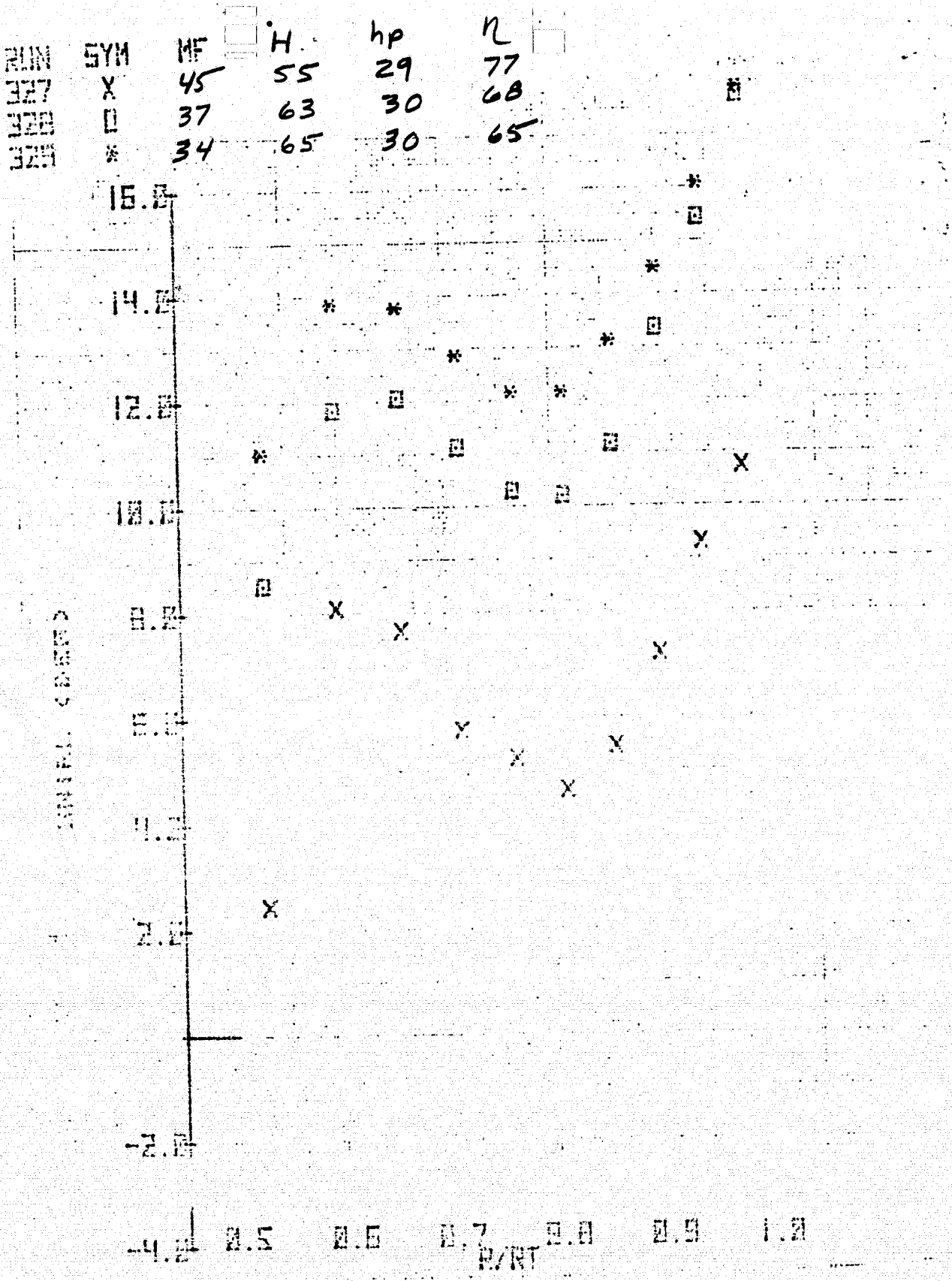

Figure 32.- Concluded.

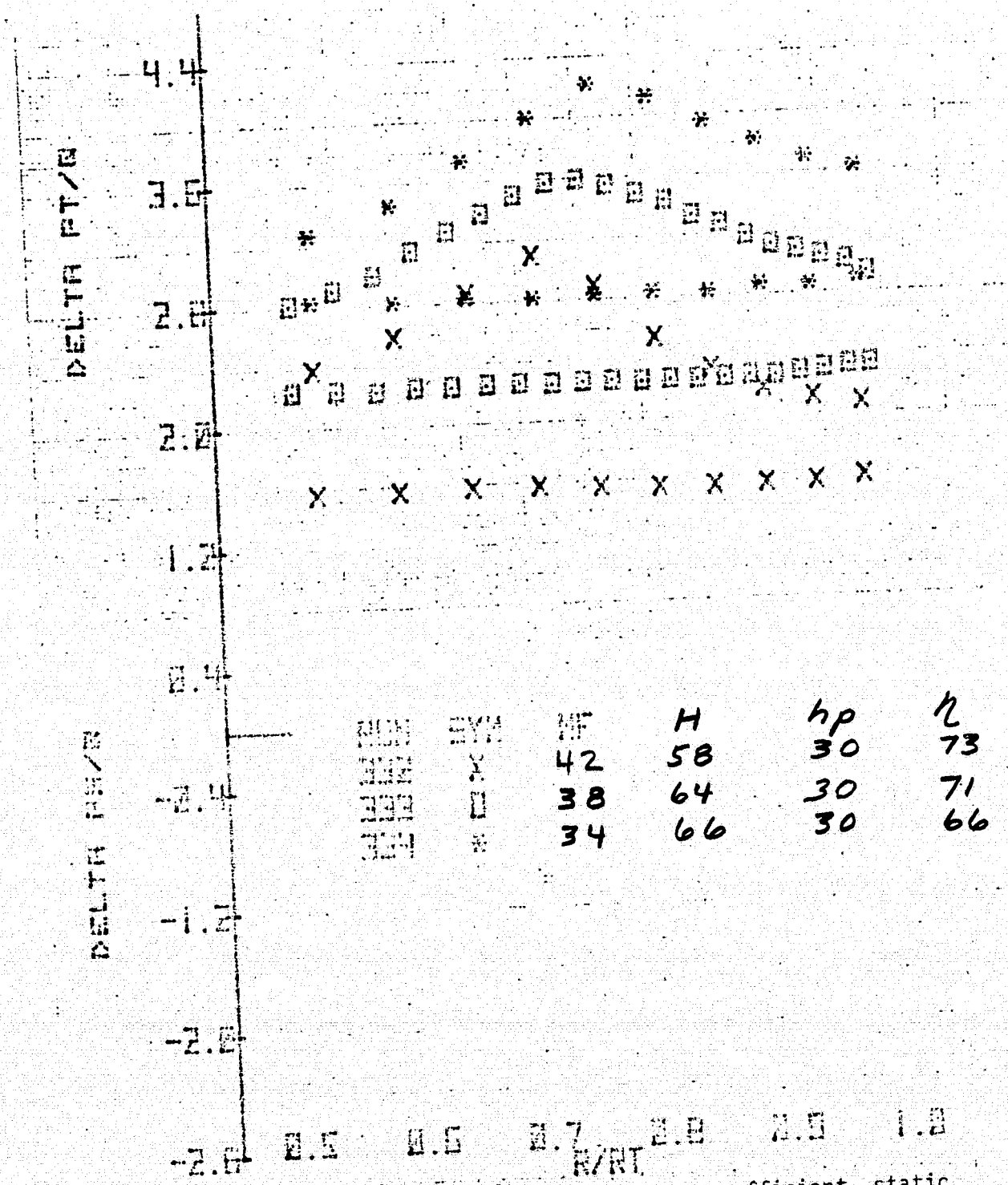

Figure 33.- Radial variation of total pressure coefficient, static pressure coefficient, and swirl angle at the port azimuth for several mass flows; modified contraction, inlet honeycomb, N = 100%, and $\xi = 62.9°$.

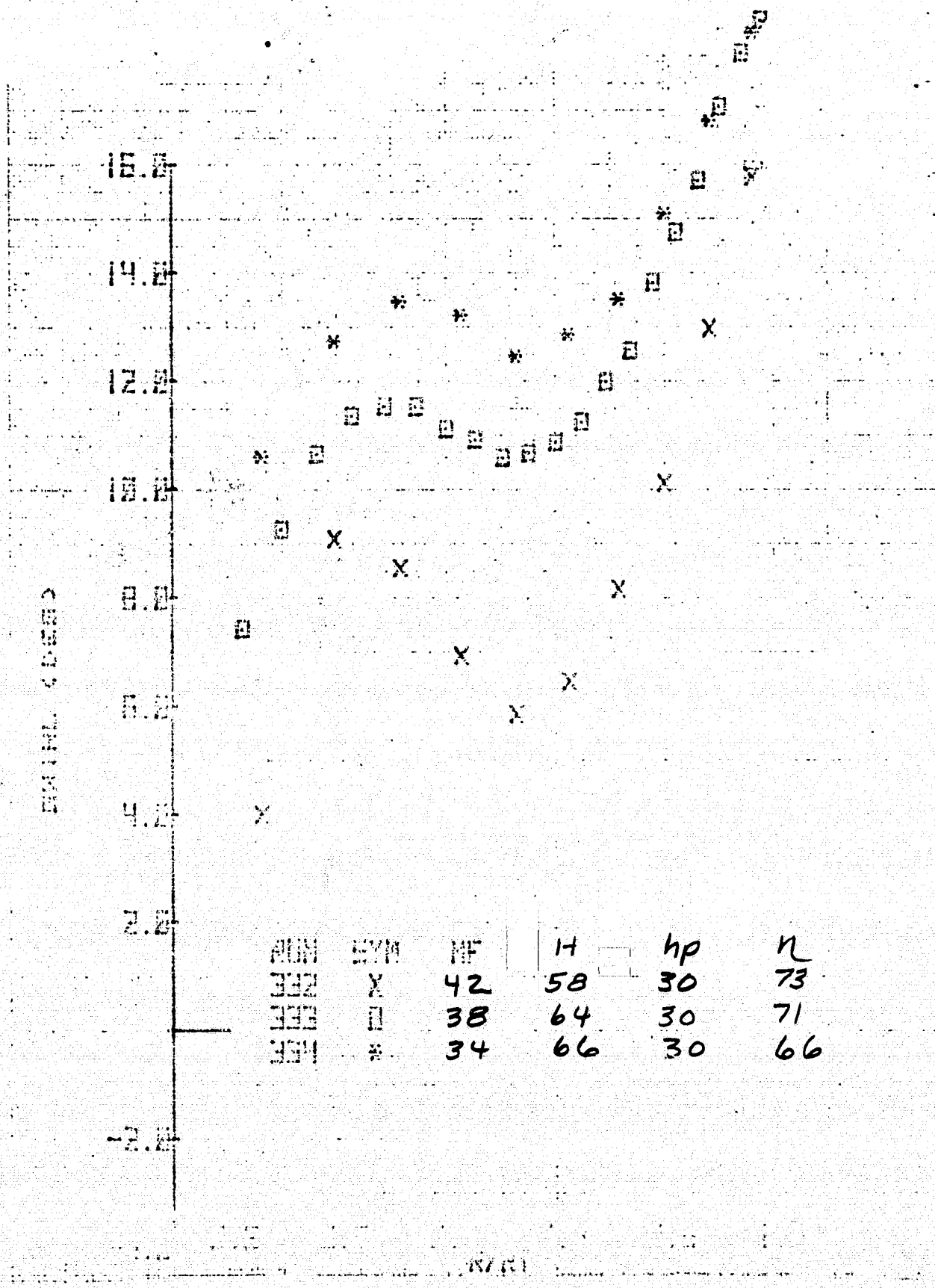

Figure 33.- Concluded.

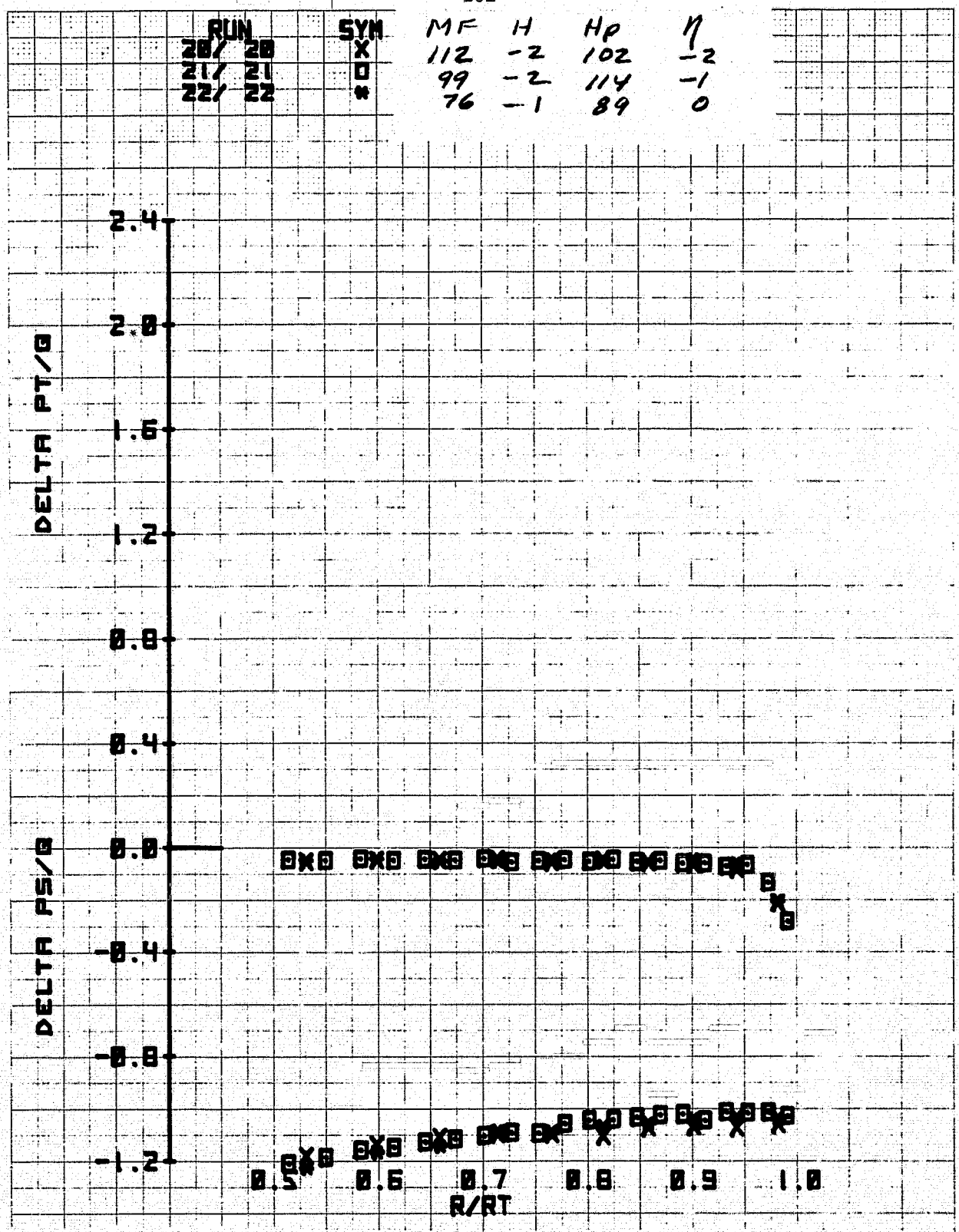

Figure 35.- Radial variation of total pressure coefficient, static pressure coefficient, and swirl angle upstream of the rotor at the port azimuth for several mass flows; original contraction, exit honeycomb, N = 100%, and ξ = 56.2°; high speed fan.

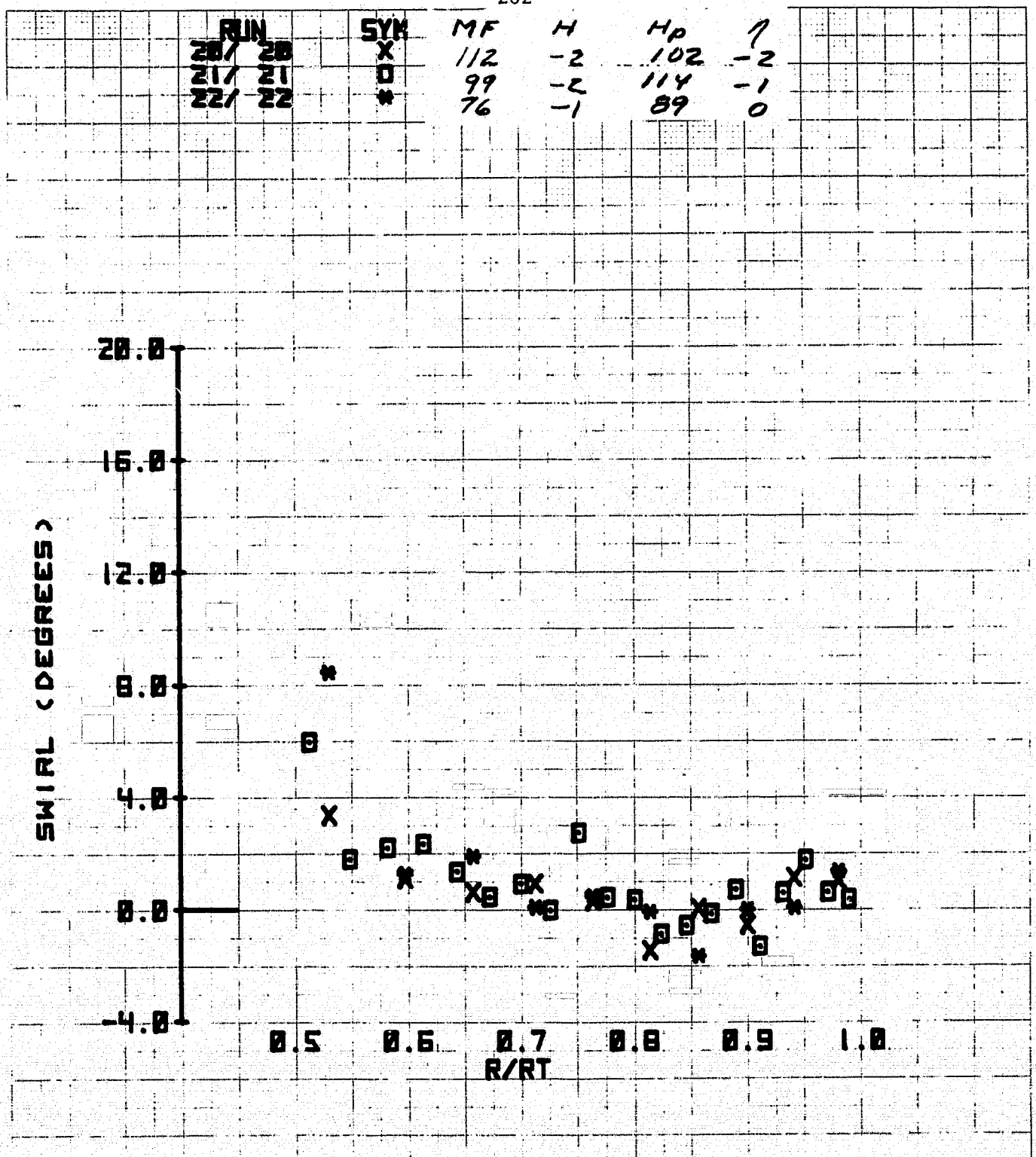

Figure 35.- Concluded.

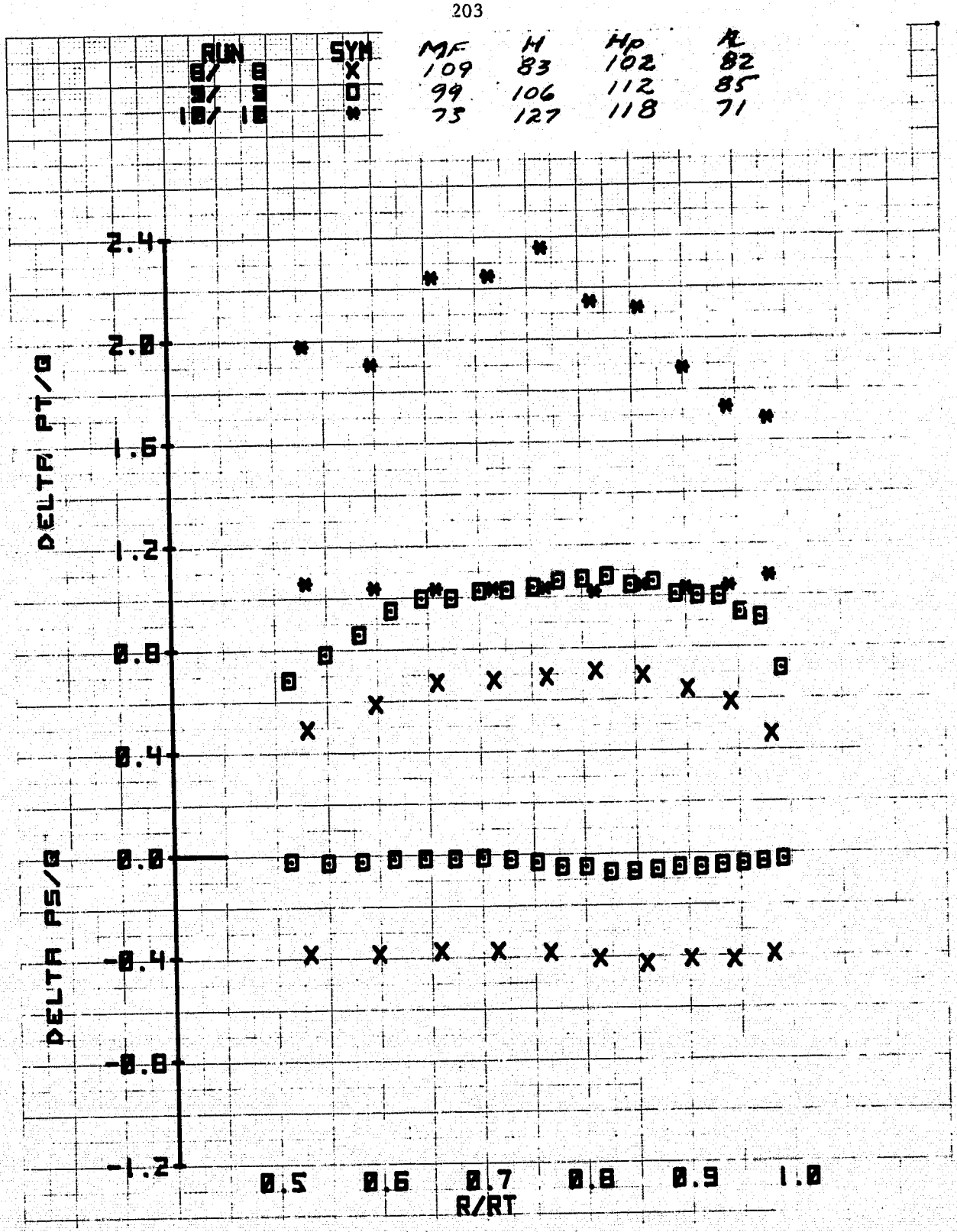

(a) Port azimuth.

Figure 34.- Radial variation of total pressure coefficient, static pressure coefficient and swirl angle downstream of the stator for several azimuths and mass flows; exit honeycomb in, original contraction, N = 100%, and ξ = 56.2°; high speed fan.

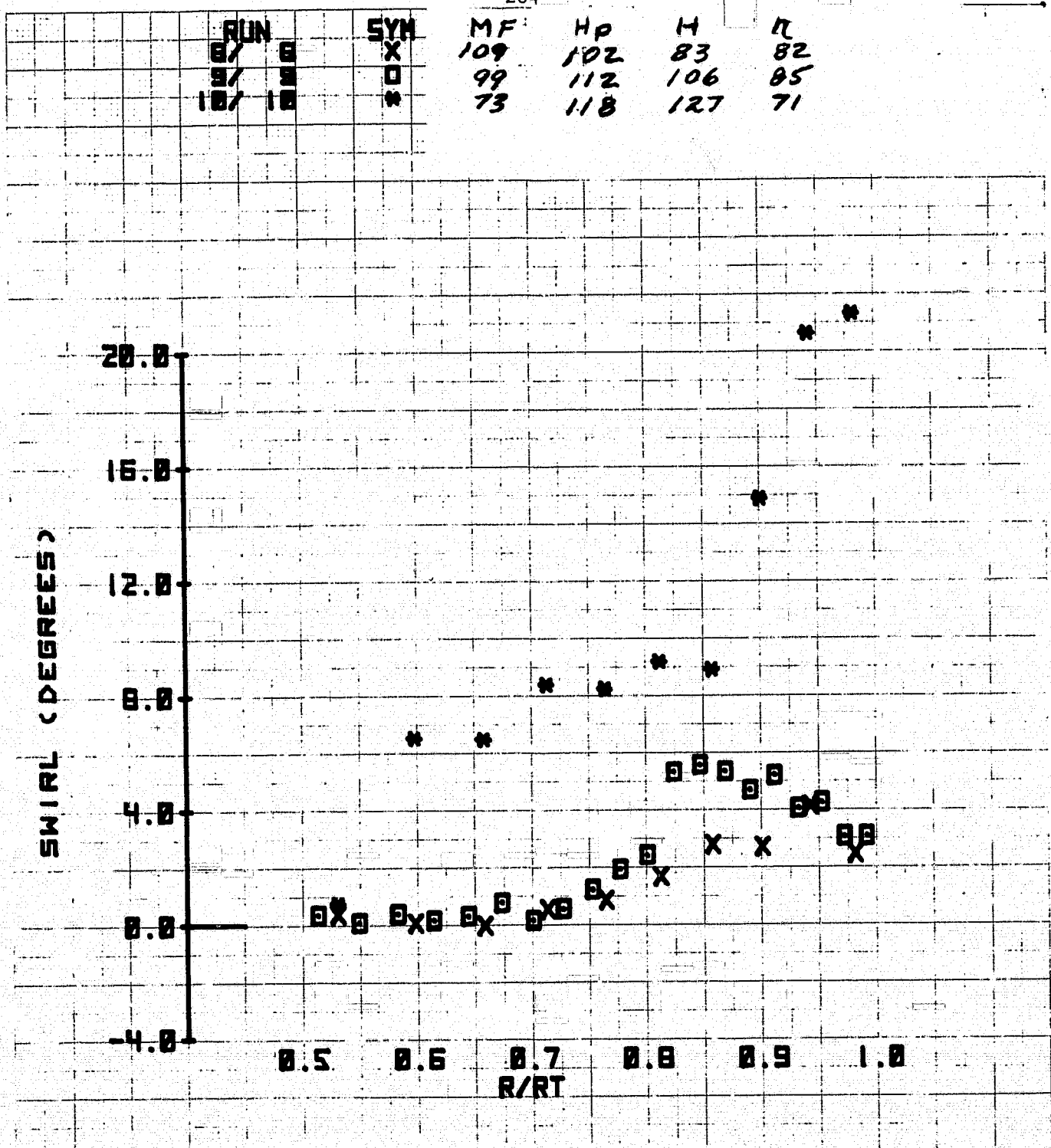

(a) Port azimuth - concluded.

Figure 34.- Continued.

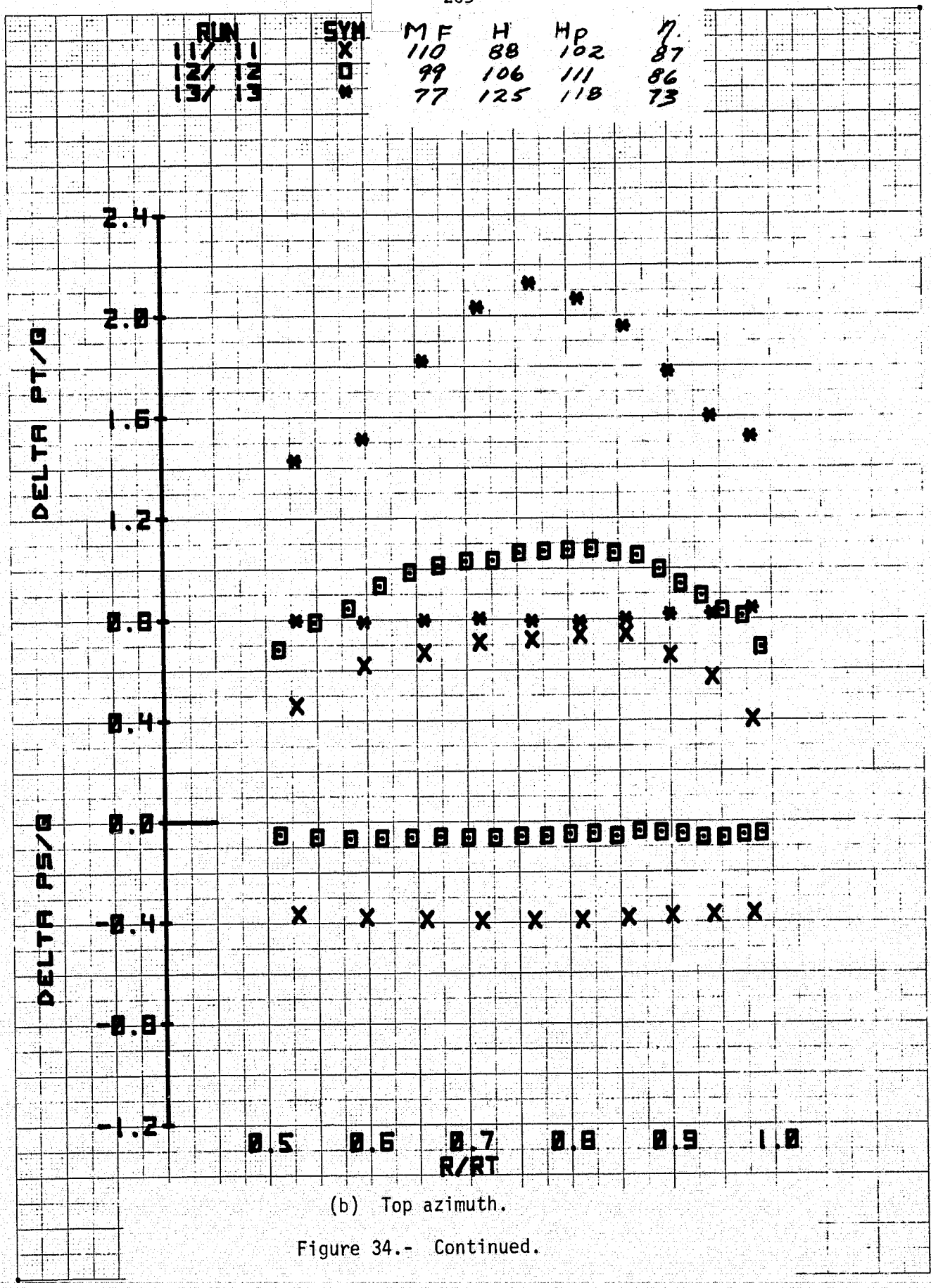

(b) Top azimuth.

Figure 34.- Continued.

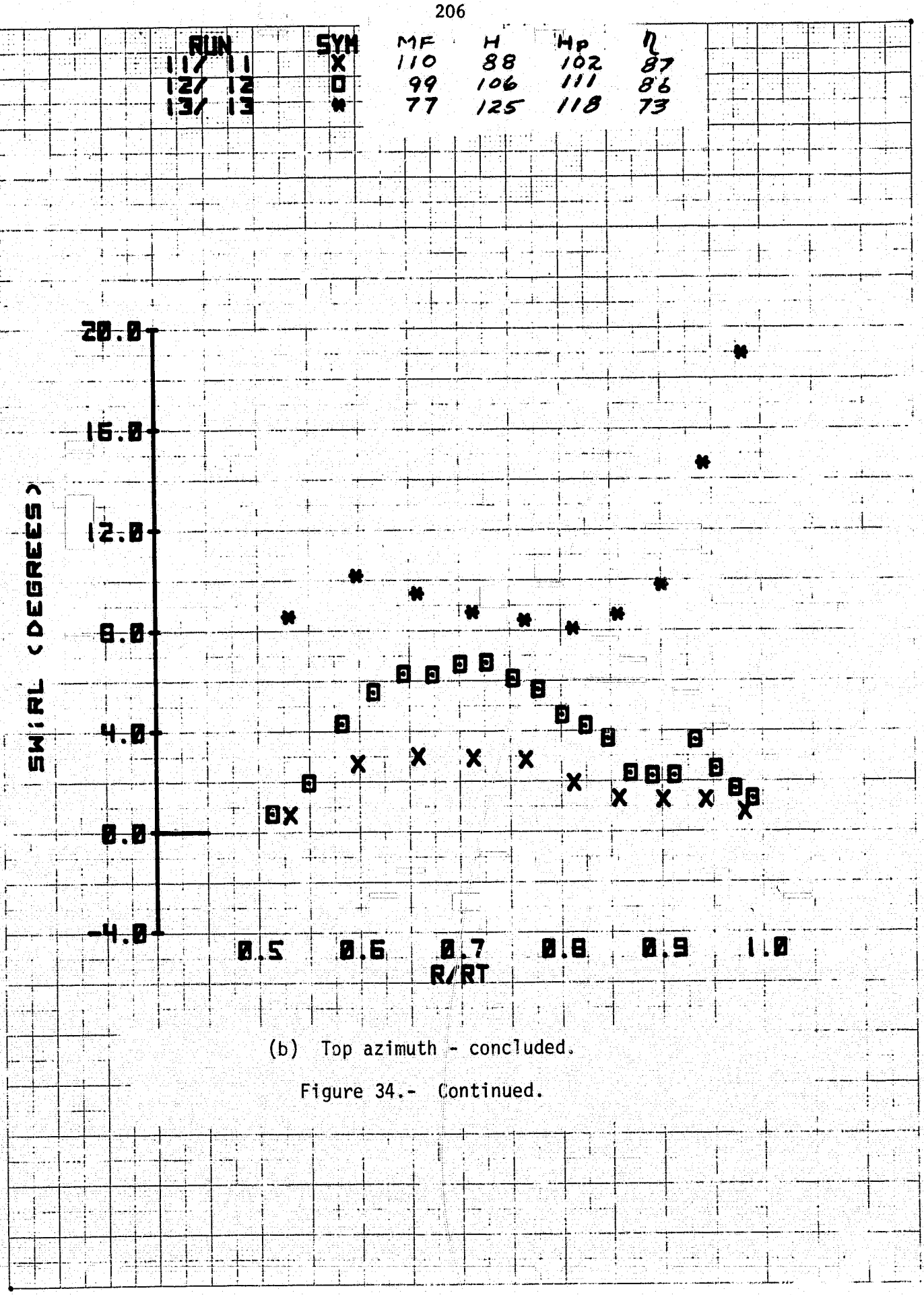

(b) Top azimuth - concluded.

Figure 34.- Continued.

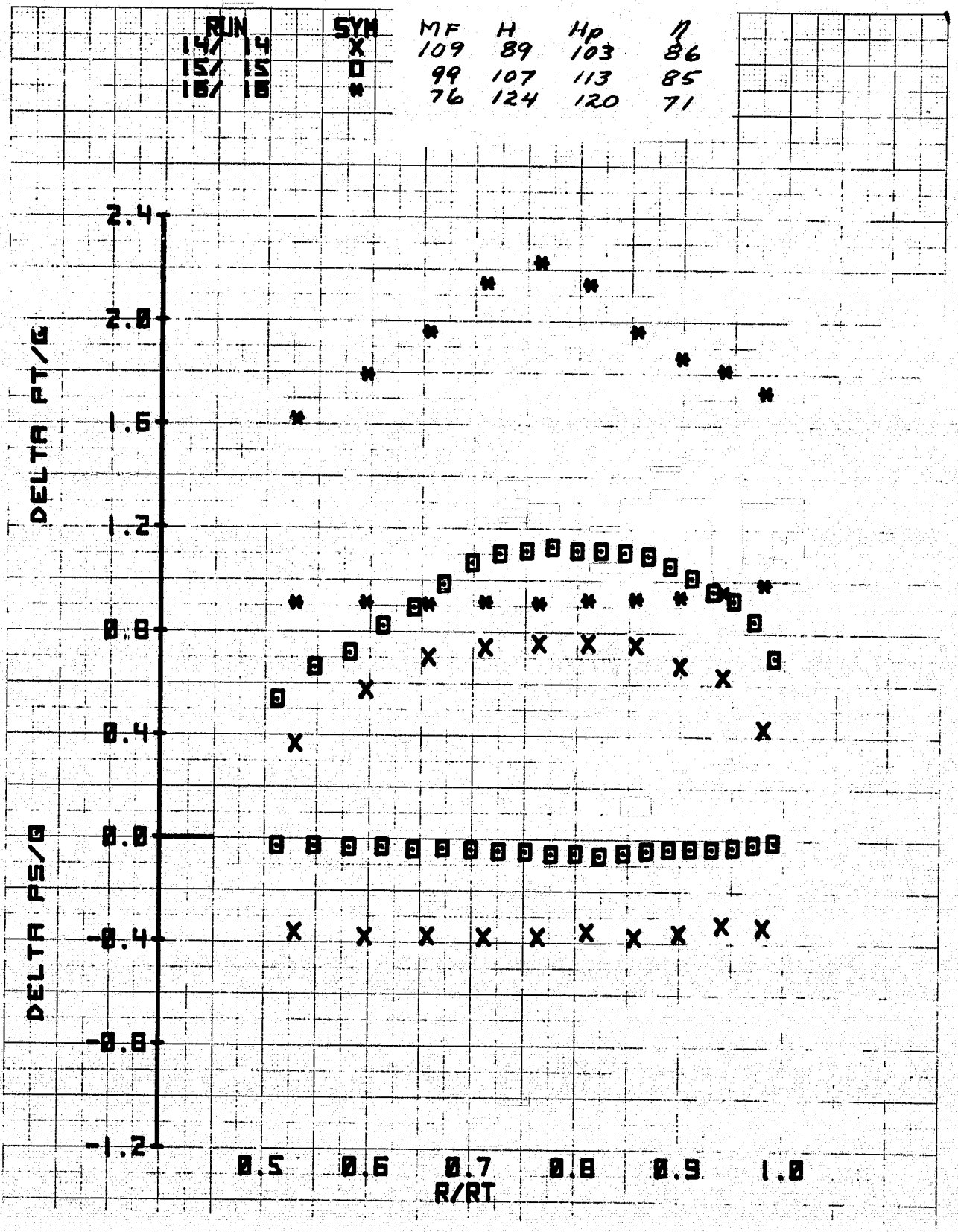

(c) Starboard azimuth.

Figure 34.- Continued.

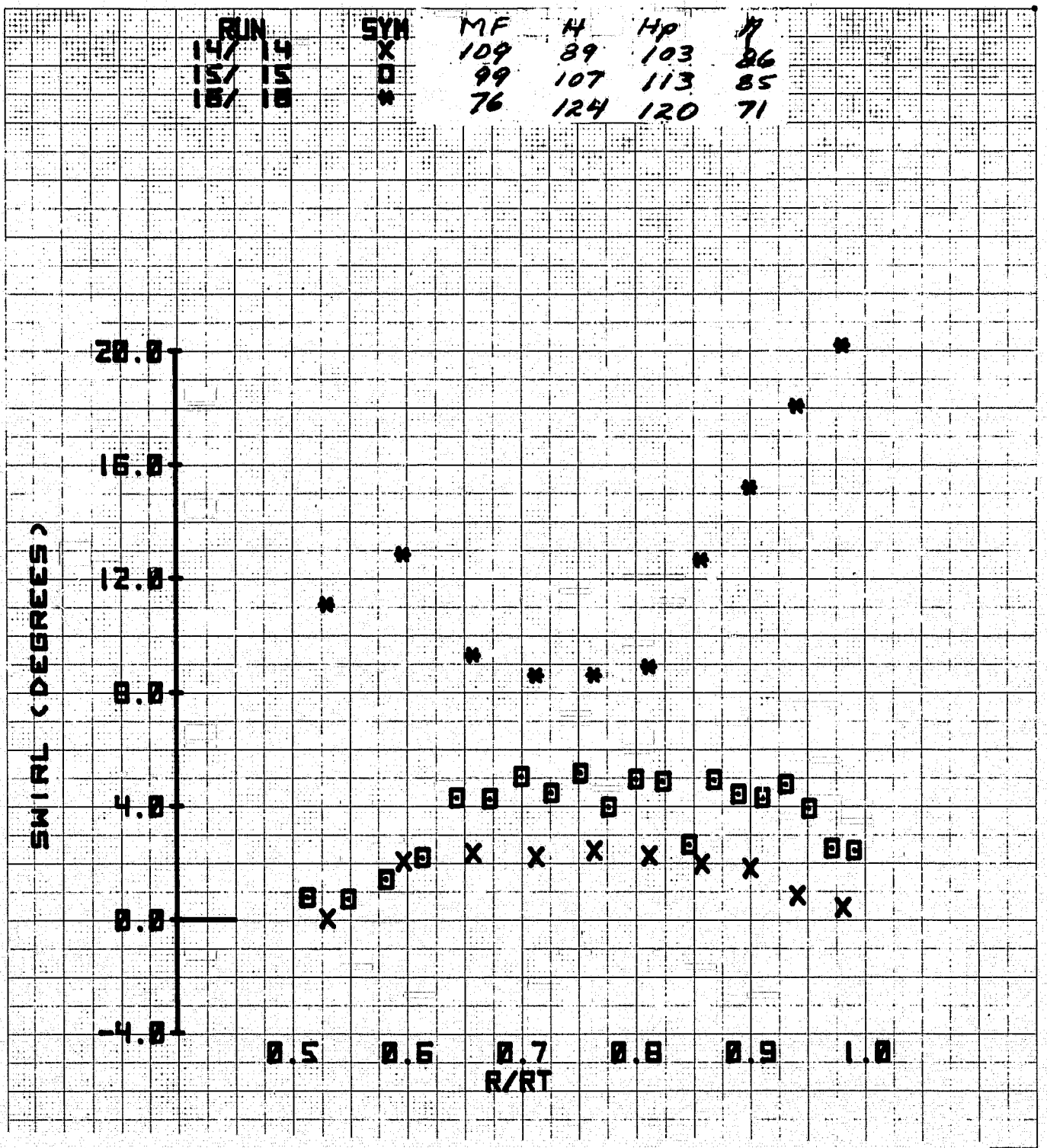

(c) Starboard azimuth - concluded.

Figure 34.- Continued.

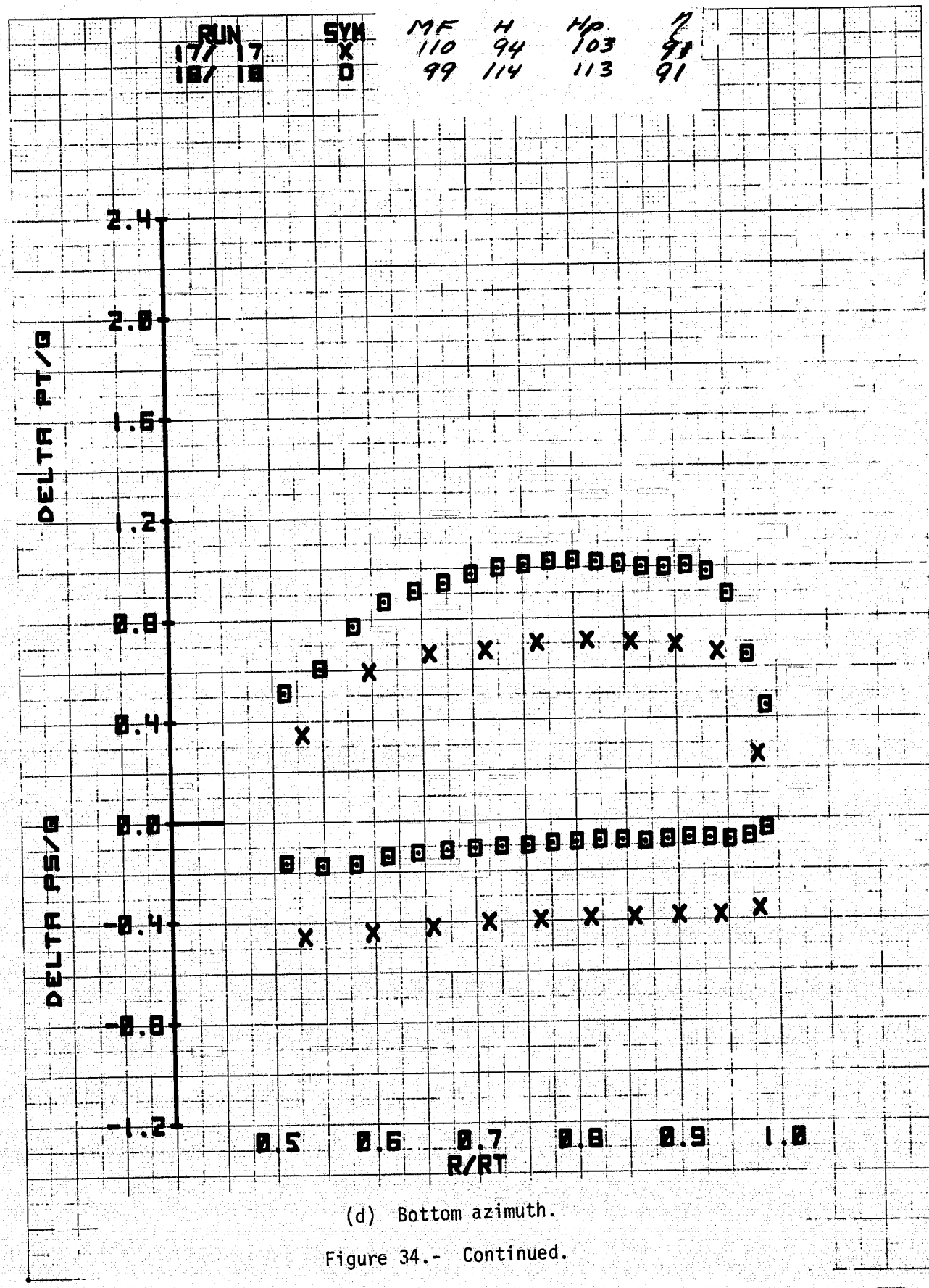

(d) Bottom azimuth.

Figure 34.- Continued.

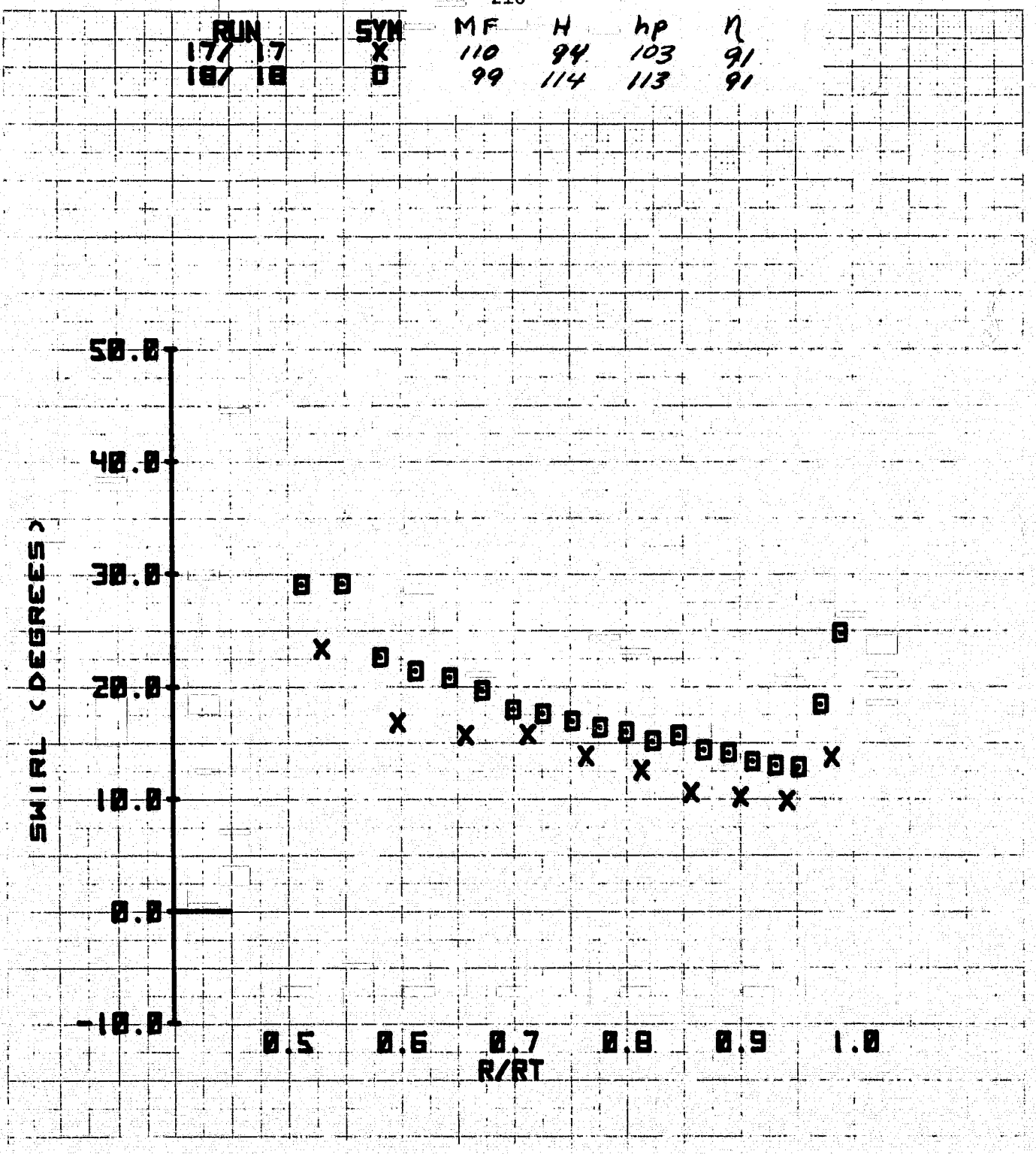

(d) Bottom azimuth - concluded.

Figure 34.- Concluded.

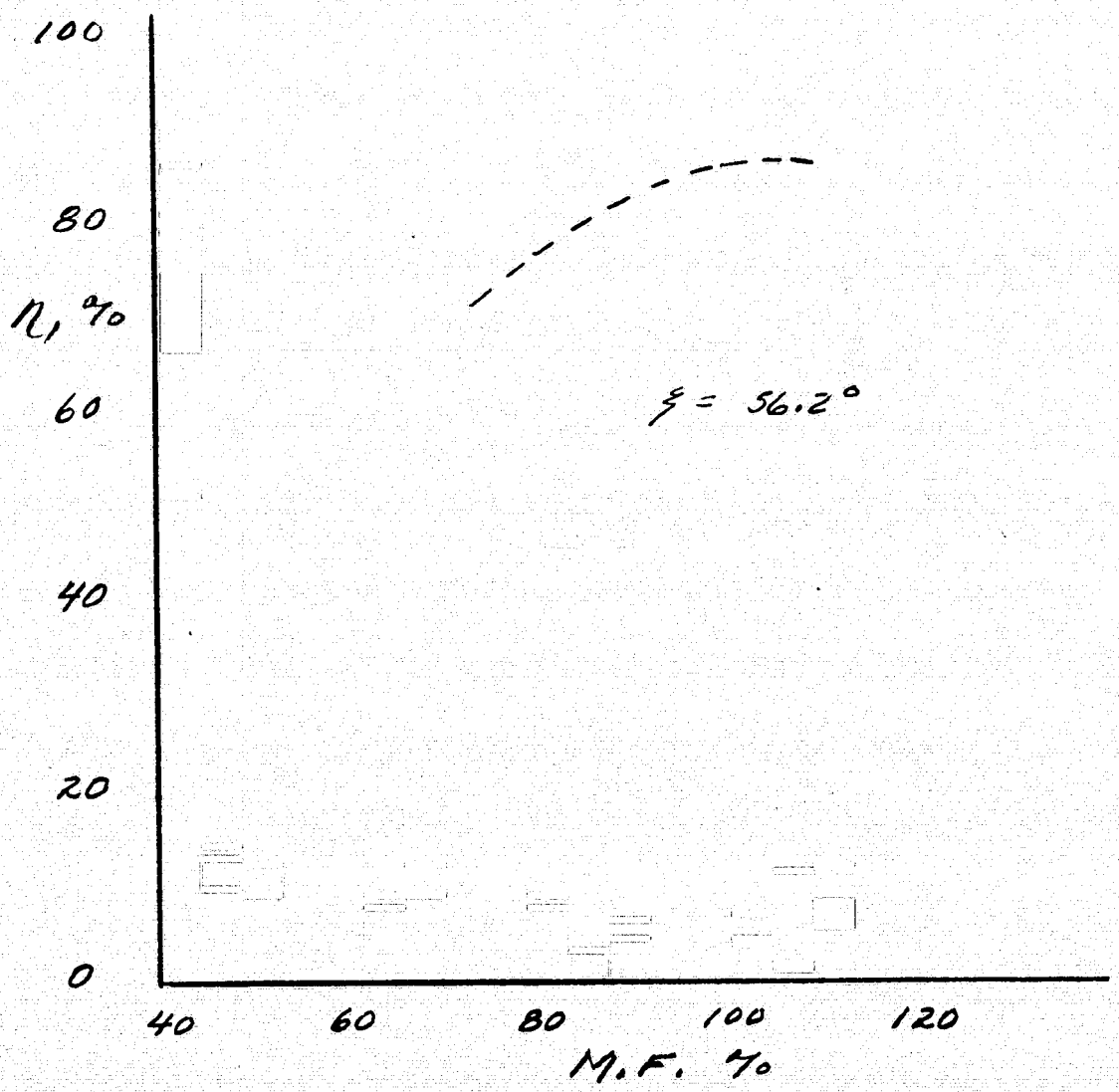

(a) High-speed fan

Figure 36.- Variation of efficiency with mass flow in percent of design.

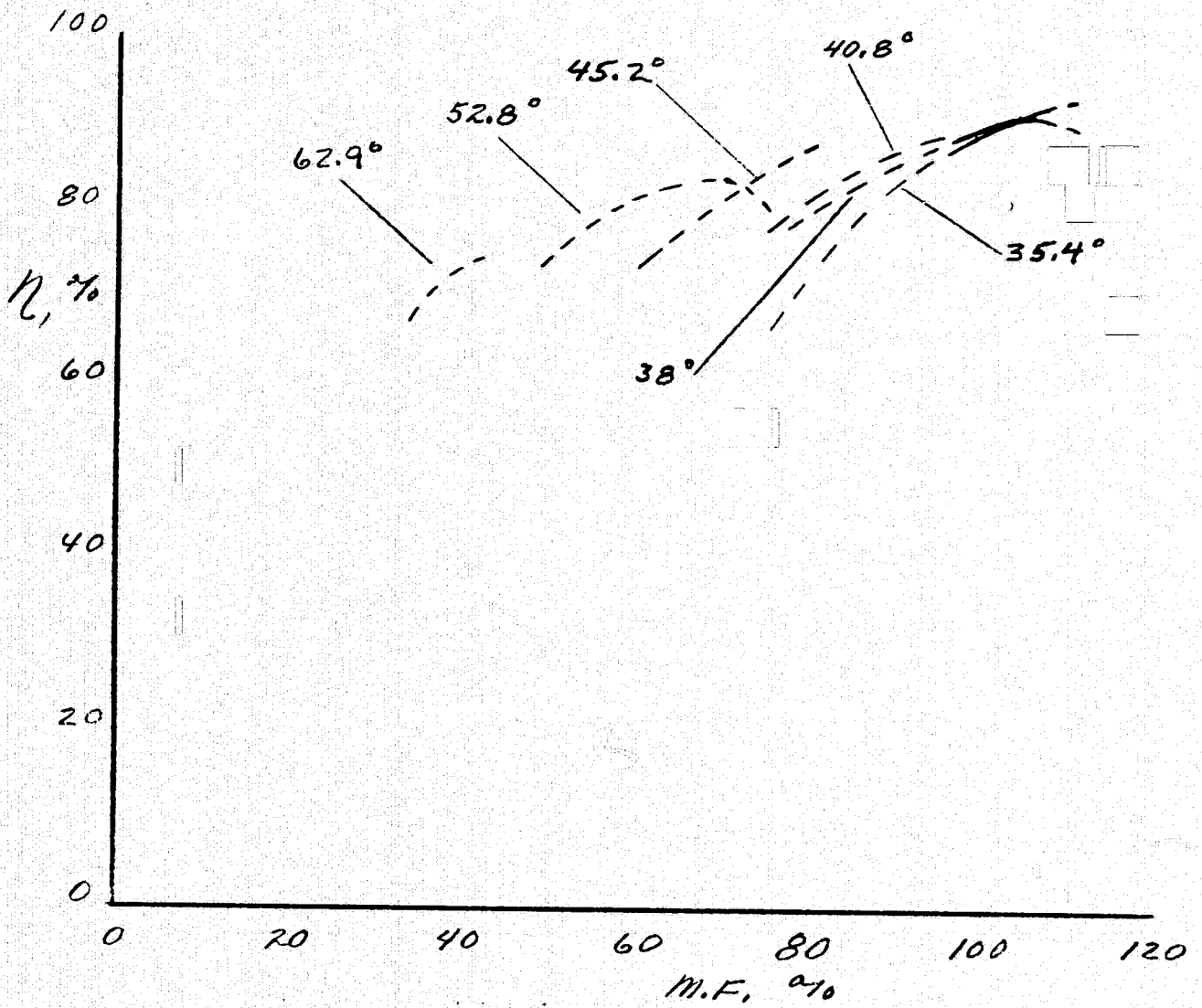

(b) Low-speed fan

Figure 36.- Concluded.

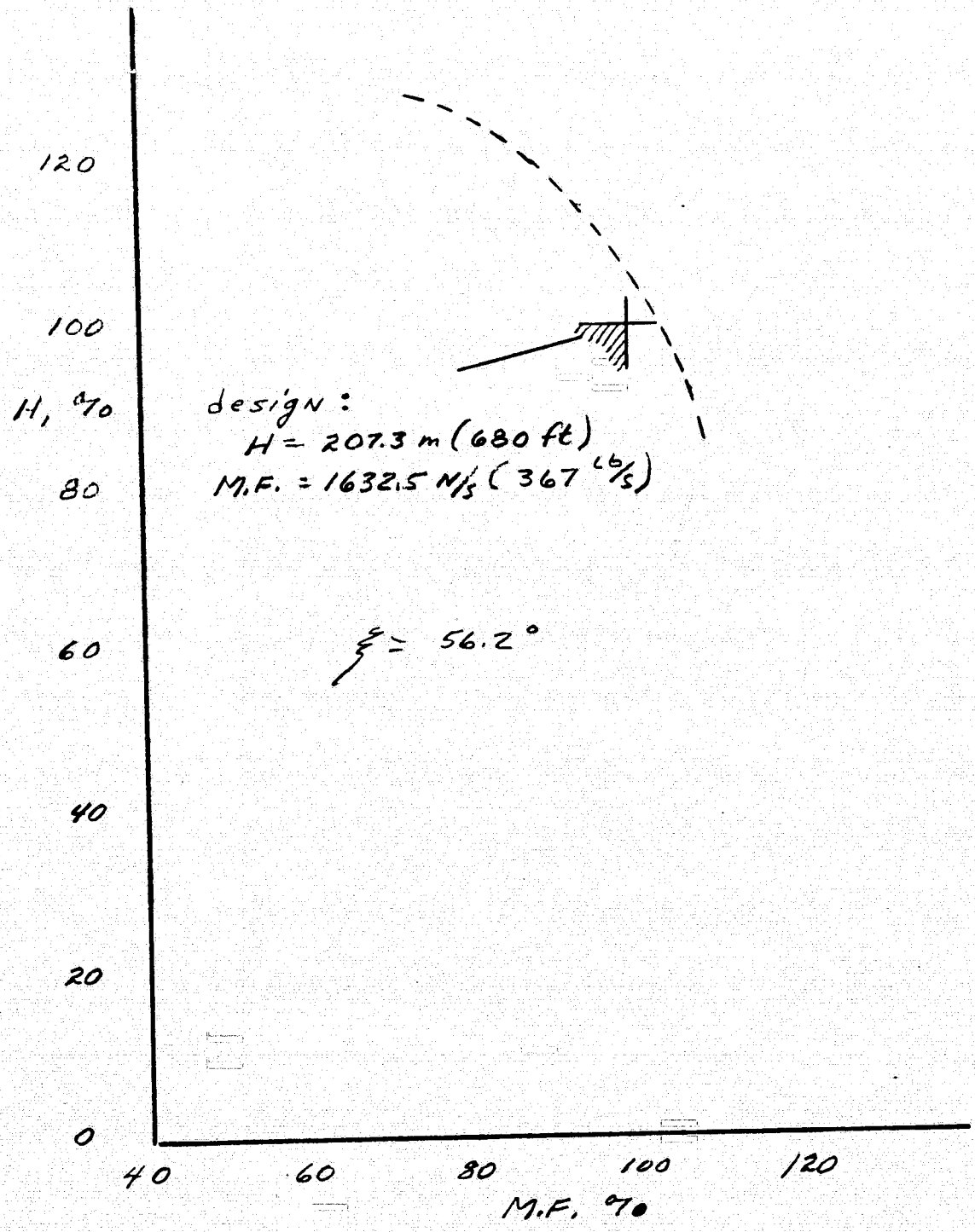

(a) High-speed fan

Figure 37.- Variation of pressure rise (head) in percent of design with mass flow in percent of design.

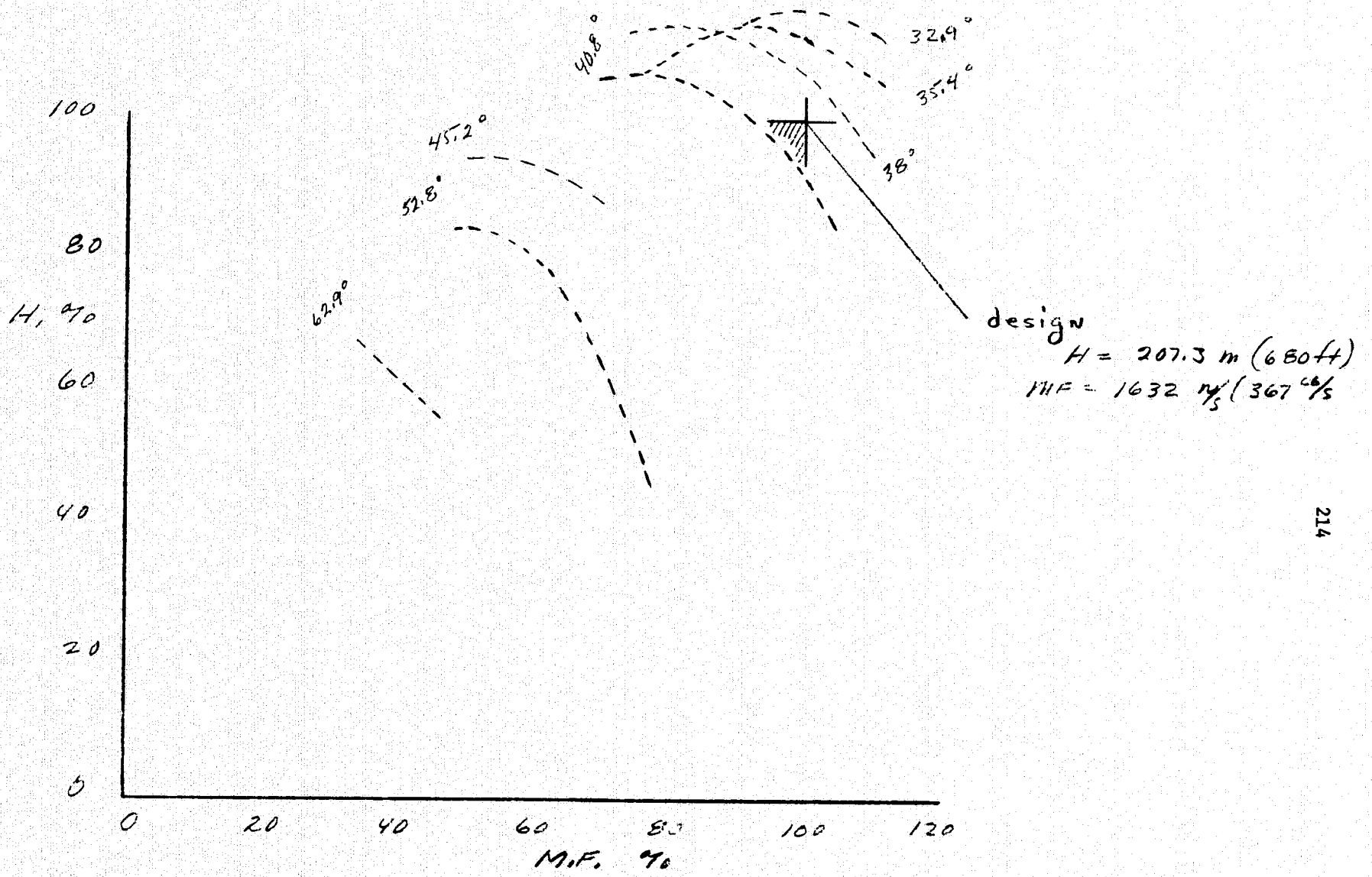

(b) Low-speed fan

Figure 37.- Concluded.

1. Report No.	2. Government Accession No.	3. Recipient's Catalog No.
NASA TM-73,175		

4. Title and Subtitle	5. Report Date
An Aerodynamic Investigation of Two 1.83-Meter-Diameter Fan Systems Designed to Drive a Subsonic Wind Tunnel	6. Performing Organization Code

7. Author(s)	8. Performing Organization Report No.
V. Robert Page, William T. Eckert,* and Kenneth W. Mort	A-6785
9. Performing Organization Name and Address	10. Work Unit No.
Ames Research Center, NASA and *Ames Directorate, USAAMRDL, AVRADCOM Ames Research Center, Moffett Field, CA 94035	505-06-31
	11. Contract or Grant No.
12. Sponsoring Agency Name and Address	13. Type of Report and Period Covered
National Aeronautics and Space Administration Washington, D.C. 20546 and U.S. Army Air Mobility R&D Laboratory, AVRADCOM, Moffett Field, CA 94035	Technical Memorandum
	14. Sponsoring Agency Code

15. Supplementary Notes

16. Abstract

An experimental, aerodynamic investigation was made of two 1.83 m (6 ft) diameter (0.15 scale) fan systems which are being considered for the repowered drive section of the 40- by 80-Foot Wind Tunnel at NASA Ames Research Center. One system was low-speed, the other was high-speed.

The low-speed fan was tested at various stagger angles from 32.9° to 62.9°. At a fan blade stagger angle of 40.8° and operating at a tip speed of 115 m/sec (377 ft/sec), the low-speed fan developed 207.3 m (680 ft) of head.

The high-speed fan had a design blade stagger angle of 56.2° and was tested at this stagger angle only. The high-speed fan operating at 191.5 m/sec (628.3 ft/sec) developed 207.3 m (680 ft) of head.

This report presents the radial distributions of static pressure coefficients, total pressure coefficients, and angles of swirl. The radial surveys were conducted at four azimuth locations in front of the fan, and repeated downstream of the fan. Data were taken for various flow control devices and for two inlet contraction lengths. The parameters of mass flow and fan rotational speed setting are tabulated for each configuration, along with the resulting fan system efficiencies.

17. Key Words (Suggested by Author(s))	18. Distribution Statement
Fans Fan stator Low pressure fans Fan performance Fan nacelle Fan rotor	Announced in STAR STAR Category - 02

19. Security Classif. (of this report)	20. Security Classif. (of this page)	21. No. of Pages	22. Price*
Unclassified	Unclassified	215	$7.25

*For sale by the National Technical Information Service, Springfield, Virginia 22161

☆U. S. GPO: 1977—792-704